



Thesis

For PhD degree

Thomas Laude

Speciality: Physics

Guest Laboratories:

- Mécanique des Sols, Structures et Matériaux, CNRS UMR 8579, Ecole Centrale Paris, Châtenay-Malabry, France
- National Institute for Research in Inorganic Materials, Namiki 1-1, Tsukuba, Japan
- University of Tsukuba, Department of Engineering, Tsukuba, Japan

Boron Nitride Nanotubes

Grown by Non-Ablative Laser Heating:

Synthesis, Characterisation and Growth Processes

**(Nanotubes de Nitrure de Bore Produits par Chauffage Laser Non-Ablatif:
Synthèse, Caractérisation et Mécanismes de Croissance)**

Presented on February 5th 2001 at the University of Tsukuba before the jury:

Prof. Eiji Kita

Dr. Yoshio Matsui

Prof. Hiroshi Mizubayashi

Prof. Ken-Ichi Ohshima

Academic supervisor

Dr. Hisanori Tanimoto

Presented on March 27th 2001 at the École Centrale Paris before the jury:

Prof. Patrick Bernier

Rapporteur

Prof. Hervé Biaußer

Rapporteur et Président du jury

Prof. Bernard Jouffrey

Directeur de Thèse

Dr. Odile Stéphan

Examineur

Dr. François Willaime

Examineur

Related Publications and Patents

- Long ropes of boron nitride nanotubes grown by a continuous laser heating, T. Laude, Y. Matsui, A. Marraud, and B. Jouffrey, Appl. Phys. Lett. 76, 22, 3239 (29 May 2000)
- “Procédé d'obtention de nanostructures à partir de composés ayant une forme cristalline hexagonale”, (Procedure to obtain nano-structures from compounds of hexagonal form), T. Laude, B. Jouffrey, and A. Marraud, French National Patent (1999)
- Extension to International Patent (2000)
- BN ropes and nanotubes: Elaboration and mechanical behaviour, T. Laude, B. Jouffrey, S. Gevrey, and A. Marraud, EUREM July 9-14, 2000
- Recent results on C and BN nanostructures, Jouffrey B., Laude T., Hamon A.L., Marraud A., International Kunming Symposium on Microscopy, Kunming, Chine, 2-5 juillet 2000
- Etude d'empilements de nanotubes de carbone en microscopie Electronique en transmission, Hamon A.-L., Bai J.B., Gevrey S., Jouffrey B., Laude T., Marraud A., Souche C., third Coll. SFmu Paris Sud 99, 28 juin-2 juillet 1999.
- Study of carbon nanotubes ropes, advancement in boron nitride nanostructures production, Jouffrey B., Hamon A.-L., Marraud A., Hebert-Souche C., Gevrey S., Laude T., Xth conference on Electron Microscopy of Solids, Warsawa-Popowo, 20-23 septembre 1999.
- Preparation and structure analysis of an ultra-hard cubic C_3N_4 predicted by a first principle calculation, S. Horiuchi, T. Ishigashi, T. Laude, and Y.G. Peng, NIRIM International Symposium on advanced materials (ISAM) 1999
- Electrical arc-discharge and laser ablation: two appropriate C and BN nanostructures synthesis methods, Hamon A.-L., Laude T., Souche C., Marraud A., Jouffrey B., Journet C., Bernier P., 14th Intern. Cong. on Electron Microscopy, Cancun, 31 august-4 september 1998. in Electron Microscopy 1998, III, 103-104.
- On EELS anisotropy problem in nanostructures: application to boron nitride, Jouffrey B., Souche C., Laude T., Hamon A.L., Marraud A., 5th NIRIM Intern. Symp. on Advanced Materials, Tsukuba, 1-5 mars 1998.
- Nano-objets : un exemple, les nanotubes., B. Jouffrey, A. Marraud, AL. Hamon, T. Laude, JB. Bai, “Centraliens” 523, 12-15, fev. 2001
- Elaboration et observation de nanostructures anisotropes (C et BN) en vue de l'étude de leurs propriétés mécaniques, Hamon A.L., Souche C., Laude T., Marraud A., Jouffrey B., Réseau Francilien de microscopie électronique, Paris 28 jan. 1998
- Elaboration de nanostructures de BN à partir d'un chauffage laser CO_2 : étude de nanotubes, cordes et rubans, Laude T., Jouffrey B., Gevrey S., Marraud A., 2ieme colloque GRD nanotubes, Strasbourg, 2-5 Novembre 1999
- Carbon and boron nitride nanostructures study, AL. Hamon, T. Laude, JB. Bai, A. Marraud, B. Jouffrey, NANOS 2000, Odeillo, 25-28 jan 2000

Further developments may be available at <http://membres.tripod.fr/thomaslaude> (check for relocation) or email: Thomas.LAUDE@nims.go.jp

History of this study and gratitude to the many people who helped

An interest in BN nano-structures at the lab. MSS-Mat (“Laboratoire Mécanique Sols Structures Matériaux, Ecole Centrale Paris”) dates to 1995. It started when C. Souche, PhD student in the team of Prof. Bernard Jouffrey, studied EELS spectra from some nano-sized BN powders [4.9]. At that time, BN onion powders were synthesised at the “Commissariat à l’énergie atomique” (CEA) by a different method: laser pyrolyse in a gas phase [4.7]. By January 1996, I had the opportunity to join the team, as part of solid state physics “DEA” (year preparatory to PhD) of Orsay-Paris XI University, and wrote an early report “Study of BN powders by high resolution TEM”.

The present PhD study started in the same team, in January 1997. The purpose was to get some knowledge on growth processes of BN nano-structures, in an experimental way. A low power CO₂ laser was long present in the lab. for educational purposes. Dr. A. Marraud and several students of the ECP previously started adapting it to the synthesis of nano-structured carbon. They especially equipped a vacuum chamber with a focal lens adapted to the infrared beam. During nine months in France, my work was to complete this installation and adapt it to BN. This was only possible with friendly advice from Dr. A. Marraud, and various help from many others in the lab., especially (but not only), I. Massip, A.L. Hamon and H. Souchay.

When deciding upon an experimental procedure adapted to a h-BN target, I was originally expecting to find nano-tubes in powders ablated from the target. This seemed reasonable, by similarity with the well-known ablation method. The first serie of experiments was collecting such powders, but it gave little positive results. (See chapter II.V.) It is only when noticing that some tubes were actually formed on target surface (only by October 98) that the main part of this study could really start.

By the time, I had the chance to be granted a Monbusho-scholarship from Japanese Government. This enabled me to pursue, from April 1998, the research at the National Institute for Research in Inorganic Materials, in Tsukuba, Japan (recently renamed “National Institute for Material Science”). I started to study in the team of Dr. S. Horiuchi but moved, after his retirement in April 1999, to the team of Dr. Y. Matsui. (The complete time of study at the NIRIM was 3 years, but several trips to France were necessary to study the synthesis.) The team of Dr. Y. Matsui is equipped with several electron microscopes of remarkable

capacities, especially, an “analytical” TEM 300 kV supporting a FEG and a PEELS, which was very useful for this study. Most observations and characterisations (which are the most time-consuming part) were undertaken at the NIRIM.

The team of Dr. Y. Matsui has been a very pleasant working atmosphere, always happy to help and most efficient to solve logistic problems. Special thanks goes to C. Tsuruta who provided excellent advice on TEM usage and to Dr. M. Uchida who was always ready to discuss scientific issues. SEM analyses were possible thanks to the technical support of Kosuda (and F. Garnier at ECP). The NIRIM is also a meeting point for many researchers enthusiastic about developments in BN nano-tubes. I would like to mention in particular Dr. O. Loutchev, with whom I enjoyed discussing the physics of tube growth, and who helped me to estimate the temperature gradient along a tube.

I would like to warmly thank Prof. K.I. Ohshima, for being my academic supervisor at the University of Tsukuba. For three years, I have been attending to weekly meetings of his team, and it was much of an emulating scientific atmosphere. A special notice is due to Dr. S. Weber, who preceded me, both in Prof. Ohshima’s team and in the NIRIM. His experience of Japan and his computer knowledge were much appreciable, as well as his coffee pauses.

Finally, I am much thankful to the members of the juries who have been reviewing this manuscript. It was quite a huge effort on the top of their busy schedules. Their many suggestions have improved the final version.

I feel obliged to all others who have been helping me during the four years of this research. A list of name is always unfair. Many more people contributed to this work with good will, advice, technical assistance, encouragement and, first of all, with everyday friendship. Thanks to them, these years have been quite an enjoyable experience.

Thomas Laude

Table of contents

3	Related Publications and Patents
4	History of this study and gratitude to the many people who helped
9	Main objectives for this study
10	Constitution of this manuscript
11	Chap. I: Introduction on nano-tubes and related nano-structures
12	I. Nano-structured particles of layered materials
12	1. Materials known to form closed nano-structures
15	2. Spherical and tubular morphologies
18	II. Properties and perspectives of applications
19	1. Some mechanical applications
20	2. Some chemical applications
20	3. Some electronic applications
22	III. Synthesis methods
22	1. For carbon
23	2. For BN
25	IV. Mechanisms of formation usually suggested
29	Chap. II: Continuous CO₂ laser apparatus
30	I. Presentation of the apparatus
30	1. Experimental procedure
31	2. Technical details
33	3. Setting procedures
34	II. Waist of the incident beam
34	1. Optical laws for Gaussian beams
35	2. Size and position of the final waist
36	3. Uncertainty on positioning
37	III. Equations for heat diffusion in the target
37	1. Introducing the formalism
41	2. Setting hypotheses
43	IV. Adapting laser power to target material
43	1. Stabilised temperatures in a large (or cooled) target
46	2. Increase of temperature due to the limited size of the target
47	V. Impurities of commercial h-BN
47	1. Smoke effusing from a raw h-BN target
49	2. Oxide impurities remaining on target despite outgasing

51 Chap. III: Techniques to observe and characterise nano-structures

52 I. Four instances of analysis techniques

- 52 1. Transmission electron microscopy (TEM) imaging (in a few words)
- 54 2. Electron diffraction on nano-tubes
- 56 3. Electron energy loss spectroscopy (EELS)
- 57 4. X-ray analysis of carbon ropes of SWNT

58 II. Analysis methods used here and their practical difficulties

- 58 1. TEM imaging
- 59 2. Electron diffraction inside TEM
- 60 3. EELS
- 61 4. Scanning electron microscopy (SEM)

63 Chap. IV: Standard experiment and global conclusions on physical processes

64 I. Standard experimental procedure

66 II. Geography on the heated surface

- 66 1 Three distinct zones
- 70 2. Frontiers between zones

73 III. Material from the crown (zone II)

- 73 1. Global aspect at low magnification
- 73 2. High resolution imaging of tubes (by TEM)
- 76 3. Electron diffraction patterns of tubes and ropes
- 78 4. EELS on ropes
- 79 5. Nano-polyhedrons (angular onions)
- 81 6. Tube extremities

81 IV. Global growth processes

87 Chap. V: Temperatures in the h-BN target

88 I. Typical times for target warming

- 88 1. Time for global warming
- 89 2. Is the semi-infinite medium hypothesis valid during the rising of temperature?
- 90 3. Time for first gradient rise
- 91 4. Temperature drop due to the formation of a liquid boron layer

92 II. Temperatures on front surface during target warming

- 92 1. Hypotheses
- 93 2. Modelisation
- 95 3. Temperatures at the end of a standard experiment
- 95 4. Is the temperature range constant between experiments?
- 98 5. Weaknesses of the model

103 Chap. VI: Mechanisms of growth around impact

104 I. Composition of the atmosphere around impact

104 1. Estimations of mean free path

105 2. Comparison of N and B fluxes

106 3. Boron flux versus temperature, from vapour pressure measurements

108 4. Diffusion of boron particles outside cavity

109 5. Particles depositing on target from gas phase

111 II. Evolution of nano-sized particles at high temperatures

111 1. Temperature gradient along a tube

116 2. What determines the evolution toward a tubular morphology?

124 3. Conditions for BN tube growth

129 Chap. VII: Influence of experimental conditions

131 I. Different durations of heating

131 1. Global influence of heating duration

133 2. Description of each samples

139 II. Influence of nitrogen pressure

139 1. Effect of nitrogen pressure on structures (HR imaging)

143 2. Influence of nitrogen pressure on global geography

146 III. Influence of laser power

149 IV. Heating in inert gas

152 V. Surface influence

155 General conclusions of the study

156 Some proposals for further Developments

157 Heating a pure boron target and a graphite target (unfinished study)

159 Are the present conclusions on mechanism extendable to carbon (and other diatomic material), and all synthesis method? (Free and opened discussion)

163 Annex 1: Mathematica language codes for calculation used here

169 Annex 2: Some physical datas: h-BN rod composition, JDPDS cards, $C(T)$, $k(T)$...

173 Bibliography

182 French and English Abstracts

Main objectives for this study

The original and main objective of this work was to study the formation of nano-tubes and related nano-structures. Such growth mechanisms are still under much controversy today. Very basic knowledge like, where does growth occur, what is the role of the atmosphere, what is the role of temperature (and phase transitions), is still not made clear. Furthermore, it is not made clear if there is a unique (or a limited number of) common process, independent of methods and materials. The origin of this low knowledge level is the fact that all present synthesis methods feature complex processes, hence fairly difficult to describe. Ablation methods usually use a pulsed laser beam (often a YAG) coupled with an oven heating. The resulting effects on a bulk material like graphite are many, and resulting structures are so dispersed in the apparatus, that growth zones are unclear. The same is true for an electric arc discharge on a bulk material.

To get some knowledge on formation processes, we tried to set up a new synthesis apparatus, which could be described simply. In violent synthesis method, like arc discharge and laser ablation/oven methods, the starting bulk material (graphite, boron or h-BN) is heated (under low pressure) up to the vapour temperature. We tried something similar but we used a laser that is both low-power and continuous. Such a beam induces no ablation, but a stable temperature gradient, radial along target surface. We will see that in that case, growth zone can be localised on front surface of the target and that, temperatures can be estimated in that zone. The experimental procedure was chosen as simple as possible: a h-BN target, with no catalyst, is heated under a static nitrogen atmosphere. The process can be discussed using a phase diagram of BN at high temperature and low pressure.

Although production was not the original purpose, the present method appeared to be efficient, compared to other synthesis methods for BN. Especially, tubes are longer than previous longest reports, by 20 times (lengths have been measured up to 120 μm). This was important because BN nano-tube synthesis methods were still quite inefficient compared to carbon equivalents. (The longest carbon nano-tubes produced by violent methods are also in the order of 100 μm .) Hence, some emphasis was given to the optimisation of the synthesis method and to the characterisation of the structures.

Constitution of this manuscript

Chapter I and chapter III-first part, are mainly reviewing the state of art in the field of nano-structures. Chapter III-second part describes the difficulties encountered when observing and characterising BN nano-structures. It is typically intended for those who will face the same problems, but it is also useful to understand some of the practical limitations of this work. Chapter II describes the apparatus. It is first useful for the description of the experimental procedure and for the introduction of the temperature formalism.

Chapter IV is a central chapter. It describes a typical heating and gives the global conclusions on the growth processes. The experimental description is continued in chapter VII, with the study of the influence of, heating duration (showing impact formation), and of other experimental parameters. Chapter V presents how to estimate temperatures on front surface of the target. Chapter VI gives some quantitative estimations of growth conditions near impact. It is separated in two parts. First part describes particles flying in gas phase. Second part, concerns the growth of structures on the hot target.

Chapter I

Introduction on nano-tubes and related nano-structures

Objective: We introduce tubular and spherical nano-structures of carbon and boron nitride, some of their possible applications, their usual synthesis methods, and some of the growth models proposed.

Abstract: Carbon and the structurally equivalent boron nitride, tend to form closed and hollow structures on the nanometre scale. Structures of concentric graphene-type layers are divided between spherical and tubular morphologies. In a tube, each layer features a helicity respectively to tube axis. Tubes tend to assemble cylinder against cylinder, as "ropes".

Proposed applications are many, but still little achieved. BN is much more chemically inert than carbon. It is especially stable against oxidation (up to 1000°C, when graphite burns from 500°C), which make it possibly suitable for high temperature applications.

For carbon, three synthesis methods are commonly used: the arc discharge method, the laser ablation method and CVD methods. CVD methods use a slow chemical deposition of a hydrocarbon over a template substrate. This typically produces extremely long nano-tubes, but very thick. In violent methods, like arc discharge and laser ablation methods, a fast growth is obtained by high temperature under low inert pressure. This produces all types of structures and thin tubes. For BN, most methods have been adapted from carbon equivalents. However, equivalent results were only obtained in recent days, by an arc discharge on boron rods in nitrogen, and by the present method of continuous laser heating.

Growth models are still under much controversy today. The main problem is to set starting hypotheses when processes involved in synthesis methods are complex. It is not obvious if tubes are growing in plasma or linked to a surface, or if tubes are growing open ended (...)

I. Nano-structured particles of layered materials

From a strict definition, a "nano-structure" is a particle of nanometer size. This designation has various meanings in literature like, cluster, big molecule, nano-crystal embedded in a matrix... In the specific case of layered materials, nanometre scale structures are topologically closed and hollow. They typically form tubular or spherical morphologies. It is especially the case for carbon, which presents a remarkable diversity of structures on the nanometre scale.

I.1. Materials known to form closed nano-structures

I.1.1 Graphite and hexagonal boron nitride (h-BN)

BN is a structural equivalent of carbon. It is mostly found in the same phases, and produces similar nano-structures. This is probably because the B-N bonding tends to be dipolar, and averages the number of electron per atom to 2 in the 2P layer, as for carbon. (carbon is $2P^2$, nitrogen is $2P^3$, bore is $2P^1$)

At low temperature and pressure, h-BN is a stable phase, although solid boron + nitrogen is clearly meta-stable. (A piece of boron under ambient air does not recombine.) The hexagonal phase of BN is very similar to graphite. (It is sometime called "white graphite", for its aspect.) Crystallographic parameters are almost equal ($\sim 1\%$). However, in h-BN, hexagons of neighbouring planes are superposed (B and N atoms in succession along the c axis), when in graphite they are shifted of half a hexagon.

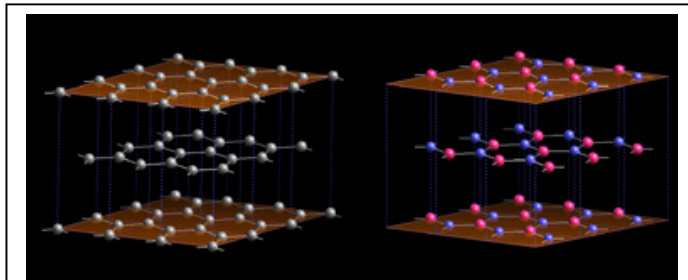


Fig. I.1 Similarities between h-BN (right) and graphite (left) The nearest neighbour distances (0.144 and 0.142 nm respectively) and the inter-layer spacings ($c/2 = 0.33$ and 0.335 nm) are almost identical. However, in h-BN hexagons of neighbouring planes are superposed (boron and nitrogen alternated along the c axis), when they are shifted of half a hexagon in graphite.

High-pressure phases of both materials (Fig. I.2-3) have been intensively studied for their interest as ultra hard material. Both materials are stable in a dense cubic phase (c-BN and diamond), although BN also forms a metastable hexagonal phase, known as wurtzite-type.

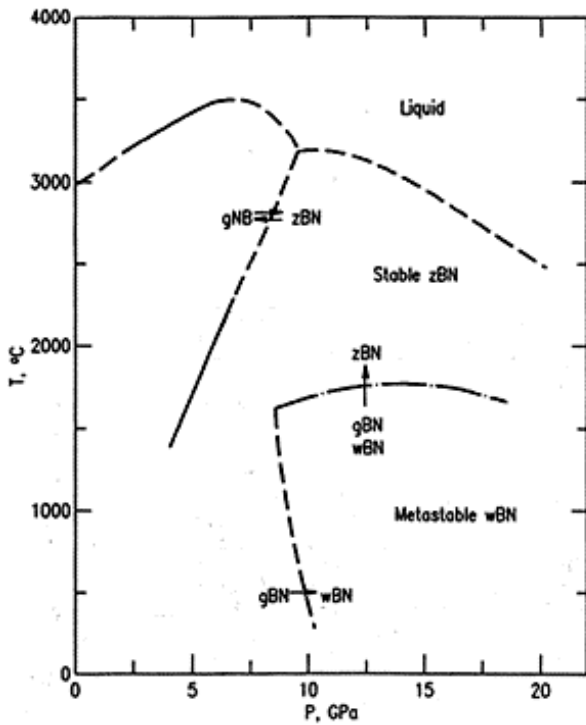


Fig. I.2 BN phases at high pressure according to [1.1.1] (unusual notations: gBN is hexagonal type, wBN is hexagonal wurtzite type, zBN is cubic type)

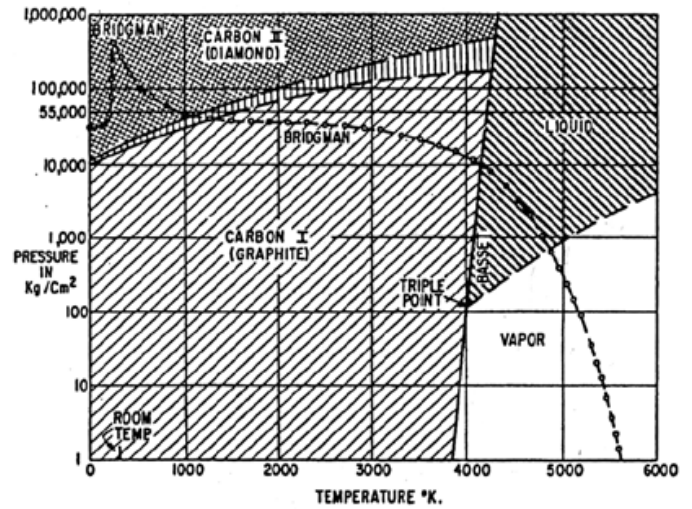


Fig. I.3 Phases of carbon according to [1.1.2]

BN, B, C Phase Diagram, at low Pressure

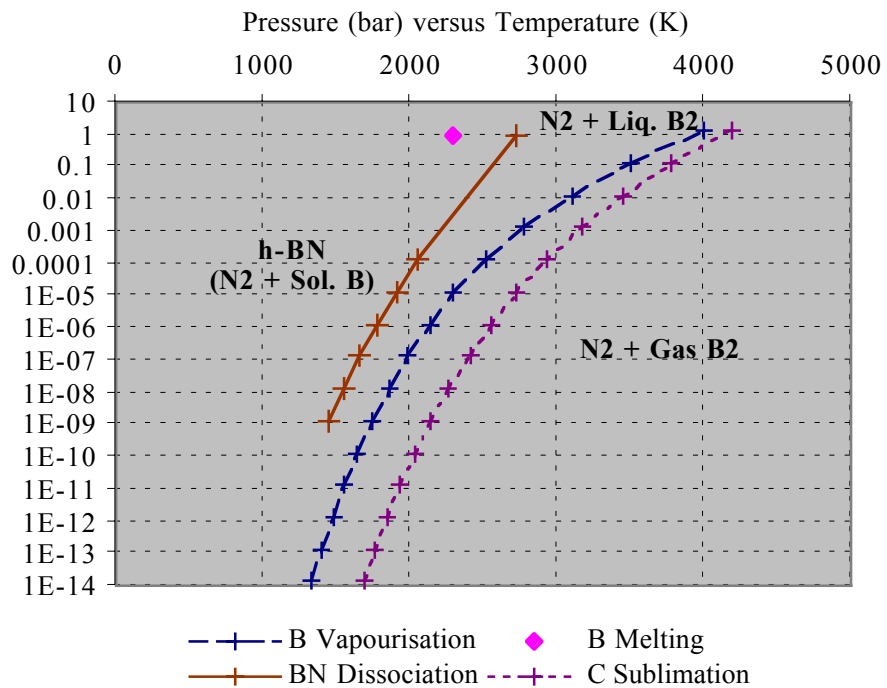


Fig. I.4 Vapours tension measurements for BN, B and C from [1.1.4] and most stable form of the B/N system as deduced.

At high temperatures but low pressures, which is the case of the present study, carbon and BN phases differ. BN tends to dissociate, when carbon is stable as a gas. Even at temperatures where both elements are vaporised, a BN molecule is unstable (JANAF, for 1 bar [1.1.3]). A phase diagram, for high temperature and low pressure, can be deduced from vapour pressure measurements of B, BN and C. [1.1.4] (Fig. I.4) Vapour pressure measurements give the equilibrium conditions of a vapour/liquid (or vapour/solid) interface, all phases being at uniform temperature. In the present case, when rising temperature over dissociation temperature of BN (2700 K at 100 mbar of nitrogen), elements are segregated as liquid boron and nitrogen gas. When getting over evaporation temperature of boron (3500 K at 100 mbar of B gas), boron and nitrogen are independent gases.

At high temperatures and high pressures (Fig. I.2-3), both carbon and BN are reported as a “liquid” phase. Isotropic carbon phase is known to be dominated by molecules, mainly C₂. Similarly, as liquid BN phase may be dominated by a stable BN molecule. The transition between segregated and liquid phase of BN, when rising pressure, is not known.

I.1.2 Merits of BN

BN is intensively used as a carbon substitute for its much higher chemical inertness, especially at high temperature. h-BN is non-reactive to molten metals (Al, Fe, Cu, Zn), to hot Si and stable against air oxidation up to 1000°C. (For comparison, graphite burns from 500°C, MoS₂ from 350°C and WS₂ from 420°C.) BN is typically an interesting material for high temperature applications. (See [1.1.5] and [1.1.6])

For nano-structures, oxidation actually starts at lower temperatures than for bulk material, because of bounding weaknesses at strong particle curvatures. Carbon tubes burn for 400°C [6.7.4], and WS₂ onions burn at 320°C [2.2].

h-BN also offers an electrically resistant counterpart to the semi-metallic graphite. This difference is more or less preserved for nano-tubes. BN SWNT are insulators, with a large band gap (~ 5.5 eV). Its resistive character is not much affected by the structural specificity of the tube (helicity, defects, multi-layering...). [4.12.2] By contrast, carbon SWNT are semi-conductors or conductors depending on their helicity and diameter. Multi-layering and rope assembling tend to increase conductivity. [6.10] However, practically, it is not yet possible to synthesis selectively SWNT with a specific structure.

I.1.3 B/C/N tubes [5] and other layered materials: MX₂ and MCl₂ [7]

Substitution of BN in carbon nano-tube has been studied by a number of authors. Tubes with various concentrations of elements have been obtained. C and BN tend to segregate as different hexagonal planes, rather than being uniformly distributed in one plane.

The metal dichalcogenids family, MX₂ (M is a metal: Mo or W. X is a dichalcogen: S, Se or Te.), and the metal chloride family, MCl₂, are also layered material with a hexagonal arrangement intra-layer. Some onions and nano-tubes tubes have been found in tungsten disulphide and molybdenum disulphide (WS₂ and MoS₂). Such tubes were short and thick. Similar onions have been found in NiCl₂.

I.2. Spherical and tubular morphologies

On nanometre size, structures are formed of concentric hexagonal layers, folded as tubes or as spheres. They are not encountered as a few structures of real repeatability, but rather as wide range of structures. Therefore, classifications are subjective and denominations partly differ from author to author.

I.2.1 Tubes

Tubular forms of carbon, commonly called “Nano-tubes”, are known since the development of high resolution TEM. For instance, they were already described by A. Oberlin and M. Endo. [6.4.1], as early as 1976. (They also proposed a growth model still relevant today.)

Tubes are cylinders of concentric hexagonal layers (one to several tens of layers), with diameter in the order of the nanometre. Tube lengths are macroscopic, so that the aspect ratio (length / diameter), can be up to 10⁵. For energy considerations, tubes are believed to be made of several concentric layers, rather than of one spiralling layer. (Because of the cost of the layer edge inside and outside the tube.) This is commonly admitted, although it was not definitely confirmed by TEM imaging.

Boundary limits after one rotation around the axis constraint a limited number of choices for the helicity of the hexagonal layer relatively to tube axis. Indeed, there must be a continuity of hexagons on the cylinder. This limits the number of possible choices for the helicity. Any vector joining two equivalent atoms in a graphene plane can form the circumference of a tube. (Fig. I.6) (Of course, this only has a physical meaning if the diameter of the tube is neither too

small nor too big.) Then, the axis of the tube is defined perpendicular to this vector. Each vector in the graphene plane defines one helicity of the tube around its axis. There are two specific cases of helicity: when the vector is parallel to a border of hexagon (“Armchair” type) and when the vector is perpendicular to a border of hexagon (“Zigzag” type). (Fig. I.6-7)

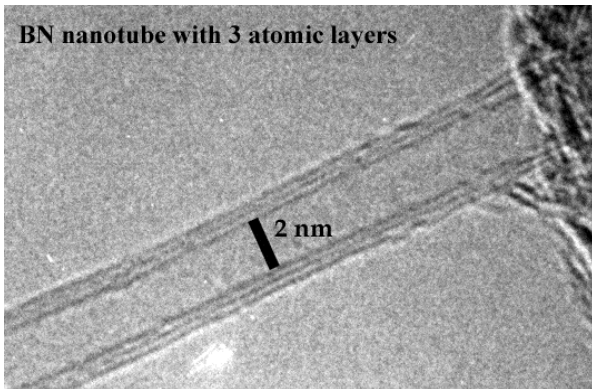


Fig. I.5 high resolution TEM image

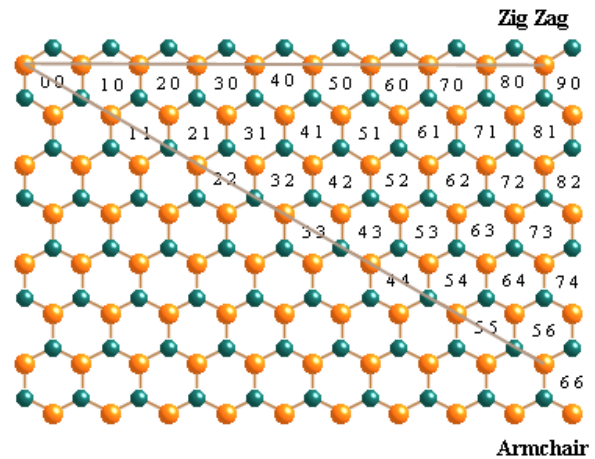


Fig. I.6 Possible choices of circumference to close a hexagonal layer as a cylinder, satisfying the continuity of hexagons. Each choice defines an helicity. (Standard notation with two indexes for each choice)

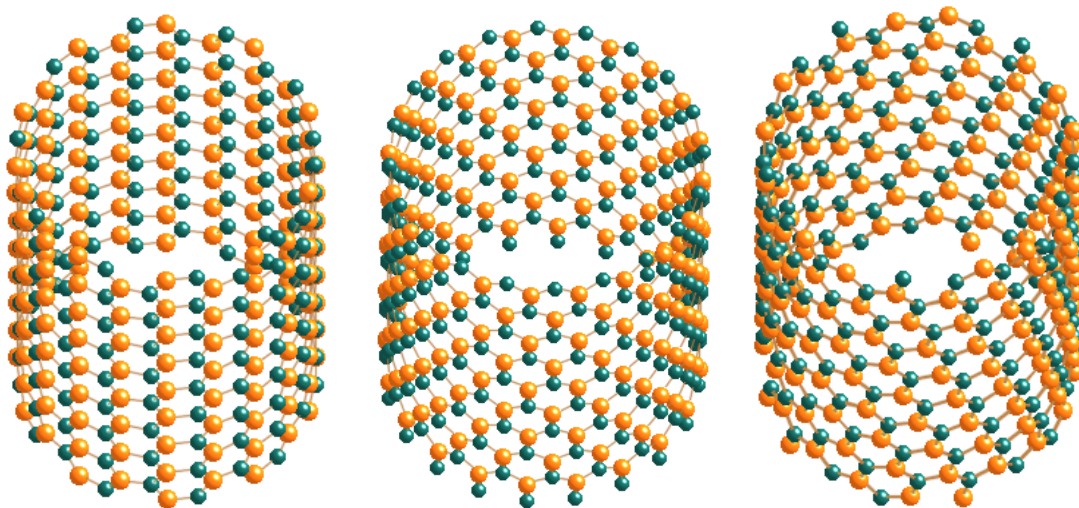


Fig. I.7 Three types of BN SWNT Armchair (10,10), Zigzag (20,0) and a non-specific helicity (15,5). (Simulation applet by S. Weber)

In a multi-walled nano-tube (MWNT, by opposition to single-walled nano-tubes, SWNT), it is usually observed that layer inter-distance respects more or less the interlayer distance of graphite. A disordered layer piling (“turbostratic” graphite) would cause a slightly wider interlayer distance. This means that a tube has to find some accommodations to respect the relative position of two neighbouring layers. Some compensation may be possible through defects, or through a change of helicity between layers. (See [6.16.3] for accommodation considerations.) The inter-layer accommodation of BN may be different from carbon, because hexagons are superposed and not shifted of half a hexagon between layers.

1.2.2 Onions (typically 10 to 300 nm)

“Onions” are particles roughly rounded, constituted of atomic layers piled as an onion. Morphologies are various. Often, an onion is closed by facets and angles, rather than by a continuous curvature, forming a “nano-polyhedron”. This is especially true for diatomic materials like BN, with no “pentagon flexibility”: Pentagons allow a hexagonal plane to curve. But for BN, the formation of a pentagon is thought to be energetically costly (because of a B-B or N-N bounding).

Onions are often irregular and full of defects. This is probably because of the difficulty to accommodate the interlayer constraints with a spherical curvature. (See [6.16.3].) Onions probably feature disordered piling of hexagonal layers (turbostratic). Highly disordered onions are known to exist in common carbon soot. These are very large (several microns), but share the same topology, being spherical and hollow.

1.2.3 The fullerene family [8]

The carbon fullerene family is a group of molecule, with chemical formula C_{2n} , ($20 < n < 50$). Amongst those, a C_{60} molecule (Fig. I.9), shaped as a “football ball”, 1 nm in diameter (dense sphere model), is the most symmetrical and the most stable structure. It is the one obtained in highest yield for most synthesis methods (usually followed by the C_{70} , shaped as a “rugby

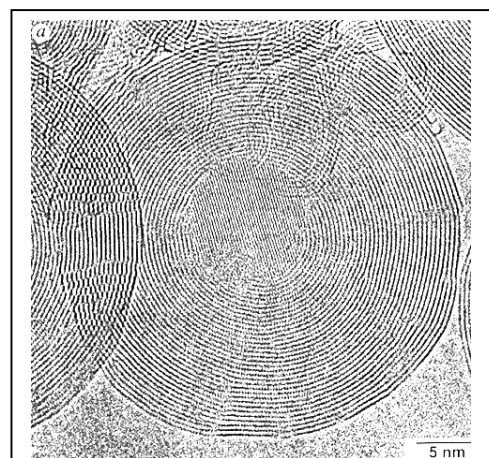


Fig. I.8 Carbon onion with a diamond core [6.9.1] The particle was heated at 700°C and irradiated by an electron beam at 1.25 MeV. After this treatment, the shell is perfectly spherical.

balloon”).

For BN, pentagons are thought to be energetically costly. However, square and octagon may be viable in a rounded structure, so that some BN closed molecules ~ 1 nm large, have been proposed to exist. [4.11.1]. Those structures are described with sharp angles and low symmetry. However, for such a dimension, the experimental characterisation by TEM imaging of an individual structure is not affordable. (No lattice of such particles was observed.)

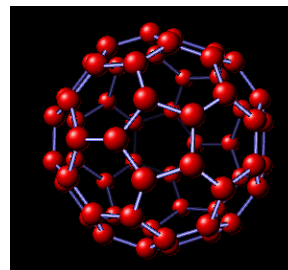


Fig. I.9 The C_{60} molecule

I.2.4 C_{60} and carbon SWNT lattices

C_{60} can assemble in a crystalline lattice. It is simple cubic at low temperature, and becomes FCC over 250 K. This is because, at high temperatures, molecules are free spinning, and become isotropic spheres to each other.

Similarly carbon tubes have a natural tendency to self assemble cylinder against cylinder, as a “rope” (also called “bundle”). Carbon SWNT with uniform diameters, form a non-directional 2D triangular lattice in the section of a rope. (See for instance [6.2.8], [6.3.1] and [6.8.3])

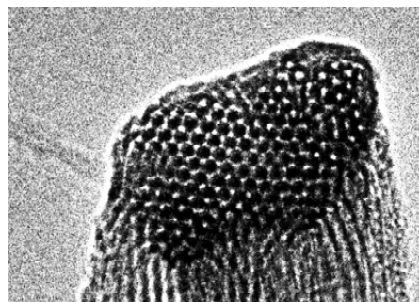


Fig. I.10 A rope of carbon SWNT
(Photo B. Jouffrey)

II. Properties and perspectives of applications

Nano-structures provide interesting perspectives of applications because of their unique properties. Many possible developments have been suggested (mainly for carbon nano-tubes), although none of them is at a stage of commercialisation yet. One practical difficulty is, obviously, the manipulation of individual structures on the nanometre range (as required for nano-electronics, for instance). This is possible in laboratory conditions, at the tip of a scanning microscope for instance. However a large-scale manipulation of individual nano-objets is not achieved. Another difficulty is that, synthesis methods are still little efficient. Similar results can now be obtained for BN and carbon tubes. But, production in kg quantities at low cost is still not achieved. Also, the technical ability in synthesising selected structures is still limited, because most synthesis methods produce particles with a large structural

diversity. There is a need to develop post synthesis techniques for particle segregation.

Note: POSSIBLE TOXICITY. It should be stressed that it is not yet clear if nano-tube-based material have some toxicity. As a volatile fibrous material, nano-tubes may cause damage to lung cells, as it is famously the case of asbestos fibres.

II.1. Some mechanical applications

II.1.1 Composite materials

The strength of a composite material is linked to the strength of the fibres embedded in the matrix. As both carbon [6.12] and BN nano-tubes (1.2 TPa [4.10]) have an exceptional elastic modulus, using them as reinforcement fibres is a possible way to obtain ultra resistant materials. For its good chemical inertness, especially to oxygen, BN is a good candidate.

The Typical problem encountered practically is the adherence at contact surface between tubes and matrix material. Tubes may actually slip along the matrix material. This may be worse for ropes, in which tubes can slip on each other. (Tubes with a spherical extremity, as synthesised by the present method, could lower this problem, because spherical extremities may fix as anchor in the matrix.)

II.1.2 Solid lubricants

Solid lubricants are used when conditions do not allow the usage of standard lubrication oil. This is typically under vacuum or in oxidising atmosphere. h-BN, graphite and WS₂ are already intensively used as a solid lubricant in industry. h-BN is especially interesting for having both a very low friction coefficient and a high range of suitable temperature in air (up to 900 °C). [1.1.5] Nano-onions powders are exceptional solid lubricants, because onions act like nanometric ball bearings. This was demonstrated for powders of WS₂ nano-onions [2.1][2.2], but it is probably true for the other materials.

II.1.3 Filters, Tissues, insulator materials...

As any fibres, tubes and ropes could be applied to filters, tissues, thermal or acoustic insulator, or any other fibrous material. The exceptional porosity of such a material, due to the high aspect ration of nano-tubes, enables a filtering of much smaller particles, and/or a higher crossing flux (because the efficient collision surface is very small). For instance, this could be

applied on a car, to filter gases in the exhaustive pipe. Other properties of nano-tube tissues are not obvious (thermal conductance, or resistance to tearing...). Further studies are clearly needed, but this first requires an improvement of mass production.

II.2. Some chemical applications

II.2.1 Nano-shielding

Nano-tubes and onions of carbon have the ability to shell many materials inside their structure. It has been confirmed for many simple elements (Y, Bi, Gd, Ti, Cr, Fe, Zn, Mo, Pd, Sn, Ta, W, Gd, Dy, Yb, Pb, Mn, Co, Ni, Cu, Si, Ge...) and for some compounds. [6.7.6]. This may be of some interest, to protect nano-material from their environment, especially from oxidation. For instance, magnetic particles for data storage could be protected from air. It also offers a possibility to synthesise diverse hybrid nano-object, like metallic nano-rods, inside a tube cavity.

II.2.2 Hydrogen containers

Industrial age is causing an exponential growth of CO₂ concentration in the atmosphere, mainly due to extensive use of fossil energy sources. The harmfulness of such a change on the ecosystem, first expected as a “global warming effect”, makes research on non-polluting energy sources a priority. Hydrogen is the ideal candidate, because its combustion produces no other release than water. Its energy per mass is higher than usual hydrocarbons. Furthermore, it is present in high quantity on earth.

Practically, the main limit to the commercialisation of hydrogen motor is the difficulty for a safe way to store hydrogen. Nano-tubes and nano-onions are thought to be a safe storage, because their cavity can absorb hydrogen molecules. Such storage was measured with variable success, between 0 and 10 wt % in carbon tubes. (See [2.10] for instance.)

II.3. Some electronic applications

II.3.1 Nano-transistors

The conductivity of a carbon SWNT depends on its diameter and helicity, hence on its structure [6.10.4]. Different carbon nano-tubes can theoretically form a nano-sized junction, which is a first step toward a "nano-electronic". A nano-transistor was realised through the

body of a carbon nano-tube. [2.4]

One practical difficulty is the manipulation on nanometre scale. A focused ion beam (FIB) can be used to make the contact electrodes, but not on a large production scale. Another problem is to synthesise carbon tubes with a specific structure. This is not affordable with present synthesis methods.

The case of BN is different, conductivity is little dependent on structure. But on the other hand, it is an insulator of large band gap ($\sim 5\text{eV}$, like diamond). To be used as a conductor, it should be efficiently doped. Diverse possibility of hetero-structures, like C/BN or C/Si are studied. (See [2.6], for instance.)

II.3.2 AFM / STM Tips

Carbon nano-tubes are very thin. They can be used as a nano-tip in both atomic force microscopy (AFM) and tunnelling microscopy, to improve the resolution of the image. Furthermore, the exceptional elasticity of the tip avoids the damage from contact surface. It also enables an improved resolution of surface irregularities, because the tip can enter small cavities. Such a carbon nano-tube tip was proved to be feasible [2.7].

One problem is the reactivity of the tip with surface material. Carbon forms bonds with many materials. BN can be used instead to avoid this problem, in the case of AFM. (BN is probably not suitable for tunnel microscope, because of its electric resistance.)

II.3.3 Electron field emission

Electron sources are essential for screens or electron microscopes. Carbon nano-tubes can emit a high electron field emission current from their tip, when submitted to a bias voltage. The threshold voltage is exceptionally low because of the tip curvature. Emitting surfaces were realised by different post-synthesis methods. A prototype display and a lighting element were already produced. Hence, this application may seem the closest to commercialisation at present. However, many technical problems are still to be solved, regarding emission surface fabrication and, the understanding of the emission phenomenon.

Carbon nano-tubes are also interesting for electron microscope emitters, because the emission from a single nano-tube is intense and very coherent. The energy dispersion of such a beam is of the order 0.2 eV , and the life length of a single tube was found in the order of 2 months, in

emission conditions. See [2.12 to 15]

III. Synthesis methods

III.1. For carbon (See especially [6.1.4].)

For carbon, synthesis methods have been intensively studied, and significant achievements have been obtained in terms of quantity, structure quality and variety. Three methods are commonly used, the arc discharge method, the laser ablation method and CVD methods.

In CVD methods, a slow (up to several days) growth is obtained by a chemical deposition on a template surface. A gaseous hydrocarbon (acetylene, ethylene, benzene...) is decomposed by high temperature (typically 700 °C) over a non-uniform substrate (for example, iron nanoparticles embedded in silica). This can produce extremely long (~ mm) multi-walled nano-tubes, but tubes are very thick. No structure other than tubes is produced. [6.4]

In violent methods, like Krätschmer arc discharge method [6.2] and laser ablation method [6.3], a fast (~ a few minutes) growth is obtained by submitting the material to a strong heating in inert gas at low pressure (Typically 50 - 700 mbar of helium, argon...). In the arc discharge method, the hot temperature is obtained by joule effect in a graphite electrode. (Current is typically 50 A.) In laser ablation methods, a graphite target is ablated by a high power pulsed laser (often a YAG), and simultaneously, the target and the ablated plume are oven heated. (See also a method by continuous laser ablation. [6.3.3]) Ablated powders are transported to a cool collecting stage, by a carrier gas.

For carbon	Slow methods (several days)	Violent methods (several minutes)
Production	<ul style="list-style-type: none"> • Large arrays of aligned tubes • Tubes are long (~ mm) but thick (~ 20 nm) 	<ul style="list-style-type: none"> • Mix of all morphologies: thin tubes, onions and fullerenes produced at once • Tubes are thin (~ nm) but shorter (< 100 μm) and tend to be in ropes of SWNT

Violent methods produce a wide range of carbon morphologies, together in one run, including tubes, onions and C₆₀. Tubes are shorter than for CVD method (~ a hundred microns), but they are much thinner. Single wall nano-tubes (SWNT) are commonly produced by adding some metallic particles, thought to act as a “catalyst”. Tubes are often found assembled in

ropes of SWNT. The fact that both methods produce the same structures suggests a common growth mechanism.

III.2. For BN

For BN, most methods have been adapted from carbon equivalents. However, equivalent results (thin tubes over the micron scale, ropes, quantity higher than what is needed for electron microscopy observations...) were only obtained in recent days, by an arc discharge on boron in nitrogen atmosphere and by the present method of continuous laser heating.

III.2.1 Arc discharge methods

The low electric conductivity of h-BN forbids using it as an electrode in an arc discharge method. But several alternatives have been found:

- Arc discharge on a hollow tungsten electrode filled with h-BN [4.2.1]

This was the first method to produce thin BN tubes. Tubes are in the order of 200 nm and have a W particle at their extremity.

- Arc discharge on a HfB₂ electrode in N₂ [4.2.2]

This was the first report of BN SWNT. (However, a diffraction pattern is needed to ensure the presence of SWNT. High-resolution images of thin BN tubes are sometimes difficult to interpret. See Chap. IV-IV.2.2.) Tubes are in the order of 700 nm, and mixed with Hf particles. Quantity produced is not known.

- Arc discharge on a ZrB₂ electrode in N₂ [4.2.4]

This method is a variant of the previous method, using Zr instead of Hf. Tubes are in the order of 100 nm and mixed with Zr particles.

- Arc discharge on B electrode in N₂ [4.2.6]

This method produces a macroscopic quantity of BN bi-layered tubes, several micron long. It also produces "nano-cocoons", very similar to the present BN nano-polyhedrons with a boron core.

III.2.2 Laser ablation method [4.3]

A laser ablation method for BN has been reported, using an excimer (pulsed) laser on h-BN target, under helium or nitrogen. This produces thin tubes merged to the bulk. Tubes (~ 100 nm on photos) are mixed with Ni or Co, depending on use of catalyst. Quantity is not known, but yield is reported high.

III.2.3 Oven heating

- Oven heating (1100 °C) of $B_2H_6+NH_3+ZrB_2$ [4.4.1]

The first method reported for BN tubes. It produces large filaments, quite long (~ 10 μm) mixed with ZrB_2 particles.

- Oven heating (1200°C) of B and L_i in a BN crucible in N_2 atmosphere [4.4.2]

This is not strictly speaking a synthesis method, but conditions in which some BN tubes (~ 30 nm on photos) were observed growing from the bulk. Tubes were found on boron amorphous particles.

- Oven heating (1000°C) of boron previously ball milled in ammonia [4.4.3]

This method produces large BN filaments (~ 5 μm).

III.2.4 Other methods

- The present method of continuous laser heating
- A high pressure compression (5-15 GPa) of c-BN micro-crystals in a diamond anvil cell induced by laser heating [4.5]

This is not, strictly speaking, a synthesis method, but conditions in which some tubes (~ 30 nm on images) have been found growing from an amorphous BN matrix.

- Plasma jet on a h-BN target in inert atmosphere [4.8]

Tubes are presents in powders ejected from the target. They are relatively thick (~ 20 nm) and in the order of 1 micron long.

- Growth on carbon tube templates in oxidising atmosphere [4.6]

This method grows BN tubes from carbon tubes, through an oxidation process. On carbon SWNT ropes, this transformation is reported to be only partial.

IV. Mechanisms of formation usually suggested [3]

Growth mechanisms of nano-tubes and related structures are still under much controversy today. Quite different models have been proposed for different synthesis methods (for carbon and BN). The difficulty is that, prior to any growth model, the researcher must state some physical hypotheses about growth conditions. This is difficult because of the inherent complexity of most synthesis apparatus. When the zone of growth is unknown, temperature and chemical conditions are also unknown. In addition, observations are mostly undertaken post synthesis so that, patterns as observed may be very different from patterns as growing.

When physical hypotheses (typically, the open-end hypothesis) are admitted, two types of study may be undertaken. Some studies are structural considerations, typically based on first principle calculations. This provides a precise estimation of a structure behaviour, but only for some specific structures, like a SWNT. Other studies concern the kinetic of the growth, which is of more general validity, but only allows rough estimations.

IV.1. Model “condensation on surface” for the growth of carbon tubes by CVD methods

This model was proposed as early as 1976. [3.1.1] Because tubes are found as aligned array on the template surface, it can be stated that tubes grow with one end fixed to the surface. Tubes are fed by carbon atoms from gas phase, because only molecules in the gas phase contain carbon. Therefore, carbonaceous particles decompose and their carbon atoms deposit on surface (on substrate or on tubes bodies).

Furthermore, tubes are mostly found with a large metallic particle at one extremity, so that, tube growth is often thought to be catalysed by these particles. Particle would “help” the capture of carbon atoms and the incorporation inside the tube. Two variants are commonly proposed, where the metallic particle is at the free extremity or at fixed extremity.

IV.2. Model “condensation in plasma” for the growth of carbon tubes by laser ablation methods [3.1.11]

For the ablation method, a hypothesis of a growth in “all in plasma”, by condensation of carbon vapours is usually proposed, although the zone of growth has not been localised

precisely. (Tubes could eventually grow on target surface and be ejected with the ablated matter. See [3.1.13] for a study of the laser plume.) This mechanism was originally proposed for C_{60} , and is proposed, as an extension, to all carbon structures. For instance, tubes have been proposed to arise from a half-formed fullerene, which would rather develop a tube then to close as a fullerene. One problem is to compare the life length of such a half-fullerene to the impinging carbon flux from the gas phase, when the composition of carbon vapours is very little known. Other authors have proposed a growth nucleated by a flying catalyst particle.

IV.3. Various hypothesis for the growth of carbon tubes by arc discharge methods

For arc discharge method, interpretations are various. For S. Iijima, SWNT and spherical structures grow in plasma, by carbon vapour condensation. This relies on the observation that onions and SWNT are found away from graphite electrodes. [6.2.6] However, other groups report that tubes are found at the tip of graphite electrodes. ([6.2.8] for instance) A distinction of the mechanisms is questionable. Even if tubes grow on electrodes, they may be collected away in the apparatus because of their low adherence to electrode surface. For other [3.1.9] the distinction between onions and tubes arises from the fact that some particles are ionized and develop as a tube along the axis of the electric field.

IV.4. Model “temperature-segregated condensation in plasma” for BN/C tubes and onions by arc discharge methods

The condensation of BCN onions and tubes from plasma phase, in the case of arc-discharge type method as been discussed. ([3.1.4] and [3.1.19]) A segregation of C and BN layer in structures has been explained by different “solidification” temperatures of the two materials. In this model, solidification starts from the outer shell of the particle. One difficulty of such approach is to treat the dynamical mechanism in which elements are not always found in their most stable phase.

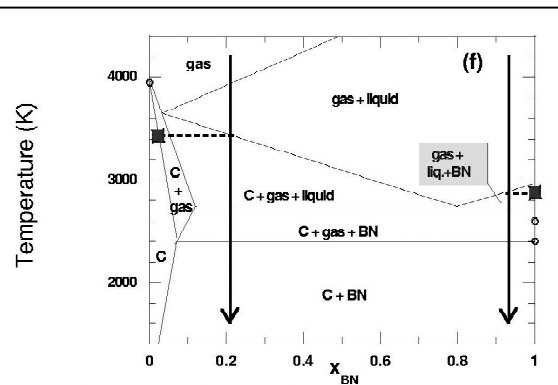


Fig. 1.11 C+BN phase diagram from [3.1.19] around 1 bar, abscise being the ratio of BN. (It is not indicated what elements are present in the “gas” and “liquid” phases and if these elements are distributed uniformly or are spatially segregated.)

Note: It is a common mistake to assume a stable liquid or gas phase of BN at high temperatures and low pressure (“atmospheric and under”). Over dissociation temperature, boron and nitrogen are segregated as two phases: boron (liquid or gas depending on temperature) and nitrogen (gas). (See paragraph I.1.1.)

IV.5. Hypothesis of “open end”

Many models admit that tubes grow keeping one extremity opened. In most synthesis methods, some tubes are actually found open-ended during TEM observations. (The argument being that, if tubes are growing open ended, some tubes should be left opened at the end of the experiment.) However, such tubes may have been broken post-synthesis as well. Some tubes have weaknesses in their structure. For instance, here, BN tubes with a diameter step along axis are commonly observed to break at this junction under the irradiating beam of a TEM.

IV.6. Hypothesis of feeding by surface diffusion [3.1.2]

According to this hypothesis, tube growth is mainly fed by atoms mobility along solid surfaces of the tube (or along a supporting substrate if there is), rather than being fed by a local condensation of atoms from gas phase at growing extremity. Atoms may move along the tube because of the non-uniformity of adsorbed atom concentration. In the hypothesis of a strongly absorbing extremity (typically an open-end extremity), the local drop of concentration may attract atoms toward tube extremity. The flux due to a temperature gradient along tube axis should also be considered. (See Chap VI-II.2.2) For BN tubes, the diffusion of B and N atoms, or of a BN molecule may be considered with different diffusion abilities.

Chapter II

Continuous CO₂ laser apparatus

Objective: We present several technical considerations about the laser heating apparatus, and its adaptation to the heated material.

Abstract: A target, kept in static low pressure, is locally heated by a focused CO₂ laser beam (infrared, $\lambda = 10.6 \mu\text{m}$). Because the laser is of relatively low power ($< 80 \text{ W}$) and continuous, a slowly rising temperature gradient is induced on target, without ablation effect.

Usual derivations for a Gaussian beam, give a waist located in the middle of the chamber and about $90 \mu\text{m}$. Uncertainty on this value, mainly due to rough positioning, is in the order of 10 %.

Estimation of temperature in the target faces several major difficulties. Target warms “globally”, due to its limited size. Losses, especially radiative losses, should be taken in account. In some cases it is possible to assume an over simple spherical gradient:

$T = (T_0 - T_\infty) \frac{r_0}{r} + T_\infty$. The minimum laser power necessary for reaching a vapour phase on a large target is estimated $\sim 55 \text{ W}$ for h-BN, 135 W for graphite and in the range $30\text{-}90 \text{ W}$ for boron. These values can be lowered by limiting target size.

In the case of a h-BN target (hot pressed platelets powders), irradiated zone and near can get over the dissociation temperature of h-BN (2700 K , in 100 mbar of N_2). Commercial h-BN is rich in impurities. Heating of a raw h-BN target produces a white smoke, mainly composed of h-BN platelets, boron oxide and calcium. No BN nano-structure is observed in such smoke. These impurities must be removed as much as possible to form BN nano-tubes and other BN nano-sized particles on target surface.

I. Presentation of the apparatus

I.1. Experimental procedure

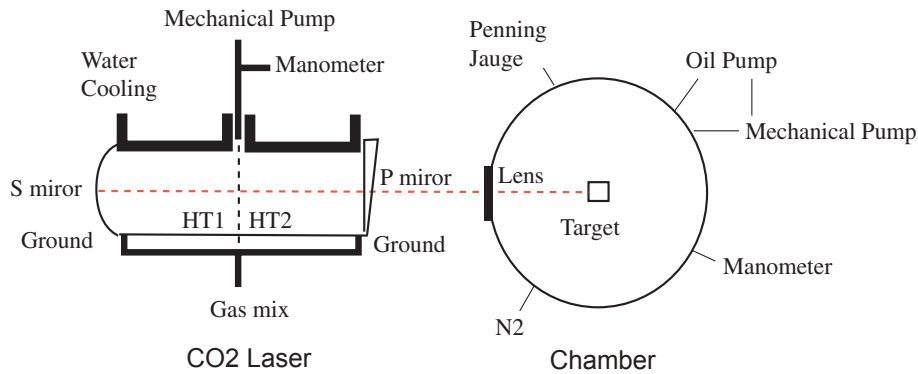


Fig. II.1 details of the laser heating apparatus

A target is locally heated by a continuous CO₂ laser beam (infrared at $\lambda = 10.6 \mu\text{m}$), focused by a ZnSe lens. The lens is fixed to the chamber mount, and its focal plane is close to the middle of the chamber. While heating, the target is kept in a static atmosphere at low pressure. As the chamber is sealed by atmospheric pressure, pressure must be lower than atmospheric (typically $< 500 \text{ mb}$).

The typical case is that of a h-BN target of hot pressed platelets powders (purity 99.5%, see composition in annex 2), heated in nitrogen atmosphere ($\sim 100 \text{ mb}$). In that case, the irradiated zone and near can get over the dissociation temperature of h-BN (2700 K, at 100 mbar of N₂). As nitrogen is effusing, the beam drills a cavity, in which boron is partially left as liquid drops, and partly evaporated.

Technical difference with ablation (in oven) methods (Whether or not both methods feature the same physical processes is discussed at the end of this manuscript.)

Unlike well-known ablation methods, here, target material is not “ablated”. An ablation effect is a violent remove of matter from surface. It is typically caused by a pulsed laser, because the instant power during a pulse is usually very high. (See [1.1.11].) Under such a beam, the irradiated zone instantly reaches sublimation temperature, causing local explosions and hence effusions, periodic with the pulse. A continuous laser of high power may also cause an ablation of the target. Such laser power should be clearly over the critic power for reaching sublimation.

In present conditions, the incident energy is very localised (~ 20 times the wavelength). For an h-BN target 5 mm large, the critic power to reach BN dissociation is measured in the order of ~ 30 W. From this value to the laser maximum (~ 80 W), there is no ablation effect (if the target is properly out-gased and not under vacuum). Almost no matter is ejected from the target (except N₂ in the first 15 s), and target drilling is very modest (less than 1 mm after 3 mn). The irradiated zone reaches boron evaporation temperature, but this evaporation is slow, and condensed boron is collected around impact.

An essential difference with pulsed laser ablation method, is that, with a pulsed laser, the global temperature of the target is low. This is because, although the instant power during a pulse is high, the “average” laser power is usually low. It is also because the instant evaporation of irradiated zone during a pulse lower the transmission of heat to the target. By opposition, here, the instant power is low, but quite high on average, and very little heat is lost by evaporation. Under the continuous beam, temperatures slowly rise in the target, until temperature stabilisation. The “global” temperature of the target is relatively high. (In the order of 1000 K) It is interesting to notice that, in pulsed ablation methods, an additional oven must be used. This actually causes a global warming of the target in the same order of temperature.

Finally, in ablation methods, nano-structured powders are collected in a separated chamber, after the ablated (and heated) material has been carried by flowing gas. By contrast, in the present method, we will see that BN nano-tubes and other BN nano-sized particles are found, after heating, on the front surface of the target.

I.2. Technical details

I.2.1 Laser

The continuous CO₂ laser produces an infrared beam closely monochromatic. Laser effect occurs in a 2 m strait cavity, separated in two tubes. It is limited at one end by a Cu spherical mirror (concave $R = 8$ m hence $f = 4$ m) and at the other end by a semi-transparent plane mirror (~ 2 cm diameter). Laser amplification medium is a gas mix of CO₂ (15%), N₂ (15%), He (70%). (No clear improvement was found by varying these percentages.) This mix is renewed by a continuous flow, and the internal pressure is kept near 11 mbar.

A population of excited vibrational state for CO₂ molecules is obtained by a high tension

(2x6kV) between cavity ends. The beam power is measured at a maximum of 80 Watt, for an absorbed intensity of ~ 40 mA. Hence the efficiency of the laser is $\sim 20\%$. Electric power is limited by high current, dangerous for HT resistors. Laser efficiency can be slightly improved by raising gas mix pressure. However, over 12 mbar, the threshold tension for laser effect is over 6 kV, hence the HT does not enable to switch the laser on. (It is possible to raise slightly the power by rising the pressure after switching on.)

The endurance of the laser at full power is a few minutes. Long use induces excessive heating of inner electrode, eventually burned joints, gas leak, deposition of dirt on the optics parts of the laser.

I.2.2 Chamber

The vacuum system is a bell jar, about 30 cm large and 50 cm high. It is equipped with a penning gauge and a high precision manometer. Secondary vacuum can be obtained by a combination of mechanic and oil diffusion pumps. Several valves enable to fill with gas and to open to air. Air sealing the caused by atmospheric pressure, pushing the upper glass bell toward the lower metallic mount.



Fig. II.2 The Chamber

A plano-meniscus ZnSe lens ($f = 13$ cm at $10.6\ \mu\text{m}$) is used as window and it is sealed on the metallic base_plate. This lens focuses the beam near the middle of the chamber, to a waist $\sim 90\ \mu\text{m}$ (see estimations, below). Front surface of target is usually set at this position. Target (mm size) is supported by a simple stand. This stand is usually a vertical rod of BN, down part fixed to a heat resistant material. Using the sample material for stand and target guarantees no contamination.

I.3. Setting procedures

I.3.1 Aligning laser optics (using a HeNe laser)

Aligning laser optics is important to have a minimum absorption of the beam inside laser cavity. First, the spherical mirror is removed, and a HeNe laser beam is directed through the cavity. The positions of glass tubes are set manually, so that the HeNe laser beam crosses at the centre of each tube extremities. Then, the semi-reflecting mirror is set by auto-collimation, so that its internal surface is perpendicular to the HeNe beam. (The two surfaces of the semi-reflecting mirror form a slight angle, and cause multiple reflections.) Finally, the spherical mirror is mounted back and also set by auto-collimation.

I.3.2 Positioning the target on the beam of the CO₂ laser

Positioning the target requires a precision of mm order. It is necessary to re-adjust the position of the target stand regularly, to compensate relative movements of laser and chamber. It should be done without damaging the surface of target and of the stand, and without risk for manipulator hands. For that, the CO₂ laser beam is changed for a HeNe laser beam, after beams have been superposed. First, a spatial mark of the CO₂ laser beam is taken near the ZnSe lens, by burning a piece of wood. Then a second mark is taken, close to laser exit. This position is memorised at the tip of a nail. Then, the HeNe laser beam is set to cross through those two marks, and can be used to position the target and its stand.

I.3.3 Switching on the laser

First the water-cooling flow is open and fans are switched on, to avoid movement of laser optics by laser warming. Then the gas mix flow is set: laser cavity is emptied by the mechanical pump, and gas flow is raised until laser pressure equilibrates to ~ 11 mbar. Finally HT is switched on. Tension is directly raised to a maximum, so that both tubes switch to laser effect simultaneously. (It is rather severe for the HT.) Then tension is lowered until intensity in both tubes is under 45 mA (60 mA is a limit for HT resistors to melt, in stable operations.) A laser effect in only one tube is dangerous for HT resistors, because intensity is double in the alighted tube.

II. Waist of the incident beam

To maximise energy density, the waist of the incident beam should be positioned on front target surface. The following calculations determine the position and size of the waist and the uncertainty allowed on target positioning.

II.1. Optical laws for Gaussian beams

Because of diffraction on circular diaphragms inside the laser, the laser beam is Gaussian. (Not to be mistaken with “Gauss conditions”.) The intensity in any plane normal to the beam at the abscise z is: $I(r) = I_0 \cdot e^{-\left(\frac{r}{w(z)}\right)^2}$, where r is the coordinate in the perpendicular plane. $w(z)$ is the section “radius”, defined by $I(w)/I_0=1/e$ (~ 0.37), where most of the energy is concentrated.

Note: The waist is often defined in term of amplitude, $A(r) = A_0 \cdot e^{-\left(\frac{r}{w(z)}\right)^2} \Rightarrow I(r) = I_0 \cdot e^{-2\left(\frac{r}{w(z)}\right)^2}$. For the present purpose (temperature calculations), an “intensity” definition is more useful.

Amplitude formulas can be deduced by replacing w with $\frac{w}{\sqrt{2}}$ in all present expressions.

Beam propagation in uniform medium is expressed by $w(z) = w_0 \cdot \sqrt{1 + (z/zr)^2}$, where, w_0 is the minimum value of $w(z)$ (waist), z is the distance from waist plane and zr is a constant characteristic of the beam dispersion (\sim speed of convergence/divergence). The dispersion between zr and w_0 is given by $zr = 2\pi w_0^2/\lambda$. Therefore, a Gaussian beam is completely determined by the knowledge of zr , waist position and λ (or by waist size, position, and λ).

Conjugation of a Gaussian beam through a thin lens (algebraic law)

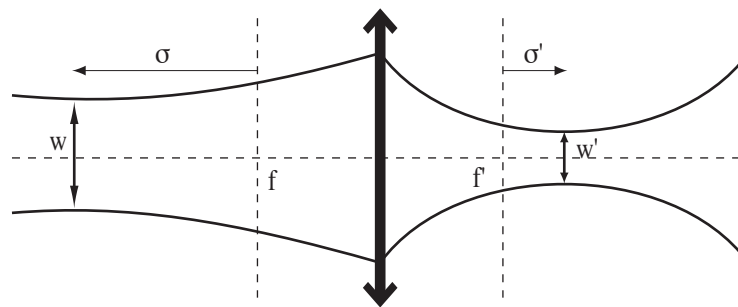


Fig. II.3 Notations

If σ and σ' are respectively, the distance from object-waist-plane to object-focal-plane, and the distance from image-waist-plane to image-focal-plane, conjugation laws are given as:

$$\begin{cases} \sigma \cdot \sigma' = f \cdot f' + zr \cdot zr' \\ \sigma' / \sigma = -zr' / zr \end{cases}$$

, which can be re-written as:

$$\begin{cases} zr' = -zr \left(\frac{f \cdot f'}{zr^2 + \sigma^2} \right) \\ \sigma' = -\sigma \left(\frac{f \cdot f'}{zr^2 + \sigma^2} \right) \end{cases}$$

In the case $zr^2 \gg \sigma^2$ (see below), the formulas further simplify to:

$$\begin{cases} zr' \approx -\left(\frac{f \cdot f'}{zr} \right) \\ \sigma' \approx -\sigma \left(\frac{f \cdot f'}{zr^2} \right) \end{cases}$$

II.2. Size and position of final waist

II.2.1 Waist inside laser cavity

Waist inside laser cavity is located on the plane mirror, hence on the semi-reflecting mirror, because of symmetry. Indeed, the beam inside cavity must be left unchanged through mirror reflections, for stable laser conditions. Waist diameter inside a spherical-mirror/plane-mirror type cavity is known. It can be expressed as a function of the distance between mirrors (d) and the curvature of the spherical mirror (R) as:

$$w_0 = \left((\lambda/2\pi)^2 \cdot d \cdot (R - d) \right)^{1/4}$$

Numerical, with $d = 2$ m, $R = 8$ m, gives $w_0 = 2.42$ mm. This is clearly smaller than the limiting aperture of the semi-reflecting mirror (~ 2 cm).

II.2.2 Final Waist

The Gaussian beam is not affected by conjugation through the plane semi-reflecting mirror. (We neglect the slight angle between surfaces of this mirror.) Hence, the beam outside cavity has same waist (position and size) than inside cavity. It is conjugated with the chamber lens to give the incident waist. With $\lambda = 10.6$ μm , $w_0 = 2.42$ mm, and $\sigma = 0.5$ m. We can neglect

$\sigma^2 \approx 0.25$ in front of $zr^2 \approx 12$. This introduces an error of 1.4% on w'_0 and 2% on σ' , which is well below the uncertainty of target positioning. (See below.) We may use the simplified form of lens conjugation law. Changing the variable zr to w_0 , and $f' = -f$, we have:

$$\begin{cases} w'_0 \approx \frac{\lambda \cdot f}{2\pi \cdot w_0} \\ \sigma' \approx \sigma \left(\frac{\lambda \cdot f}{2\pi w_0^2} \right)^2 \end{cases}$$

With, $f = 13$ cm, $\sigma' \sim 1$ mm. The waist is not much distant from the focal plane of the chamber lens, which is the middle of the chamber.

The final waist is: $\boxed{W'_0 \sim 90 \mu\text{m}}$ ($zr' \sim 7.6$ mm. If the waist was defined in amplitude, it would be $\sim 130 \mu\text{m}$.)

II.3. Uncertainty on positioning

II.3.1 Rough positioning of the target in the chamber

The uncertainty on target positioning, δz , induces an uncertainty on the diameter of the zone irradiated by the laser, $\delta w'$, given by: $w'_0 + \delta w' = w'_0 \sqrt{1 + (\delta z / zr')^2}$

Thus, for a given error of $x = \delta w' / w'_0$ on irradiated zone, $\delta z = zr' \cdot \sqrt{(1 + x)^2 - 1}$

For instance, to have an incident diameter not exceeding the final waist of more than 10 % ($x = 0.1$), δz should be smaller than 2 mm. This order of precision is compatible with the manual positioning of the target.

II.3.2 Rough positioning of the chamber (and lens) relatively to the laser

The uncertainty on this positioning, $\delta \sigma$, does not cause any change in final waist diameter (nor in the final beam dispersion), because w'_0 (and zr') is independent of σ (in the approximation $zr^2 \gg \sigma^2$). However it causes an uncertainty on the final waist positioning $\delta \sigma'$, which is equivalent to a positioning uncertainty of the target δz . As σ and σ' are proportional:

$$\frac{\delta \sigma'}{\sigma'} = \frac{\delta \sigma}{\sigma} \Rightarrow \delta \sigma = \frac{\sigma}{\sigma'} \delta \sigma' \approx 5 \cdot 10^2 \delta \sigma'$$

Taking the same limit than above (10%), $\delta\sigma'$ should not exceed 2 mm. $\delta\sigma$ may be up to ~ 1 m without affecting the incident surface. Thus this uncertainty is drastically negligible. (This actually results from the fact that the beam is very little dispersed at the exit of the laser.)

III. Equations of heat diffusion in the target

In the followings, we will need two types of temperature estimations. First, we need to estimate what laser power it necessary to reach the dissociation/evaporation/sublimation temperature for a given material, graphite, boron or h-BN. This requires estimating the final temperature at equilibrium considering a finite target size. Then, in a chapter V will need to describe the evolution of temperatures in a h-BN target, locally around impact. This is a complex problem, where an accurate estimation can only be reached by fitting with empirical observations.

III.1. Introducing the formalism

The conservation of heat in the material is expressed as $\text{div}\mathbf{Q} + \rho C \frac{\delta T}{\delta t} = f(\mathbf{r}, t)$, f being the density of heat production. With the empirical law of linear behaviour: $\mathbf{Q} = -k \text{grad}T$, we have the equation of heat diffusion:

$$\rho C \frac{\delta T}{\delta t} - \text{div}(k \text{grad}T) = f(\mathbf{r}, t)$$

In the general case, where k is a function of T and therefore of time and position, k can not be extracted from the div operator. The functions $k(T)$ and $C(T)$ are usually known from literature (See annex 2) Because of the cylindrical symmetry of the problem, the cylindrical coordinates are used and T is only function of r and z .

$f(\mathbf{r}, t)$ is due to the incident laser beam, considered to be Gaussian:

$$f(\mathbf{r}, t) = \gamma \epsilon P_{\text{laser}} \exp(-\alpha z) \exp\left[-\left(\frac{r}{w}\right)^2\right]$$

- ◆ $w \sim 90 \mu\text{m}$ is the laser waist defined for intensity (Previous paragraph)
- ◆ α is the attenuation coefficient of the material at $\lambda = 10.6 \mu\text{m}$. at temperature of irradiated zone. (In the order of 3000 K) ($1/\alpha$ is the attenuation length.)

Practically, only little data is available from literature, all of them for ambient temperatures. For h-BN, $1/\alpha_{\text{BN}} \sim 100 \mu\text{m}$. [1.1.18] For carbon, a value $1/\alpha_{\text{C}} \sim 0.07 \mu\text{m}$ at $\lambda = 2 \mu\text{m}$, can be extracted from the value of the dielectric function as given by [1.1.15]. For boron, very little is known of properties in the infrared region. In crystalline rhombohedral boron, $1/\alpha_{\text{B}} \sim 10 \mu\text{m}$ [1.1.14].

For graphite (semi-metal), the (very strong) absorption in the infrared is mainly due to conductive electrons of the π band. In that case α should have a metallic behaviour with temperature and frequency, and be proportional to $\sqrt{k(T) \times \lambda}$. Near 4000 K and at $10 \mu\text{m}$, $1/\alpha_{\text{C}}$ is not much different from the value at ambient temperature and $\lambda = 2 \mu\text{m}$. [1.1.18]

For dielectric materials, like h-BN and B, absorption is due to a limited number of resonant frequencies of electrons linked to the structure. This absorption may not vary much with temperature. However, the liquid phase of boron may have a very different coefficient from the crystalline phase.

- ◆ ϵ is the absorbance (absorbed flux / incident flux) of the irradiated surface for $10.6 \mu\text{m}$ and at temperature of irradiated zone. (In the order of 3000 K)

Practically, these values are also little known (See [1.1.10]). For h-BN at $T \sim 1000 \text{ K}$, $\epsilon_{\text{BN}} \sim 0.9$. However, the total absorbance (integrated on all frequency) is reported to be decrease at high temperatures, down to half at 2700 K, hence $\epsilon_{\text{BN}} \sim 0.45$. This is surprising for a dielectric material where absorbance is expected to depend little on temperature. (Unfortunately this high temperature study is unique, and the behaviour of the target reported strongly suggest a high influence of impurities in the sample.) For graphite, at high temperature an average value of $\epsilon_{\text{C}} \sim 0.4$ is reliable. For crystalline boron $\epsilon_{\text{B}} \sim 0.7$ at ambient temperature. However, like for attenuation, this value may be very different in the liquid phase. The vanishing of roughness after fusion also affects (diminishes) absorbance.

In the case of a h-BN target, the irradiated surface is often a mix of B and BN. Furthermore there possibly absorption and diffusion from vapours in front of the beam. We will usually chose an average value of $\epsilon \sim 0.6$, but keeping in mind a huge uncertainty ± 0.2 .

- ◆ γ is a correction to the absorption coefficient, to account for the cavity of the hole (= 1 if there is no cavity). A quantitative estimation is proposed in Chap. V-II.5.1. We will usually take an average value of $\gamma \sim 1.5$.

Limit conditions impose that heat fluxes on target surfaces is equal to the sum of surface losses:

- ◆ Losses by black body radiation: $-\sigma \epsilon' T^4(\mathbf{r}, t)$.

ϵ' is the **total** emittance (integrated on all frequencies) of a surface at a given temperature (practically, the average temperature of the target ~ 1000 K). ϵ' (total, near 1000K) is usually different from ϵ (at $10.6 \mu\text{m}$, near 3000 K). (For opaque materials, the total emittance ϵ' is equal to the total absorbance at same temperature.) In the range 500 - 2000 K, $\epsilon'_C \sim 0.85$, $\epsilon'_{BN} \sim 0.75$, $\epsilon'_B \sim 0.75$ (crystalline boron). Again, the value for liquid boron is probably different. (See [1.1.10])

Note: For h-BN and graphite, target is made of condensed powders with no favoured orientation. In the case of “pyrolytic” h-BN or graphite, where there is a dominant orientation of the platelets, emittance strongly depends on the orientation of the emitting surface.

With $\sigma \sim 5.67 \cdot 10^{-8}$, $T \sim 1300$ K for most of the target, and emissive surface $\sim 8 \cdot 10^{-5} \text{ m}^2$, The radiated flux is ~ 10 W This is not negligible compared to the incident power $\gamma \epsilon P_{\text{laser}} \sim 60$ W. And it will increase quickly with global target temperature.

- ◆ Conductive and Convective losses in the atmosphere. Those are usually supposed proportional to the local difference between surface temperature and surrounding atmosphere: $-A_{\text{atmos.}}(T(\mathbf{r}, t) - T_{\text{atmos.}})$, A depending on gas pressure and composition. Temperature gradient in gas phase should be considered.

Roughly, heat transfer from target to atmosphere is the flux of molecules incident from gas phase multiplied by target surface and by the heat transfer transmitted during one collision: $J_N \times Surf \times \frac{2}{3} k(T_{\text{surf}} - T_N)$. $J_N \sim 1.6 \cdot 10^{26}$ (estimated in Chapter VI). T_{surf} is ~ 1300 K. $k \sim 1.38 \cdot 10^{-23}$. If T_N could be considered as ambient, power lost in gas phase would be ~ 120 W. This value is not physical, because it is higher than absorbed power.

Indeed there is a temperature gradient in gas phase so that T_N is close to T_{surf} on zone near target. (There is a hot gas layer around target.) In any case, losses in atmosphere can be expected in the same order than radiative losses.

- ◆ Conductive loss in the holder. If the holder is a vertical h-BN rod ($R = 3$ mm, $l = 7$ cm). The thermal flux through it is $J = -k_{BN} \nabla T = k_{BN} \frac{(T_{up} - T_{down})}{l}$. The power lost through this rod is $P = \pi R^2 J$. With a h-BN target, if $T_{up} - T_{down} \sim 1000\text{K}$, $k_{BN} \sim 30$ SI, the power lost is ~ 1.2 W. This is small compared to the incident power ~ 60 W. The holder influence will be neglected in the following.
- ◆ Chemical absorption (Latent heat of phase transformations). To evaporate a quantity of liquid boron of the size of the cavity induced by the laser, we need ~ 16 J (Volume of cavity $\sim 1.25 \cdot 10^{-4} \text{ cm}^3$ x Density $\sim 2.5 \text{ g cm}^{-3}$ x Latent heat $\sim 5 \cdot 10^4 \text{ J g}^{-1}$). If this happens during cavity formation (15s), it requires less than 1 W. The latent heat of BN dissociation is about 5 times smaller. We will neglect both.

III.2. Setting hypotheses

III.2.1 Semi-infinite medium hypothesis

In the present case of heating by continuous laser, heat is continuously transmitted to the target, increasing the global temperature until equilibrium is found. If we want to estimate target temperatures, during temperature rise or after final equilibrium, it is simple to consider the target as a semi-infinite medium. This case is simple because thermal energy is supposed released at infinite.

If target has already reached its final equilibrium and if it has a spherical symmetry, it can be considered as an imaginary part of a semi-infinite medium. Indeed, on backside of a semi-spherical target, temperature and heat flux are uniform. It is possible to imaginary “fill the missing medium” without changing these limit conditions. Therefore, a semi-infinite hypothesis is valid for the equilibrated case.

Note: In the present case, target has no spherical symmetry, but temperatures are converging quickly compared to the size of the target. (This is checked a-fortiori, and it is true for all present calculations.) Hence it is possible to imaginary “carve” the target as a semi-sphere, without much affecting temperatures.

In the equilibrated case, temperature at infinite of the imaginary medium is imposed by the energy balance in the target. It is usually different from ambient. However, it is close to ambient for a very large target. Indeed, surface to release energy is large, so that temperatures on the target border do not rise much. Alternatively, it is true for a target on a cooling holder.

We also need to consider the unstable case, when temperatures are rising. Varying temperatures in a semi-infinite medium is a sum of a varying temperature gradient plus a constant temperature at infinite. For a target of limited size (partially isolated from the rest of the apparatus) not equilibrated, the heat evacuated on back-sides is lower than the incident flux, so that there is an accumulation of heat in the target, hence a “global” warming with time. We will see in chapter V that the time for global warming is much longer than the time for equilibration of a semi-infinite medium. Therefore, at any time during temperature rise, temperatures in the target are that of an equilibrated semi-infinite medium, with a given temperature at infinite. In other words the total temperature rise is the sum of a quickly changing gradient inside target and a slowly rising temperature at target border.

III.2.2 Losses on surfaces

Final equilibrium is found when losses (radiation, conduction in gas...) equilibrate the energy absorbed from the laser. Therefore, for temperature estimations, losses can only be neglected strictly in the beginning of the warming. Losses by conduction are roughly proportional to the surface temperature and could eventually be taken in account for. However, radiation losses can not easily be taken in account, because they are proportional to the fourth power of surface temperature.

We can usually suppose no losses at front surface, on a circle around the impact. This is locally true if losses fluxes are much smaller than conductive fluxes in the material. We can check this afterward. This does not mean that surface losses are globally negligible. But it means that losses only affect the infinite temperature, and not the gradient shape near impact.

III.2.3 Simplest form of the gradient

With no loss on front surface around impact, and a spherical symmetry near impact, (If a cavity is formed, cavity should be spherical, with constant temperature on its cavity. If not, beam penetration depth should be equal to beam waist.) the problem is of spherical symmetry.

If, in addition, we make the hypothesis that k , the thermal conductivity, is independent of temperature, (This is true in a range of high temperature like 1000 - 2000 K for h-BN.) temperature in the target can then be written as:

$$T(t) = (T_0 - T_\infty) \frac{r_0}{r} + T_\infty(t)$$

This is the simplest possible modelisation for temperature. (A similar form could be considered for cylindrical symmetry.)

IV. Adapting laser power to target material

Reaching h-BN dissociation requires a lower laser power than reaching carbon sublimation. Firstly, the dissociation temperature of h-BN (2700 K) is low, compared to the sublimation temperature of graphite (3800 K). Secondly, h-BN has a thermal conductivity twice lower than graphite, inducing a stiffer gradient. More generally, we need to quantify roughly what is the power needed to reach the dissociation or the sublimation on the target, for different materials, especially h-BN, carbon and amorphous boron.

For that, we need to estimate the maximum temperature reached, hence temperatures after stabilisation. For that, the surface of impact can be considered as a plane with no cavity. (For the case of h-BN, absorbance is not yet affected by a liquid boron layer.) Temperatures are rather estimated inside target, than on front surface, where radiations may affect the shape of the gradient. (The local radiative loss near impact is not taken in account.) We consider that temperature gradient is stiff, so that T_∞ is equal to temperature on target back surfaces. (This is more or less correct.)

IV.1. Stabilised temperatures, in a large (or cooled) target

If target is very large, or cooled during irradiation, temperatures do not rise much on back surfaces. Target may be simply considered as semi-infinite medium with T_∞ equal to ambient temperature.

IV.1.1 Simplest model

With a simple model, using all approximations previously described, we can write temperature in the target as $T = (T_0 - T_\infty) \frac{r_0}{r} + T_\infty$. With $J = -k \text{ grad } T$, temperature can be re-written as

$T = \frac{J_0}{k} \frac{r_0^2}{r} + T_\infty$, $T_\infty = T_0 - \frac{J_0 r_0}{k}$. If we consider that the maximum temperature T_0 is reached

along a half-sphere around impact, at $r_0 = w$ where $J_0 = \frac{\varepsilon P_{laser}}{2\pi w^2}$, maximum temperature is a

function of laser power as: $T_0 = T_\infty + \frac{\varepsilon P_{laser}}{2\pi k w}$

IV.1.2 With attenuation coefficient and temperature dependence of thermal conductivity (“lax-type” model)

In a better approximation, we can use a literal calculation for the irradiation of a Gaussian beam on a plane surface. Then, we can account for a limited attenuation coefficient α in the material. We can also take in account the variation of thermal conductivity $k(T)$ with temperature, assuming a standard variation $k(T) = K(T_0)(T_0/T)^{1+\varphi}$. [1.2.1] Temperature is given as:

$$T(r, z) = T_{\infty} \left[1 - \frac{\varphi}{T_{\infty}} \left(\frac{\varepsilon P_{laser}}{2\pi k(T_{\infty}) w} \sqrt{\pi} \right) N\left(\frac{r}{w}, \frac{z}{w}, \alpha w\right) \right]^{-\frac{1}{\varphi}}$$

$$\text{with, } N(R, Z, W) = \frac{W}{\sqrt{\pi}} \int_0^{\infty} J_0(\lambda R) \exp\left(-\frac{\lambda^2}{4}\right) \frac{W \exp(-\lambda Z) - \lambda \exp(-WZ)}{W^2 - \lambda^2} d\lambda$$

Maximum temperature is found on front surface ($r = 0, z = 0$). It is a function of laser power as:

$$T_0 = T_{\infty} \left[1 - \frac{\varphi}{T_{\infty}} \left(\frac{\varepsilon P_{laser}}{2\pi k(T_{\infty}) w} \right) \times \int_0^{\infty} \exp\left(-\frac{\lambda^2}{4}\right) \frac{\alpha w}{\alpha w + \lambda} d\lambda \right]^{-\frac{1}{\varphi}}$$

Numerical: with $w \sim 100 \mu\text{m}$. (waist plus 10% uncertainty)

- For h-BN, $\alpha = 1/(100 \mu\text{m})$, $k(300 \text{ K}) = 50 \text{ SI}$, $k(2200 \text{ K}) = 18.3 \text{ SI}$, $T_{diss} = 2700 \text{ K}$, $\varepsilon \sim 0.75$. (Absorbance is very uncertain for h-BN. ε may be between 0.9 and 0.45. A value $\varepsilon \sim 0.75$ is chosen to fit the experimental minimum dissociating power (30 W) of next paragraph.)
- For graphite, $\alpha = 1/(0.07 \mu\text{m})$, $k(300 \text{ K}) = 162 \text{ SI}$, $k(3300 \text{ K}) = 26 \text{ SI}$, $T_{diss} = 3800 \text{ K}$, $\varepsilon \sim 0.45$
- For boron $\alpha = 1/(10 \mu\text{m})$, $k(128 \text{ K}) = 190 \text{ SI}$, $k(2338 \text{ K}) = 9.85 \text{ SI}$, $T_{diss} = 3700 \text{ K}$, $0.25 < \varepsilon < 0.75$ (Absorbance is almost unknown for liquid boron. Therefore, ε is considered in a range.)

We can conclude from Fig. II.4-6 that, for a large target, the critic power is $\sim 55 \text{ W}$ for h-BN, $\sim 135 \text{ W}$ for graphite, and in the range $30 - 90 \text{ W}$ for boron. (Simple and Lax-type models give similar results.) Such values for “large target”, can be interpreted as “power needed to study the material without any need to reduce target size”. (The values for a target of limited size are expected smaller.) Hence, we may say that, to study those tree materials comfortably, a laser power of 150 W or more would be well suited. (Unfortunately, our laser is limited to $\sim 80 \text{ W}$.)

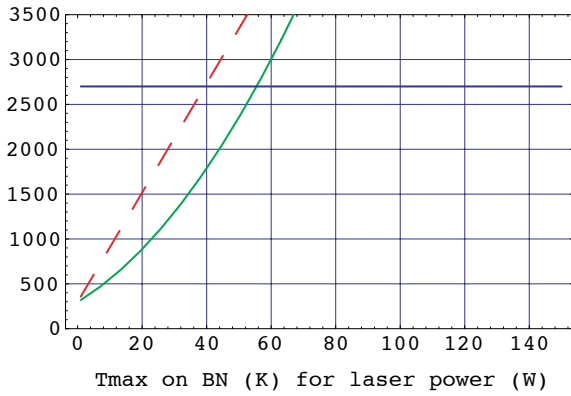


Fig. II.4 Maximum temperature for a large h-BN target. Dashed line: simple model Plain line: Lax-type Strait line: dissociation of BN

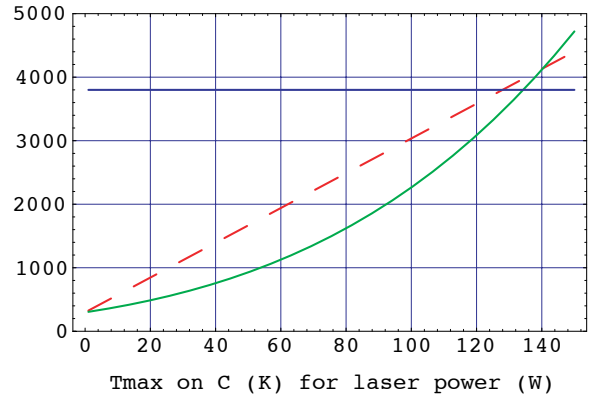


Fig. II.5 Maximum temperature for a large graphite target. Dashed line: simple model Plain line: Lax-type Strait line: sublimation of C

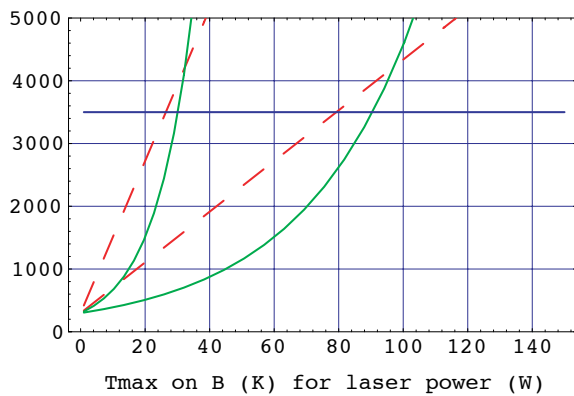


Fig. II.6 Range of maximum temperatures for a large boron target. Dashed lines: simple model Plain lines: Lax-type Strait line: evaporation of B

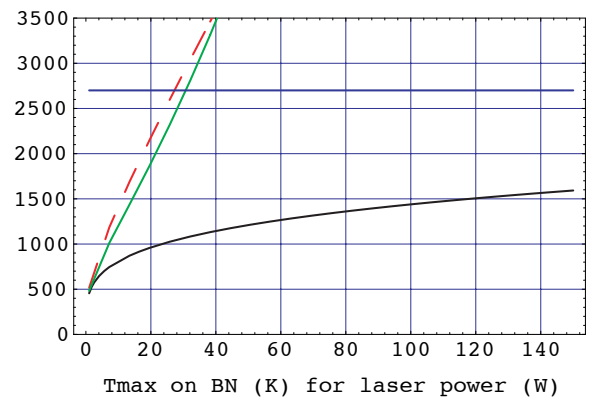


Fig. II.7 Maximum temperature for a h-BN target, ~ 4.5 mm large. Dashed line: simple model Plain line: Lax-type Lower plain line: contribution of target size (T_{∞}).

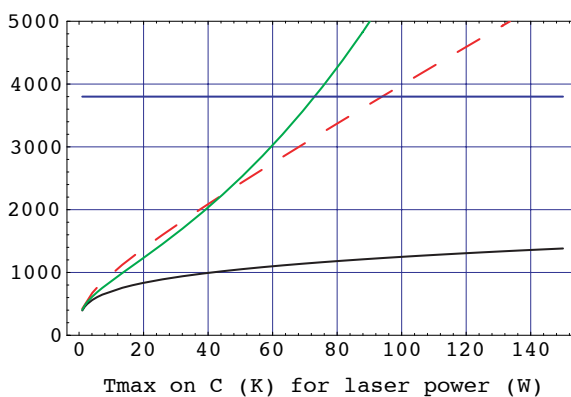


Fig. II.8 Maximum temperature for a graphite target ~ 4.5 mm large. Dashed line: simple model Plain line: Lax-type Lower plain line: contribution of target size (T_{∞}).

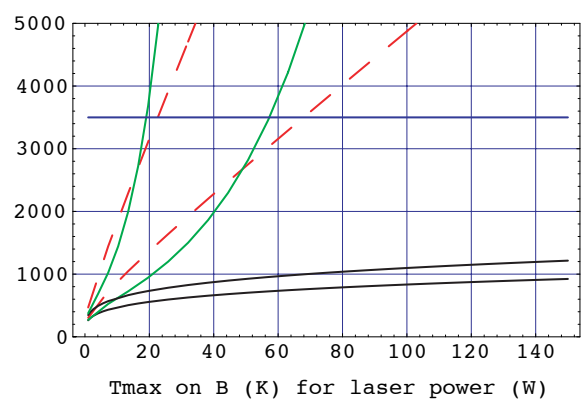


Fig. II.9 Range of maximum temperatures for a boron target ~ 8 mm large. Dashed lines: simple model Plain lines: Lax-type Lower plain lines: contribution of target size (T_{∞}).

IV.2. Increase of temperature due to limited size of the target

By using a small target, isolated from the rest of the apparatus, it is possible reach higher temperatures, so that the power necessary to reach vapour phase is lower. Indeed, temperature on back surfaces of the target rises until an energy balance is found with surface losses. If we only consider radiative losses in the energy balance (which is not correct.), T_{∞} is roughly given by:

$$\varepsilon P_{laser} = \text{target surface} \times \varepsilon' \sigma T_{\infty}^4 \Rightarrow T_{\infty} = \left(\frac{\varepsilon P_{laser}}{\varepsilon' \sigma \text{Surf}} \right)^{1/4}$$

Numerical: (See figures II.7-9)

For h-BN, $\varepsilon' \sim 0.75$ and cube thickness ~ 4.5 mm. For graphite, $\varepsilon' \sim 0.85$ and cube thickness ~ 4.5 mm. For boron, $\varepsilon' \sim 0.75$ and cube thickness ~ 8 mm. Other values are same as above. On figures, T_{∞} is coefficiented by 0.75 to account roughly for non-radiative losses.

Parameters have been set so that h-BN dissociation is reached near 30 W. Carbon sublimation should be reached, near 75 W. Experimentally, a heating near 70 W (in 100 mb N₂) left the target unaffected. For boron, evaporation should occur between 20 and 55 W. Experimentally a heating at 70 W (in 100 mb N₂), left an impact on the target. A local melting could cause this, but the presence of some power around impact rather indicates some evaporation. (See the end of this manuscript for carbon and boron.)

Could we consider also conductive losses?

If we consider that both losses in the holder and in the atmosphere are proportional to $(T_{surface} - T_{ambient})$ (which is not obvious), we can write the global energy balance as:

$$\varepsilon P_{laser} = A (T_{\infty} - T_{amb}) + \varepsilon' S \sigma T_{\infty}^4$$

We cannot easily express T_{∞} as a function of laser power. However, we can replace T_{∞} by $T_{\infty}(P_{laser}, T_0)$, as deduced from previous simple or improved estimations. For a given $T_0 = T_{diss}$, we can solve the resulting equation numerically and find P_{laser} .

The constant A should be approximately independent of the material, assuming that we are using the same atmosphere, the same holder, and the same target size. It can be found empirically from the case of h-BN. We can have an empirical value of T_{∞} (~ 1300 K) and

deduce A from:
$$A = \frac{(1 - \varepsilon)P_{laser} + \varepsilon'S\sigma T_{\infty}^4}{(T_{\infty} - T_{amb})}$$

V. Impurities of commercial h-BN

V.1. Smoke effusing from a raw h-BN target

Our first attempt to synthesise nano-structured BN was to collect the material effusing from a raw h-BN target. This procedure was influenced by the ablation-type methods, where ablated material is collected away from the target. However, the expected nano-structures were not found in these powders. Instead it appeared that, although commercial h-BN is so-called 99.5% pure, the smoke effusing at high temperatures is a mix of various impurities and h-BN platelets.

V.1.1 Experimental procedure

In a typical experiment, the target was a small cylinder (6 mm_4 mm) of raw h-BN, as sliced (by SiC rotating saw) from a commercial rod of h-BN. It was introduced into the chamber, at the tip of a metallic holder. The chamber was pumped to a secondary vacuum ($\sim 10^{-5}$ mbar), and then filled with nitrogen. The plane section was facing the beam.

In the first seconds of the heating (during about 20 s), a white smoke was released around the target and rose in the nitrogen atmosphere. This effusing material was collected on aluminium receptacle, held up-side-down, a few centimetres over the target. The smoke deposited as a thin, but visible, white powder on the aluminium surface. The receptacle was then filled with a solvent, and the material was dispersed by ultrasounds. A few drops of the resulting liquid were deposited on a copper/carbon micro-grid for TEM observations and EELS analysis.

Experiments were undertaken with different N₂ pressures (from 100 mbar to 900 mbar, by steps of 100 mbar), in secondary vacuum ($\sim 10^{-5}$ mbar), with atmospheres of He, Ar and air.

V.1.2 Results and analysis

A high quantity of boron oxide (Most probably of B₂O₃) was found in the smoke, as amorphous nano-filament. The so-called 99.5% pure h-BN actually contains up to 5 % oxygen, because only metallic elements are taken in account in chemical rating. (See composition annexe.) To a naked eye, boron oxide is very similar to h-BN, but it is easily identified by

solvating in water. Indeed, boron oxide is very hydroscopic and readily dissolves in water. In the specific case of heating under air, pure boron oxide smoke is produced continuously under the beam.

A large yield of calcium was also found in the powder. In EELS spectrums, L-absorption edge of Ca was often found together with B and O edges. Ca may either form CaB₆, CaO or ternary Ca_xB_yO_z particles. CaB₆ and CaO compounds are actually present from the start in commercial h-BN, because they are by-products of the industrial synthesis of h-BN: $3\text{CaB}_6 + \text{B}_2\text{O}_3 + 10\text{N}_2 \xrightarrow{(1500\text{C}^\circ)} 20\text{BN} + \text{CaO}$. Other minor impurities are present in the target, especially a Si edge was sometimes found in EELS spectra.

Nano-structured BN was not observed in the smoke. Instead, a large fraction of the powders consisted of h-BN micro-platelets, probably ejected as is, from the target. Other forms of h-BN were exceptionally observed, like disordered sheets.

A few metallic nano-crystals were also found, probably coming from the metallic holder. Its metallic surface may release some vapours at high temperature. The holder was also found to react with the target at zones of contact.

V.1.3 Interpretation and conclusion

When heated at high temperature, a commercial rod of h-BN releases B₂O₃, CaO and other impurities as a white smoke. This effusion damages target surfaces and locally ejects h-BN platelets. The part of the h-BN rod near the external surface of the cylinder (rod shell) is responsible for most of this effusion. A non-uniformity of matter in the rod is proved, when heated, because the external shell tends to be ejected as mm-large flat pieces. Furthermore, the target will out-gas drastically less if this shell has been previously removed. It is possible that more oxide is accumulated in external parts of the rod, in contact with air, possibly during hot pressing. It is also possible that some water is accumulated from air, because boron oxide is very hydroscopic.

A growth of nanotube around impact was not observable on that serie, because most material around impact had been washed away during smoke effusion. Some BN nanotubes were finally observed using a different collection: instead of the smoke deposit, the complete heated target was vibrated in the solvent. In conclusion, to observe tube growth on surface, the target should be carefully freed from impurities prior to heating. The external part of the rod is easily

removed by sandpaper polishing. (Target is shaped as a cube.) Most remaining impurities can be removed by out-gazing in vacuum. However, despite this, impurities are still eventually found on the target after heating, often as black spots on surface. To have no impurities from the holder, it is best to use the same material than the target. A simple h-BN rod can make a suitable stand for the target, but it should be freed from impurities, as the target is.

V.2. Oxide impurities remaining on target despite out-gazing

Despite out-gazing, as described for a standard experiment (Heating under vacuum for ~ 5 min. See chapter IV), remaining impurities (mainly boron oxide) are regularly found during SEM observations. (Fig. II.11-12) Oxide is mainly present on target, far from impact, where surface temperature was low.

Oxygen is not completely removed by the out-gazing stage. The time for complete out-gazing of oxygen is actually unknown. 5 min is rather a limit of endurance of the laser in normal use. Experimentally, a rise of pressure is observed in the first ten seconds of out-gazing. After that, pressure drops back to initial pressure. It means that oxygen flux exiting surface is temporally higher than the debit of the oil-diffusion pump or that, equilibrium pressure of oxygen over B₂O₃ gets over the minimum pumping pressure of the diffusion pump (~ 10⁻⁵ mbar). According to B₂O₃ vapour pressure measurements, this is obtained when the average temperature of the target gets higher than 1200 K. (See Fig. II.13)

This does not mean that target is completely out-gazed after ten seconds. Indeed, the quantity of oxygen evacuated from the target does not only depend on target temperature, but also on the distribution of oxygen in the target. Oxide near external surface is quickly removed, creating a temporally high flux of oxygen. But oxide from inner parts of the target may exit at a much slower rate.

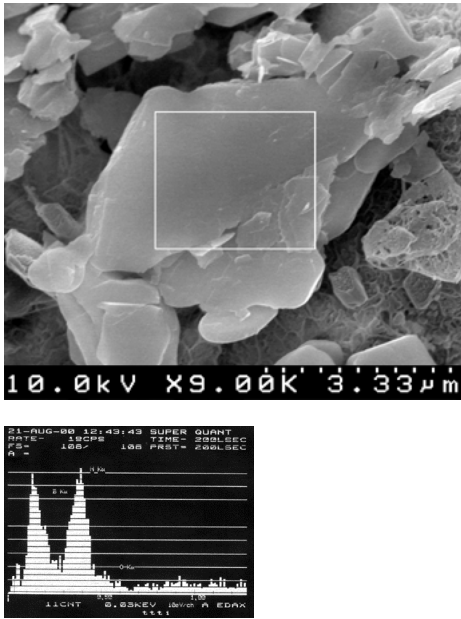


Fig. II.10 h-BN platelet (for reference) (SEM)

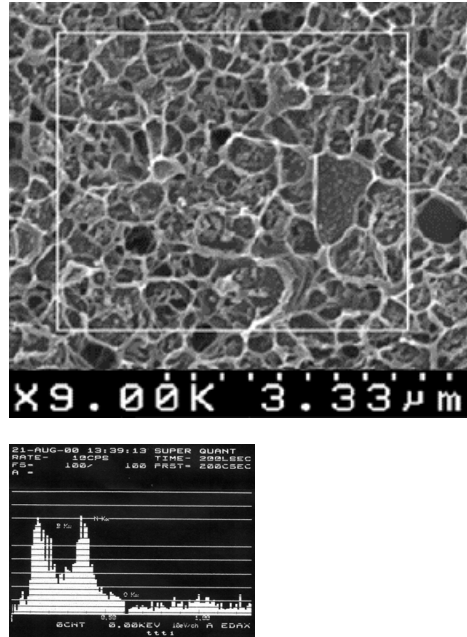


Fig. II.11 Typical oxide pollution on h-BN surface (SEM) (EDX Signal is little informative because of the depth of penetration of the beam.)

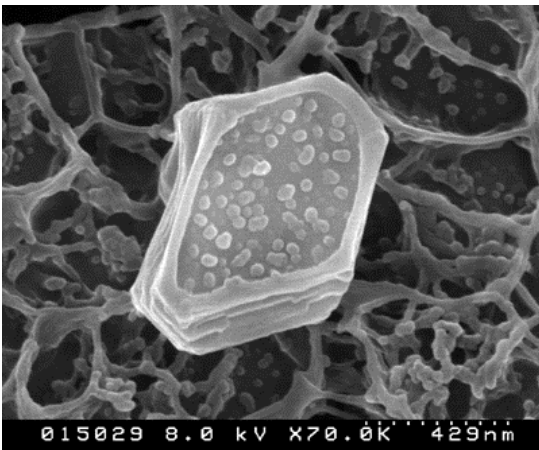


Fig. II.12 Typical oxide pollution on the h-BN surface of the target (SEM)

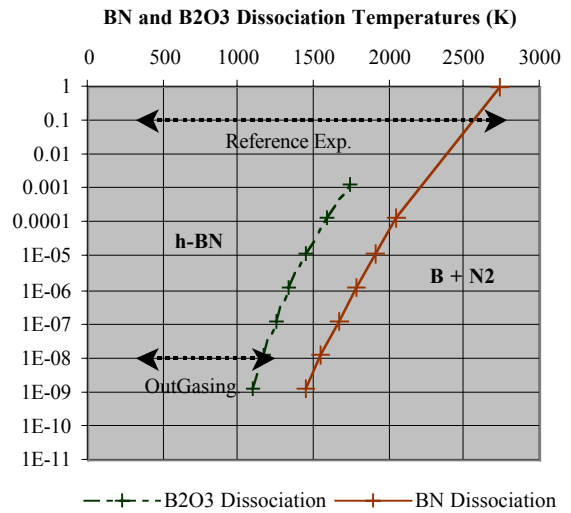


Fig. II.13 vapour tension measurements of BN and B₂O₃, and most stable phases of the BN system (Pressure bar, versus temperatures, K) from [1.1.4]

Chapter III

Techniques to observe and characterise nano-structures

Objective: We review several techniques commonly used for the observation and analysis of nano-structures. We describe how we used them and the difficulties we encountered.

Abstract: Transmission electron microscope (TEM) enables high resolution imaging of individual structures. Interlayer distance of h-BN is large ($\sim 3.3 \text{ \AA}$) compared to the resolution power of a modern microscope ($\sim 1.7 \text{ \AA}$), so that imaging could be easy. However, BN particles are unstable under the beam, because BN is electrically resistant and accumulates charges.

Electron diffraction under the beam of the TEM is complementary to imaging. For a tube, it can characterise multi-layering and helicities of internal layers. Some specific modulations also arise from the limited diffracting area. The weakness of the diffracted pattern is cumbersome, often making observation conditions drastic.

Electron energy loss spectroscopy (EELS) gives a quantitative composition and structural analysis, adapted to light element like B and N. Analysis probe is small enough to study individual structures. The main problems are carbon contamination and electron charging, critical for small particles on which the beam must be focused. Practically, EELS was only affordable for relatively large structures ($> 20 \text{ nm}$).

In a scanning electron microscopy (SEM), the BN target can be observed almost as it is. This allows the observation of structures at their growth position. A SEM enables a high-resolution imaging ($\sim 10 \text{ nm}$), however a metallic coating as thick as 30 nm is necessary to evacuate electrons absorbed from the beam.

I. Four instances of analysis techniques

I.1. Transmission Electron Microscopy imaging (in a few words)

Transmission electron microscopy (TEM) is mostly similar to traditional optical microscopy. The electron beam inside a TEM column behaves as a wave, like photons in an optical microscope. Beam aberrations are roughly proportional to the electronic wavelength, given by De Broglie's relation. By consequence, resolution power is increasing with accelerating voltage. For high voltages (100 kV up to 1300 kV), resolution power is close to one angstrom. Microscopes used here offer $\sim 1 \text{ \AA}$ for the H1500 Hitachi 1300kV, $\sim 1.7 \text{ \AA}$ for the HF3000 Hitachi 300 kV and 1.9 \AA for the CM20 Phillips 200 kV.

Unlike optical microscopes, electron microscopes are limited by spherical aberrations, rather than by diffraction on apertures. This is because correcting spherical aberration requires a divergent lens, not available with standard magnetic coils. (Electron lenses are magnetic coil where magnetic field is concentrated in the centre and approximately bell-shaped along the axis.) Chromatic aberration is also limiting for thick sample because of the energy loss by inelastic scattering. Astigmatism can be corrected with beam deflectors inside column.

I.1.1 Quick description of the apparatus:

- **Emission gun:** In a standard “thermo-emission” gun (TEG) like in present CM20 Phillips, electrons are emitted by thermo-electronic effect and accelerated in the strong electric field. Practically, a tip (typically LaB₆) is strongly heated ($\sim 2700 \text{ K}$) and set to high voltage, with microscope body at ground voltage. By opposition, in a “cold field emission” gun (FEG), like in present HF 3000 Hitachi, electrons are emitted by field emission effect (quantum tunnelling), without heating. Such an electron source is of higher spatial coherence and can be focused to less than one nm. Therefore it is typically well suited for small probe analysis. However, field-emission guns have a lower emission current than thermo-emission guns and require drastic vacuum conditions.
- **Condenser lenses:** Condenser lenses (typically two for a TEG, three for a FEG) project source image (“cross-over”) on the sample. An aperture is usually set after the second lens (“condenser aperture”), so that irradiation zone and irradiation angle are set by both, aperture size and current in condenser lenses. (They influence beam coherence as well.) A

pair of deflectors is used to align the emerging beam perpendicular to the objective lens. Another pair is used to correct astigmatism of illumination beam.

- **Objective lens:** Objective lens is responsible for the first magnification of the object. The current through the coil (hence the focal) is kept close to an ideal value of use. The object (sample) plane is set close to the object focal plane so that objective magnification is fixed at a maximum value. For that, the vertical position of the sample in the column is adjusted manually. Image plane and focal plane are (more or less) fixed in the apparatus. These planes are provided with apertures (respectively of “selected area” and “objective” apertures).
- **Projective lenses:** Projective lenses conjugate on final observation screen either, objective image (“imaging mode”), or objective focal plane (“diffraction mode”). The observation screen is an electron-sensitive fluorescent screen. Image can be further magnified with a binocular microscope. Alternatively, image can be visualised on a TV screen through an array of CCD detectors. A precise focus of the final image after projective lenses is found by slight variations of objective lens current.

I.1.2 Image contrasts

An image contrast arises from the fact that the wave incident on the sample is affected differently along the sample. In the limit where sample is thick, contrast is mainly due to differences of absorption along the sample, hence to inelastic scattering. For thin samples, which are of primary interest, elastic scattering is dominant over inelastic scattering. Two kinds of contrast can appear:

Elastic electrons are scattered with different angles along the sample. Those are shut or not by objective aperture, resulting in an amplitude-type contrast in final image. If objective aperture is centred on beam axis, it selects non-deflected background beams, and background appears white. (“Bright field” image) On the opposite, if the objective aperture shuts the central non-deflected spot, background appears black. (“Dark field” image) Such diffraction contrast is very useful at intermediary magnification, to distinguish between zones of different crystallinity or of different orientation. However, it can not give an atomic level resolution.

Elastic electrons are also scattered with a phase shift, non-uniform along the sample. In final image plane, these phase shifts are reproduced. In planes neighbouring focus plane (defined

by a slight defocus), beams travelling through different parts of the objective lens make Fresnel-type interferences. Modulation of intensity in these planes corresponds to phase changes along the sample. The optimum defocus for best contrast is constraint by spherical aberration, at Scherzer defocus.

The image obtained by phase contrast is, strictly speaking, a figure of interference that should be interpreted carefully. In particular, final contrast depends on sample thickness and defocus amount. It is usually possible to simulate numerically a lattice image, if crystal structure is known. For simple structures like graphite or h-BN, lattice fringes larger than microscope resolution, are interpretable in terms of atomic distances.

I.2. Electron diffraction on nano-tubes

It is possible to study the diffraction from an individual nano-tube under parallel electron beam with a TEM. For carbon nano-tubes, this technique was described by several authors. [6.16] Such diffraction typically indicates what types of helicities are present in a tube. However, it does not indicate what, and how many, layers corresponds to one helicity. Electron diffraction should ideally be complemented by HR imaging, to count the number of concentric layers in the diffracting tube.

Diffraction spots from a carbon nano-tube can be indexed with graphite indexes. (We use hexagonal notations for the unit cell.) The symmetry group of graphite is $P 6_3/m m c$, but the symmetry of one (graphene) layer is $6mm$. Therefore the reciprocal lattice of a graphene layer is also of $6mm$ symmetry.

Although the symmetry group of h-BN is $P 6_3/m m c$, strictly speaking, the symmetry of a BN hexagonal layer is $3mm$. But in any case, due to the very close form factor of B, C and N atoms, there should not be much difference in diffraction pattern from the two materials, and considerations below apply both to carbon and BN.

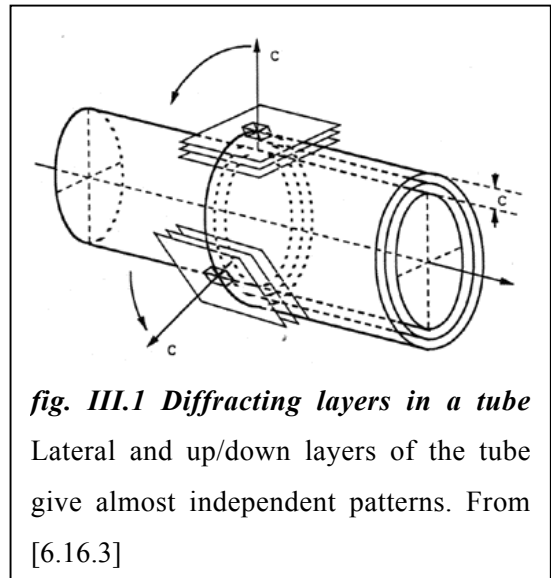
I.2.1 Diffraction from a standard (multi-walled) tube (made of coaxial rolls)

Diffraction from a tube can roughly be interpreted as the sum of diffraction from the lateral parts, parallel to the beam, and up/down parts, perpendicular to the beam. Because of multi-layering, diffraction from lateral parts causes a strong 0002 spot in the direction perpendicular

to the axis of the tube. This spot characterises multi-layering and enable to measure the inter-layer distance.

All other spots follow a 2mm symmetry. They are found on two concentric circles which radius corresponds respectively to the 10-10 and 11-20 reflections of graphite. Spots of each circle can be grouped in sets of hexagons, each similar to the diffraction from a unique graphene layer perpendicular to the beam. Indeed, the global pattern is a superposition of diffractions from all layers perpendicular to the beam.

There are two diffracting layers per roll: up and down parts. Considering the helical model, up and down part of a roll are oriented symmetrically to tube axis. In the general helical case, one roll produces two distinct hexagons pattern, rotated of $\pm \alpha$ from the tube axis. (α is the helicity of the tube) In the specific case of an armchair or a zigzag roll, up and down parts of one roll have same orientation. The diffraction pattern of the roll is a unique hexagon. For an armchair tube, one spot of the most inner hexagon is on the direction perpendicular to the axis. For a zigzag tube, one spot of the most inner hexagon is on the direction of the axis. These spots are unique to armchair and zig zag types. Hence, armchair and zig-zag types are easily identifiable in a diffraction pattern.



The complete pattern is a superposition of different helicities. The number of helicity is usually lower than the number of rolls in one tube, because several concentric rolls share the same helicity. A rough indication of the number of layers for each helicity may be guessed by spot intensity for a given helicity.

I.2.2 Effect of the limited tube diameter

Because of the limited diameter, all graphite like spots (0002 and hexagons) are convoluted by the Fourier transform of a cylinder (Bessel function). This causes a streaking of spots in the direction perpendicular to the axis, clearly observable for any tube.

In addition, this convoluting function has hills and nodes, which periodicity corresponds to tube diameter. Such modulation can be observed for very thin tubes. It was observed for a carbon SWNT [6.16.5]. In that case, the 0002 reflection was absent and the small diffracting zone caused an extreme weakness of contrast. Such a modulation was also observed here from a BN rope. (See Chapter IV.)

I.2.3 Effect of zones neither parallel nor perpendicular to the beam

Additional spots are usually not observed for intermediate zones of the tube. However, such spots may appear for very large tubes. Intermediate zones probably participate to streaking spots, perpendicularly to tube axis, in the external direction.

I.3. Electron energy loss spectroscopy (EELS) (in a few words)

The energy lost by an electron beam when it crosses an individual particle characterises the structural and elemental composition of the particle. Such analysis is performed inside a TEM, where the electron beam can be focused to the dimension of an individual structure (typically 20 nm diameter here). For that, a FEG-type gun is especially well suited, because it enables a probe as thin as 1 nm. In the specific case of scanning TEM (STEM), the very small probe of a FEG can be scanned across a particle. This can be useful to determine the local B/N stoichiometry along the particle.

The inelastic scattering of high-energy electrons in matter is mainly due to plasmon resonances and to K-L-M-ionisations of deep electrons, closest to atom nucleus. Plasmon losses give little information about the composition, and are usually considered as a background here. On the opposite, the K-loss spectrum characterises well the composition of light elements. It is especially intense for light elements, like B and N. (The K-ionisation of N is weaker than that of B, but clearly identifiable from plasmon background.) In addition, for diatomic materials, it is possible to have a rough estimation of the relative stoichiometry of the two elements. For that, the relative intensities of the two absorption edges are compared, after background removal. However, the uncertainty of this technique is high (typically 15 %).

Structure boundings cause some slight shifts in energy loss spectra, from the reference value of individual elements. This is observed as a fine patterns near K-loss energies. For h-BN, the ionisation toward π^* and σ^* levels causes a separation of K-edges as two distinct peaks. (This

is also observed for BN nano-tubes.) Such a fine patterns of the K edge characterises structure boundings. The relative intensities of this fine pattern depend on the orientation of the structure respectively to the beam. Therefore, they depend on the irradiation/collection angles of the electron beam, and on the local orientation of the irradiated zone. (See [4.9] and [4.2.3].)

I.4. X-ray analysis of carbon ropes of SWNT (mainly from [6.3.3])

A rope of tubes with uniform diameters is expected to form a 2D hexagonal-centred (triangular) lattice, in its section. This is because of the non directional inter tube bounding. To characterise this lattice, a TEM can be used to image the section of the rope. Alternatively, X-ray powder technique can be used. However the quantity of diffracting powder must be high (typically 1 cm^2). (Such analysis was not possible here, with the quantity yet obtained.)

Because of the large crystalline parameters ($\sim \text{nm}$), the diffracted signal is dominated by low angle scattering. For carbon SWNT ropes, the strongest reflections were found between $0.44 \text{ \AA}^{-1} < q < 1.8 \text{ \AA}^{-1}$. Such a spectrum must be interpreted carefully. After removing the background (At low q , it is mainly some diffuse scattering from air and amorphous carbon.), the diffraction pattern does not simply correspond to a hexagonal lattice. Indeed two effects conjugate to alter the diffracted pattern (position, intensity and shape of the peak):

- The effect of the limited diffracting size must be taken in account (Like for previous electron diffraction pattern on thin tubes). A single tube form factor is the cylindrical Bessel function $J_0(qR)$, where R is the tube diameter. As R diameter is small, the distance between two nodes in J_0 is short.
- Peaks are broadened by the finite rope diameter and crystalline disorder.

A modelisation of the diffraction spectrum is obtained by convoluting $J_0(qR)$ and the intensities expected from a triangular lattice, considering a peak broadening corresponding to the average rope diameter. Fitting this model with measured spectrum gives R , the distance between tubes, and the inter-tube distance. Incertitude is expected low. ($\sim 2\%$)

Other reflections of graphite are to be expected at larger angles. The 0002 reflection, at 1.85 \AA^{-1} , arise from multi-layering or from graphite remains. The 10-10 reflection of graphite, at 2.95 \AA^{-1} , may be weak for thin tubes, due to high curvatures.

II. Analysis methods used here and their practical difficulties

II.1. TEM imaging

TEM observations were mainly performed on a Hitachi HF-3000 operating at 300 kV and equipped with a FEG gun. Powders for observation were collected manually on target surface with small tweezers, and deposited on a carbon micro-grid supported by a copper grid. Sometime, a drop of solvent was added to help spreading.

The product available for imaging is only a small fraction of the product deposited on the micro-grid. This is firstly because, entangled fibres have a poor ability to spread on the micro-grid. In most regions, the product is compact and too thick to transmit the electron beam. (Thickness should typically be under 100 nm for light elements like B, C, N.) Secondly, only regions at hole edges of the carbon micro-grid can be observed without an underlying carbon layer.

As the interlayer distance of h-BN is large ($\sim 3.3 \text{ \AA}$) compared to the resolution power of the TEM ($\sim 1.7 \text{ \AA}$), high-resolution imaging could seem rather affordable. However, the electric resistance of BN causes an accumulation of charges under the beam, and hence structures are unstable. Pieces of the product, which are not well linked to the supporting carbon grid, tend to move away from the beam. At high resolution, individual particles vibrate with atomic-large amplitudes, causing blur images.

This problem is especially critical when observing long tubes, because those are linked to the supporting carbon layer by only a few contact points. Charges have to travel along a fraction of tube length before escaping to the supporting carbon layer. Most of all, the electron beam affects fibre free extremities because, those are usually far away from a contact point with the carbon micro-grid. (Unfortunately, imaging of tube extremities is important for discussing tube growth processes.)

In the extreme case of intense irradiation, particles are easily damaged. This commonly observed when focusing the beam on the extremity of a fibre. Tubes extremities are destructed, by ejection of their constituent atoms. Ropes extremities often split into their constituent tubes before being destructed.

4 practical ways to undermine the electron charging effect for imaging

- A high-resolution image of a tube is best realised near end of the tube that is a fixed to a another particle. Tube has less amplitude for vibrating and, the local charge is more easily evacuated to the neighbouring particle.
- As the material is deposited as islands of agglomerated particles on the carbon micro-grid, it is usually better to observe small islands. Those suffer less from charging effect, because they have closer contacts to the supporting carbon layer.
- It is often worth limiting the irradiated zone to the observed structures. The beam collected by the material out of the observing area contributes to the global charging effect. To focus irradiation beam on observed particle without an over-powerful beam, it is necessary to select a small condenser aperture.
- The incident electron beam affects the stability of the structures. Therefore, after focus has been set for photo, the condenser lens current should not be changed.

Note: A lower accelerating voltage may also undermine electron charging effect.

II.2. Electron diffraction inside TEM

When diffracting a parallel electron beam on some particles, the selected area aperture controls the diffracting area. However, the smallest aperture (~ 200 nm in the HF-3000 Hitachi microscope) is quite large, compared to the size of an individual particle.

Practically, such diffraction can not be undertaken for an individual onion. However, diffraction can be undertaken on a group of agglomerated onions. This gives as polycrystalline-type diffraction. (Alternatively, convergent diffraction could be used for individual onions, if damages from the beam can be avoided.)

Diffraction on an individual tube, away from the rest of the material, is possible, but difficult. Indeed, the diffracting surface is very small, compared to the total irradiated surface. By consequence, diffracted spot are very weak compared to the non-deviated spot. This problem increases with thinner tubes. It is critical for tubes with a few atomic layers.

4 ways to enhance the signal diffracted from a tube (with a FEG):

- It is sometimes better selecting the smallest selected area aperture. (If R is the aperture radius, tube-diffracting area varies as R , but non-diffracting area varies as R^2 .)
- The tube should be on one diameter of the aperture, to diffract on a maximum length.
- It is better to select the largest condenser aperture, to have a signal as strong as possible, after the beam has been spread (for parallel irradiation.).
- It is necessary to select a very long exposure time (typically, 2 min with Hitachi FEG) because of the very weak signal. Most often, the diffraction pattern is so weak that it is not observable on screen when taking the photo.

In the product, zones favourable to tube diffraction are few. Ideally, the diffracting tube should be well away from the rest of the material to avoid undesirable patterns. Also, the observed tube should be perpendicular to the beam and as straight as possible. A tube curved in the plane perpendicular to the beam induces a distortion of the diffraction patterns.

Unfortunately, tubes best suited for diffraction are often not well suited for good imaging. This is because parts of the tube that are away from the rest of the material (suited for diffraction), often suffer a high electron charging when imaging. It is often not possible to have simultaneously a good diffraction pattern and a high resolution imaging for the same tube.

Finally, diffracting area does not strictly correspond to selected area, because of spherical aberration. Practically, a diffracting margin should be foreseen around selected area, when taking the photo.

II.3. EELS

EELS can give a composition analysis of individual particles, complementary to TEM imaging and electron diffraction. We use a Gatan parallel electron energy loss spectrometer (PEELS) at the bottom of the HF-3000 Hitachi microscope. The FEG electron gun enables an analysis probe down to 0.9 nm large, which is much lower than the typical dimension of the structure studied. The estimation of the B/N ratio is possible through a standard routine of

Gatan EL/P 3.0.1 software, which subtract signal background and compares the relative intensities of the peaks.

For EELS acquisition, the beam must be concentrated to the dimension of the particle studied. Practically, relatively large structures (onion or fibre of diameter > 20 nm) can endure the electron beam. However, for smaller diameters, concentrated irradiation tends to damage the particle. In addition, tubes tend to drift away from the beam because of charging effect, so that the beam is not longer crossing through the tube.

For small particles, it is possible to weaken the beam, by using a smaller condenser aperture. However, in that case, the acquisition time must be risen to increase the signal, and long time of irradiation favours carbon pollution on the particle: Inside TEM column, some positive carbon hydrogenic radicals are formed by ionisation under the beam. Such carbonic ions are continuously trapped toward the negative charge of the electron beam, and deposit on the sample. As this pollution is proportional to the time of irradiation, it eventually becomes detectable in the spectrum. This can happen for acquisition times as short as 5 s.

II.4. Scanning electron microscopy (SEM)

In a SEM, a focused electron beam is scanned along the sample, and the reflected beam is measured in the specular direction. The SEM is appreciated for being simple to use, little destructive and because it gives a 3D information. If it is equipped for X-ray energy dispersive spectrometry (XEDS), it can also analyse rays-X back-warded from irradiated particles. (But the deepness of electron beam penetration in the material is problematic for local analyses.) The resolution power of a SEM is however not comparable to that of a TEM..

Here, SEM observations were mostly performed with a high-resolution (~ 10 nm) Hitachi microscope, equipped with a FEG and XEDS (non-quantitative). Some observations were also performed on a Phillips XL-30. The SEM was especially important to observe particles at their growth position. Indeed, target can be observed almost as it is.

However, the BN target must first be coated by a conductive metallic layer. (No observation on BN is possible without coating.) A layer (typically ~ 20 nm) is deposited in an evaporating chamber. Because of the thickness of this coating, the thickness of particle observed has little meaning. Both tungsten (when using Hitachi microscope) and gold (when using Phillips

microscope) were used, with no obvious difference. The non-uniformity of the coating, as a nanometric wavy pattern, was sometime observed at high-resolution imaging.

For size limitation of the sample in the Hitachi microscope, target height had to be reduced from 4 mm to 2mm. (The Hitachi SEM uses a “TEM-type” sample holder, with very limited space for the specimen.) This was done by polishing the facet opposed to the heated facet, with sandpaper. Sandpaper was wet with ethanol to preserve the zone of interest from drawback h-BN powders.

Chapter IV

Standard laser heating and global conclusions on physical processes

Objective: We describe a typical heating experiment, the structures obtained and the geography near impact. Then, we draw global conclusions on growth processes.

Abstract: A h-BN target is out-gazed and submitted to a “thermal shock”. When the laser beam is focused on its surface, under low pressure of nitrogen, a radial temperature gradient is imposed. h-BN dissociates locally, forming a cavity partially filled with liquid boron.

After 3 min. of heating, BN nano-tubes are found on target front surface, on a ring around cavity. This product forms a crown perpendicular to target surface. Tubes are made of stoichiometric BN, and mostly contain few layers. They tend to be self-assembled in ropes. Such fibres have been observed as long as 120 microns. Their extremity is often merged to a nano-sized boron rich BN particle.

Boron rich BN (BN/B) particles are found scattered around cavity. Inside the crown they are faceted BN onions, whose cavity is often occupied by a boron nano-crystal. Further away from the cavity, they contain very little nitrogen and are assembled in micro-cluster, which size is decreasing from the centre of impact.

The growth of nano-structures does not occur directly from h-BN platelets. Instead, after dissociation, boron evaporation from the cavity and condensation in atmosphere, boron rich particles are spread on target. On a specific ring around cavity, boron recombines with atmosphere. This ring of recombination corresponds to a specific range of temperature, where boron is liquid. In this zone, the growth of tubes is initiated by the recombining boron rich particles.

I. Standard experimental procedure

A standard experimental procedure for a h-BN target was chosen, in order to study later the influence of each adjustable parameters independently (Chap. VII). These experimental conditions were determined after a serie of experiments with various (arbitrary) experimental conditions. It was checked that the standard procedure gave reproducible result.

I.1. Target preparation

Target is a cube $\sim (4 \text{ mm})^3$ of hot-pressed h-BN (micro-platelets) powders. A small cylinder is cut from a commercial h-BN rod (6 mm \varnothing) with a SiC rotating saw. The resulting section surface is relatively smooth and little oxidised. It is used for the laser irradiation.

When heated without treatment, such a h-BN cylinder target has a tendency to release smoke and to eject flat pieces from its external cylinder surface. Commercial h-BN usually contains a large amount of impurities (boron oxide $\sim 5 \%$, calcium... (See Chap. II-V) To avoid this pollution, as well as instability of the target on its stand during warming, (Target can easily be ejected from the stand under back-warded impulsion from ejected pieces.) the cylindrical surface is polished with sandpaper. The target is shaped as cube and corners are removed. It is finally cleaned with an air throw.

I.2. Out-gazing

To remove the remaining impurities, target must be out-gazed in vacuum at high temperature. (During out-gazing, diffusion at high temperature may also rearrange the target toward a more homogeneous material.) For this, target is positioned in the chamber, on a specific h-BN stand, away from the centre. At this position, target is facing the laser beam, but away ($\sim 8 \text{ cm}$) from the waist plane. With a beam out of focus, dissociation temperature is not reached at impact, and surface is not degraded.

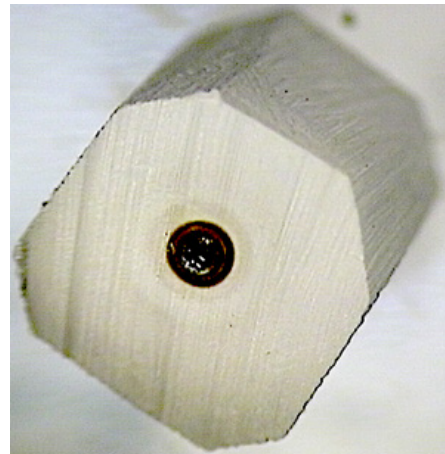


Fig. IV.1 h-BN target after heating

The surface of the cylinder was polished to get rid of most impurities. Rod section was used for the heating.

The surface corresponding the rod section, that was latest cut, is facing the beam. Atmosphere is evacuated to secondary vacuum ($\sim 10^{-5}$ mbar) and kept under pumping. The target is heated by the laser at 70 W, for ~ 5 min. Front facet, which was at highest temperature, is used for the final heating.

I.3. Thermal shock

After laser was switch off, and target has cooled down, target is irradiated again, in same conditions, but for a short time (~ 5 s). This induces a thermal shock in the target, whose reason is not yet clear. However, it was found experimentally, to be important for the quantity of material produced and for repeatability of the experiment. It may result from the importance of surface quality. (Discussed in Chap. VII-V)

I.4. Heating

Target is moved to the central h-BN stand, in the middle of the enclosure, so that front surface is near waist plane of incident beam. For this, the chamber must first be opened to air. To minimise air pollution on the target, the pressure rise (up to one atmosphere) is obtained by filling the chamber with nitrogen gas. After target as been positioned, the chamber is evacuated to a secondary vacuum again, and filled with nitrogen (**100 mbar**). The exposition to air at that stage is less than one minute.

Front facet of the target is irradiated for **3 min**, laser set at **70 W**. Beam is focused to a diameter $\sim 180 \mu\text{m}$ (waist $\sim 90 \mu\text{m}$) in the middle of the facet. After heating, the target is left to cool down several minutes before opening, to avoid an eventual oxidation. Final pressure rise for opening is also obtained by nitrogen gas filling.

II. Geography on heated surface

Heating in standard conditions results in a growth around the impact of the laser beam. On an inner ring around the cavity (zone II), a powder-like product is growing perpendicular to the surface, forming a “**crown**”. It is where tubes are found.

II.1. Three distinct zones

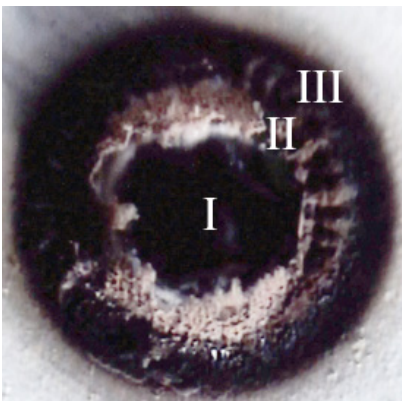
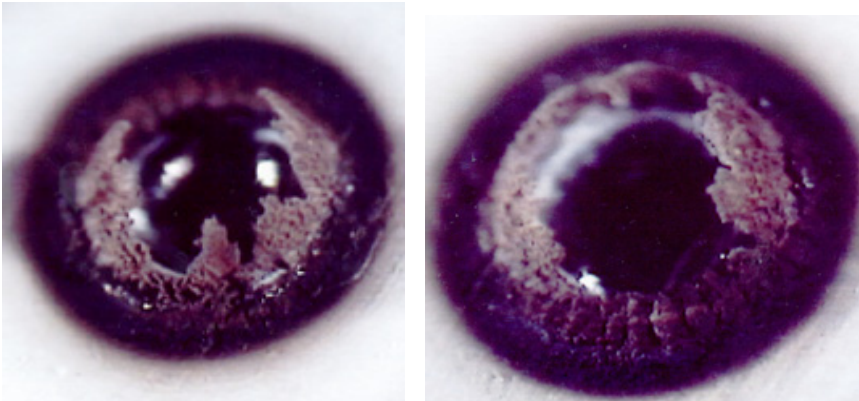


Fig. IV.2 Growth around laser impact, for standard conditions
(Binocular microscope image)

Zone I: Cavity partly filled with drops of solidified boron.

Zone II: mixed BN nanotubes (self-assembled in ropes) and BN/B onions, form a crown growing perpendicular to target surface.

Zone III: Surface is covered by a deposit of boron rich particles organised in micro clusters.

Diameter of zone III ~ 1 mm.

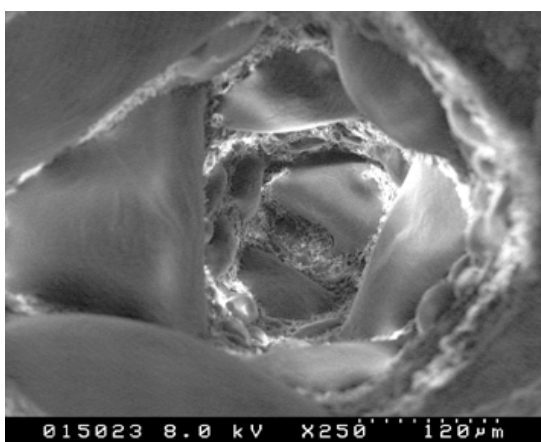


Fig. IV.3 Zone I, SEM view inside the cavity
The cavity is partially covered with solidified boron drops.

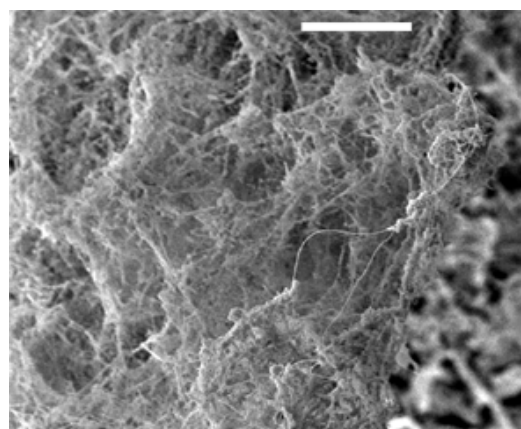


Fig. IV.4 Zone I, SEM view of the crown-like material Tangled BN tube (in ropes) are mixed with BN/B onions particles. Scale bar 10 μm.

II.1.1 The cavity (Zone I)

After heating, the h-BN surface is hollowed on a volume roughly conical, where temperatures went over dissociation temperature of BN ($\sim 2700^\circ\text{K}$). Liquid boron resulting from h-BN dissociation was partly evaporated. However, a fraction of boron is left inside cavity, as drops solidified during target cooling. Surface inside cavity is therefore a mix of boron and h-BN. The bottom of the cavity is flat on a region ($\sim 110\ \mu\text{m}$) slightly thinner than beam diameter ($\sim 180\ \mu\text{m}$).

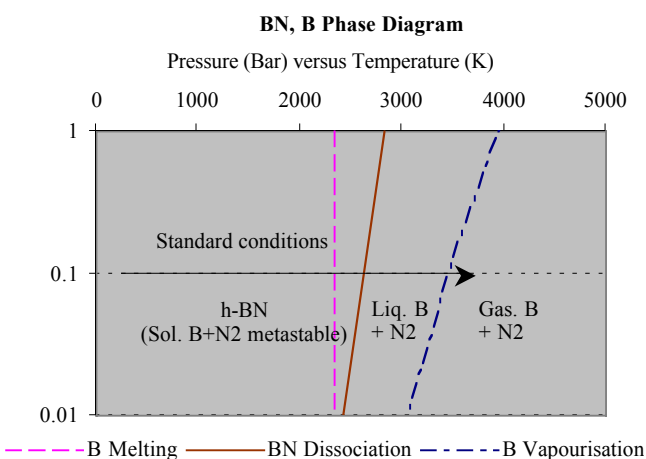


Fig. IV.5 Stable phases of the B/N system

II.1.2 Crown material (Zone II)

The crown growth is about $200\ \mu\text{m}$ high and about $130\ \mu\text{m}$ large. (It is visible with a naked eye.) Its material is a fibrous product, composed of a mix of tubes, assembled in ropes, and B_xN_y nano-sized particles. EDX analysis in different areas of this product reveals that B/N ratio is often boron dominated. This ratio is however non-uniform. (But in some area, where product is shallow or little dense, the electron beam may reach the underlying h-BN surface.)

Where surface beneath the crown is observable, it is a mix of various nano-sized particles, often with characteristic BN-shells. Some large rounded particles (Fig. IV.9), with stoichiometric B/N ratio, suggest that some boron liquid drops have recombined completely with nitrogen atmosphere in this zone.

II.1.3 Deposit (Zone III)

Surface further away is covered by spherical nano-particles, looking similar to that of zone II in the SEM. But, unlike in the tube growth zone, those nano-particles are extremely boron rich. They are agglutinated in spherical micro-clusters (fractal pattern), which size is decreasing from the cavity. Nano-particles probably stick to each other, because of structural merging at high temperature. The global thickness of this deposition is decreasing when going to outer regions, where surface is only h-BN platelets after some distance.

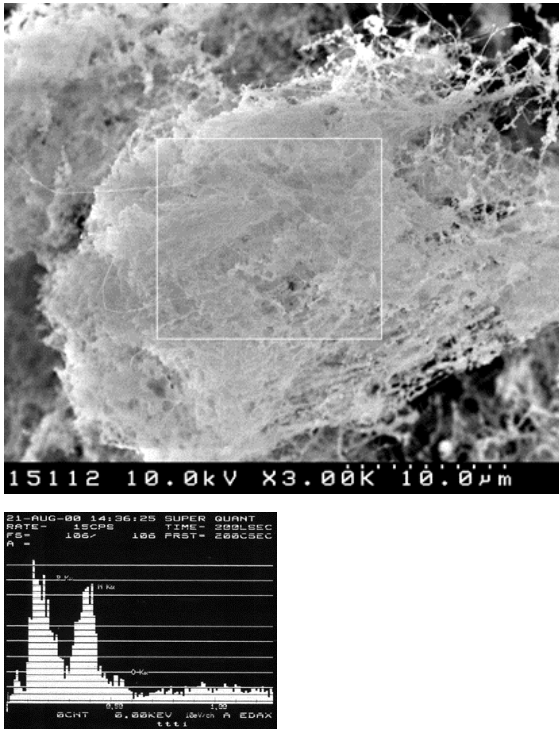


Fig. IV.6 EDX spectrum from a local area of the crown BN is almost stoichiometric. (See Chap. II-V.2 for a reference h-BN spectrum.)

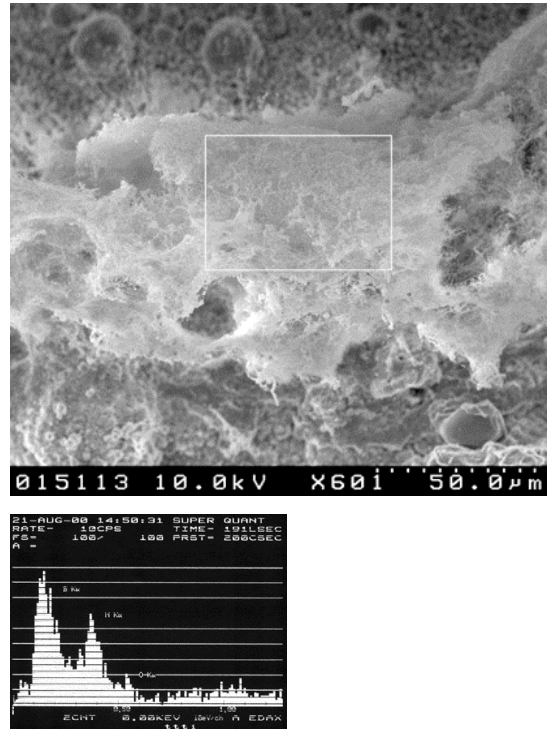


Fig. IV.7 EDX spectrum from a large area of the crown Boron absorption peak is slightly dominant over nitrogen peak.

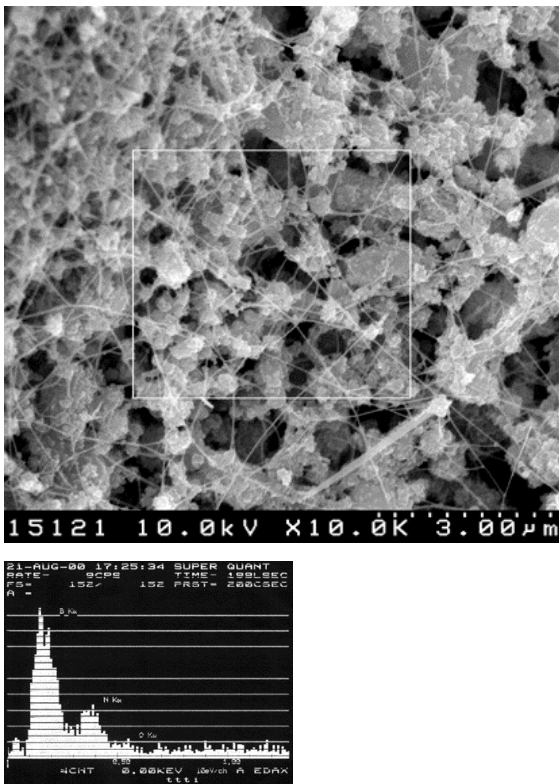


Fig. IV.8 At target surface in the middle of zone II Boron is clearly dominant over nitrogen.

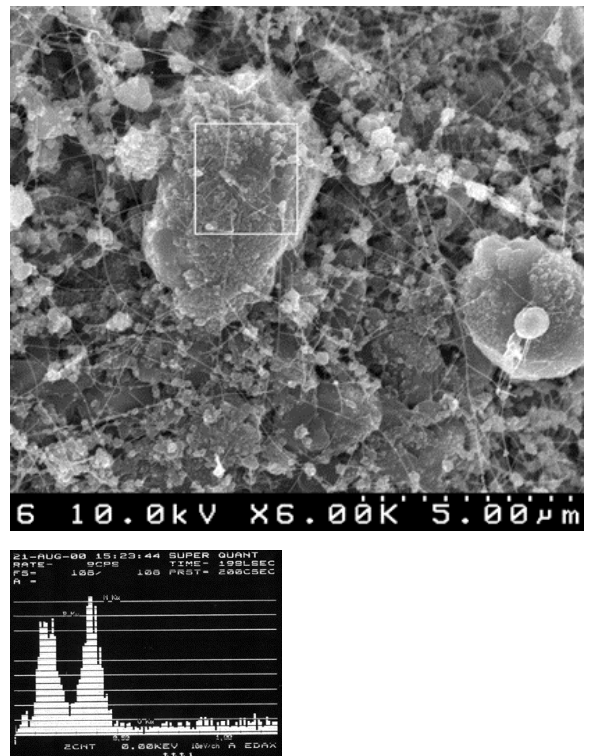


Fig. IV.9 A micro-particle of pure BN at surface of zone II It is probably a drop of boron completely recombined under nitrogen atmosphere.

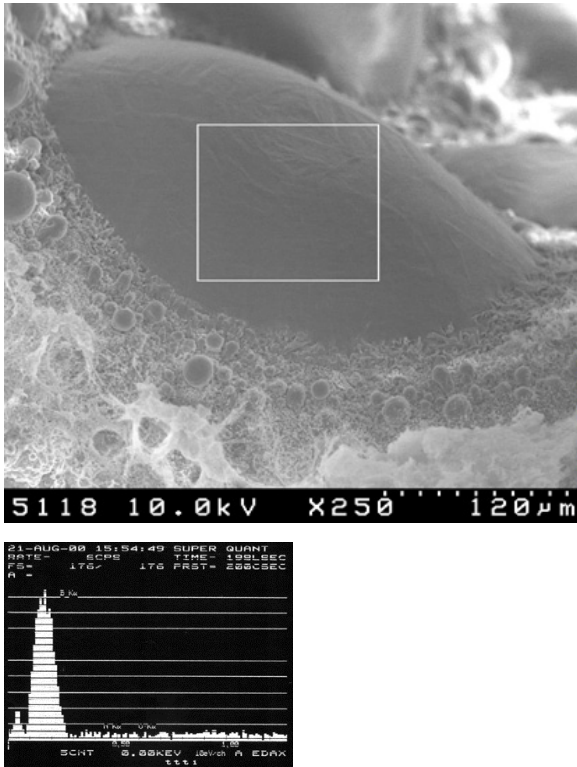


Fig. IV.10 A boron drop near the edge of the cavity EDX spectrum shows very pure boron composition.

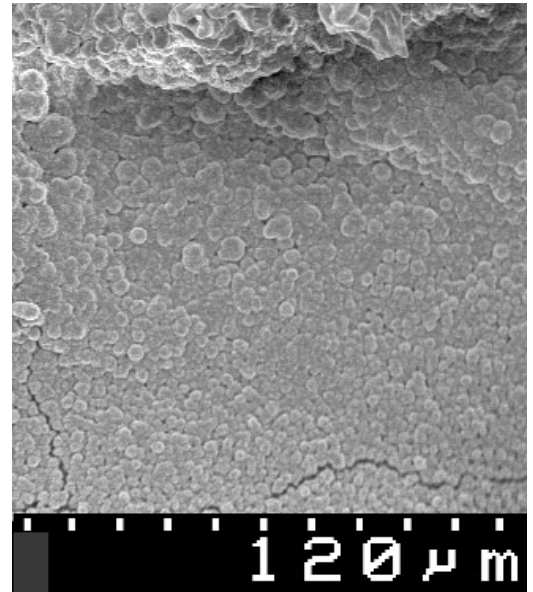


Fig. IV.11 Zone III Nano-particles are agglomerated in micro-clusters, whose size is decreasing away from impact.

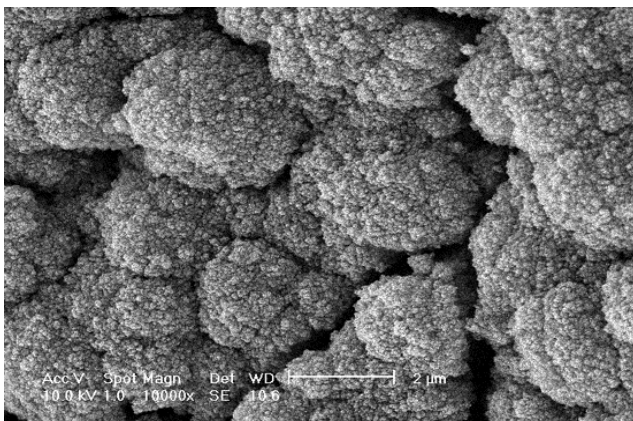


Fig. IV.12 Zone III Agglomeration of nano-sized boron rich particles in micro-clusters

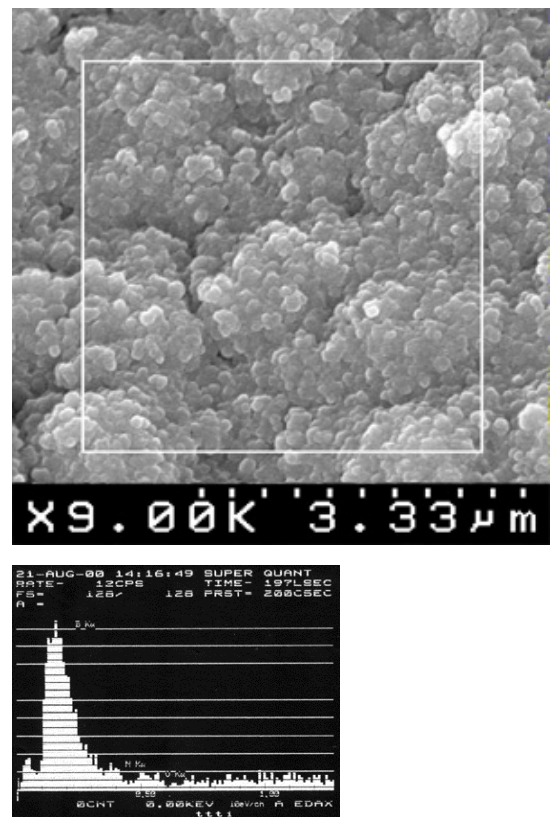


Fig. IV.13 Nano-particles in zone III Particles are extremely rich in boron and tend to stick to each other.

II.2. Frontiers between zones

II.2.1 At the edge of the cavity

The most outer boron drop in the cavity roughly borders the most inner nano-particles (onions and tubes) of zone II. By consequence, the upper most temperature at which tubes and onions are present is roughly the dissociation temperature of h-BN (2700 K at 100 mb of nitrogen). Some nano-particles may cover the most outer boron drops on some distance, or else there is sometime a zone of pure h-BN between zone I and II, for part of the periphery. But, at most, such mixed regions are a few tens of microns large.

II.2.2 At the frontier Between II and III

(Fig. IV.15-18)

The frontier between zone II and III is delimited by a pure boron front. This front follows the frontier periphery, although it is usually not present on whole periphery. It only appears for times of heating longer than 3 minutes. It is shaped as a solidified melt and sometime tends to rise perpendicular to the surface. This front is very limited in thickness. Tube ring surface next to it clearly different (nitrogen rich), marking a clear frontier between zones.

The probable origin for a boron front is a thermal convection of liquid boron on target surface, beneath zone II. At inner extremity of zone II, temperature is ~ 2700 K (± 100 K). At that temperature, boron is liquid, and readily migrates away from the cavity due to the stiff surface temperature gradient. This concerns mainly boron beneath zone II, because it is not in contact with nitrogen atmosphere, and can not recombine into BN.

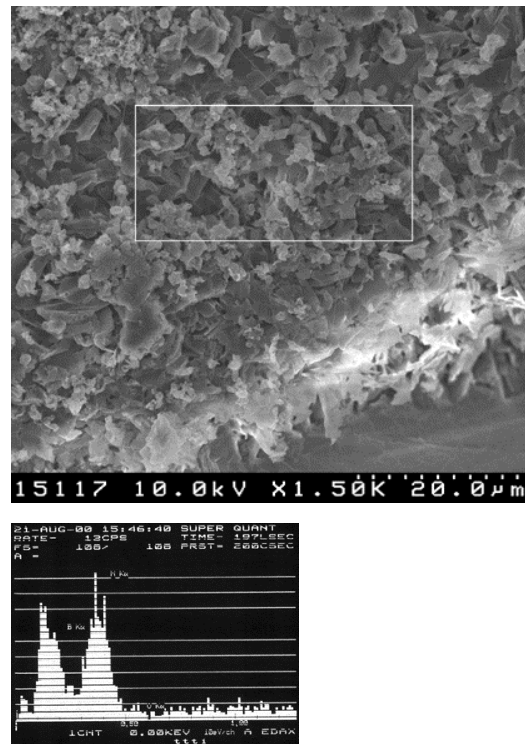


Fig. IV.14 In zone II, near the most outer boron drop of the cavity Surface is a mix of h-BN platelets, nano-sized particles and tubes. EDX spectrum indicates B/N ratio closely stoichiometric.

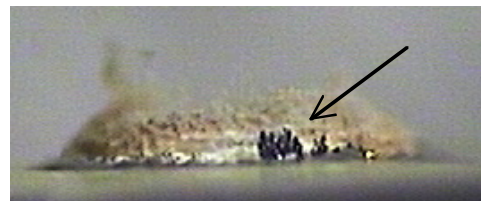


Fig. IV.15 Side view of the crown growth A black boron melt is rising perpendicular to target surface.

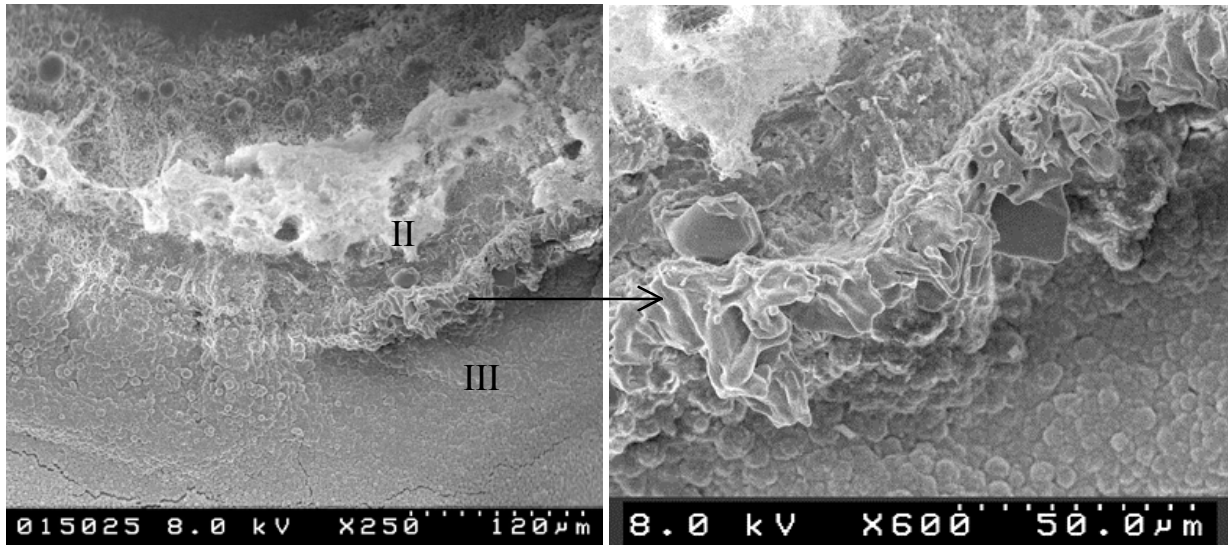


Fig. IV.16 Boron melt at the outer extremity of tube growth ring (SEM at low magnification)

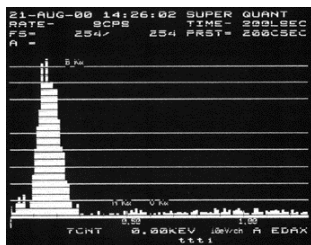
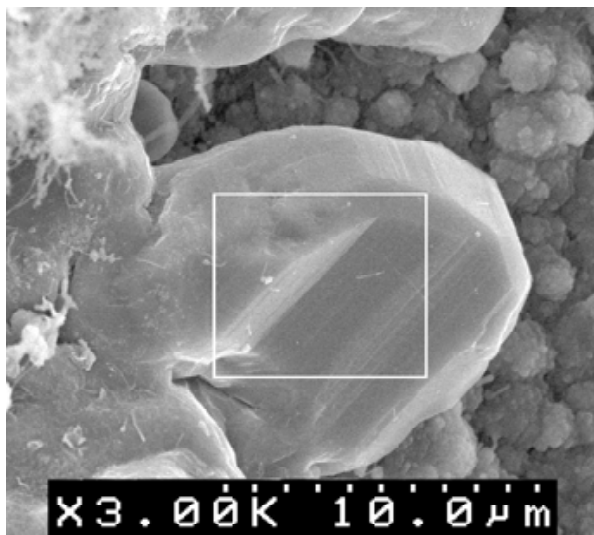


Fig. IV.17 A small area of the melt EDX spectrum shows very pure boron.

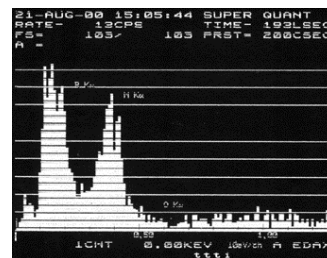
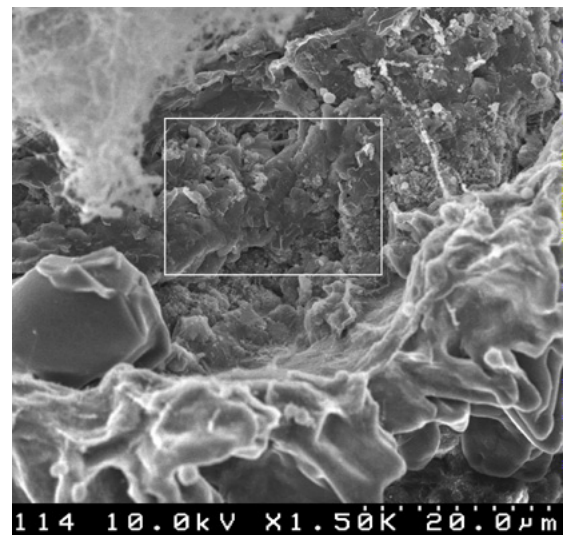


Fig. IV.18 Surface of zone II, adjacent to the melt. The spectrum reveals almost stoichiometric BN.

Boron convection stops where boron becomes solid, hence at fusion temperature of boron (2350 ± 100 K). Therefore boron accumulates on a symmetrical circle of iso-temperature. Boron accumulation grow upward because of pressure from drifting liquid boron on fixed solid front. This is similar to the patterns obtained during solidification lava flowing from a volcano.

For the present study, this gives a very useful indication. The lower temperature of zone II is ~ 2350 K. Tubes grow on ring limited by temperature between 2700K-2350 K, where BN is not dissociated and where boron is liquid. This is to be confirmed by temperature estimations of chapter V. However, it should be kept in mind that both value of dissociation and fusion are known very imprecisely from literature (± 100 K), so that the temperature range is little known. A value between 200 K to 500 K can be expected.

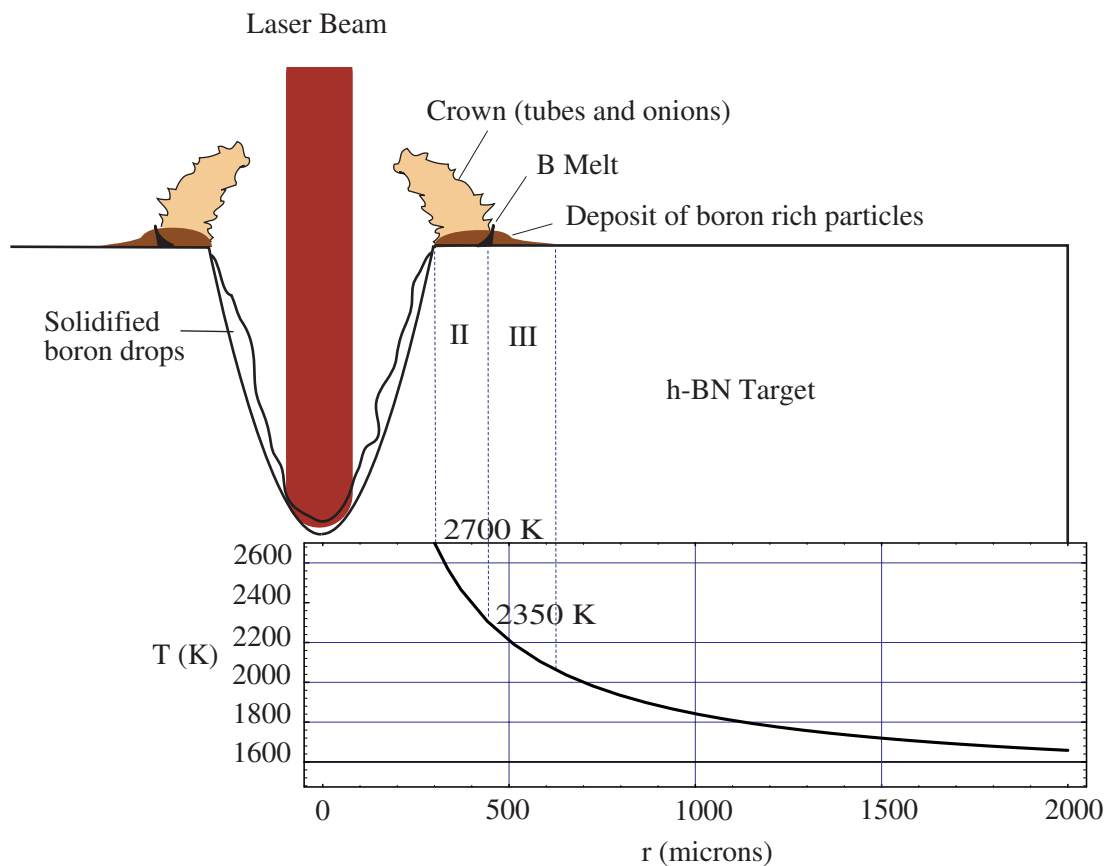


Fig. IV.19 Summary of geography around impact. (Temperature gradient as estimated in Chap V-II.2.2)

IV. Material from the crown (zone II)

IV.1. Global aspect at low magnification

At low magnification, material from the crown appears as a mix of fibres (ropes or tubes) and nano-spherical particles (BN/B onions). Tubes and nano-particles readily adhere to each other, through weak Van der Waals interactions, or through structural merging. Powders and fibres are never separated in the crown, although their relative yield is not

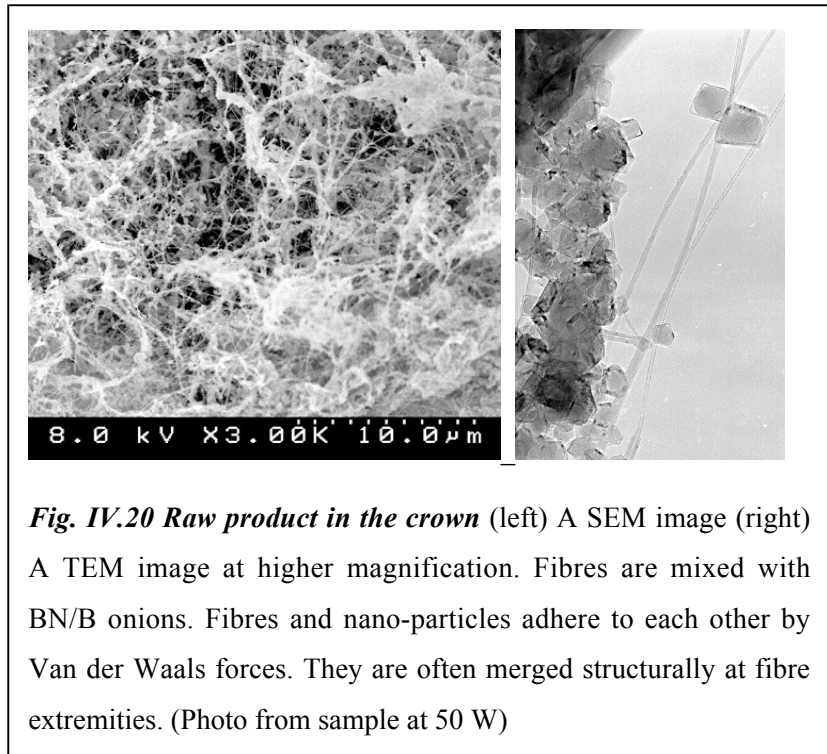


Fig. IV.20 Raw product in the crown (left) A SEM image (right) A TEM image at higher magnification. Fibres are mixed with BN/B onions. Fibres and nano-particles adhere to each other by Van der Waals forces. They are often merged structurally at fibre extremities. (Photo from sample at 50 W)

uniform. The top of the crown is sometimes rich in nano-particles. (It is not clear if tubes only grow at target surface, or also up-crown, away from target surface.)

Fibres are very long and entangled, forming tissue-like patterns. A measurement of the average length of fibres is not possible with a SEM. Fibres are only observable between knots. They are typically discerned from the rest of the material on several tens of microns. The longest observation was 120 μm , and was obtained for the longest duration experiment. (See Chap.VII-I.2.6) Some several microns long fibres are sometimes observable on their full length.

IV.2. TEM high resolution imaging of tubes

IV.2.1 Rope ordering

TEM observations reveal that most fibres are BN nano-tubes self-assembled in ropes. A rope contains a few tubes, up to several tens. Ropes are often branched along their length, one or several tubes diverging from the main rope. Under intense electron irradiation, rope

extremities tend to split into their constituent tubes, forming a brush like extremity, and attesting for the weakness of the inter-tube bounding.

The internal tubes can be observed by imaging a thin rope laterally. (Fig. IV.21) However, large ropes are thick, so that they may appear as uniform ribbons without contrast. Imaging a rope in its section (Fig. IV-a) is difficult because of electron charging under the beam. A rope loop must be oriented closely parallel to the electron beam. But when such loop gets ionised, its orientation and position is unstable. The result is a blurred image. On Fig. IV-a, the atomic layer pattern is not resolved, but individual hollow tubes are discernible in the section. Because of this difficulty, an eventual 2D triangular lattice inside the BN rope could not be characterised by imaging. A X-ray study (See Chap II-I.4) could be more suited to characterise a BN inter-tube lattice, but this requires a quantity of product higher than presently available.

IV.2.2 BN tubes

Tubes can be imaged at high resolution if they are separated from a rope, or inside a very thin rope. Most tubes are very thin (typically 2, 3 or 4 layers). Bi-layered tube may be dominant inside ropes, although only a small fraction of these are observable in high resolution. Tube diameters are remarkably constant along tube axis. (Fig. IV.21) The inner diameter is often close to 2 nm. This is also a minimum value, probably due to a constraint specific to BN: A strong curvature is structurally costly for the inter-layer accommodation in a tube with several layers. (Inner diameter is ~ 8 nm at most.) Exceptionally, the section of an individual tube could be imaged by TEM. (Fig. IV.22b) This section is circular (and not polygonal), but does not allow confirming that layers are concentric and not spiralling in the tube.

SWNT were not evidenced. Tubes with only one fringe on each side at high resolution were observed. However, these are more probably bi-layered tubes vibrating under the electron beam. For such tubes, it was sometime possible to resolve a two fringes pattern on a more stable zone of the tube. The thickness at mean contrast of one fringe was never under 6 Å. (~ 2 layers) (This however does not prove that SWNT are strictly absent in the product.)

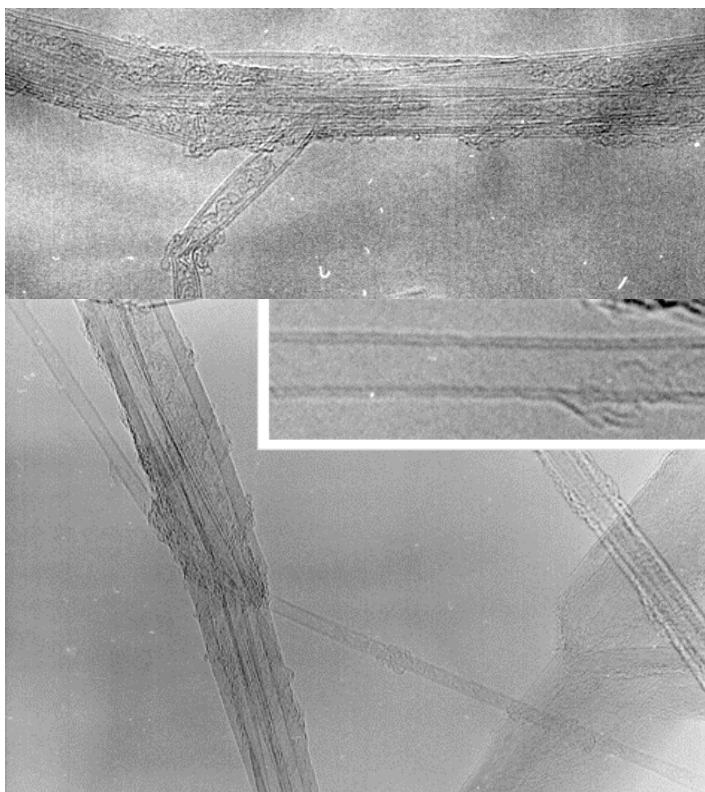


Fig. IV.21 TEM imaging of BN tubes (up) Lateral TEM image of a thin rope (Photo from sample at 300 mb) (down) A bi-layered tube at 2 different magnifications. The diameter is remarkably constant. (Sample at 50 W)

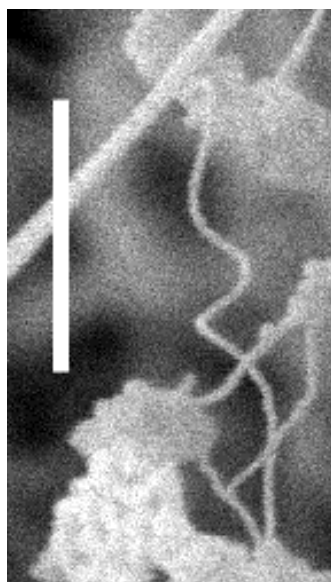


Fig. IV.23 A Spiral fibre branched on a larger fibre (SEM) This is probably the result of a torsion around axis. Scale bar 1 μm .

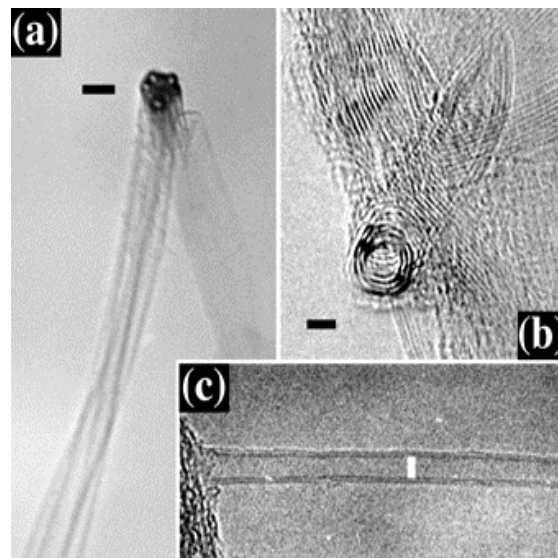


Fig. IV.22 TEM imaging of BN tubes (a) A loop of a rope. A section of a rope, which is perpendicular to the electron beam, appears contrasted. It contains ~ 10 tubes. During the imaging, the rope is slightly vibrating due to the charging effect under the electron beam, causing blurred image. Scale bar 10 nm. (b) Section image of a three-layer tube showing a circular section. Scale bar 2 nm. (c) Two-layer tube. Scale bar 2 nm.

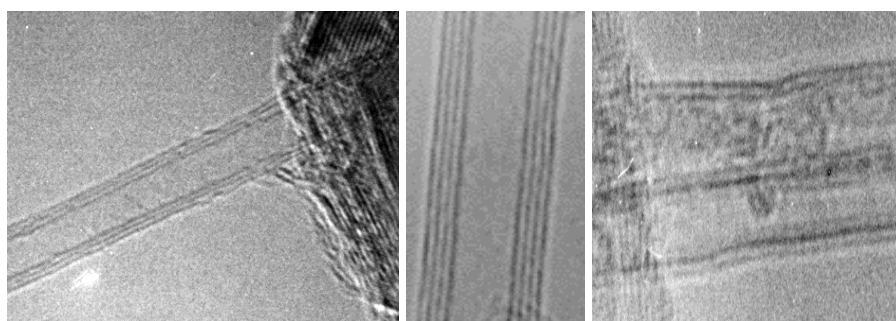


Fig. IV.24 TEM imaging of BN tubes (left) A 3 layer tube (middle) A 4 layer tube. (Sample at 50 W) (right) Lateral view of two collateral tubes, each with two layers. (Sample at 50 W)

Various other tubular morphologies are observed. Some individual tubes are thick (typically, ten layers), and very straight (because of little flexibility). The diameter of the fibre may be changing along axis, by steps or continuously. Half merged BN(+B) onions can also agglutinate along a fibre. BN/B onions have the ability to merge to each other and to fibres (at high temperatures). Their constituent B/N atoms seem to diffuse along the fibre axis on some distance, ultimately forming h-BN layers parallel to the fibre surface. Indeed, fibres are sometime covered locally with an irregular shell of h-BN layers. (See Chap VII-II.1)

Sometimes thin fibres are spiralling. This may result from a specific structure or, more probably, from a mechanical torsion around the axis of the tube. The flexibility of thin tubes is evidenced by their ability to curve when charged by the irradiation of the electron beam.

Also, some amorphous material is sometime present on tubes body, possibly amorphous BN, amorphous boron, or eventually, carbon contamination inside TEM.

IV.3. Electron diffraction patterns from tubes and ropes (See Chap. III-II.1 for how to interpret tube diffraction.)

Diffraction from thin tubes requires drastical observation conditions (See Chap. III-II.2), so that a limited number of photos could be obtained. Diffraction could be obtained for several thin tubes and one thin rope. (See Fig. IV.25-27)

All diffraction patterns show a (weak) 0002 reflection, perpendicular to the tube axis. For an individual tube, this is characteristic of multi-layering. (A single walled nano-tube has no 0002 reflection). For a rope, this reflection could also correspond to an inter tube distance, although in the case of carbon SWNT rope, the distance between tube cylinder is found notably smaller (3.15 Å) than the inter layer distance of graphite (3.33 Å). [6.3.3]

All other spots (10-10 and 11-20) are characteristic of the helicities of hexagonal layers in the tube. (Some helicities may not be observed because of too weak diffraction.) Several types of helicities are observed, but armchair and zig-zag types are more common. Inside one tube, the same helicity seems prevalent. A superposition of concentric layers of same helicity may lower the structural cost of the inter-layer accommodation. (Although the misfit of periphery length between neighbouring layers must be compensated elsewhere in the structure, unless the tube is constituted of one spiralling layer. See [6.8.4])

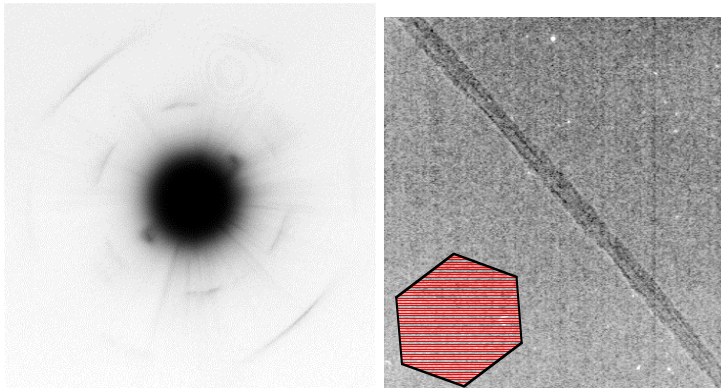


Fig. IV.25 Two parallel thin tubes. The 0002 spots indicates multi-layering. Diffracting layers are of armchair type helicity. A slight curvature of the tubes induces imperfect symmetry and circular arc instead of straight lines. (From sample at 50 W)

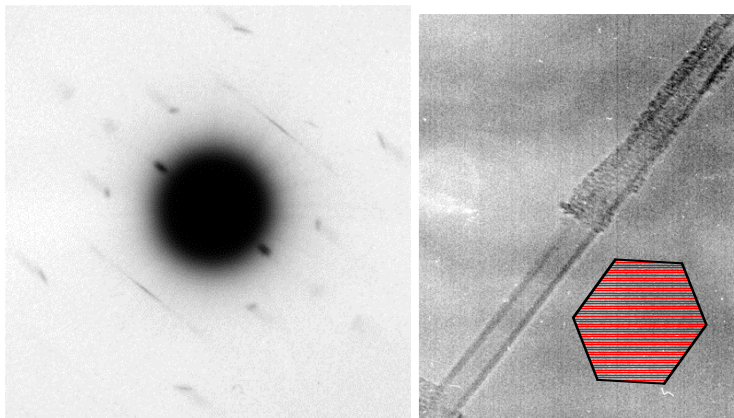


Fig. IV.26 A tube with rather large inner diameter. The 0002 spot indicates multi-layering. Diffracting layers are of zig-zag type helicity. (From sample at 50 W)

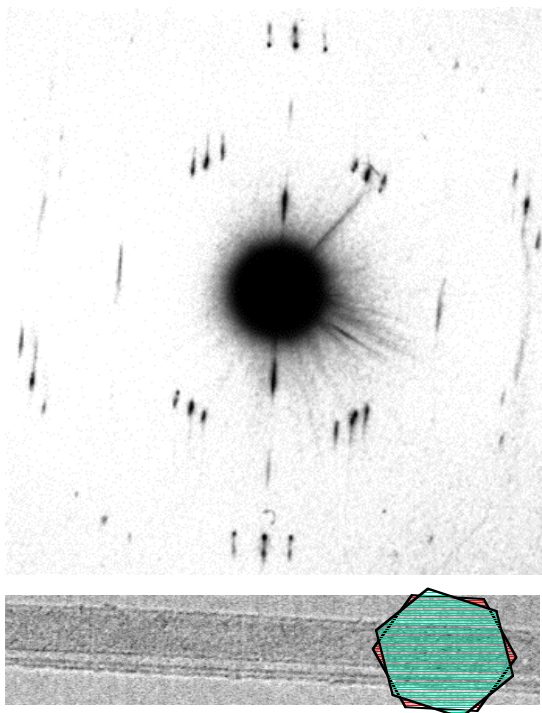


Fig. IV.27 Diffraction on a rope of thin tubes A 0002 spot indicates multi-layering, and may also be broadened by a typical distance between tube cylinders. Two helicities are present, zig-zag type, and $\alpha \sim 10$ deg. A modulation of some spot perpendicular to tube axis, is caused by the limited diameter of tubes. It proves uniform diameter for all tubes about 2 nm. (From sample at 50 W)

It is remarkable that, inside one rope the same helicity also seems prevalent for each tubes (Fig. IV.27). This supports the idea that tubes are not assembled together after their respective growth, but grow, influencing each other. This arrangement lowers the structural cost of the inter-tube accommodation.

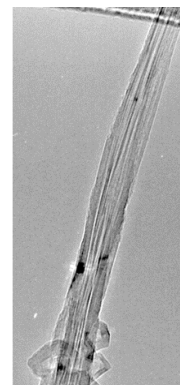
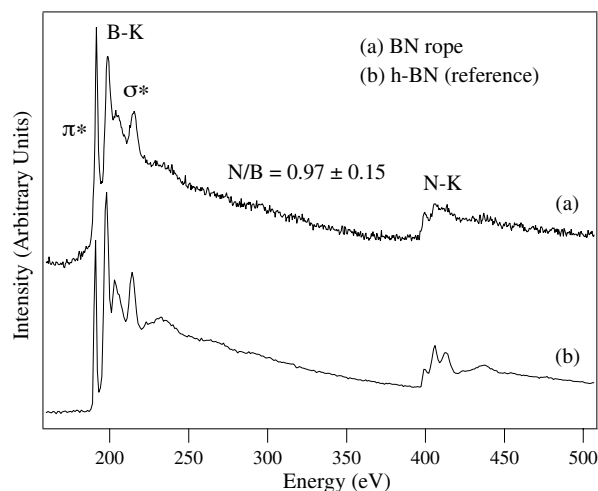
In Fig. IV.27, a modulated spreading of non-0002 diffraction spots in the direction perpendicular to the tube axis, shows that constituent tubes are thin and of uniform diameter ~ 2 nm. The effect of a limited tube diameter is to modulate the diffracted spots, with a periodicity equal to the diameter of the tube. (See Chap. III-I.2.2) If constituent tubes were of non-uniform diameters, this pattern would be lost in interference between tubes.

IV.4. EELS on ropes

A spectrum is easily be obtained from a large rope (Fig. IV.28). Such spectrum is very similar to that of pure h-BN. It is difficult to obtain the EELS spectrum from an individual tube, because tubes are quickly polluted by carbon contamination under the focused electron beam. (See Chap. III-II.3)

Boron and nitrogen K loss are clearly identified. No other element is detected. The ionisation edges π^* and σ^* , the energy loss near edge structure (ELNES), corresponding to the sp^2 hybridisation of BN are clearly resolved. (The relative intensities of π^* and σ^* losses are not interpreted easily. They depend on the local orientation of the irradiated structure and on the collection angles of incident/transmitted electron beams.)

Fig. IV.28 EELS spectrum from a BN rope Beam is focused to the diameter of the rope (~ 40 nm). The inelastic electron energy loss is very similar to that of (stoichiometric) h-BN. Spectra have been background corrected, vertically expanded to an equal N-K loss and vertically shifted of an arbitrary offset. (Reference spectrum for h-BN is from Gatan software library.)



The N/B atomic ratio of ropes is found stoichiometric ~ 1 , from the peak intensity ratio in the spectrum. This technique allows only a low precision $\pm 15\%$. Different studies, using a scanning probe, have shown that BN tubes can be boron rich inside cavity. [4.2.3]

IV.5. Nano-polyhedrons (angular onions) in the crown

All nano-spherical particles in the crown have a BN shell with h-BN type layers concentric and parallel to the external surface. This shell is often polyhedron-like, with angle and facet. (It is thought that, because of the absence of pentagons/heptagons in BN, structures have a tendency to form angular structures.) However, curved shells are also common. The structural dispersion of particles is very large. Sizes vary from 10 nm to 200 nm. Morphologies are many, often including defects.

All particles are hollow but, for many, their cavity is partially or completely filled with a boron core. Boron is identified in EELS analysis of large individual particle, by a low atomic ratio N/B. (EELS analysis of small particles is difficult because of the carbon contamination under the electron beam.)

The boron core is often crystalline. Electron diffraction patterns from such particles correspond to a rhombohedral form of boron with $a = 10.9 \text{ \AA}$, $c = 23.8 \text{ \AA}$ in a pseudo hexagonal cell. (See annex 2) This phase is known to be the most stable solid phase of boron at high temperature. Such crystalline particle must have been at a high temperature for the time of crystallisation, but under the solidification temperature of liquid boron ($\sim 2350 \text{ K}$).

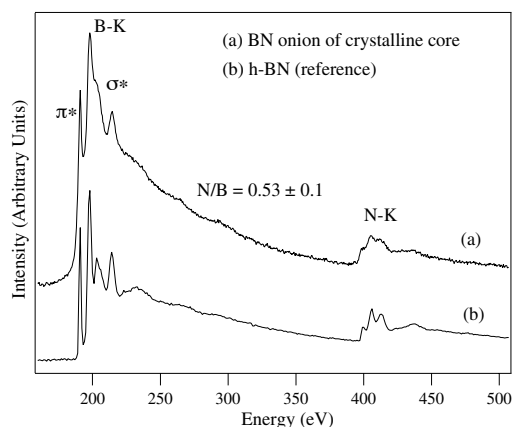


Fig. IV.29 EELS spectrum from a large ($\sim 50 \text{ nm}$) BN nano-polyhedron containing a boron nano-crystal (probe $\sim 20 \text{ nm}$) The N/B ratio is non-stoichiometric. Spectra have been background corrected, vertically expanded to an equal N-K loss and vertically shifted of an arbitrary offset.



Fig. IV.30 TEM imaging of a small BN nanopolyhedron containing a boron nano-crystal (in zone II) (direction 0001, hexagonal indexing). New layers of BN seem to be emerging from the boron core (arrow) in a process of combination with nitrogen from atmosphere. Several defects are observable in the shell. It merged on left side with another particle. Scale bar 10 nm. (Photo for 300 mb experiment)

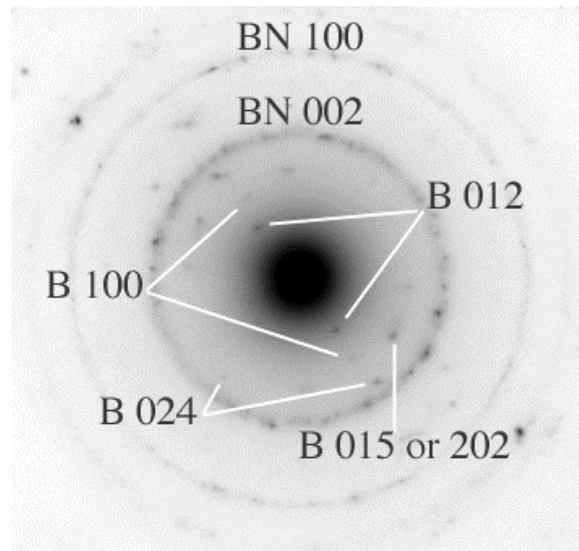


Fig. IV.31 Diffraction on a zone of agglomerated BN/B onions (in crown material) Pattern was indexed with the h-BN reflections (diffracted from particle shells). All additional diffracted spots (from particle core) correspond to a rhombohedral form of boron. Measurements are (Å): 7.49 (012), 5.03 (012), 4.27-4.34 (015 or 202), 3.71 (024) (See annex 2.)

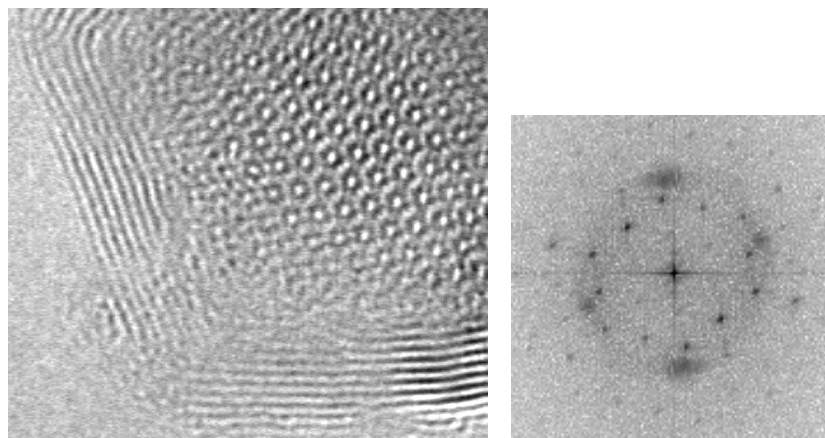


Fig. IV.32 Crystalline boron in a BN shell and its Fourier transform (Particle from the crown. Experiment at 50 mb)

IV.6. Tube extremities

At extremity, **tubes are often chemically merged with a BN spherical shell** much similar to nano-polyhedrons previously described. This type of “seed”-like extremity is observed very generally, both in SEM and TEM. (See Fig IV.33-36) (“Usual” types of extremities, angular or spherical without spherical ending, are also present.)

TEM imaging shows an almost systematic presence of boron in such a seed cavity. A h-BN wall may or may not close the path between shell and tube cavities. In any case, boron is not observed inside tube cavity. Unfortunately, such extremities are difficult to image because of electron charging effect and often a large thickness of the zone. (See Fig. VI.15-17)

SEM observations show that, seed-type extremities are sometime linked at target surface, to a h-BN platelet or to any large BN micro-particle. They are also often linked to the cylinder of another fibre. This configuration forms branch-like patterns in the fibres. They are also often free standing inside the crown material. For short tubes, which can be observed on their full length, a seed-type extremity is exceptionally observable at both ends.

V. Global growth processes (Using some conclusions from following chapters)

Growth does not occur directly from transformation of h-BN platelets at high temperature. (No growth without dissociation):

This is easily demonstrated. Indeed, when laser power is weak enough for surface temperature to keep under dissociation temperature of BN (2700 K), there is no growth at all.

Condensation from gas phase spreads boron rich, BN/B, spherical nano-particles around the cavity:

Under the beam, boron is vaporised. Boron rich spherical particles nucleate in the cold and reactive nitrogen atmosphere near impact, and are spread on the surroundings of the cavity. This atmospheric origin is attested by the large presence of those particles around the cavity (mixed with crown material on zone II, as well as assembled in micro-clusters over the surface of zone III).

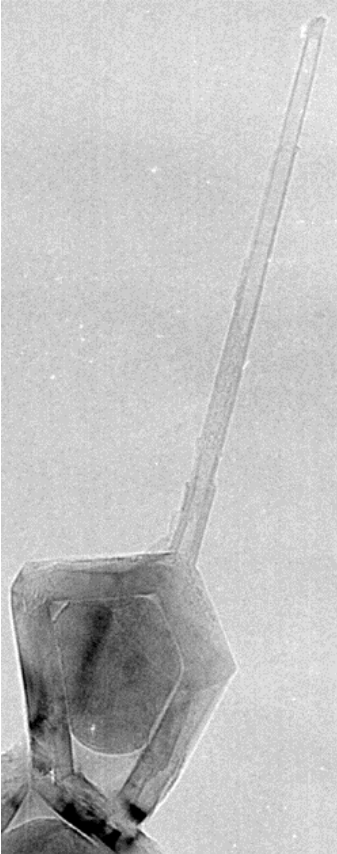


Fig. IV.33 Tube emerging from a BN/B particle (TEM) Boron core is on the same side than tube root. Tube and particle cavities are separated by a large BN wall. (This could have stopped the growth.) (Photo from sample at 500 mb)



Fig. IV.34 Seed-like ending at tube extremities (SEM) Extremities are linked to the surface of a micro BN particle at surface of zone II. (From experiment at 50 mbar)

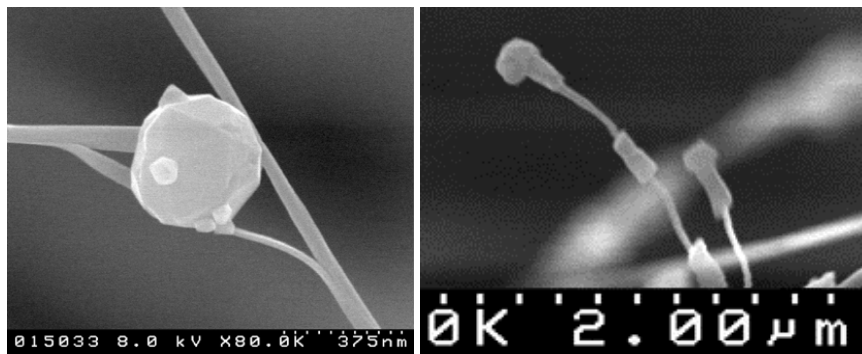


Fig. IV.35 Seed-like ending at tube extremities (SEM) (left) Extremities are linked to a larger particle. (right) The merging of some particles on fibre cylinder is also observable. (From experiment at 50 mbar)

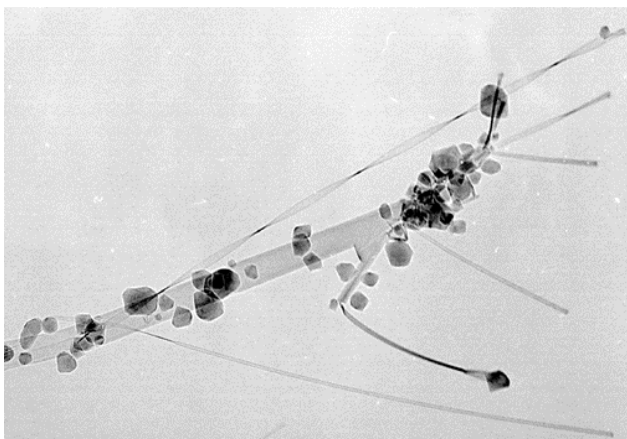


Fig. IV.36 A branching pattern Particles collected on the main fibre start new tubes (From experiment at 50 mb)

Experiments led for short duration heatings account well for this phenomenon. Spreading mostly occurs during in the first seconds (~ 15 s) of the heating, when the cavity is forming, but not yet deep. (See Chap. VII-I.)

Note: Boron is not exclusively spread by evaporation/condensation mechanism. Some boron drops (several micron large), recombined or not, are also commonly found scattered around the cavity on zone II and III. They probably have been ejected from cavity without vaporisation phase, possibly because of nitrogen effusion.

Boron collected recombines with nitrogen atmosphere, but only on zone II:

Spherical particles in vapour phase partially recombine in atmosphere, but they are still much boron dominant when they are collected on surface. After collection, they can further recombine under the influence of atmosphere, but only in zone II.

This is simply observable in an optical microscope, by the paler colours of zone II, compared to zone III. (B/N ratio is lower.) It is also consistent with the previous EDX spectra, taken from local zone around the cavity. It is more generally confirmed by Electron Probe Micro Analysis (EPMA), when scanning an electron beam radially through the three zones, and detecting B and N absorption edges (Fig. IV.37). In zone III boron is drastically dominant over nitrogen. By contrast, in zone II, the relative fraction of nitrogen is much higher.

The influence of nitrogen atmosphere in the tube growth is well illustrated when looking inside a crack through the deposit. In zone II, the below product, which is not exposed to atmosphere contains no fibres. (Similarly in zone II, the micro-clusters agglomeration is only on surface.)

Zone II is defined by a temperature range between BN dissociation and, boron fusion (where B is liquid):

The fact that tube grow on a specific ring cannot be due to a specific distribution of boron on target during boron spreading. Indeed, the EPMA spectrum (Fig. IV.37) shows that boron is present much further than tube ring zone, and short duration heatings show that boron rich particles are widely spread on target, indistinctly on zone II and III.

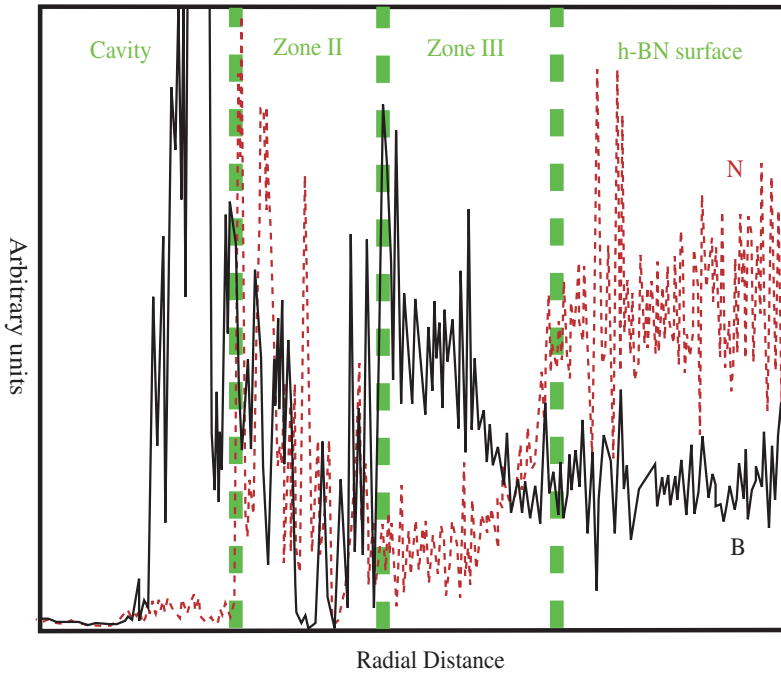


Fig. IV.37 EPMA line scan, radial through the 3 zones, detecting B and N absorption edges. Irregularities are due to the unevenness of the surface (especially for zone II). N detector is more sensitive than B detector, but the ratio $B/N = 1$ of h-BN is found on the right part of the figure, when the scanning beam is away from cavity. Zone III shows a clear dominance of boron, although nitrogen is not absent. Zone II is also boron dominant, but the relative portion of nitrogen is much higher. Inside cavity, close to the edge, boron is very pure. When the beam gets deep inside cavity, it is no longer reflected in the detectors.

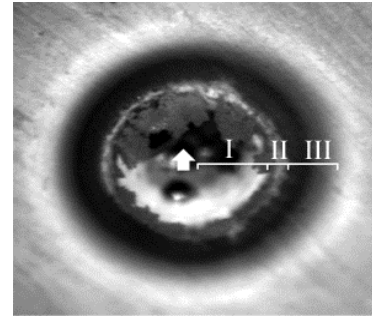


Fig. IV.38 Case of non-symmetry of crown growth. When boron drops inside cavity are much dominant on one side of the cavity, the height of the crown often seems enhanced on the same side (arrow). Likely, more boron is spread outside cavity on this side.

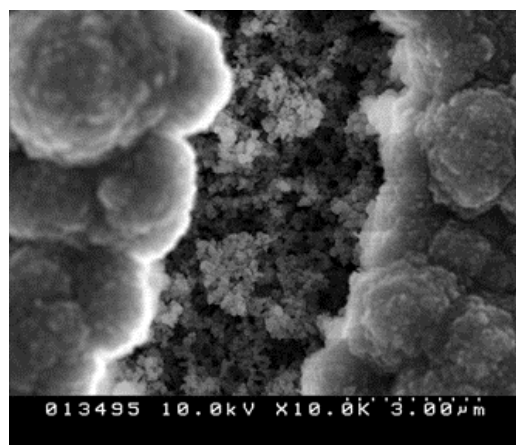
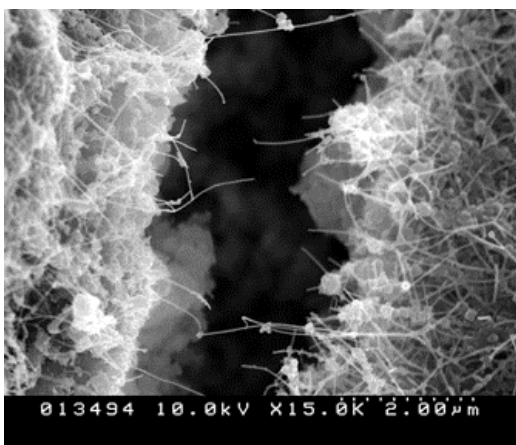


Fig. IV.39 A crack in zone II and in zone III (SEM). Beneath surface, the product is a uniform nano-powder. This shows the effect of nitrogen atmosphere. (From experiment at 30s)

This specific ring corresponds to a specific range of temperature, in which boron recombines and tubes can grow. For an experiment under helium, where a change of atmosphere composition does not change much target temperature, zone II thickness is conserved. (See Chap VII-IV.) Similarly, experiment with varying nitrogen, showed a small variation of zone II thickness, compatible with the variation of dissociation temperature with pressure. (See Chap VII-II.)

On the opposite, experiment with varying laser power (Chap VII-III) and short duration heating (Chap VII-I.), which affect temperature a lot, showed a drastic change in zone II thickness. Those measurements are compatible with the fact that tube growth zone is changing, preserving the same range of temperature.

We have seen that zone II should correspond to a range of temperature 2700 K-3500 K, where boron is liquid. We will see that temperature estimations are compatible with this range of temperature in Chap V. Incidentally, we can draw a very general conclusion: **Combination of boron with nitrogen is only possible at temperatures where boron is liquid.**

Boron rich nano-particles evolve toward tubes

The recombination of boron on zone II does not only produce tubular BN. For instance, some micro-drops of boron recombine, forming large BN particles. The specific growth of tube seems to be rather nucleated by the presence of the nano-sized BN/B particles. We have already seen that many tube extremities are merged to small BN/B particles. In addition, tube and BN/B particle positions are correlated: There is no zone of tube growth where BN/B particles are absent. This is especially remarkable for zones very close to the cavity edge where the last tubes are growing, and for the 1s experiment, in which tubes grow inside the cavity. (See Chap.VII-I.2.1)

Under the influence of nitrogen atmosphere, BN shells form on liquid boron nano-particles. (In TEM observations, no boron particle was ever observed without a BN shell.) The shell growth in constrained space may favour the emergence of tubular structures. (Growth mechanism is discussed in Chap. VI.II)

Chapter V

Temperatures in the h-BN target

Objective: We seek an estimation of temperature gradient near impact, to show that tube ring zone corresponds to a determined range of temperatures between dissociation of BN (~ 2700 K) and fusion of boron (~ 2350 K).

Abstract: Typical time for global target warming (~ 5 s) is long compared to typical time of temperature gradient stabilisation in the target (~ 1 ms). Therefore, even if target is out of equilibrium for most part of the heating, equilibrium formula are valid for short periods of time. As the size of zone of interest is of same order as that of cavity, cavity shape should be accounted for in temperature estimations.

Temperature at cavity edge is supposed to be dissociation temperature. Shape of temperature gradient is known from symmetry, or else can be approximated as linear. In a simple model, the radial heat flux (hence temperature derivative) at cavity edge is supposed equal to the ratio: power absorbed from the beam / surface of the cavity.

Such a simple model is compatible with the expected range of temperature, known from literature to be between 200K and 500K. But, rather than giving an absolute value, the model should account for the evolution of dimensions near impact, when changing experimental parameters that affect temperatures. The model accounts well for different durations of heating and for the influence of nitrogen pressure. However it fails to explain the variation with laser power. Several weaknesses of the model can be considered, but the most probable is a temperature shift on target front surface after long lasting heating.

I. Typical times for target warming

I.1. Time for global warming

When target is heated, temperatures rise globally until equilibrium is found between losses (radiative and convective) and incident power. If we consider that most of the target is at uniform temperature T_∞ (hypothesis of a stiff gradient), the global energy balance of the target gives the time for temperature rise. (We do not take in account that the absorption coefficient, $\epsilon\gamma$, changes with time because of cavity drilling and varying thickness of the liquid boron layer.)

$$\gamma\epsilon P_{laser} dt = \rho v C(T_\infty) .dT_\infty + s\sigma T_\infty^4 dt + AsT_\infty dt$$

$$\Rightarrow \Delta t = \int \frac{\rho v C(T_\infty)}{\gamma\epsilon P_{laser} - s\sigma T_\infty^4 - AsT_\infty} dT_\infty$$

An estimation of the minimum stabilisation time can be obtained by removing terms of heat loss. (An estimation of this integral is possible, but we should estimate A, the coefficient for convective losses.) Using a heat capacity C ($\sim 1.3 \text{ Jg}^{-1}\text{K}^{-1}$), constant between ambient temperature and a given stabilisation temperature (roughly, $\sim 1300 \text{ K}$), with h-BN density $\rho = 2.08 \text{ g/cm}^3$, and volume of the cube $v = 64.10^{-3} \text{ cm}^3$, we have:

$$\Delta t > \frac{\rho v C \Delta T}{\gamma\epsilon P_{laser}} = 4 \text{ s}$$

The actual time is, of course, longer, mainly because of energy losses. The real time of global warming is more or less the time for cavity formation on the target. Cavity formation can be observed empirically (Fig. V.1), by several heatings with increasing duration. (See Chap. VII-I for the complete description of these samples.)

In these samples, both cavity diameter and depth rise at a similar logarithmic law until a time between 5 and 15s. Global warming may be closely linear in the beginning (when there are no

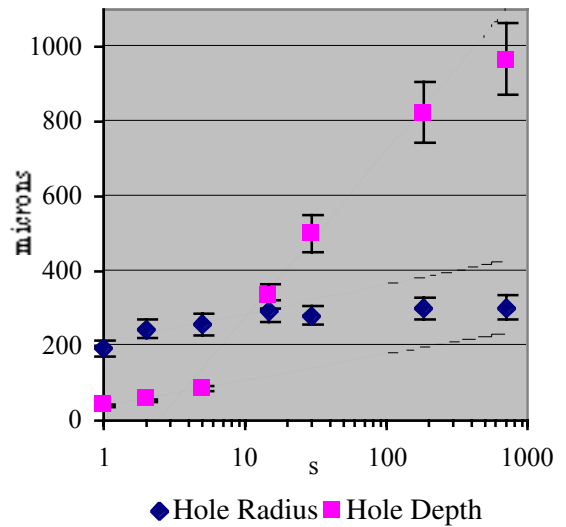


Fig. V.1 Evolution of the cavity during target warming

loss at surface), and is slower when reaching higher temperatures, because losses (radiative and conductive) and specific heat increase with temperature. After that time, global warming is completed, and cavity diameter stabilises.

After global warming, cavity depth still increases, but with a different behaviour. This is because the evaporation of the boron under the beam becomes dominant in the drilling. Boron is relatively slowly removed from the cavity, so that, boron evaporation continues long after target is warmed. As boron is vaporised under the beam, temperatures rearrange in the cavity, and it gets deeper. Temperature gradient is not stabilised before all boron is evaporated. This drilling at the speed of evaporation is observed for until the end of the experiment. Therefore, strictly speaking, the whole experiment is under out of equilibrium conditions.

I.2. Is the semi-infinite medium hypothesis valid during the rising of temperatures?

We have seen (Chap. II-III.2.1) that a target may be considered to be a piece of a semi-infinite medium if it is at equilibrium and temperature gradient is stiff for target size. In that case temperature is the sum of temperature gradient and a constant temperature at infinite.

Now, during target warming, gradient is stiff, but target is not at equilibrium. Nevertheless, target may still be considered at equilibrium for any short time during warming, as long as target back-side temperatures (global temperature) are little changing. Then, the semi-infinite medium hypothesis is valid, and the total evolution of temperatures during all warming is a sum of a quickly varying temperature gradient plus slowly varying infinite (global) temperature.

However, this is only true if, the time for gradient stabilisation in the medium is very small compared to the time of global warming inside target. (Temperature gradient should rearrange very quickly when temperatures increase on back-surfaces.) Indeed, in the case of a stiff gradient, considering equilibrium during dt , is equivalent to impose that, during dt , fluxes from back surfaces are equal to the incident power $\gamma \epsilon_B P_{laser}$ minus lost from front surface. In other words, it is equivalent to neglecting the accumulation of heat in the target during dt , hence neglecting global warming. This is correct if, during dt , the increase of temperature due to global warming is negligible, compared to the typical temperature range of the gradient considered (typically $\Delta grad \sim 1000$ K). This can be written:

$$\frac{\gamma \varepsilon P_{laser} dt}{\rho v C} \ll \Delta grad \quad \text{or} \quad dt \ll \frac{\rho v C \Delta grad}{\gamma \varepsilon P_{laser}} \approx 3s$$

Therefore, any stabilisation of temperature inside target can be computed with a semi-infinite hypothesis if its order of time is much smaller than 3s. We will see in next paragraph that a typical time for gradient stabilisation is actually much quicker than 3s.

I.3. Time for first gradient rise

We can evaluate the time for temperature equilibration at hottest point (impact centre) after $t = 0$. For this, we can use a literal calculation for a continuous laser beam. Target is supposed to be a semi-infinite medium with ambient temperature at infinite, and losses from surfaces are negligible. (Because the global temperature is low in the beginning of the heating.) However we have to make two drastic simplifications:

- We consider no penetration of the laser in the material, hence $\alpha \rightarrow \infty$.
- We consider the thermal conductivity, k , and the specific heat, C independent of temperature.

With $a = \frac{k}{\rho C}$, thermal diffusivity, and F_{laser} the energy flux at impact: [1.1.18]

$$T(t) = \frac{F_{laser} w}{k \sqrt{\pi}} \text{Arc tan} \left[\left(\frac{4at}{w^2} \right)^{1/2} \right]$$

$$\text{with, } F_{laser} = \frac{\varepsilon_{BN} P_{laser}}{\pi \left(\frac{w}{2} \right)^2}$$

$$T(t) = \frac{4 \varepsilon_{BN} P_{laser}}{k \pi^{3/2} w} \text{Arc tan} \left[\left(\frac{4at}{w^2} \right)^{1/2} \right]$$

With this estimation, gradient stabilisation in the target is achieved in the order of **a few millisecond**. (At impact, the dissociation temperature of h-BN is reached in the same order of time.) This time is small compared to the previous 3s, therefore, the hypothesis of semi-infinite medium is correct for this estimation. As this is a typical time of gradient stabilisation

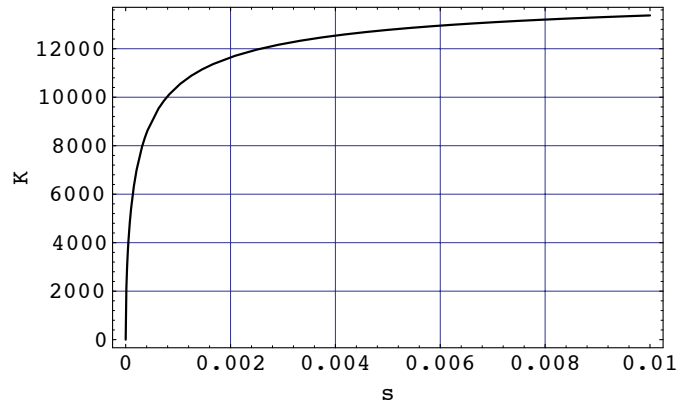


Fig. V.2 Temperature rise at impact, with $P_{laser} = 70W$, $\rho = 2.08 \cdot 10^6 \text{ gm}^{-3}$, $k \sim 40 \text{ Js}^{-1}\text{m}^{-1}\text{K}^{-1}$, $C \sim 1.5 \text{ Jg}^{-1}\text{K}^{-1}$, $\varepsilon_{BN} \sim 0.85$

in the medium, it is also correct for estimating temperatures at any time during target warming.

Note: The maximum temperature as given by this model is greatly over estimated. Indeed, if we use it for evaluating the minimum laser power for reaching dissociation, we find

$$P_{\min} = \frac{k\sqrt{\pi}wT_{\text{diss}}}{2\varepsilon_{\text{BN}}} \sim 13 \text{ W}, \text{ which is different from the experimental observation } \sim 30 \text{ W. This is}$$

because this model does not take in account a penetration of the beam in the material. As a dielectric, h-BN actually has a low absorption coefficient and therefore a deep penetration ($\sim 100 \mu\text{m}$). To take this in account literally is only possible in the stable case, with a Lax-type calculation. (As done in Chap. II-IV.1.2)

I.4. Temperature drop due to the formation of a liquid boron layer

When the h-BN target reaches dissociation temperature, a liquid boron layer forms in front of the beam. This causes an increase of reflectivity for the laser beam at impact. For cold h-BN $\varepsilon_{\text{BN}} \sim 0.85$, but for hot liquid boron, ε_{B} is uncertain. A value between 0.25 and 0.75 can be considered. In any case the incident power will drop, decreasing temperature.

Eventually, temperature at impact may drop under dissociation temperature. This can happen just after dissociation is reached, hence after a few milliseconds. After that, temperature at impact may rise again over dissociation temperature because of the global temperature warming. However, this will require at relatively long time (in the order of seconds).

This is actually observed experimentally to occur between 1 and 2 s of heating. Indeed, after 1s, although a cavity with liquid boron is formed, some BN tubes are present inside cavity, showing that the impact zone is actually cooler than dissociation temperature. By contrast, after 2s, BN is absent from cavity. Furthermore, after 1s, cavity diameter increases continuously, proving that dissociation temperature is reached again. (See Chap. VII-I)

II. Temperatures on front surface during target warming

We would like to confirm the observations, that the lower temperature of tube ring zone is close to the fusion temperature of B (2350°K at $1\text{bar}^{\text{janaf}}$, which should be close to the value at 0.1 bar), independently of experimental parameters.

II.1. Hypotheses

During target warming, temperature on back-surfaces is slowly increasing with time. We have seen that we can use equilibrium formula with the semi-infinite medium hypothesis at any time during warming. Hence at any time, temperature can be written $T(r) + T_{\infty}$, with $T_{\infty} \sim T_{\text{BS}}$. (temperature of back surfaces) $T(r)$ being a stable solution of thermal equation.

We can have a direct measurement of T_{∞} by fitting temperatures at the cavity edge. Indeed, we can assume that cavity edge is at the dissociation temperature of h-BN (2700 K). Having a fitting point close to the zone of interest is a condition for an accurate description of temperatures.

It is not obvious if radiative losses from front surface can be neglected in the estimation of $T(r)$, when temperatures are high on front surface. However, we can generally neglect radiative losses in a sphere of radius R , close to the irradiated zone, where thermal heat-flux inside target is much higher than the radiative flux on its front surface. (This is checked a posteriori.)

Note: If radiative losses are negligible on the whole front surface, temperature can be estimated on the whole front surface. In that case, temperatures could also be fitted with back surface temperature, measurable by colour spectrometry.

For high temperatures near impact, k little depends on temperature. (See annex 2.) It can be assumed constant. This is true in h-BN, as long as temperatures are in a range $\sim 1300\text{--}2700\text{ K}$. However, it may not be true far from impact for short lasting experiments.

There is fundamental difficulty in evaluating the coefficient of absorption of the beam, ϵ . Absorption under the beam is linked to the thickness and shape of the boron layer in the region of irradiation. If boron was covering the cavity uniformly, with a thickness higher than

the penetration depth of the beam in boron ($\sim 10 \mu\text{m}$), the absorption would be purely due to liquid boron.

However, practically, liquid boron is rather present as drops than forming a continuous layer (although drops could be formed while cooling). (Fig. V.3) In addition, liquid boron tends to flow to cavity sides (by convection or, under the tension of evaporation), partly uncovering the h-BN beneath. Therefore the absorbing surface is a mix of liquid boron and h-BN, and absorption occurs both on B and BN surfaces.

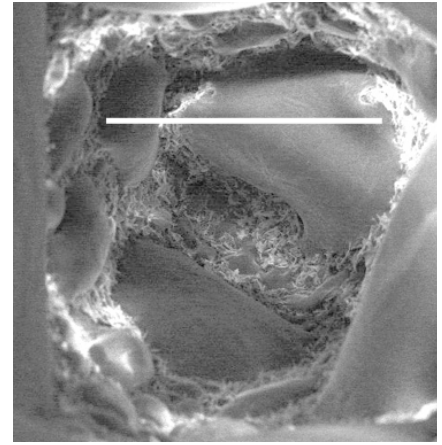


Fig. V.3 Irradiated surface down cavity (Standard exp.) Scale bar, $120 \mu\text{m}$ (Beam waist is $\sim 180 \mu\text{m}$.)

Absorption coefficient of the two materials may be very different. For h-BN we may assume ~ 0.75 . For liquid B coefficient may be in a range $0.25 - 0.75$. For estimation we will chose an average value $\epsilon \sim 0.5$, but remembering a drastic incertitude on this value ($\pm 50\%$).

On the other hand, a low absorption would be partly compensated by cavity trapping of the beam. If we consider $\gamma = 1.5$, the actual absorption is $\gamma\epsilon \sim 0.75$. Because γ compensates the eventually low ϵ , the uncertainty on $\gamma\epsilon$ is lower that of ϵ . We may say that the uncertainty on $\gamma\epsilon$ is in a range $\pm 25\%$. We will see that the final range of temperature is proportional to $\gamma\epsilon$.

II.2. Modelisation

The zone of interest, zone II, is small ($< 200 \mu\text{m}$) compared to the target. It is of the same order than the impact cavity (radius $\sim 300 \mu\text{m}$, depth $\sim 800 \mu\text{m}$). Therefore, cavity shape and local heat transfer near impact determine temperatures of zone II. Complex phenomena near impact can not be described very accurately. Instead, we will use a rough modelisation, to link the radial heat flux at cavity edge to empirical values (cavity dimensions and laser power).

II.2.1 If the cavity is \sim a half ellipsoid

In experiment with shallow cavity, cavity may be described as an ellipsoid. For temperatures on front surface, we can use the simplest form of the gradient, with spherical

symmetry, $T = T_0 - \frac{J_0 r_0}{k} (1 - \frac{r_0}{r})$. If we fix temperature at the dissociation point $r_0 =$ radius of the cavity, $T_0 = T_{\text{dissociation}}$. We only need to evaluate the radial flux J_0 (parallel to front surface).

We state that J_0 is equal to an average value over the cavity:

$$J_0 = \frac{\text{absorbed power}}{\text{ellipsoid surface}} = \frac{\gamma \epsilon P_{\text{laser}}}{\pi l_{\text{hole}}^2}, \text{ with } l_{\text{hole}}^2 = r_{\text{hole}}^2 + z_{\text{hole}}^2$$

$$\text{then, } T = T_{\text{diss}} - \frac{\gamma \epsilon P_{\text{laser}} r_{\text{hole}}}{\pi k l_{\text{hole}}^2} (1 - \frac{r_{\text{hole}}}{r})$$

If zone II ends at $r_{\text{hole}} + \Delta r$, it represents a range of temperature:

$$\Delta T = \frac{\gamma \epsilon}{\pi k} f_s, \text{ with } f_s = \frac{P_{\text{laser}} r_{\text{hole}} \Delta r}{l_{\text{hole}}^2 (r_{\text{hole}} + \Delta r)},$$

In this model, f_s depends strictly on experimental parameters and the front factor is independent of experimental parameters.

II.2.2 If the cavity is ~ a cone

In most experiments, and especially for a standard heating (Fig. V.4), the cavity is deeper than large. In this case, cavity shape is best described as a cone. Then, it is not correct to consider a spherical symmetry near impact. A local cylindrical symmetry can be considered for a cone: $T = T_0 - \frac{J_0 r_0}{k} \ln(\frac{r}{r_0})$. (If r is in a small range around r_0 , this expression and the spherical one are equivalent, as well as to a linear approximation $T = T_0 - \frac{J_0 r_0}{k} (\frac{r}{r_0} - 1)$). However, as distances are measured on the front surface,

$$r \text{ and } r_0 \text{ must be corrected by } \cos \alpha: T = T_0 - \frac{J_0 r_0}{k} \cos \alpha \ln(\frac{r}{r_0})$$

With the same hypothesis than previously, but considering the cavity as a cone: $J_0 = \frac{\gamma \epsilon P_{\text{laser}}}{\pi l_{\text{hole}} r_{\text{hole}}}$

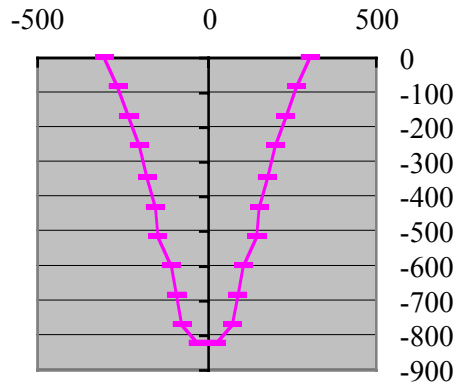


Fig. V.4 Cavity section for a standard experiment (microns on both axis) Cavity diameter is measured by optical microscopy at each altitude. Cavity shape is closely conical.

$$\text{It gives: } T = T_{diss} - \frac{\gamma \varepsilon}{\pi k} \frac{P_{laser}}{l_{hole}} \cos \alpha \ln\left(\frac{r}{r_0}\right)$$

$$\Delta T = \frac{\gamma \varepsilon}{\pi k} f_C, \text{ with } f_C = \frac{P_{laser}}{l_{hole}} \cos \alpha \ln\left(1 + \frac{\Delta r}{r_{hole}}\right)$$

II.3. Temperatures at the end of a standard experiment (Fig. V.5)

A standard experiment is best described by a conical model. The temperature range for the growth of tube is ~ 400 K and fits with the range expected. (Between 200 K and 500 K) This value is affected at least by a 25 % incertitude due to the unknown absorption coefficient.

Temperature at extreme border of the target, $T_{BS} \sim 1650$ K, is roughly compatible with the radiation colour observed during experiment. (A precise measurement was not undertaken for back surface temperature.) However, temperatures with a conical model are not obviously valid far from the cavity, because symmetry away from cavity is rather spherical than cylindrical. (T_{BS} is over-estimated.)

Validity of hypothesis (Fig. V.6-7)

$T_{max} - T_{BS}$ is about 10 times higher than $T_{BS} - T_{\infty}$. Therefore, the hypothesis of stiff gradient was roughly correct. Target shape little influences temperatures.

For the whole front surface, the radiative flux is negligible compared to the radial heat flux. (Fig. V.7) The hypothesis of no radiative losses from front surface is fully satisfied. The total (integrated) radiative power from the 5 back surfaces is ~ 30 W (with an over-estimated value for T_{BS}). The radiative power of front surface is ~ 6 W. For comparison, power absorbed from the laser $\gamma \varepsilon P$ is ~ 60 W. Other losses are mainly conductive losses in the gas phase.

II.4. Is the temperature range constant between experiments?

Two experimental parameters affect temperatures notably on front surface of the target: laser power and duration of the heating. By consequence zone II dimension varies a lot with these two parameters. We want to check if the previous model can describe the relative variation zone II / temperature, as preserving a constant temperature range ~ 400 K. (Only significant experiments are taken in account: For 1 s and 2s zone II is uncertain. For 50 W experiment, the cavity shape is very different from both ellipse and cone.)

(For standard experiment)

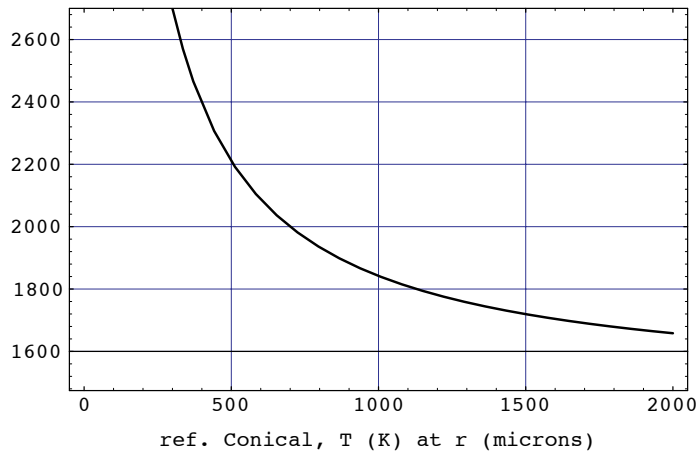


Fig. V.5 Radial temperature gradient for standard conditions, with a conical model.

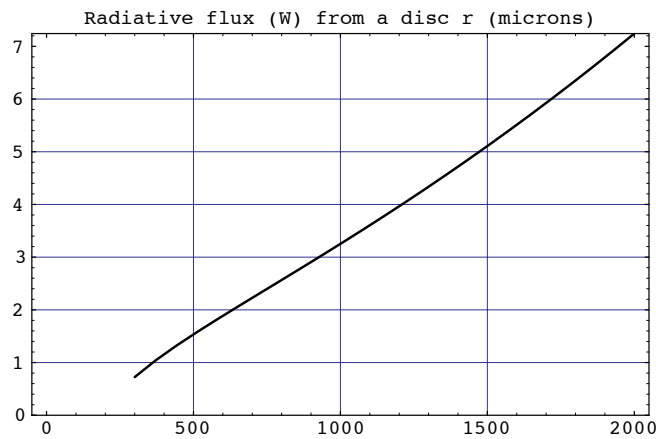


Fig. V.6 Total radiative flux from a disk r around impact, as estimated with the gradient of Fig. V.5

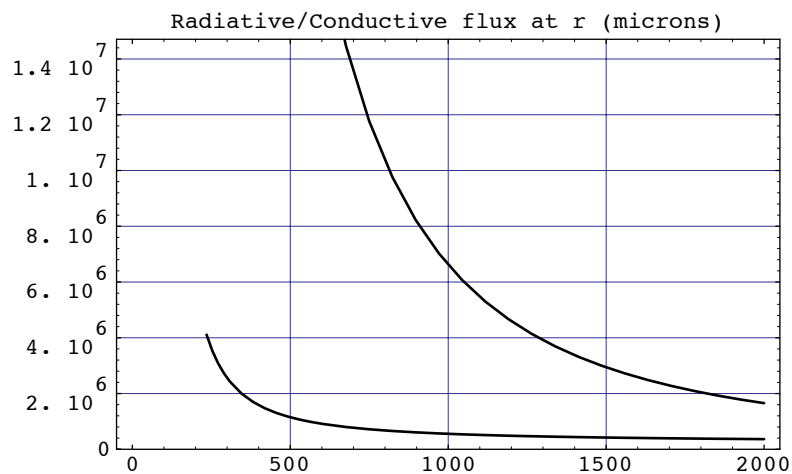


Fig. V.7 Along front surface, comparison of the local radiative flux (below) with the radial conductive flux (above), (W/m^2)

Both are estimated with the gradient of Fig. V.5.

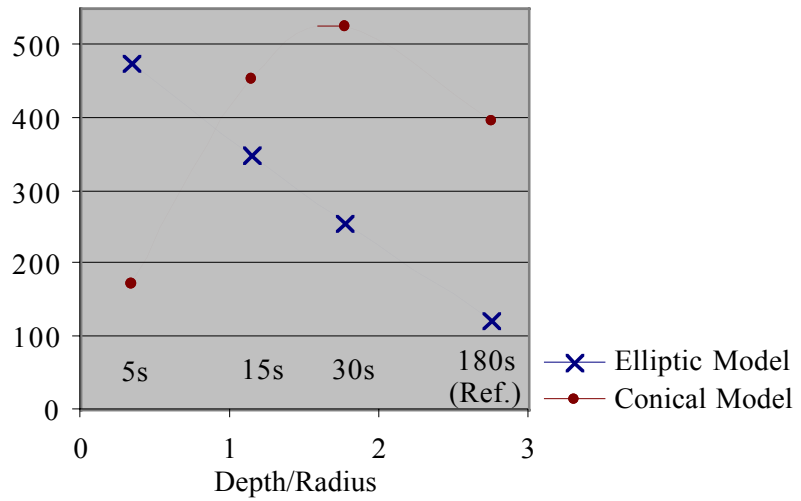


Fig. V.8 Temperature range (K) for different durations of heating, plotted as a function of cavity depth

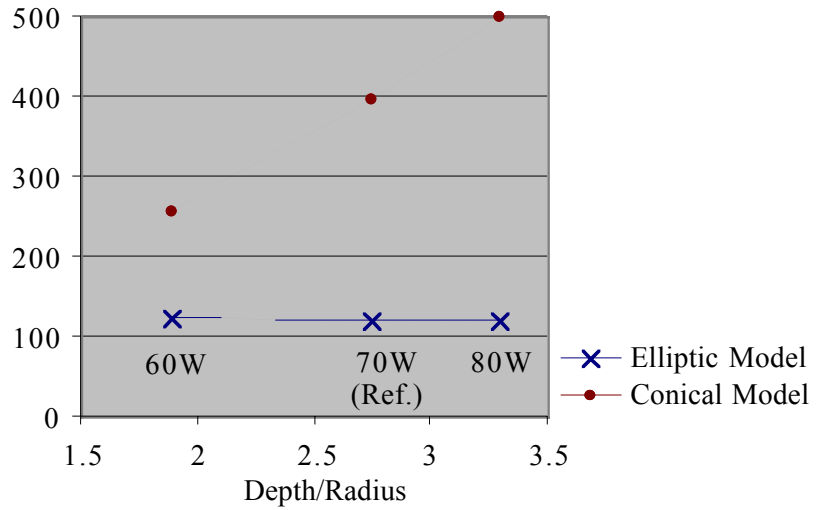


Fig. V.9 Temperature range (K) for different laser powers

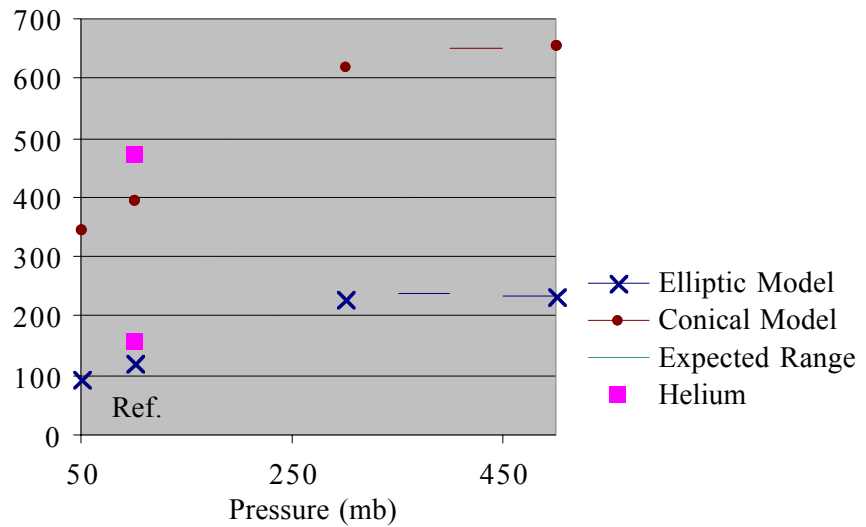


Fig. V.10 Temperature range(K) for different nitrogen pressures and for helium at 100 mb

For the duration serie (Fig. V.8), the model fits well the prediction. The conical model is best suited after 15s heating, because cavity is deep. The conical model gives a constant range ~ 400 K at the expected value. The spherical model seems to apply best for the 5s experiment, when the cavity is shallow..

On the other hand, the power range serie (Fig. V.9) is problematic. The conical model, which should be suited for all samples, gives a non-constant temperature range for deep cavity. (Surprisingly, the spherical model, which is not well suited for deep cavity, gives a constant range, although with a value very different from 400 K.) We will discuss four weaknesses of the model that may explain this misfit. The most probable is a shift of temperatures near irradiation for long lasting heating.

When changing nitrogen pressure (Fig. V.10), temperature on front surface of the target should not be affected much. However, the dissociation temperature of BN is increasing with pressure. Therefore an increase of the temperature range is expected. This increase can be estimated from the phase diagram (green strait line). The conical model follows well this variation with pressure.

II.5. Weaknesses of the model

II.5.1 We could consider the increase of absorption with cavity dimension.

We have been using as constant value $\gamma \sim 1.5$. Now, we consider with variation of γ with cavity dimensions. We consider that $\tau = 1 - \frac{\alpha}{\pi}$ % (α , solid angle of the cavity) of any reflected beam is incident again inside cavity. At first incidence εP_{laser} is absorbed from the beam. (We have chosen an average value for the absorption at under the beam, $\varepsilon \sim 0.5$). We can consider that elsewhere inside cavity absorption is mainly due to boron. So that, at second incidence, $\varepsilon_B P_{laser} (1 - \varepsilon) \tau$ is absorbed, at third $\varepsilon_B P_{laser} (1 - \varepsilon) \tau^2 (1 - \varepsilon_B)$, at fourth $\varepsilon_B P_{laser} (1 - \varepsilon) \tau^3 (1 - \varepsilon_B)^2 \dots$

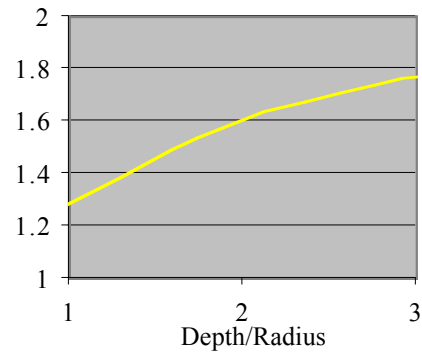


Fig. V.11 Variation of γ with cavity
 $\varepsilon = 0.5$ and $\varepsilon_B = 0.25$ (chosen arbitrary) (No units.)

We deduce,

$$\begin{aligned}\gamma &= \frac{\sum \text{incidences}}{\varepsilon P_{\text{laser}}} = 1 + \frac{\varepsilon_B(1-\varepsilon)\tau}{\varepsilon} \sum_{n=0}^{\infty} [\tau(1-\varepsilon_B)]^n \\ &= 1 + \frac{\varepsilon_B}{\varepsilon} \times \frac{\tau(1-\varepsilon)}{1-\tau(1-\varepsilon_B)}\end{aligned}$$

(See Fig. V.11) This result may improve slightly the results of the conical model of time-serie, but it does not explain the misfit of the laser power serie.

II.5.2 We could consider a variation of absorption ε with laser power.

The observation of irradiated surface, down cavity, shows that there is much more liquid boron at higher laser power than at lower power. As we expect a lower absorption on boron surface than on h-BN surface, ε could be considered decreasing with laser power. However, to explain the misfit of 100% of the laser power serie, we need a decrease of 100% of $\gamma\varepsilon$. (And we forget that lower ε is partly compensated by higher γ .) A decrease of 100 % of $\gamma\varepsilon$, for an increase of only 30 % of laser power, would mean that the energy absorbed from the beam is actually lower for higher power. This is not consistent with the increase of cavity dimensions with power.

Note: The increase of boron layer with laser power is difficult to modelise. It results from the competition between fusion and evaporation fronts. Fusion front follows global temperature rise, which is faster at higher laser power. Evaporation rate is more or less proportional to the maximum temperature under the beam. As long as thickness is equal or shorter than penetration depth in boron (known $\sim 10 \mu\text{m}$ for solid boron at ambient temperature), temperature is more or less constant in the boron layer $\sim T_{\text{diss}}$, and evaporation flux does not depend on layer thickness. For a thicker layer, maximum temperature is proportional to the thickness of the boron layer. With a one dimensional approximation: (The waist is large compared to the thickness of the layer.)

$$\begin{aligned}k \frac{dT}{dz} &= \mathbf{Q}_{\text{incident}} = \frac{\varepsilon_B P_{\text{laser}}}{\pi w^2} \\ \rightarrow \Delta T &= \frac{\varepsilon_B P_{\text{laser}}}{k\pi w^2} \Delta z\end{aligned}$$

Therefore after a limit thickness, evaporation is also increased with laser power. The boron layer may not become very large because maximum temperature rises quickly, causing a

strong evaporation. For instance with only 40 μm of liquid borons, $\Delta T \sim 1000\text{ K}$, and the evaporation temperature $\sim 3700\text{ K}$ is reached.

II.5.3 We could consider a decrease of J_0 with laser power

We admitted that J_0 is equal to an average value of J over the cavity (normal to cavity). This is an extremely ideal case where heat fluxes are supposed homogeneous inside the cavity. It relies on the idea that several disordered mechanisms causes a redistribution of heat flux inside the cavity: the cycle of boron evaporation/condensation, the absorption of beams multiply reflected, conduction and convection in the liquid boron layer, absorption in the gas phase...

The opposite ideal case would be to consider that laser power is purely incident at the bottom of the cavity, on an area defined by the laser waist, without any heat redistribution. In that case, cavity surface would not be at uniform temperature, but cooler up-cavity. This is actually observed in two cases where there is no liquid boron facing the beam. First, for heating in vacuum: The final cavity is drilled as a cylinder because temperatures are closely spherical around beam waist. Second, for very long lasting (12 min.) heating: Tubes are growing inside cavity, when boron has been completely evaporated. (See Chap. VII-I.2.6.)

The real case is probably in between those two ideal cases. Heat is redistributed inside cavity, but not uniformly. Heat fluxes are probably lower near surface than in the bottom of the cavity. Therefore, a lower J_0 could be considered for deeper cavity. This could explain the misfit obtained in the laser power serie.

To have an idea of how much heat is redistributed inside cavity by diffusion in gas phase, it is interesting to compare cavity depth with diffusion length of boron in atmosphere. (Fig. V.12) This diffusion length is more or less measured by the

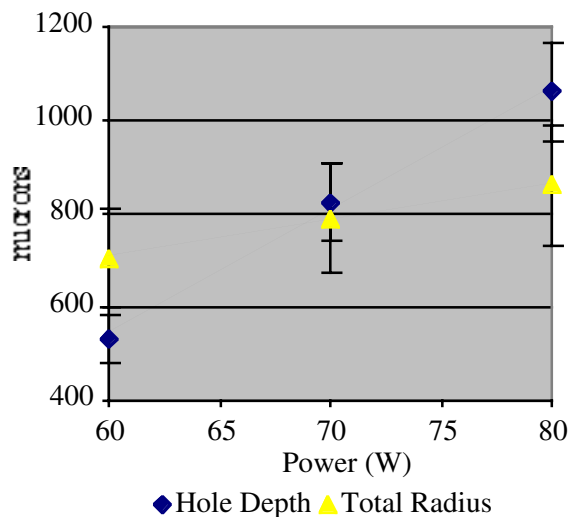


Fig. V.12 Comparison of cavity depth and diffusion ability of B in the gas phase, as indicated by the radius of total deposition (zone III) around cavity.

radius of boron deposit over target. Depths and diffusion lengths are of same order. However, for higher power, heat is less transmitted to the upper part of the cavity.

II.5.4 We could consider that T_0 decreases after some time of heating.

As long cavity border is at dissociation temperature, measuring zone II dimension (by nano-tube presence), is measuring the temperature range, when gradient was the flatest during heating. As J_0 is decreasing continuously during heating, we actually measure last temperatures before laser was shut down.

However, after some time of heating, if cavity is deep and boron is becoming rare, heat is no longer transmitted to the upper part of the cavity. At some time, temperature at cavity border may decrease under dissociation temperature. (Although the global temperature of the target is not decreasing.) In that case, tube growth zone is shifted toward the cavity, and nano-tubes are growing inside cavity. By measuring zone II, we no longer measure last temperatures before laser shut down, so that we can not link thickness of zone II to the (final) size of the cavity. In that case the model uses over-estimated values, both for cavity dimensions and zone II thickness.

Experimentally, such a presence of BN nano-tubes inside cavity is clearly observed for 12 min. of heating. On smaller scale, it is also observed for the 80 W experiment, on $\sim 40 \mu\text{m}$ near cavity edge: nano-tubes cover boron drops. The same is observed for the standard experiment on a zone $\sim 20 \mu\text{m}$. This is probably the main reason for laser power serie misfit.

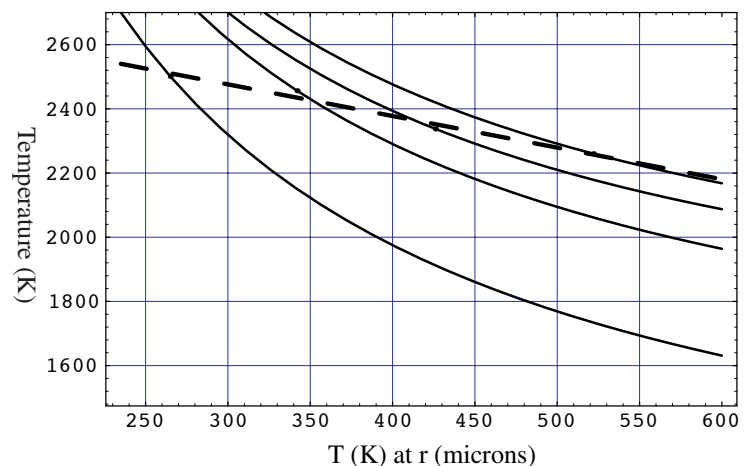


Fig. V.13 Temperatures for 50, 60, 70 and 80 W, as estimated with erroneous conical model. The dashed line crosses the edges between zone II and III, as measured. For a constant range of temperature, it should be a horizontal line. A correction of zone II thickness measurements, from temperature shift, may bring back a correct horizontal. (A correction of cavity dimensions should also be considered.)

Chapter VI

Mechanisms of growth around impact

Objective: We propose several approaches to the very complex phenomena appearing in plasma and to the problem of evolution of BN/B particles kept at high temperature on target surface.

Abstract: Typical mean free path of a small boron molecule in nitrogen is 3 to 30 μm , depending on local temperature of nitrogen. This is small compared to dimensions around impact, therefore particles tends to cool and agglomerate (if reactive) before being collected on target surfaces. Boron flux is such that boron is rarefied in nitrogen, hence it obeys diffusion laws. Inside the cavity, under the beam, maximum temperature is ~ 3700 K. Atmosphere is segregated in two regions: Near irradiation zone, temperatures do not allow recombination with nitrogen, so that pure boron particles agglutinate. Further away, flying boron particles may recombine with nitrogen. However, they are still largely boron-dominated when collected on target surface.

On target surface, these particles further recombine with atmosphere, but only where boron is liquid. When spherical particles develop a tubular extrusion, an exponentially decreasing temperature gradient arises along the tube, mainly because of thermal radiations from its cylinder. The temperature difference between hot and cool extremities is in the order of 200 K, as soon as the tube is ~ 10 microns. The drop of temperature in the tube may be the motor of tube growth by atomic diffusion. This idea is compatible with an exponential decrease of speed of growth with tube length, as observed experimentally. The boron core of an onion has enough matter to feed tube growth on several hundred microns, although the hypothesis of a boron feeding from atmosphere can not be completely excluded.

I Composition of the atmosphere around impact

I.1. Estimation of mean free path

The mean free path of a rarified gas A, in a B atmosphere, considering that particles have a “radius” r_A and r_B is given by: [1.1.19]

$$l = (n_B \cdot \pi (r_A + r_B)^2)^{-1}$$

Where r is a “particle radius”, and n is the atomic concentration. For a di-atomic molecule, a rough approximation of the particle radius is found as $2^{1/3}$ x Atomic radius (because $V \propto R^3 \rightarrow R \propto V^{1/3} \propto N^{1/3}$). Atomic radius of both B and N are around 1 Å

If gas B can be considered at equilibrium, $P_B = \frac{3}{2} n_B k T_B \rightarrow n_B = \frac{2P_B}{3kT_B}$

B₂ molecules in cool (T_{ambient}) in N₂ atmosphere (away from surface):

P _{N2}	10 ⁻³ mbar	50 mbar	100 mbar	300mbar	500 mbar
l	30 cm	6 μm	3 μm	1 μm	0.6 μm

B₂ molecules in hot N₂ atmosphere (near irradiated zone):

P _{N2}	100 mbar
l at T _{diss} =2700 K	28 μm
l at T _{evap} =3700 K	39 μm

B₂ molecules in cool He atmosphere:

Taking $\Gamma_{He} = 0.5$ A, at P_{He} = 100 mbar, T_{ambient}, **l = 6 μm**

Note: The equilibrium hypothesis is not really correct near impact. A correct estimation of the mean free path near target requires the value of $n_{N_2}(r)$, for out of equilibrium conditions. If we can assume a “local equilibrium” hypothesis, equilibrium relations are still valid on a small zone around r , and $n_B(r) = \frac{2P_B(r)}{3kT_B(r)}$. If we can also make the common simplification that

pressure is uniform near impact zone. (This is equivalent to neglect local gas convections, according to Navier-Stokes equation.), above values are correct locally.

However, the local equilibrium hypothesis is only valid as long as typical lengths of gradients in gas phase are long compared to the mean free path. Typical length of the temperature gradient may be roughly that of other diffusion processes in the gas phase ($\sim 500 \mu\text{m}$). This is longer than all mean free paths measured above ($\sim 20 \mu\text{m}$), but not drastically. Therefore the local equilibrium hypothesis may not be completely correct. Above values for mean free path at high temperature should rather be understood as an upper limit, than a real value.

I.2. Comparison of N and B fluxes

The atmosphere composition near impact is determined by the respective flux of boron evaporated, J_B , and flux of N_2 particles striking the surface, J_N . J_N is easily obtained, considering nitrogen as an ideal gas, locally at equilibrium. (We consider no pressure gradient in gas phase.)

$$J_N = \xi_N P_N = \frac{P_N}{(\sqrt{2\pi m_N k T_N})^{1/2}}$$

$$\begin{aligned} k &= 1.38 \cdot 10^{-23} \text{ J/K}^{-1} \\ m_N &= 2Z_N \text{ Amu} \\ \text{Atomic weight, } Z_N &= 14,01 \\ \text{Amu} &= 1.66 \cdot 10^{-27} \text{ kg} \end{aligned}$$

$$\text{Far from impact, } T_N \sim 300 \text{ K} \quad J_N \sim 3.4 \cdot 10^{26} \text{ m}^{-2}\text{s}^{-1}$$

$$\text{On most target surface, } T_N \sim 1300 \text{ K} \quad J_N \sim 1.6 \cdot 10^{26} \text{ m}^{-2}\text{s}^{-1}$$

$$\text{Near impact, if } T_N \sim 2700 \text{ K} \quad J_N \sim 1.1 \cdot 10^{26} \text{ m}^{-2}\text{s}^{-1}$$

I.2.1 Boron flux exiting cavity

J_B , the boron flux near zone II, is more or less the flux exiting from the cavity. This flux is not constant during experiment. A rough measurement of J_B at several stages of the heating, can be obtained by considering the hollowed volume from cavity between different duration of heating. (We neglect liquid boron left inside cavity.)

If during Δt , a volume of h-BN Δv is hollowed, containing ΔN pair BN, the flux of hypothetical B_2 molecules is:

$$J_B \sim \frac{\Delta N/2}{\pi r_{\text{hole}}^2 \Delta t} = \frac{\rho \cdot \Delta v}{2\pi r_{\text{hole}}^2 \Delta t (Z_N + Z_B) \cdot \text{Amu}}$$

$$\begin{aligned} \text{h-BN density, } \rho &= 2.08 \text{ g/cm}^3 \\ \text{Atomic weight, } Z_B &= 10.81 \text{ Amu} \end{aligned}$$

This estimation (Fig. VI.1) shows that boron flux outside cavity is decreasing during the heating. The flux gets small after the spreading of material around the cavity ($\sim 15 \text{ s}$). (The modulation of the flux during the first seconds may not be significant because the uncertainty

for shallow cavity is very high.)

The deeper the cavity, the less boron can exit from it. Indeed, boron particles are collected on cavity surface. If the average atmosphere temperature in the cavity is near the dissociation temperature of BN (2700 K), boron molecules in vapour are cooler than vaporisation temperature, and therefore absorbed on the cavity each time they collide. As soon as cavity depth is of same order than diffusion length of boron in nitrogen, a majority of evaporating boron may be collected inside cavity.

1.2.2 Boron flux evaporated under the beam

J_B , boron flux exiting from the cavity is not equal to J_{B0} , boron flux evaporated under the beam, because vaporised boron only partly exit from the cavity. We may consider that J_{B0} is roughly constant for most of the heating. If this is true, evaporating flux is given by the flux in the beginning of the heating, when there is no cavity. Evaporating flux over the surface of the waist is then roughly equal to the flux exiting from the cavity over cavity diameter,

$$\pi w^2 J_{B0} = \pi r_{hole}^2 J_B \Rightarrow J_{B0} = \left(\frac{r_{hole}}{w}\right)^2 J_B \sim 1.4 \cdot 10^{24} \text{ m}^{-2} \text{ s}^{-1}$$

Therefore, even near irradiated zone, boron flux is still 20 times lower than nitrogen flux. Nitrogen molecules may not be washed away from cavity by the flux of boron molecules. Boron can always be considered as rarefied in nitrogen.

1.3. Boron flux versus temperature, from vapour pressure measurements

A phase diagram at high temperature and low pressure, for h-BN and boron (Fig. VI.2), can be drawn from vapour pressure measurements of a vapour/liquid or vapour/solid interface at uniform temperature. [1.1.4] By definition, phase transition between solid (or liquid) and gaseous species is reached when evaporating species equal condensing species, all phases being at same and uniform temperature. An ideal gas of molecules A, in contact with a surface, causes an incident flux on surface $\xi_A P_A$, with $\xi_A = \frac{1}{(\sqrt{2\pi m_A k T_A})^{1/2}}$. If we assume that all

incident molecules are absorbed by the surface, this is also the flux collected by the surface. If

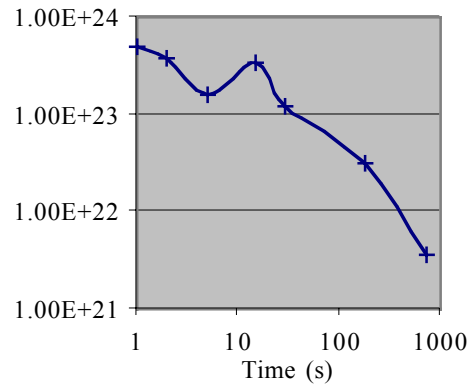


Fig. VI.1 Boron flux J_B ($\text{s}^{-1} \text{m}^{-2}$) outside cavity is quickly decreasing during target warming because cavity is getting deeper.

we note respectively J_{A0} and P_{A0} , the flux exiting from surface at equilibrium, and the pressure at equilibrium, we have $J_{A0} = \xi_A P_{A0}$. The phase diagram gives $P_{A0}(T)$, hence it links the gas flux exiting at equilibrium to surface temperature.

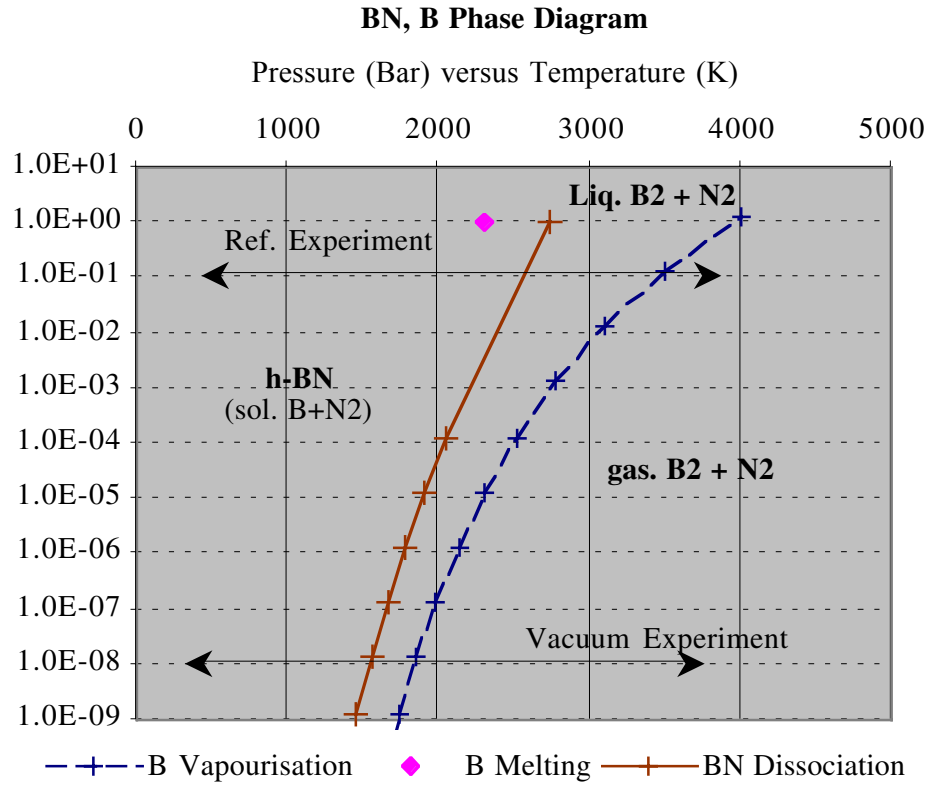


Fig. VI.2 Vapour tension measurements for BN and B from [1.1.4] The stable phases of the BN system are deduced and indicated in bold.

For the non-equilibrium case (all phases are still with uniform temperature), where evaporation and condensation fluxes are not equal, there is a non-zero flux J_A between the two phases. It is commonly supposed (although it is not obvious) that:

$$J_A = J_{A0} - \xi_A P_A = \xi_A (P_{A0} - P_A).$$

In the limit case of “free-evaporation”, where atmosphere pressure of gas A is very small, $J_A = J_{A0} = \xi_A P_{A0}$. In that case, we can (roughly) link the exiting flux to surface temperature. The free-evaporation is valid for the present boron vapours, because boron do not accumulate in atmosphere. It is continuously absorbed by any cold surfaces. (On the opposite case, if boron behaved as a standard gas, the global pressure of boron would tend to be uniform in the enclosure and equal to the equilibrium vapour pressure.)

Maximum temperature under the beam

Knowing the boron flux exiting from surface, we can use this relation to estimate the maximum temperature under the beam. The flux evaporating down the cavity is equal to the flux emitted by a boron surface of same temperature T at equilibrium with an imaginary boron gas: $J_{B_0} = \xi_B P_{B_0}(T)$. If we plot the function $\frac{J_{B_0}}{\xi_B} = (\sqrt{2\pi} m_B kT)^{1/2} J_{B_0}$, its intersection with $P_{B_0}(T)$, as given by the phase diagram (Fig. VI.3), gives $T \sim 3700$ K.

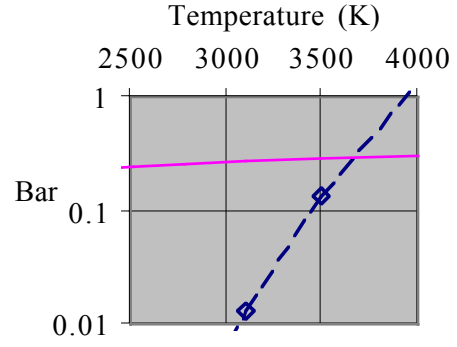


Fig. VI.3 Graphical estimation of maximum temperature under laser beam. Intersection of $P_{B_0}(T)$ (dashed line) and $\frac{J_{B_0}}{\xi_B}$ (plain line)

I.4. Diffusion of boron particle outside cavity

In gas phase, boron flux is much smaller than nitrogen flux, even during first seconds. Therefore, boron can be considered rarefied in nitrogen and hence, boron concentration in atmosphere obeys the usual diffusion equations:

$$\begin{cases} \frac{\partial n_B}{\partial t} + \nabla J_B = 0 \\ J_B = -D \frac{dn_B}{dr} \end{cases}$$

Generally speaking, D depends of mean free path, therefore of temperature, and hence of r . If D can be considered uniform, we can use the simple form, $\frac{\partial n_B}{\partial t} = D \Delta n_B$.

Strictly speaking, limit conditions should express that boron is continuously collected when it reaches a surface ($J_B = \xi_B P_B$). But, if we can neglect this absorption locally around impact (like we neglected radiation locally in target temperature estimations), the stationary solution is of spherical symmetry: (This is just the same function than the “simplest gradient”, already used for temperature estimations.)

$$\begin{cases} n_B = n_{B_0} \frac{r_0}{r} + n_\infty \\ J_B = J_{B_0} \frac{r_0^2}{r^2} \end{cases} \quad \text{with} \quad n_{B_0} = \frac{J_{B_0} r_0}{D}$$

As boron is completely absorbed in the chamber, $n_\infty = 0$. The distribution of boron on the

target should follow a $1/r$ law. This seems compatible with the deposit spreading of most experiment. However, it is only valid after stabilisation of diffusion. For a heating of one second, boron is not spread on target as $1/r$. (See Chap. VII-I.2.1.)

Boron concentration is proportional to total flux evaporated from the cavity $\sim J_0 r_0^2$. Boron concentration also varies with the inverse of the diffusion coefficient $1/D$. D is roughly proportional to the mean free path of boron particle in nitrogen, which is roughly proportional to the inverse of nitrogen pressure. Hence in nitrogen, boron concentration is roughly proportional to nitrogen pressure (For same $J_0 r_0^2$). Boron particles will reach a distance on surface more or less proportional to \sqrt{D} , hence to the square root of mean free path. In nitrogen atmosphere, this is proportional to $1/\sqrt{P}$. These relations are idealistic. Experimentally, a variation $1/P^{0.2}$ is measured. (See chapter VII-II.2.)

I.5. Particles depositing on target from gas phase

For a boron molecule evaporated under the beam, the flying distance to tube growth zone (250 μm at minimum) is long compared to the mean free path ($\sim 20 \mu\text{m}$), therefore each molecule should have a lot of collision in gas phase, before being collected on surface. Any particle will tend to thermalise (by loss of kinetic energy) and, if collisions are reactive, to agglomerate. (Boron is not stable as a gas.)

The reactivity of particles in atmosphere can not be simply deduced from previous phase diagram, although it can give a rough idea. Indeed, the phase diagram describes a surface equilibrium, ie a statistical quantity of matter in equilibrium. (For which pressure has a meaning.) In the case of small particles, the reactivity depends on their composition, on their size and on their kinetic energy (temperature).

In the gas phase near irradiated zone, temperatures are higher than dissociation temperature of BN on some distance (typically inside cavity). Maximum temperature is that of evaporating boron $\sim 3700 \text{ K}$. In this zone, only pure boron particles can agglomerate. As boron vapours are concentrated, boron-boron collisions may be numerous. Further away, in cooler zones, nitrogen is much dominant, and lower temperatures allow the reaction of boron particles with nitrogen. BN layers will form on boron particles. In even further zones, where gas temperature drops under fusion temperature of boron, particles will stop absorbing nitrogen.

Guess of reactivity for particles possibly present in gas phase Italic-green characters and underlined-red characters are zones of the plasma where temperatures are respectively, lower and higher, than dissociation temperature of BN (to be defined for small particles).

Particle Reactivity	BN ($T < T_{\text{diss}}$)	BN/B ($T < T_{\text{diss}}$)	B $T < T_{\text{diss}}$	N ₂ $T < T_{\text{diss}}$	B $T_{\text{diss}} < T < T_{\text{evap}}$	N ₂ $T_{\text{diss}} < T < T_{\text{e vap}}$
BN ($T < T_{\text{diss}}$)	<i>yes</i>					
BN/B ($T < T_{\text{diss}}$)	<i>yes</i>	<i>yes</i>			(Symmetrical)	
B $T < T_{\text{diss}}$	<i>yes</i>	<i>yes</i>	<i>yes</i>			
N ₂ $T < T_{\text{diss}}$	<i>no</i>	<i>yes (over fusion)</i>	<i>yes (over fusion)</i>	<i>no</i>		
B $T_{\text{diss}} < T < T_{\text{evap}}$	not obvious	not obvious	yes	not obvious	<u>yes</u>	
N ₂ $T_{\text{diss}} < T < T_{\text{evap}}$	not obvious	not obvious	not obvious	no	<u>no</u>	<u>no</u>

Note: There may also be some degree of ionisation under the laser beam.

Particles are continuously collected on target surface around the cavity. The percentage of recombination during flying time can be measured by the composition of zone III deposit (that does not further recombine). EPMA analysis (Fig. IV.37) showed that this deposit is heavily boron dominant, for a standard heating. Recombination of boron particles while flying may be minor. However, for higher nitrogen pressure, the pale aspect of zone III, suggests that this percentage of recombination is increased. (See Chap. VII-II)

It is essential to know if small molecules (boron or BN) are present in depositing species around impact. Indeed, if tube growth is feed from gas phase, such molecules should be present. It is only possible if boron atoms can escape from irradiated zone without many boron-boron agglomerations.

II. Evolution of nano-size particles at high temperatures

In a first part (II.1.) we will show that there is a drastic temperature gradient along tubes, which are linked to a hot zone, mainly because of radiation from tube cylinder. Temperature decreases exponentially with tube length, on a distance of typically 10 microns and for a temperature range of a few hundred degrees.

The evolution of this gradient should influence tube growth. Atoms diffuse under the effect of the temperature gradient. Reciprocally, the temperature gradient changes with the diffusion of atoms. The description of such a local process is however uncompleted. (part. II.2)

The conditions of growth of the BN tubes produced here as observed by electron microscopy are described in part. II.3. This description is difficult, mainly because high-resolution imaging is used post-nucleation and is limited by the interpretation of images.

II.1. Temperature gradient along a tube

If one end of a structure is kept at constant (high) temperature (T_{\max}), by an unlimited heat exchanger, and if the structure loses heat from its surface, temperatures are not uniform inside the structure. In our case, the heat exchanger is typically the hot target, to which a particle is linked. The structure exchanges heat on its surface because of thermal radiation, and because of thermal conduction in the gas phase.

When the tube extends from the hot surface, the free extremity is cooling down. There is a minimum temperature (T_{\min}) reachable at this extremity imposed by the system. It is such that external gains and losses are equilibrated on the surface of the structure. We will estimate this minimum temperature and the typical length necessary for a tube to reach it.

II.1.1 Gradient along a tube, considering only simple radiative losses

Hypothesis: We consider a tube kept at fixed high-temperature, T_{\max} , at one extremity. First, we only consider radiative losses. If we suppose that we can use the Stephan law, local loss is $\sigma T^4 dS$. In addition, far environment is supposed to maintain a minimum temperature T_{away} . We consider all radiative emission/absorption coefficients equal to unity.

This model is not valid for the present experiment, because it does not account for the effect

of the gas phase and for radiation from the hot target. However, it is simple and it can apply in some cases like, a structure in vacuum at the extremity of very sharp hot tip, for instance.

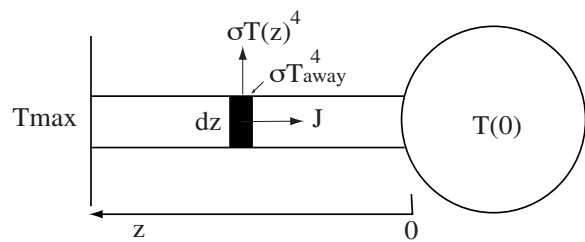
Note: If a spherical particle is present at the free extremity of the tube, it is supposed at uniform temperature. We could show that this is more or less correct as long as its dimension is smaller than 10 microns.

For a slice dz of a tube of external radius R ($= 1.6$ nm for numerical applications), the energy conservation between transmitted heat flux along tube axis, J , and radiation on slice cylinder is written:

$$\pi R^2 \times dJ = -2\pi R dz \times \sigma (T^4 - T_{away}^4)$$

with $J = -k \frac{dT}{dz}$,

$$\boxed{\frac{d^2T}{dz^2} - \frac{2\sigma}{kR} (T^4 - T_{away}^4) = 0}$$



Note: k is the axial thermal conductivity of a tube, which is only known by an order of magnitude. k is more or less the “in-plane” conductivity of h-BN multiplied by $1 - \left(\frac{R_0}{R}\right)^2$, to account for a hollow tube of inner diameter R_0 . The “in-plane” conductivity of h-BN is not known. For numerical applications, we use 150 SI, which is half of graphite’s value at 2000 K. [1.1.9] We multiply this by 0.86 ($R_0=1$ nm, $R=1.6$ nm).

This equation is not affordable literally. We can solve it numerically, for a given T_{away} , if we know $T(0)$ and $\frac{dT}{dz}(0)$ at cool extremity $z = 0$. (It could also be linearised.) $\frac{dT}{dz}(0)$ can be

approximated to zero, as soon as the tube is much longer than the dimension of free extremity. The knowledge of $T(0)$ imposes tube length. Alternatively, the knowledge of tube length imposes $T(0)$. (See Fig. VI.6-8.)

Note: Strictly speaking, $\frac{dT}{dz}(0)$ depends on the morphology of the cold extremity. For instance, if free extremity is a particle of radius R_p , the limit condition at

Latent heat of BN diss.	10000 J/g
ZN	14.01
ZB	10.81
Amu	1.66E-24 g
a parameter	2.5E-10 m
Tube radius	1.6E-09 m
Speed of length	0.00001 m/s
Speed of surface	1.00531E-13 m ² /s
Surface density	3.69504E+19 m ⁻²
B/N flux for a bi-layer tube	3714661.098 s ⁻¹
Mass flux	1.53048E-16 g/s
Comb. latent heat flux	1.53048E-12 J/s

cool extremity is $\pi R^2 J(0) = 4\pi R_p^2 \sigma (T(0)^4 - T_{away}^4)$, hence $\frac{dT}{dz}(0) = -4 \left(\frac{R_p}{R}\right)^2 \frac{\sigma}{k} (T(0)^4 - T_{away}^4)$.

This limit condition could be completed by a chemical heat flux for BN combination. However, this term is expected small in front of radiative terms in the beginning of the growth. Considering a growth speed of 10 $\mu\text{m/s}$, the latent heat released by BN combination is $\sim 1.5 \cdot 10^{-12}$ J/s. For comparison, the radiation from a disc of radius 1.6 nm at 2000 K is $\sim 7 \cdot 10^{-12}$ J/s.

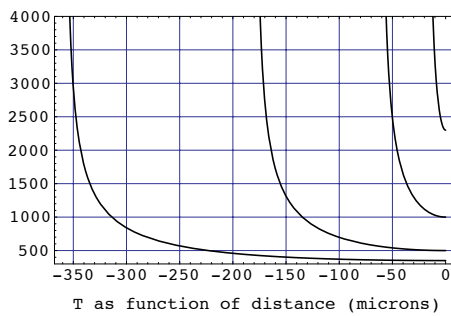


Fig. VI.6 Temperatures along a tube with simple model for $T_{away} = 300$ K and for several $T(0)$. Tube free extremity at $z = 0$. When fixing T_{max} , the length of the tube is determined.

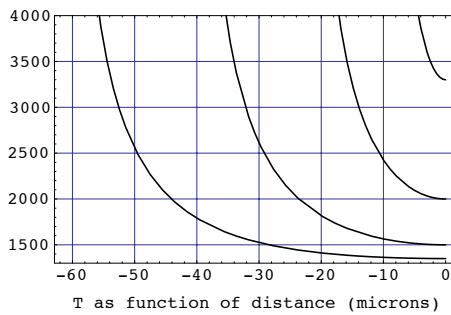


Fig. VI.7 Temperatures along a tube with simple model for $T_{away} = 1300$ K

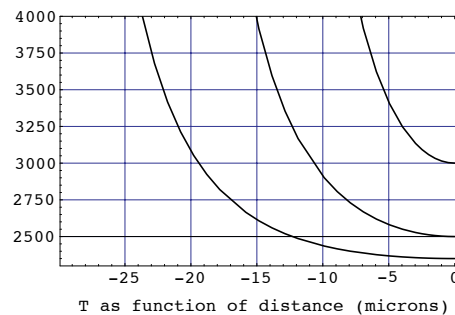


Fig. VI.8 Temperatures along tube with simple model for $T_{away} = 2300$ K

When tube is getting longer, $T(0)$ tends toward a minimum value T_{min} . In this model, $T_{min} = T_{away}$. It is such that external losses and gains at cool extremity are locally equilibrated. Mathematically, this limit case is $T(z) = T(0) = T_{min}$. A tube should theoretically extend infinitely to reach most stable structure.

However, the temperature decrease is of exponential type, so that when a tube is getting longer, the maximum temperature range ($T_{max} - T_{min}$) is approached for a finite tube length. For instance, if chamber walls are at ambient temperature $T_{min} = 300$ K, and $T_{max} = 2700$ K, temperature range is about 2400 K as soon as tube length $> 150 \mu\text{m}$. This value is quickly decreasing with T_{min} . It should be noted that these estimations of length depends on thermal conductivity, which is only known with precision of one order of magnitude.

Note 1: Computed gradients for temperature $T(0) > T_{min}$, may be structurally unstable. However, they are physical as intermediate stages of growth. Indeed, temperature stabilisation of a gradient (~ millisecond) is much faster than tube growth (~ seconds). (Else, in the dynamic problem, the equation should be completed by a term of thermal inertia $C \frac{dT}{dt}$.)

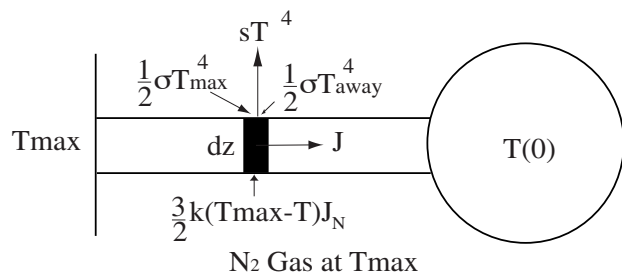
Note 2: Gradient shape near hot extremity, is little changing with increasing tube length. Therefore, temperatures at tube foot are little affected by tube extension. As a consequence, matter fluxes along the tube (if any) which depend on first derivative of temperature, may be expected constant during tube growth.

II.1.2 Taking in account gains from gas phase and from radiative target

Hypothesis: For the present experiment, we can estimate temperatures along a tube more reasonably, by taking in account gains from gas phase and, radiations from hot target surface. We consider a tube perpendicular **or not** to target surface. Surface is at uniform temperature, T_{max} , on a zone much larger than tube dimensions. Gas phase near this area is also considered at uniform temperature T_N , equal to T_{max} . This supposes the presence of a thick thermal layer in the gas phase. (A lower value would decrease T_{min} , increasing the gradient.) Furthermore, we neglect radiation from chamber walls. (This is correct, as long as $T_{away}^4 \ll T_{min}^4$.)

Note: This model is not only valid for our experiment, but for all experiments where tubes are linked to one hot surface and, where the other half of the solid angle is cold. It is especially the case for the arc discharge method. For methods with an oven heating in the whole solid angle, and/or with a gas flow, the equation should be corrected.

The radiation flux collected from target surface on a small area of the tube is $\frac{1}{2} \sigma T_{max}^4$ (0.5 time Stefan law). Indeed, if the tube is perpendicular to the hot surface, radiation is collected in only half of the solid angle. If tube is parallel to target surface, the coefficient is the same because only one side of the tube is collecting.) The heat gain of tube surface from nitrogen gas can be idealised as $J_N \frac{3}{2} k_B (T - T_{max})$. (J_N is the incident flux of nitrogen molecules



that we computed previously in I.2. There may be a limiting factor, in which case T_{\min} is lower.) Those two energy gains are to be subtracted from previous energy loss σT^4 , so that the actual energy balance is:

$$\pi R^2 \times dJ = -2\pi R dz \times [\sigma(T^4 - \frac{1}{2}T_{\max}^4) - J_N \frac{3}{2}k_B(T_{\max} - T)]$$

and hence,
$$\boxed{\frac{dT}{dz} - \frac{2}{kR} [\sigma(T^4 - \frac{1}{2}T_{\max}^4) - J_N \frac{3}{2}k_B(T_{\max} - T)] = 0}$$

Temperatures along the tube can be computed numerically as in the previous model, for intermediate stages, where $T(0) > T_{\min}$ and $\frac{dT}{dz}(0) = 0$. However, T_{\min} must first be found numerically. It is such that $\sigma(T_{\min}^4 - \frac{1}{2}T_{\max}^4) - J_N \frac{3}{2}k_B(T_{\max} - T_{\min}) = 0$. **(With this model, T_{\max} and T_{\min} are not independent.)**

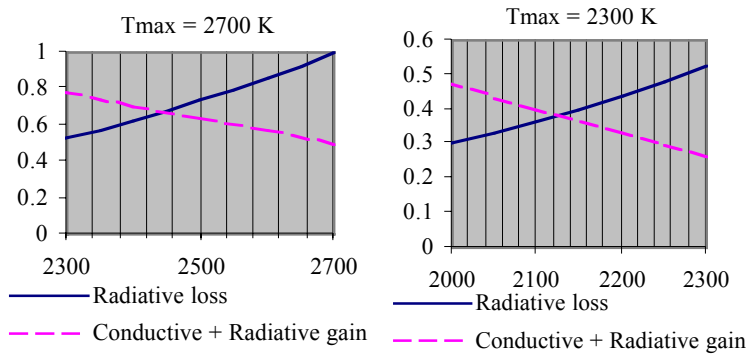


Fig. VI.9 For $T_{\max} = 2700$ and 2300 K, Graphical comparison of the radiative loss σT^4 and of the gains $\frac{1}{2}\sigma T_{\max}^4 + J_N \frac{3}{2}k_B(T_{\max} - T)$. T_{\min} is found at their intersection. (Arbitrary units on ordinate, same for both figures.)

Numerical:

For $T_{\max} = 2700$ K, $T_{\min} = 2446.52$ K

For $T_{\max} = 2300$ K, $T_{\min} = 2124.87$

For $T_{\max} = 1000$ K, $T_{\min} = 987.634$ 8

for $T_{\max} = 4000$ K, $T_{\min} = 3481.57$ (Apply to graphite but not to h-BN.)

Most conclusions from previous model are still valid. However, with this model, the maximum range of temperature ($T_{\max} - T_{\min}$) is limited (because of the additional external heat). It is ~ 250 K for $T_{\max} = 2700$ K, down to ~ 12 K for $T_{\max} = 1000$ K. (For our h-BN target, 2700 K $< T_{\max} < 2350$ K.) Hence, this model is similar to previous model, but only at equal (high) T_{\min} .

Because T_{\min} is high, maximum temperature range is approached for short tube lengths. For instance, **for $T_{\max} = 2700$ K, temperature range on a tube is about maximum (~ 250 K), as**

soon as tube length $> 15 \mu\text{m}$. Hence, in the present method, many tubes on target surface should have a temperature gradient close to the maximum range $\sim 250 \text{ K}$

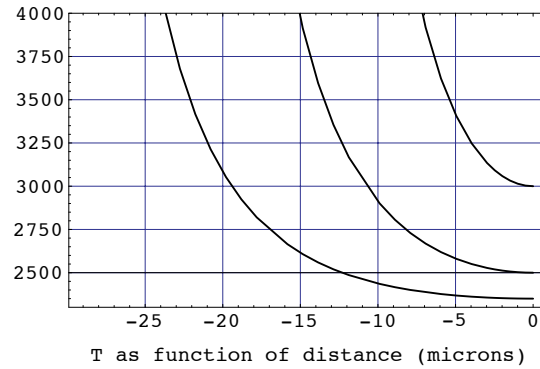
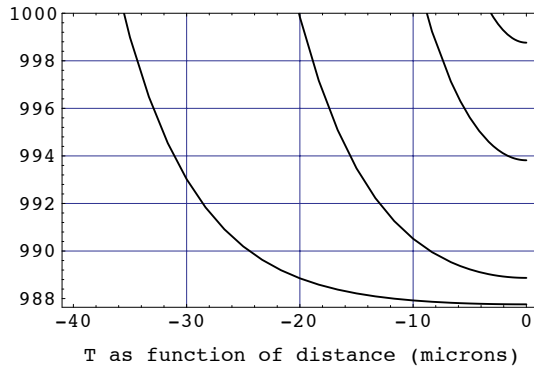


Fig. VI.10 Temperatures along tube considering gas and hot target for $T_{max} = 1000 \text{ K}$

Fig. VI.11 Temperatures along tube considering gas and hot target for $T_{max} = 2300 \text{ K}$

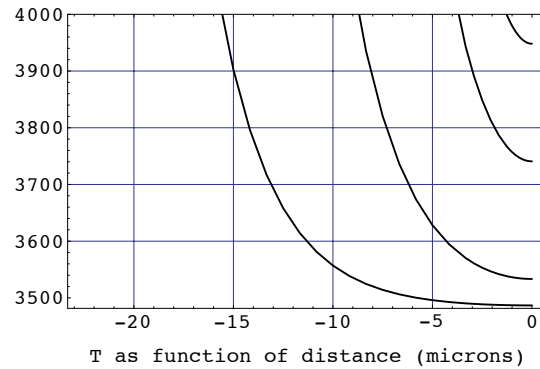
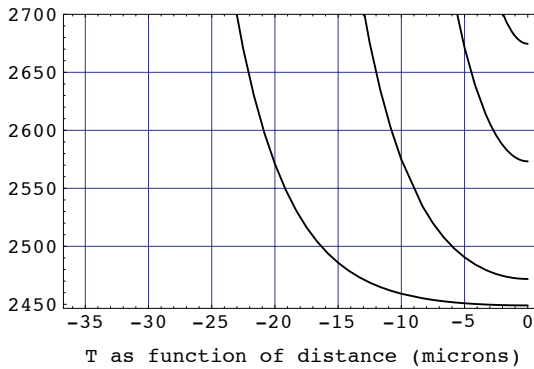


Fig. VI.12 Temperatures along tube considering gas and hot target for $T_{max} = 2700 \text{ K}$

Fig. VI.13 Temperatures along tube considering gas and hot target for $T_{max} = 4000 \text{ K}$

II.2. What determines the evolution toward a tubular morphology?

In this part, we are concerned with the complex problem of what may determine the evolution of a structure toward a tube, rather than another morphology. As a first approach, we consider a small change of morphology of the structure such that it does not affect the total number of atoms, N , and the inner pressure, P . Temperature is not always uniform and may decrease with morphology because the environment imposes so. (The structure is not isolated.) n atoms are concerned by the change (from 1 to N). In addition, we consider no phase transition or such that the latent-heat is dissipated without contribution to the process.

II.2.1 Why the surface/constraint energy contribution is small?

At high temperature, the agitation is such that atoms have a relatively high mobility. This is either because of surface diffusion or eventually because of volume diffusion. If the evolution is reversible, the structure will statistically evolve with the energy $\delta u = dH - TdS$. (H being the enthalpy function)

Note 1: Free enthalpy $d(H-TS)$ is not the driving energy unless temperature can be considered constant.

Note 2: (Reversibility) Strickly speaking, the process is not reversible. If the process were reversible, the variation of entropy over the total system would be $dS_{total} = \frac{\delta Q}{T_{min}} - \frac{\delta Q}{T_{structure}} \neq 0$

(The heat released δQ is finally totally dissipated to the cool source at T_{min} .), which is impossible. However, this term is small compared to $\frac{\delta Q}{T_{structure}}$, so that the system may be considered reversible during its transformation. The system can also be considered at thermal equilibrium during each step of the transformation. Indeed, the thermal equilibrium requires milliseconds, when tube growth requires seconds.

Note 3 (estimation of δQ): If we imagine internal energy as the sum of kinetic and potential energies, the release of heat is due to the decrease of both, kinetic energy ($\frac{1}{2}kdT$ per degree of freedom) and, potential energy (through the decrease of inter-atomic distances with T). When the structure extends, the release of heat

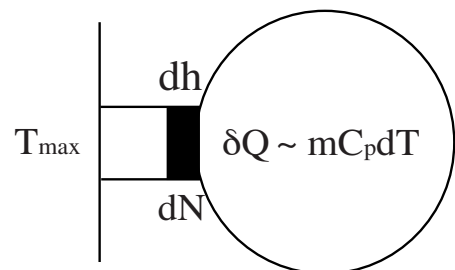


Fig. VI.5 Extension from a spherical particle to a tube.

during the transformation is $\delta Q \cong -\rho \int_{volume} C_p(T(r))dT(r) dv$, with, ρ being the material density, C_p being the heat capacity at constant pressure. For simplification, we can consider that most of the decrease is obtained at cool extremity. In addition, C_p can be considered constant on the temperature range (correct at very high temperatures):

$$\delta Q \cong -N \frac{m_B + m_N}{2} C_p dT_h(0). \text{ } m_B \text{ and } m_N \text{ are the atomic mass of boron and nitrogen atoms.}$$

If we first consider that the structure is isolated (constant temperatures), all thermodynamic variable (N,P,T) are fixed so that $dS = 0$ during a change of morphology. The structure is

changing with dH , minimising its internal energy.

The variation of energy in the structure is the sum of surface energy, and constraints energy (due to any distortion from perfect lattice like curvatures, inter-layer misfit, lattice boundaries, and other defects): $dH = dH_{\text{surface}} + dH_{\text{constraint}}$. If matter was isotropic, a change of morphology would not affect constraint energy on average, $dH_{\text{constraint}} = 0$. The structure would reduce its surface energy, and shape as a sphere. However, for a layered (anisotropic) structure, the surface cost does not only depend on surface dimension. It also depends on the type of boundings that are not satisfied at surface.

For reducing surface cost, layers should be parallel to the surface. However, for a structure of limited size, this requires curving or angles, hence some structural constraints. Therefore, when changing morphology, there is a competition between surface cost and, constraints cost, with two opposed cases: A spherical morphology, minimises surface cost, but not constraint cost. (Mainly because it is more difficult to keep the layer to layer arrangement with a spherical curvature than with a cylindrical one.) On the opposite, a tubular morphology minimises constraint cost but not surface cost. In between, many meta-stable structures may exist.

In any case, the **sum of the two structural terms may not drive the change of morphology**. This idea is supported by the fact that both tubes and onions are morphologies are stable at uniform (low or high) temperature. If one of the two terms was dominant enough, then only one of the morphologies would be stable. The constraint cost of an onion may be close to the surface cost of a tube because the disordered piling of layers in an onion (imposed by the spherical closure) is a cost very comparable to the surface cost of a tube.

II.2.2 Diffusion due to the gradient (in a structure non uniformly heated by its environment)

Here, we consider that the influence of structural energies is negligible in the process (previous paragraph). On the other hand, we consider that the change of morphology affects temperatures in the structure.

II.2.2.1 Possible mechanisms

If the forces working in the structure were only dissipative $dH = TdS = \delta Q$, and $\delta u = 0$. There should be no evolution of the structure. However, during the dissipation, the morphology can change spontaneously: Atoms diffuse under the effect of the temperature gradient, and reciprocally, the temperature gradient changes with the diffusion of atoms.

For instance, we may expect a “standard” (by opposition to “self”) surface diffusion along axis due to the temperature gradient. The driving force on one moving atom may be expected roughly proportional to $-\nabla T$. (We consider adsorbed-atoms as a 2D gas of uniform concentration.) This force works on moving atoms and compensates the dissipation caused by their movement. With a classic law of dissipation, the atomic flux can be expected proportional to the driving force: $J = -D\nabla T$.

The temperature gradient may not only move atoms along an existing tube, but also increase tube length. (Else, atoms would simply accumulate at tube extremity.) For instance, we may consider the spontaneous fluctuations of atoms at the frontier tube/extremity caused by surface diffusion. When a number of these atoms move toward extremity, tube length increases and temperature decreases at cool extremity. For the next fluctuation of opposite direction, we may expect an amplitude slightly smaller, because diffusing atoms have lost some kinetic energy. Hence, on average, tube length is increasing. This is a type of “self”-diffusion process. By similarity with standard diffusion laws, we may expect a driving force on one moving atom proportional to $-\frac{dT_h(0)}{dh}$, and a diffusion flux $J = -D\frac{dT_h(0)}{dh}$, where T, temperature along the tube, is indexed by tube length h.

Note 1: $\frac{dT_h(0)}{dh}$ can be approximated by $\frac{dT_H}{dz}(h - H)$. In other words, the derivative of T at cool extremity is equal to the derivative of temperature at same distance, but as computed for a very long tube. (To be further demonstrated. This is because, when tube is getting longer, temperatures are only affected near cool extremity.)

Note 2: With such process, the driving force on one moving atom is increasing with the temperature difference between its initial and final position. However, if n atoms are moving simultaneously, this temperature difference increase with n. Hence, the process is expected to be collaborative. One consequence is that the driving force is expected higher for a tube with

a large diameter.

II.2.2.2 Speed of growth with tube length

If such diffusion, or self-diffusion, process is driving tube growth, the speed of growth is proportional to the diffusion flux, J .

To check if this process can feed the growth, we may say that, for the growth to occur at the speed measured (say $10 \mu\text{m/s}$), the diffusion flux J should be sufficient. However, to evaluate that flux, we need the diffusion coefficient, D , hence we should describe completely the diffusion process.

On the other hand, we can check that J varies as if following the evolution of temperature at cool extremity: If this is the case, the speed of growth should fall exponentially with tube extension. This is actually compatible with experimental observations for short duration heatings, which showed that tube length decreases very fast with heating duration. (See paragraph II.3.5)

Note: (About maximum tube length) Practically tube extension is limited. This is may be because source material is lacking. In that case, the tube should stop growing without matter left at free extremity and temperature at cool extremity may be far from T_{min} . Else, temperature at cool extremity may drop under what is necessary for combination of B and N : $T(0) < 2350 \text{ K}$. If those limits do not apply, the growth is interrupted by the end of the experiment (and some matter remains at free extremity). In that case, tube length is increasing with experiment duration.

According to the second temperature model, tube length should also increases with T_{max} . Indeed, for higher T_{max} , the temperature gradient is stiffer (See figures IV 10-13). (In the first temperature model, where T_{min} and T_{max} are independent, tube length decrease with T_{min} ($= T_{away}$) and is little influenced by T_{max} .)

II.2.2.3 Path of maximum temperature decrease

It is remarkable that the spontaneous evolution of a structure toward a tubular structure is such that there is a maximum decrease of temperature locally on the structure. Indeed, the fastest thermal isolation from hot zone is obtained by a (eventually tubular) one-dimensional morphology. By opposition, we could imagine that a tube would extend and grow thicker

simultaneously. Such evolution causes a decrease of temperature, but of less amplitude than that obtained by a simple extension of the tube.

We may speculate that this actually the origin for the preferential formation of a tubular structure. If the driving force on moving atoms is increasing with the temperature decrease of a cool extremity, atoms such that their move decreases the most this temperature will move with the highest probability. Hence, the spontaneous evolution of such structure is such that the temperature decrease at cool extremity is fastest.

II.2.2.4 Maximum thermal energy available for tube growth

When an atom is moving along a gradient, on average it exchanges a kinetic energy, kdT , with its environment, where dT is its own variation of temperature in the gradient. This energy, which is dissipated in the system, is the cause of the average movement of the atom in the gradient. Hence we can say that the energy available for the move of the atom is its own variation of kinetic energy. We can define an imaginary driving force, such that its work during the move is kdT . Then, if we imagine a continuous movement of the atom along the gradient, we should also imagine a dissipation of heat equal to the work of the driving force.

Similarly, for a “self” diffusion process, as described above, the energy for the move of one atom is kdT . But, dT is due to the move of n ($<N$) atoms simultaneously. If n atoms are moving simultaneous to the cool extremity of the tube, $kdT = k \frac{dT}{dN} n$, where $\frac{dT}{dN}$ is the decrease of temperature when the tube extends of one atom. We deduce $|kdT| < Nk \left| \frac{dT}{dN} \right|$. (This

is slightly less than the total heat released per atom by the structure, $\left| \frac{\delta Q}{dN} \right|$.) This value can be

estimated as $Nk \left| \frac{dT_h(0)}{dh} \right| \frac{dh}{dN} = Hk \left| \frac{dT_h(0)}{dh} \right| \sim 0.5 \text{ eV}$, for $T_{\max} = 2700 \text{ K}$, in the beginning of the growth when $\frac{dT_h(0)}{dh} \sim 55 \text{ K}\mu\text{m}^{-1}$, and if matter is enough to growth a tube of $H = 100 \mu\text{m}$.

This value is only a maximum energy available for the move. Depending on the efficacy of the diffusion process, a large part of the kinetic energy available may be dissipated to the cool source (T_{\min}) without contribution to the growth. This value is increasing linearly with the size of the structure and, falling exponentially with the length of the tube.

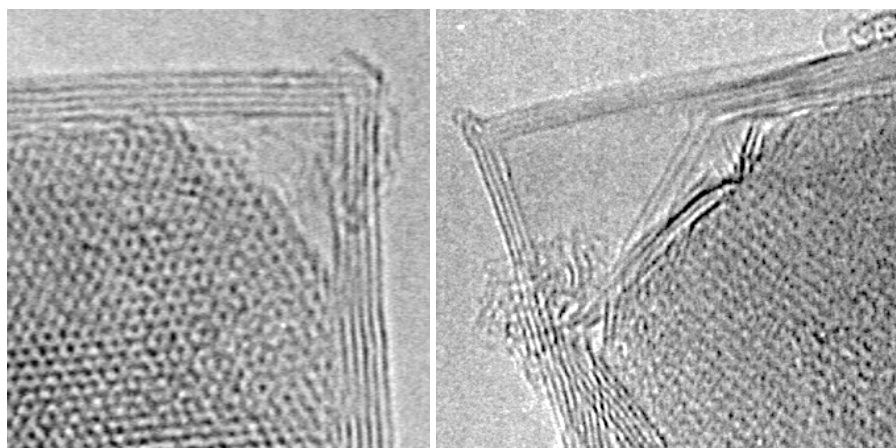


Fig. VI.14 *The emergence of BN layers from a boron core* (TEM)
 The growth of BN layer on boron particle may constraint the shell until rupture. This may help the extrusion of a tube. (From 50 mb experiment)

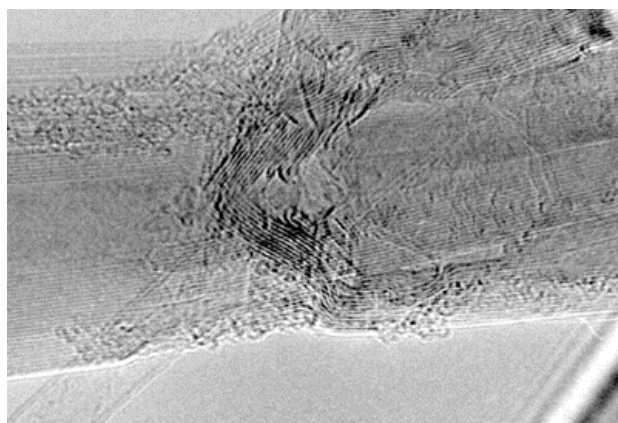
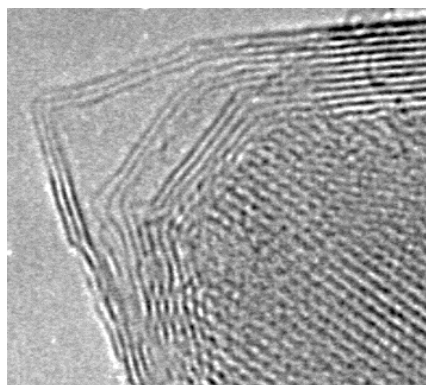


Fig. VI.15 *A tube grow from the disorder of the BN shell* (TEM) (From 50 W experiment)

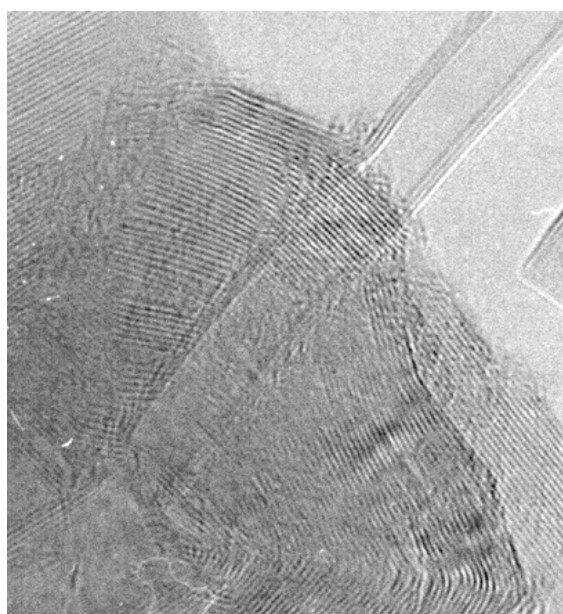


Fig. VI.16 *A tube rooted deep inside a BN shell* (TEM) A cavity through the shell is indicated by the level of grey. Tube and particle cavities are not separated. (From 50 W experiment)

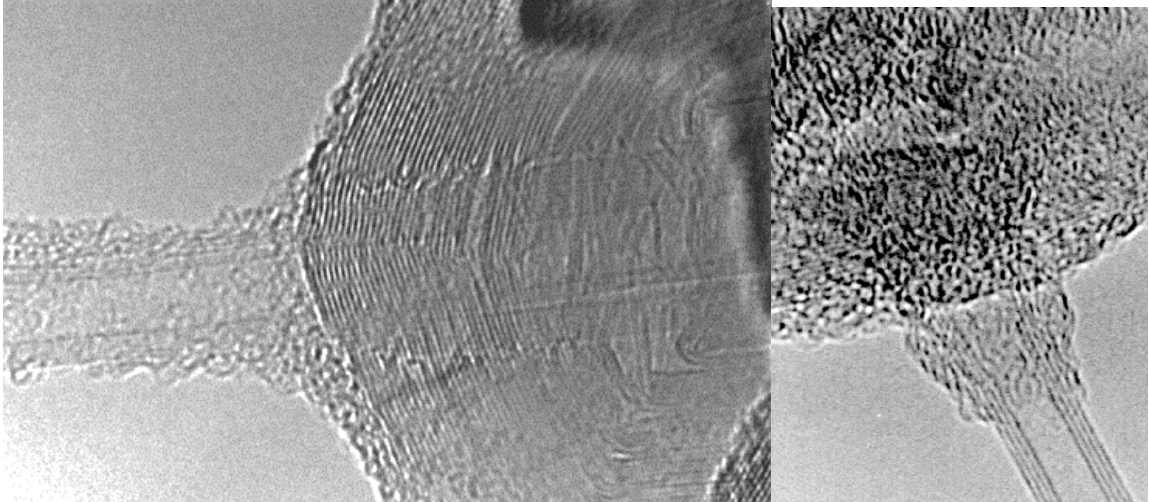


Fig. VI.17 Emergence of a tube (TEM) Amorphous material may be moving along external surfaces (From experiment at 50 W) (Such an image is difficult to interpret.)

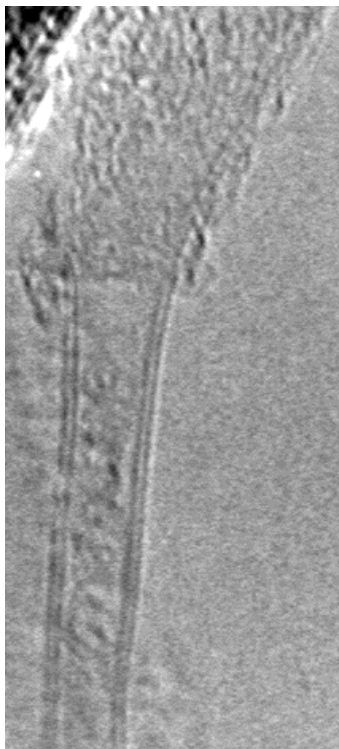
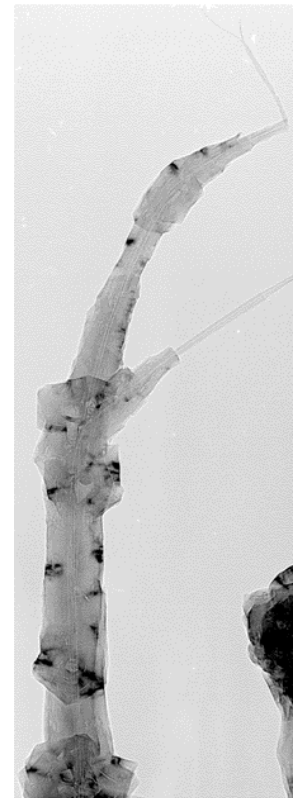


Fig. VI.18 Extremity of bi-layered tube (TEM) The presence of an amorphous material may also help tubes to form.

Fig. VI.19 A fibre saturated by merging particles (TEM) matter from BN/B particles spreads along fibre axis. (From 500 mb experiment.)



II.3. Conditions for BN tube growth

A precise description of tube growth is difficult, and not mature at present. Here, we will only discuss the conditions and processes that may enable the growth, considering experimental results.

II.3.1 Combination of a liquid boron surface with nitrogen

The natural behaviour of a hot liquid boron surface under nitrogen atmosphere is to get covered by h-BN layers, parallel to the external surface. Liquid boron recombines independently of particle size. Indeed, micro-size boron particles are also combining with nitrogen at the surface of zone II.

It is not clear if the forming BN shell grows from the inside (N diffusing through the shell) or from the outside (B diffusing through the shell). A growth from the inside of the shell seems more probable because some tubes can be observed rooted from the inside of a spherical particle (Fig. VI.16). Nitrogen flux inward the BN shell may be high, because nitrogen molecules have an incident velocity, when coming from gas phase (~ 0.4 eV). This may help to overtake local energy barriers of the shell. By opposition, boron atoms have to break their B-B bondings to get inside the shell, and therefore must go through an energy barrier at the B/BN interface.

If the shell mainly grows from inside, some constraints should occur inside the shell. Indeed, volume occupied inside particle increases, without an increase of the external shell. The boron core will double its volume through recombination (boron and h-BN have comparable atomic densities). Such constraints should lead to many ruptures of the h-BN shell over the boron core. In HR imaging, ruptures of this shell are commonly observed, as a structural disorder, locally on an onion. These ruptures may help a tube to start growing, when some BN layers are extruded from the particle. Such constraints may be more drastic in particles of small size.

II.3.2 Feeding in boron from atmosphere or from seed particles?

Feeding in boron atoms can be provided by seed particles. The typical size of these particles is compatible with the quantity of atoms necessary to grow a tube several hundred microns long. We can draw (Fig. VI.20) boron particle radius versus tube length as:

$$\frac{\rho}{m_B} \frac{4}{3} \pi R_{seed}^3 = \frac{1}{2} \rho_s 2\pi LR \quad (\rho_s = \frac{4}{\sqrt{3}} \frac{1}{a^2} \text{ is the}$$

surface density of an hexagonal layer.) For instance, with a typical particle of radius 50 nm, a bi-layer tube can be fed up to 200 μm .

On the other hand, tube can also be fed from gas phase, both in boron and nitrogen, by collection on tube body. The global flux of both elements is more than enough to feed tube growth, considering a speed growth of 10 $\mu\text{m/s}$ and a bi-layer tube. (Fluxes of boron and nitrogen were estimated previously, and are summed on a reference collection surface of 1 μm . Fig. VI.21) The collection surface could even be limited to tube extremity. This is true even near the end of the experiment, when boron flux outside cavity is small. (This is because tube growth speed is relatively slow.)

However, it is not obvious if such flux of boron can feed the growth as a continuous rain of small B or BN molecules from atmosphere. Indeed, the presence of large particles will rather cause a saturation of matter. Such collection of large BN/B particles on the body of fibres is commonly observed, especially for experiments at highest nitrogen pressure. (See Fig. VI.19 and Chap. VII-II.1) Their constituent matter tends to spread along external surfaces of the fibres, causing thickening and diameter discontinuity of the fibre along its axis. Unfortunately, the distribution of size of boron particles in the gas phase is still little known.

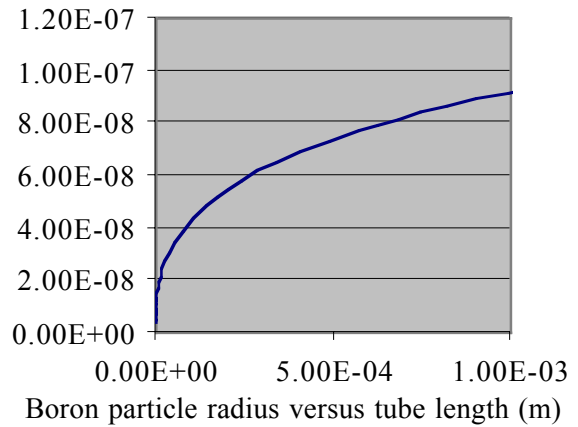


Fig. VI.20 Mass correspondence between a spherical particle and a bi-layered tube

With B density, $\rho = 2.1 \text{ g/m}^3$, Atomic weight, $Z_B = 10.81 \text{ Amu}$, $\text{Amu} = 1.66 \cdot 10^{-24} \text{ g}$, $R = 1.6 \cdot 10^{-9} \text{ m}$, $a = 2.5 \text{ \AA}$

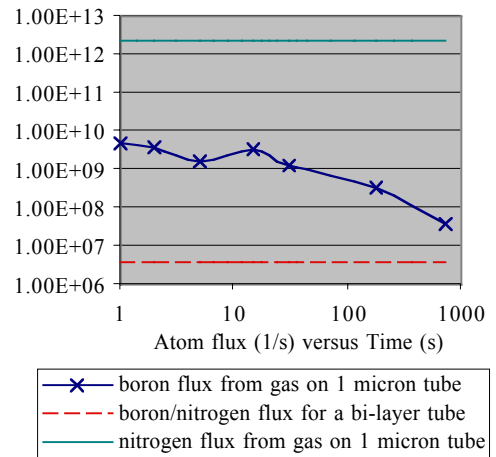


Fig. VI.21 comparison of feeding fluxes for a tube near cavity.

II.3.3 Incorporation of atoms in a growing at tube

While a tube is growing, atoms may be incorporated at extremity. A tube extremity has low energy barriers for incorporation because of bounding weaknesses. If this extremity is a seed particle, nitrogen atoms should move inward the spherical particle to meet boron atoms at the BN/B interface. In that case, the tube should be continuously extruded from the particle, until all boron inside the seed is recombined or cooler than fusion temperature. The seed is at free (and cool) extremity according to SEM observations for 2s of heating (Fig. VII.7).

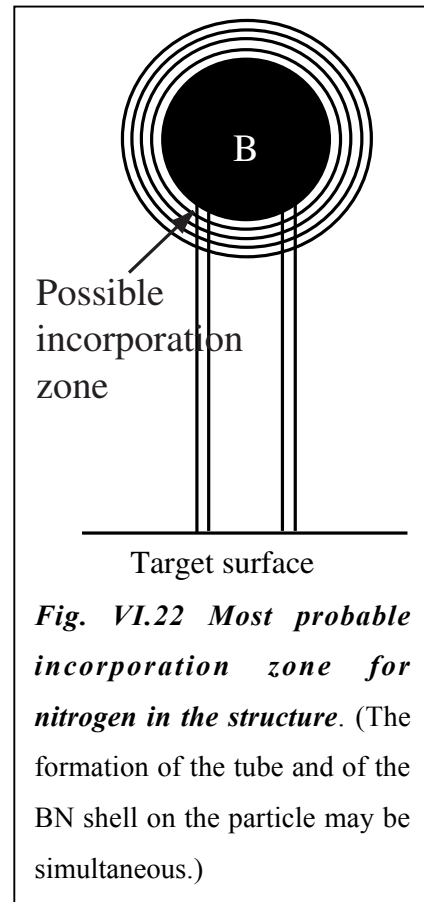


Fig. VI.22 Most probable incorporation zone for nitrogen in the structure. (The formation of the tube and of the BN shell on the particle may be simultaneous.)

II.3.4 Mobility of atoms along the tube

An atomic diffusion along tube is proved by the way merged particles spread along tube axis (Fig. VI.19). Atoms may move on cylinder surfaces, both internal and external. A surface diffusion flux at constant temperature

due to the non-uniformity of concentration of adsorbed atoms: $J_D = -D_n(T) \frac{dn}{dz}$ was proposed

by those authors. [3.1.2] A similar flux is to be expected from the non-uniformity of temperatures along the tube. (See II.2.2) Such a flux is highest near target surface, where temperature gradient is stiff.

II.3.5 Speed of tube growth

Because tubes are found inside cavity after 1s of heating, tube growth speed is at least 10 $\mu\text{m/s}$ at growth start. (See Chap. VII-I.2.1) Growth speed is then decreasing quickly with tube length. Indeed, if tube growth was constantly faster than 10 $\mu\text{m/s}$, 100 μm long tube should be grown in 10 s. However, after 15s of heating, the longest tubes (close to cavity edge) which have been in the range of temperature 2350-2700 K for $\sim 10\text{s}$, are only 20 μm long. Therefore growth speed must be dropping considerably in the first seconds of growth. This explains why the longest tube (120 μm) was observed for the longest heating (12 min). An accurate measurement of speed versus time should be undertaken with a finer study of duration range

between 1 s and 5s.

A violent decrease of growth speed with tube length is compatible with the idea that growth is driven by temperature decrease. (II.2.2.2) However, growth speed may also be limited by nitrogen/boron feeding fluxes. In the hypothesis of growth from a seed particle, the speed of growth may not be limited by boron flux. In the hypothesis of an incorporation surface exposed to the gas phase, the flux of nitrogen is very high and may not limit growth speed. This may be checked experimentally by a study of pressure influence for short heating durations.

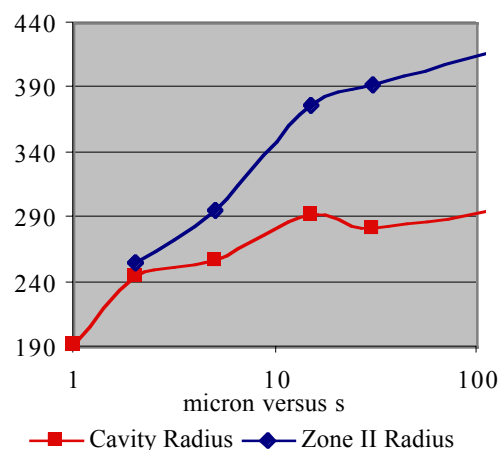


Fig. VI.23 Evolution of the dimension of zone II during target warming

II.3.6 Why tubes grow where boron is liquid?

Tube growth is conditioned by the presence of BN, which is conditioned by the ability of boron to recombine, so that tubes grow only where boron is liquid. However the liquid phase of boron may not be necessary, structurally, for the growth of tubes.

Nevertheless, there are some reasons why liquid boron may help structures to form. Liquid boron is “structurally flexible”. It may be forming an intermediate amorphous-BN phase, before incorporation of atoms in the structure. Also, liquid boron may provide a higher mobility of atoms than solid boron.

II.3.7 Formation of ropes?

The formation of ropes could not be made clear. (They could not be imaged by TEM at extremity.) Tubes may not grow individually and assemble later under Van Der Waals forces. Else, ropes would not have a uniform diameter on long distances. In addition, Fig. IV.27 showed that a common helicity is shared by many tubes inside a rope. Tubes in a rope may form altogether and then extend along the axis of the rope. Alternatively, some spherical particles, collected on the body of one starting tube, may develop new tubes, copying the structure of the first tube.

Chapter VII

Influence of experimental conditions

Objective: We describe systematically the influence of adjustable parameters of the experiment, such as time of heating, nitrogen pressure, laser power,...

Abstract: Spreading of boron on target surface as boron rich particles mainly occurs during the first 15 s, while cavity is still shallow. Crown emergence mostly occurs later, under a lower boron flux from atmosphere. The evolution of zone II ring follows target warming. After 1s, tubes are present inside the cavity, and indicate a minimum growth speed of 10 $\mu\text{m/s}$. After 2s, on starting zone II ring, all tubes have a spherical end at free extremity. Their lengths vary with distance from the cavity, hence with time of heating. After 12 min, all boron is evaporated from the cavity and tubes grow inside cavity.

Structures are drastically more recombined in higher nitrogen pressure. Fibres tend to be saturated with layers of h-BN on their external surface, probably because BN/N particles merge on their body. Increasing pressure causes a decrease of most dimensions around impact, but an increase of zone II ring. This is compatible with the influence of pressure on dissociation temperature as given by the phase diagram.

Under the minimum laser power for dissociation, there is no material growth. If dissociation is reached, power has no observable influence on obtained structures. However, all dimensions near impact increase linearly with laser power.

With He atmosphere, similar BN nano-structures are found. Indeed, some nitrogen is present in atmosphere, from cavity formation. Tubes are few and short. Structures are characteristic of nitrogen lacking. As target temperatures are not much affected by atmosphere composition, zone II ring and cavity dimensions are preserved.

Surface quality is important because it conditions the adherence of particles on target surface.

Measurement and analysis methods:

Taking the standard experimental procedure as reference, the effect of each adjustable parameters was studied, in the range experimentally accessible. Samples were prepared at nitrogen pressure 50, 100, 300, 500 mbar, in He (100 mbar), in vacuum ($\sim 10^{-5}$ mbar with continuous pumping), at laser power 40, 50, 60, 70, 80W, for time length of 1, 5, 15, 30 s, 3 and 12 min.

SEM and TEM observations were performed as described previously. All samples could be observed by SEM, but for TEM, only those for which some crown material could be collected, were observed.

For each sample, cavity dimension (zone I) and total deposition diameter (total diameter of the three zones) were measured using an optical microscope, respectively, at edges of boron drops in the cavity and, at limit visibility in microscope. Thickness of the tube growth ring (zone II) was measured during SEM observations, by the presence of nano-tubes at target surface. Measurements were averaged over several radial directions.

Measurement dispersion was found relatively high and is estimated $\pm 10\%$. This is due to deviance from circular symmetry of the impact, because the beam is not perfectly Gaussian. It is also due to the unevenness size of targets. Volumes of different target may be even by $\pm 10\%$, and this affects the global temperature in the target. It is finally due to unclear edge positions. The outer edge of zone III is a continuous decrease of particle concentration, so that an edge is only roughly defined by limit-visibility in optical microscope. (Furthermore, deposit thickness is probably affected by its adherence on target during heating.) An edge is usually clearly defined between zone II and III, by the presence or absence of tubes. At cavity edge, the frontier defined by tube presence, and that defined by boron drop presence, are often slightly different. This is probably because of a temperature decrease on target front surface after some time of heating. (See Chap. V-II.5.4.)

I. Different durations of heating (1s to 12 min)

I.1. Global influence of heating duration

Data of Fig. VII.2-3:

Pressure (mbar)	1s	2s	5s	15s	30s	3min (ref.)	12 min	Fitting function
Cavity Radius	192	245	257	292	282	300	302	$33 \ln t + 204$
Cavity Depth	40	55	87	333	499	824	966	$29 \ln t + 38$ and $194 \ln t + 180$
Total Radius	307	412	525	760	727	790	805	$136 \ln t + 316$
Zone II thickness ($\mu\text{m} \pm 10\%$)	No	0-20	38	84	110	126		$27 \ln t$

I.1.1 Effect of temperature rise on boron deposition and cavity formation

Boron is mainly scattered around the cavity, as boron rich nano-particles, during ~ 15 s. (See Fig. VII.1 and VII.3.) This time for particle spreading is related to the time for global target warming (between 5-15s), although the phenomenon is complex. As long as there is no cavity, boron spreads on the target, only limited by its diffusion in nitrogen. At that stage, the increase of total deposition (zone III) is due to the increasing evaporating flux under the beam. However, this expansion will stop as soon as, cavity depth is of a similar order than the diffusion length of boron in nitrogen (between 5 and 15 s). Indeed, as the cavity becomes deeper, boron gets collected inside cavity. Simultaneously, the evaporating flux under the beam probably reaches a maximum, because target is warmed.

During global target warming, the cavity expands in lateral and beam axis directions at similar speed ($\sim 30 \ln t$). This is because both directions follow the global temperature rise. Later, when global temperature has stabilised, the cavity stops increasing on its sides. However, cavity depth continues to increase because the liquid boron layer becomes thinner under the beam, affecting temperatures locally. The liquid layer may become thin under the pressure back warded from boron evaporation, or else because of thermal convections in liquid boron. This is observable experimentally: liquid boron drifts from the centre of the cavity to the sides of the cavity between 5 and 15s. From that stage, evaporation drills the cavity continuously. An equilibrium depth will only be reached after all boron was evaporated from the cavity. (Observed at 12 min.)

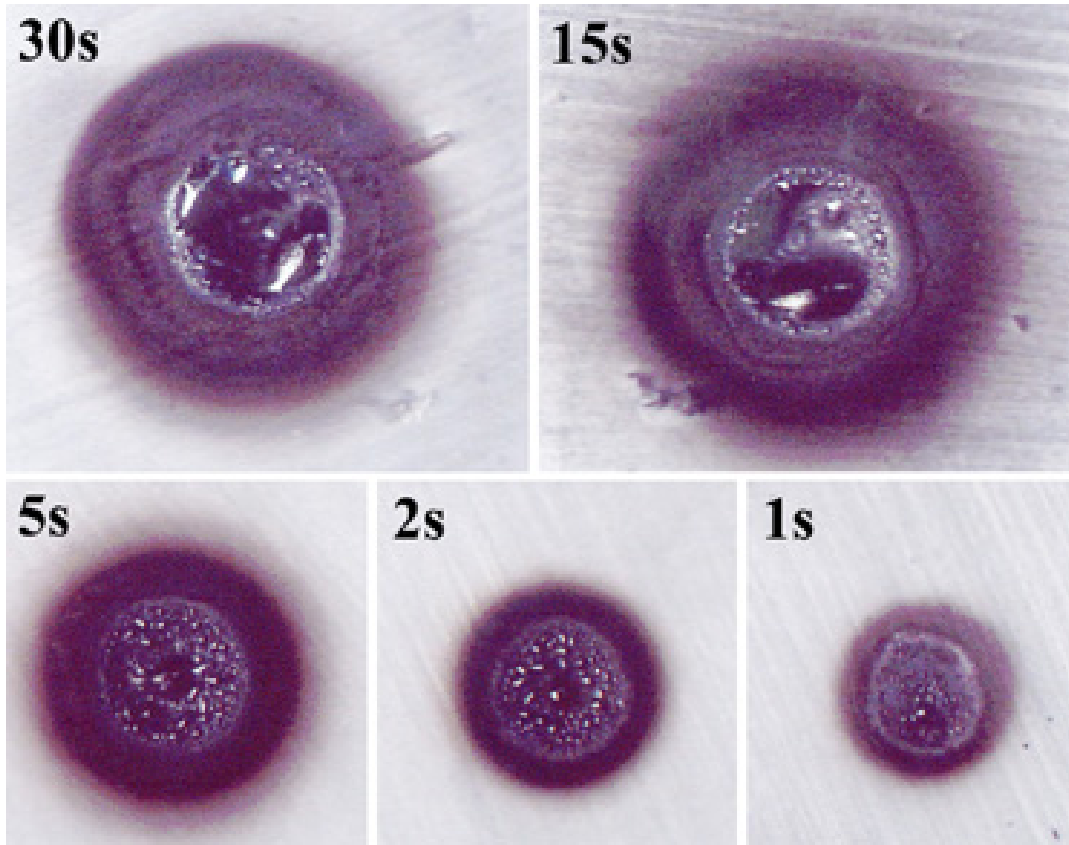


Fig. VII.1 Impact after short duration heatings (binocular optical microscope) After 15s, cavity radius and deposition zone no longer increase. This is correlated with a shift of boron drop inside cavity toward cavity sides, between 5s and 15s.

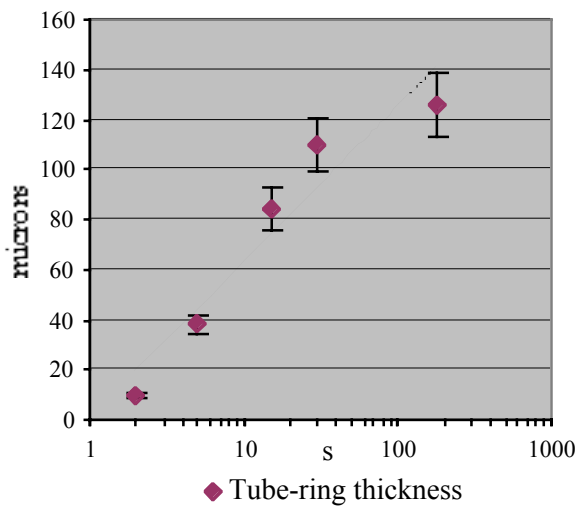


Fig. VII.2 Variation of zone II with duration

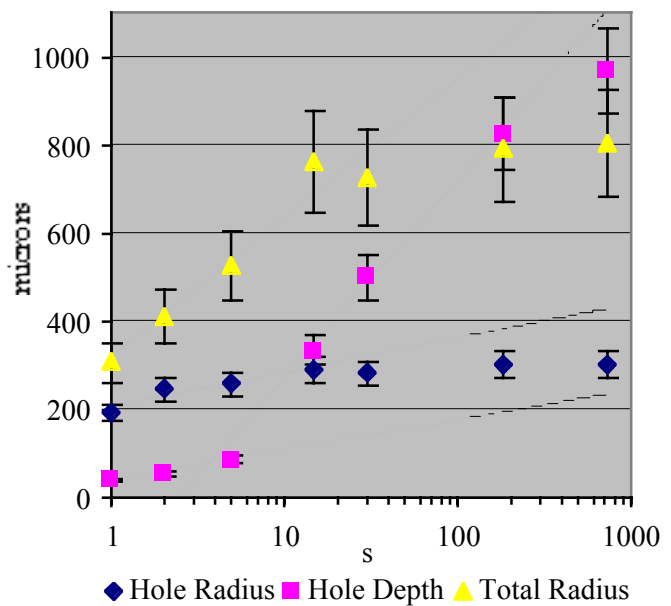


Fig. VII.3 Variation of cavity dimensions and deposition (zone III) radius with duration

Note: For any time of heating, some large (several microns) boron droplets are often found scattered outside the cavity in zone II and III. These are probably drops ejected from boron boiling inside the cavity. For 15s and longer heating, some of them are not covered with onions and tubes (if in zone II), indicating that they have been ejected after the major boron spreading of the first seconds.

I.1.2 Growth of tubes

The main phase for a crown-like growth is when cavity is deep (after 30 s). It is when the atmospheric flux of boron toward zone II is at the lowest. The emergence of the crown is observable from 1 min of heating with an optical binocular microscope. After that, it develops to a maximum height, possibly limited by the quantity of boron available for combination with nitrogen, and by the adherence of matter on target surface. Tube growth possibly occurs down the crown, rather than in the material away from target surface. Structures away from the target are cooler (Possibly near T_{\min}), eventually under boron fusion temperature.

However, tubes are already growing on target surface from the very first second of the heating. They are located on a ring (zone II) for all duration of heating (except for 1s, see I.2.1.). The thickness of this ring (Fig. VII.2) follows remarkably the global temperature warming of the first seconds. Indeed, it follows the same law than cavity dimensions ($\sim 30 \ln t$). After global target warming, zone II continues to increase, although cavity edge has stabilised. This is because temperature gradient on surface gets flatter with deeper cavity, and because of the temperature shift on front surface. (See Chap V-II.5.4.)

I.1.3 Boron melt at zones II/III frontier

A frontier of pure boron, as a solidified melt between zone II and zone III (See Chap. IV-II.2.2.) is only found for durations of 3 min and 12 min. Hence, the formation of this frontier is relatively slow, compared to other processes near impact. This is consistent with the hypothesis of a melt formed by convective drifting of liquid boron on target surface.

I.2. Description of each samples

I.2.1 After 1s (Fig. VII.4-5)

After 1 s, boron is deposited as nano-sized particles on target surface around the cavity. This deposit is not agglomerated as micro-particles, but forms a uniform powder. It is mostly

concentrated at a distance from the cavity, showing that distribution is not simply $1/r$, as could be expected from a stabilised diffusion law. (See Chap VI-I.4.) Hence, the diffusion of boron in atmosphere is still unstable after 1s of heating.

Tubes are strictly absent on target surface, outside cavity. However, some tubes, shorter than $10\ \mu\text{m}$ in length, are present **inside** cavity. Their presence is correlated with some nanometre-sized particles. BN tubes can only growth under dissociation temperature of BN, hence the cavity was cooler than dissociation temperature after 1s. This is probably because of a change of surface reflectivity, after the liquid boron layer formed. (See Chap. V-I.4.) This observation gives a **minimum for the growth speed of starting tubes** $\sim 10\ \mu\text{m/s}$. However, growth speed must be quickly decreasing with tube length. (See Chap. VI-II.2.2.2.)

Note: Inside cavity tubes have not grown after the laser was switched off, during target cooling. Else, similar tubes would be found for longer duration heatings, when they are absent. A growth during target cooling would mean a growth speed one thousand time higher $\sim 10\ \mu\text{m/ms}$. Indeed, the time of vanishing gradient is close to the time of establishing gradient ($\sim 1\ \text{ms}$). There is no thermal inertia of the target after 1s, because it is not yet warmed.

I.2.2 After 2s (Fig. VII.6-7)

After 2 s, and for any longer heating, tubes are absent inside cavity. Dissociation temperature is therefore reached inside the cavity between 1 and 2s. Nano-particles are present on target surface, all around cavity. They start to agglomerate as micro-clusters.

Zone II is present as a thin ring, where fibres emerge from the surface of the deposit. However, this ring is still irregular in thickness and it is absent for some parts of the circumference. The longest tube observed is $\sim 7\ \mu\text{m}$, which is consistent with the previous order of growth speed. **The longest tubes are usually located closer to cavity edge.** Indeed, such tubes have been in the range of temperatures 2350-2700 K for a longer time.

All fibres have a nanometre size particle at the free extremity. The other extremity seems merged to agglomerated micro-clusters. (The thickness of tubes is difficult to interpret because of the W coating before SEM observation.)

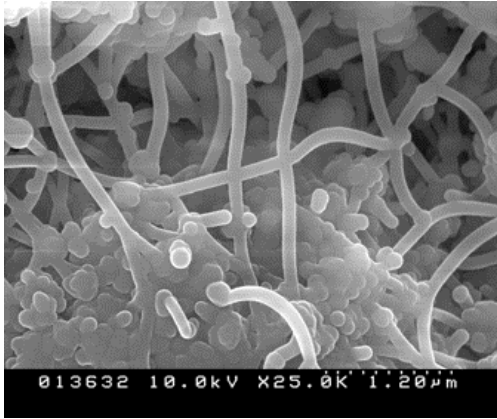


Fig. VII.4 Tubes inside cavity after 1s (SEM) Inside cavity, tube are present together with some nano-spherical particles.

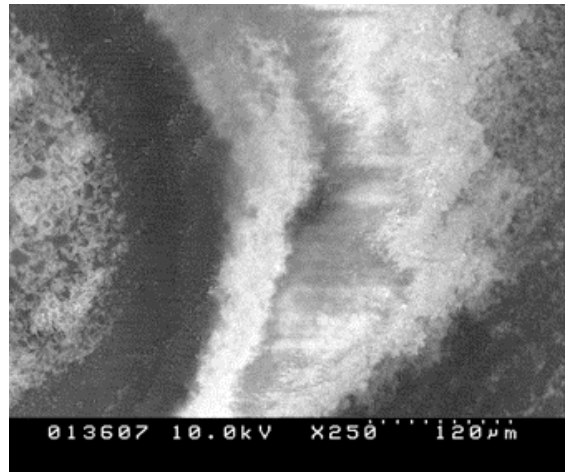


Fig. VII.5 Cavity border after 1s (SEM) Onion powders are mostly at a distance from the cavity because boron diffusion in gas phase is still unstable.

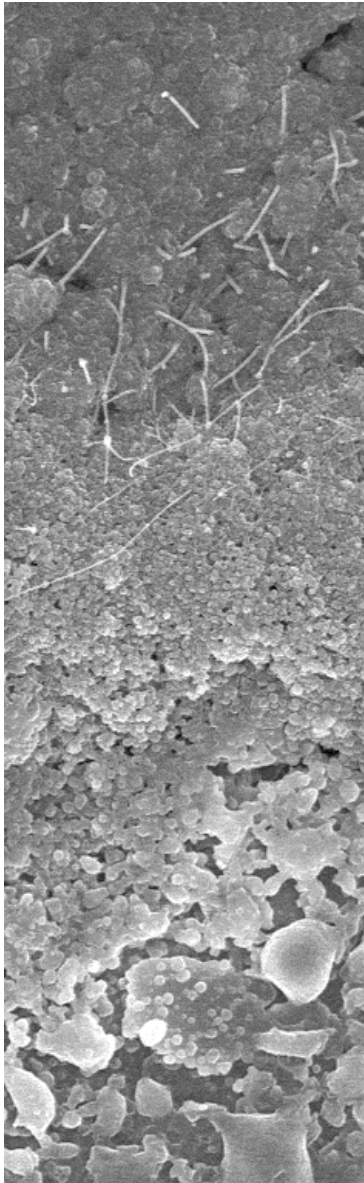


Fig. VII.6. Zone II and cavity edge after 2s (SEM) At that stage, zone II is just forming. Simultaneously, cavity is quickly expanding, decomposing particles at the edge, so that tube lifetime is short. Longest tubes are found close to cavity edge. These tubes have been in the range of temperatures 2350-2700 K for a longer time.

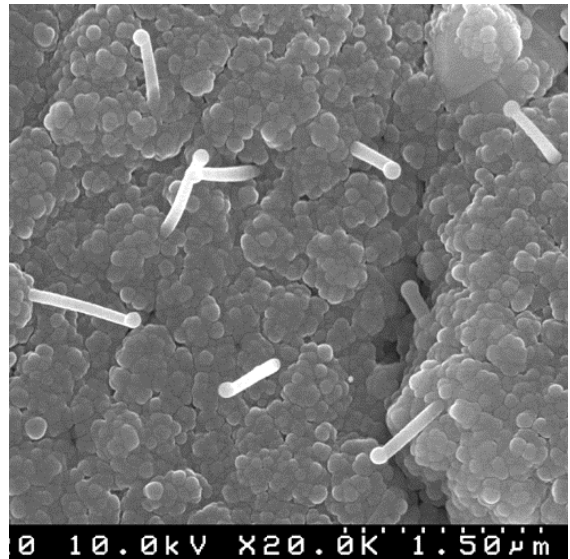


Fig. VII.7 After 2s, first tubes on zone II (SEM) All tubes have a spherical particle at free extremity.

For 2s and any longer heating, up to 15s, cavity edge is complex between first tubes of zone II and last boron drops inside cavity. This region is covered by some spherical particles, typically a few hundreds of nm large, size decreasing from the cavity. As the cavity edge is advancing during cavity formation, BN (h-BN, onions and fibres) decomposes to form these particles.

I.2.3 After 5s, zone II is regular in thickness ($\sim 40 \mu\text{m}$ large) on the whole periphery. A frontier is now clear between zone II and zone III, where nano-particles are agglomerated in micro-clusters. It may be significant that the first micro-clusters are rather cylindrical than spherical.

I.2.4 After 15s, zone II is well developed ($\sim 90 \mu\text{m}$) and supports a dense mat of long fibres (measured up to $20 \mu\text{m}$ long). Again, the longest tubes are found closest to the cavity edge.

I.2.5 After 30s, SEM observations are already very similar to that of the standard experiment (with 3 min of heating). The cavity edge is clearly defined, and tubes start very close to it, because lateral expansion of the cavity was stopped.

Further heating will lead to the vertical emerging of the crown, and of the boron melt between zone II and III.

I.2.6 After 12 min (Longest heating) (Fig. VII.8-11)

After 12 min of heating, boron has been completely evaporated from the cavity, leaving a clean h-BN surface under the beam. This means that the dissociation temperature of BN is no longer reached under the beam and equilibrium temperatures are found inside target. (This equilibrium is made possible by the shape of irradiated surface down cavity: the beam faces a slope, so that the density of heat flux is low.)

The crown has developed up to $\sim 300 \mu\text{m}$ high. This is not much more than for 3 min of heating, but the symmetry of the growth, well developed on the whole periphery, contrasts with shorter heatings. According to the still dim colour of the crown, there is still some boron to recombine with nitrogen after 12 min.

The **longest observed fibre** ($\sim 120 \mu\text{m}$) was found in this sample. (Fig. VII.9) **Tubes also grow inside cavity**. (Fig. VII.11) Tubes are found, along with nano-particles, on most of cavity surface (except for a $200 \mu\text{m}$ large circle corresponding to irradiated zone). After 12

min, boron has vanished from the cavity, so that temperatures are not longer uniform inside cavity. The upper region of the cavity became cooler than dissociation temperature of BN. Some BN/B particles, lately spread on cavity, have developed a shallow mat of nano-tubes on cavity surface.

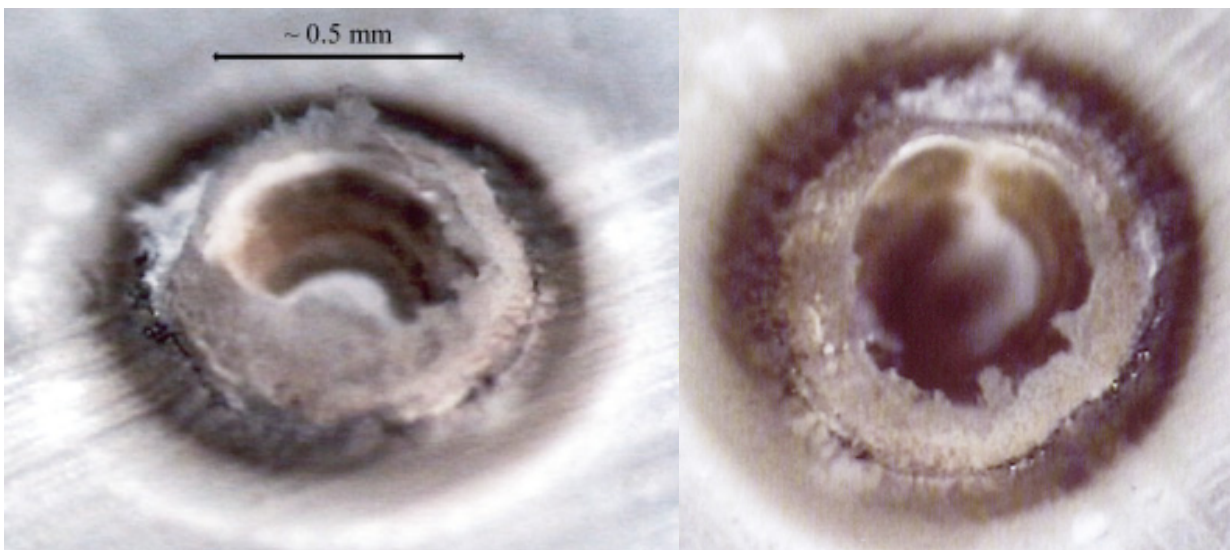


Fig. VII.8 After 12 min of heating (binocular microscope) The crown growth is well developed on whole periphery, and has reached a maximum height. Inside cavity, liquid boron has vanished. Instead, a brownish mat of tube covers the most outer parts of the cavity.

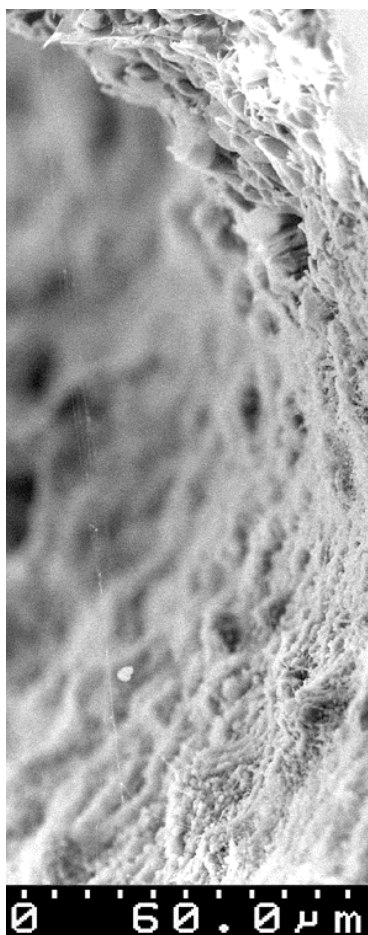


Fig. VII.9 A fibre ~ 120 μm after 12 min. (SEM) This is the longest BN fibre observed. (It is hardly contained in the focal range along its length.)

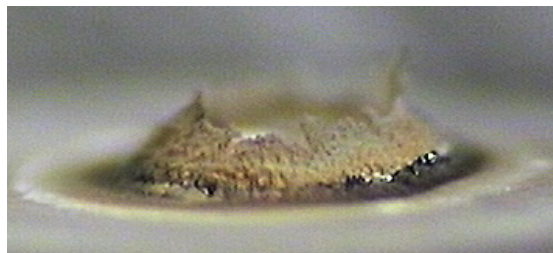


Fig. VII.10 After 12 min of heating (binocular microscope) The crown growth is ~ 300 μm high. The boron melt at frontier II/III is also well developed (especially on the right side of the photo).

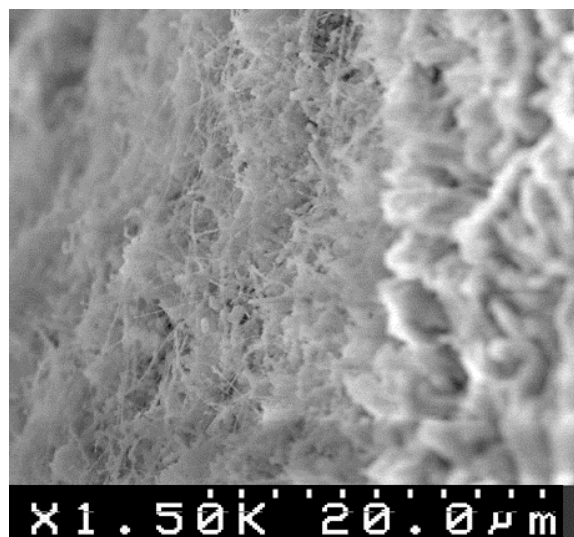


Fig. VII.11 Fibres inside cavity after 12 min of heating (SEM) The drop of temperature, due to the vanishing of liquid boron inside cavity, allow tubes to grow inside cavity. They form a dense but shallow mat. Nano-sized particles are also present.

II. Influence of nitrogen pressure (from 50 to 500 mbar and in vacuum)

Nitrogen pressure influences the experiment drastically. With higher pressure, mean free path in nitrogen gets smaller, so that, deposition do not extend as far from the cavity. On the other hand, nitrogen pressure moderately affects zone II thickness. Indeed, target temperatures are little affected by pressure.

At high resolution, structures are typically thicker for higher pressure. In a binocular microscope, the crown material presents a fibrous texture for higher-pressure samples, different from the powder-like texture of a standard heating.

Deposited boron shows a more complete recombination for higher pressure. Colours around impact are paler. (Fig. VII.12) The flux of nitrogen on the boron rich particles determines their evolution. This increase of recombination affects both particles in atmosphere, and on target surface. Indeed, both zone II and zone III are both paler for higher pressure.

II.1. Effect of nitrogen pressure on structures (HR imaging)

At higher pressure, BN/B onions tend to have a thicker BN shell. An increase of shell thickness may seem natural, considering that the growth speed of a BN shell increases with nitrogen flux. The actual time exposure to nitrogen, for most boron particles may be limited. Particles are first exposed while flying in atmosphere, before deposition. (They accumulate nitrogen only if their boron is liquid.) Then, after collection on target surface, particles are exposed, but quickly covered by other depositing particles. Finally, when the crown rises, uncovered particles may be exposed to nitrogen again.

For higher pressure, if large shells are already formed on BN/B particles before they reached target surface, it may be more difficult for a tube to emerge from the particle. Experimentally, tube structures are very affected by nitrogen pressure, however, it was not possible to say if the ratio fibres/onions is affected by nitrogen pressure. Thin tubes, assembled in ropes, are found at any pressure. However, at higher pressure, most fibres are covered with diverse form of BN material, on their external cylinder. This cover is often an irregular shell of h-BN layers, parallel to the external surface of the fibre. (Fig. VII.16) Alternatively, the cover this often an agglutinated chain of BN(+B) onions half merged along the fibre. (Fig. VII.15)

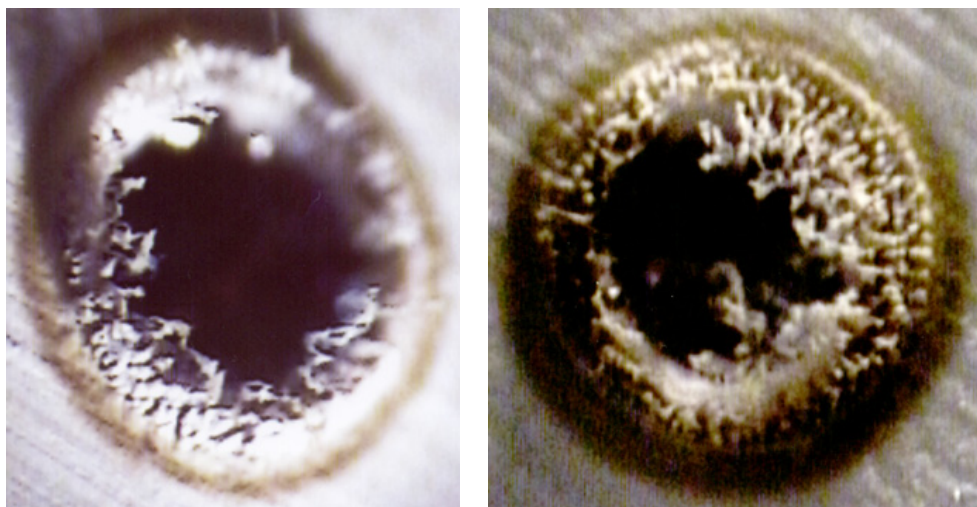


Fig. VII.12 Growth around impact at 500 mb (left) and at 300 mb (right) (binocular optical microscope) With rising pressure, fibres seem to “stick” to each other, causing a fibrous aspect. Products are also paler, indicating a more complete recombination of boron into BN.

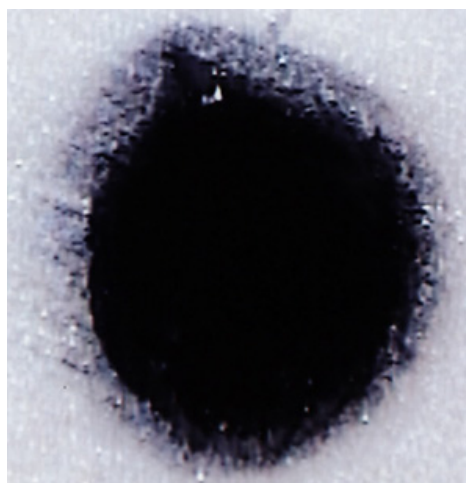


Fig. VII.13 Heating under (pumped) vacuum (binocular optical microscope) No tube are growing. At such pressure, the dissociation temperature of h-BN is low (Fig. I.4). The cavity is very deep and cylindrical.

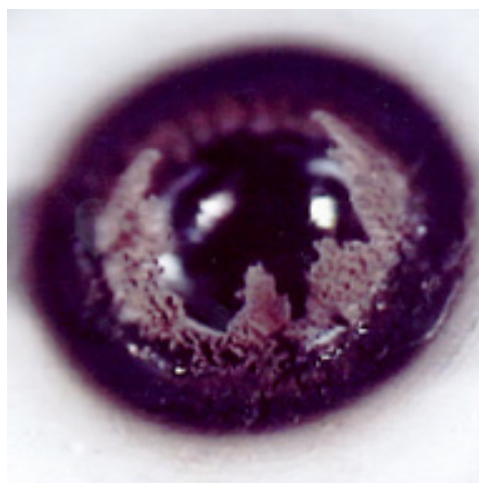


Fig. VII.14 Heating in standard conditions for reference (binocular optical microscope) With pressure of 100 mb. The crown is “powder” looking and globally dark.

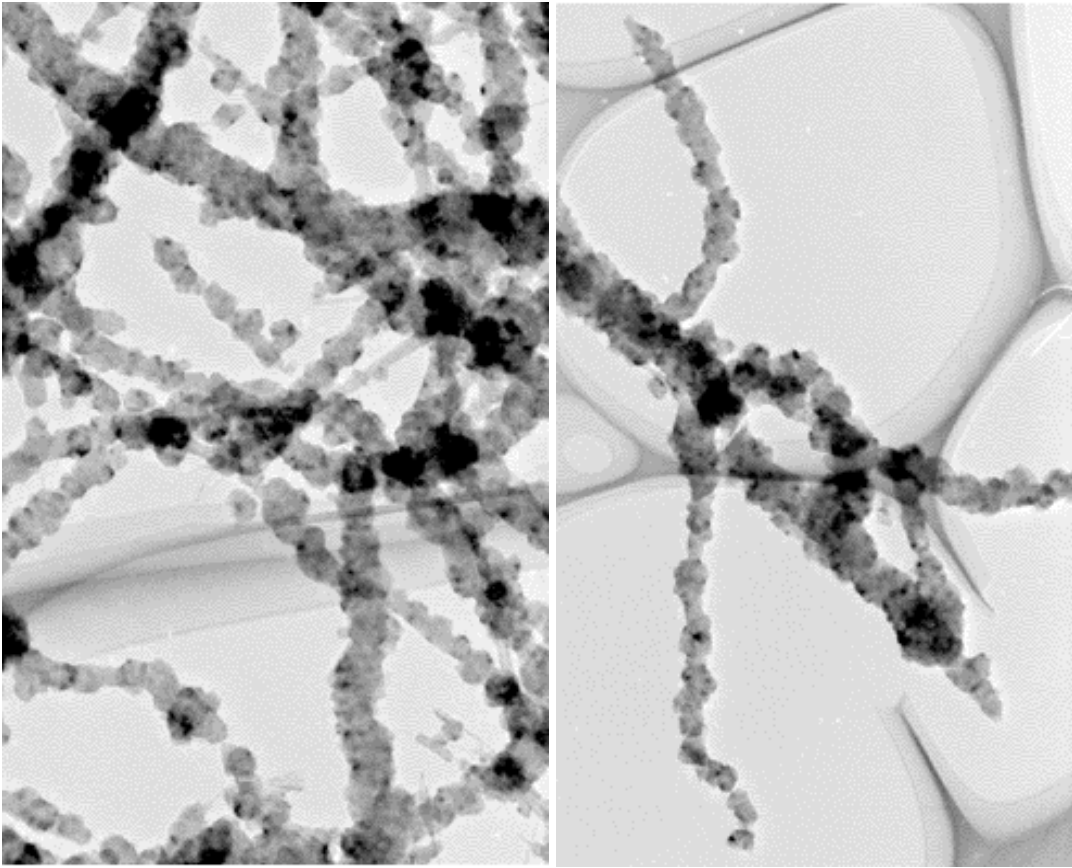


Fig. VII.15 At 500 mb of nitrogen, fibres are often covered with half merged BN/B particles (TEM) The increased thickness of BN shells may favour their merging. It may also inhibit the formation of new tubes.

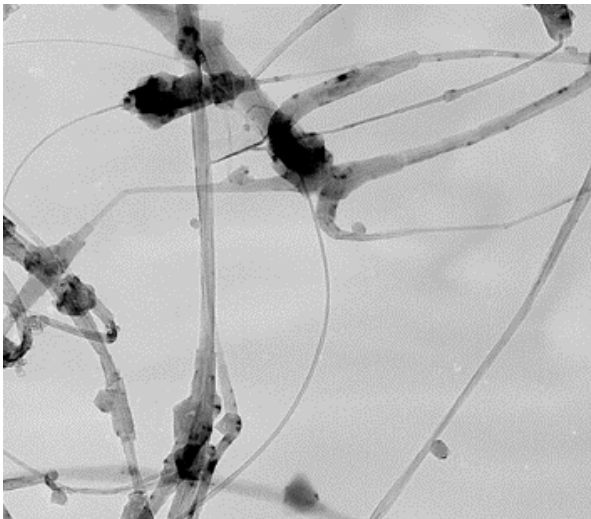


Fig. VII.16 Fibres covered with irregular BN layers for 300 mb of nitrogen (TEM) The BN from merging spherical particles seems to extend along fibre axis, and thickens fibres locally.

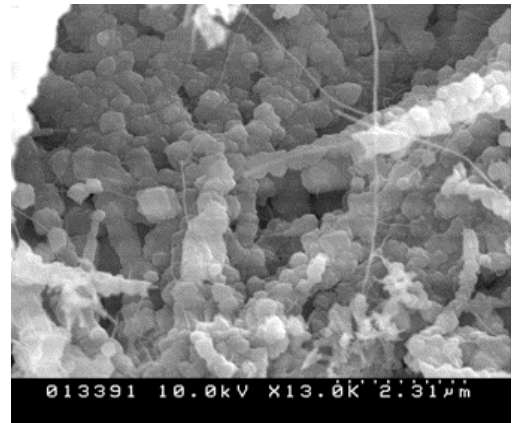


Fig. VII.17 Surface of zone II for 500 mb (SEM) Fibres are agglutinated in a powder of almost pure BN onion, merging to their body.

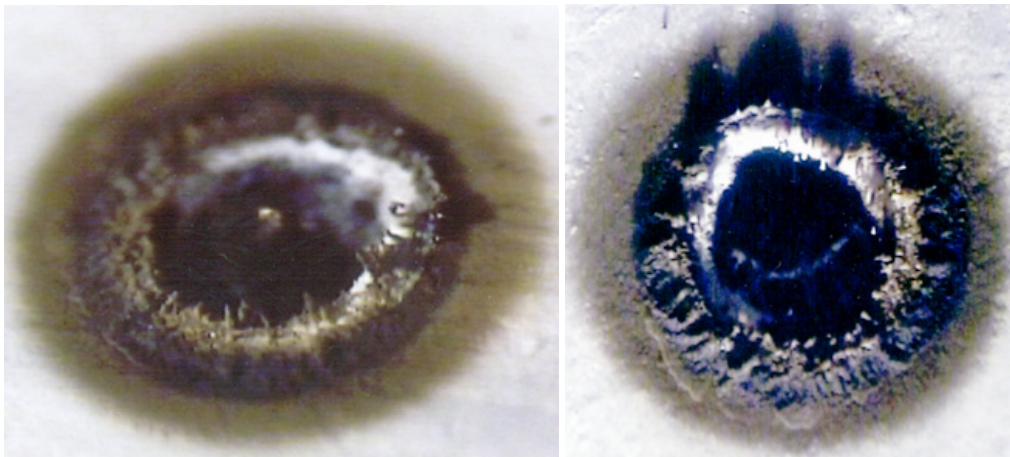


Fig. VII.18 Growth on target surface at 50 W (SEM) The crown growth is very little developed. The product may have a low adherence to the target during experiment, possibly because of little merging between structures.

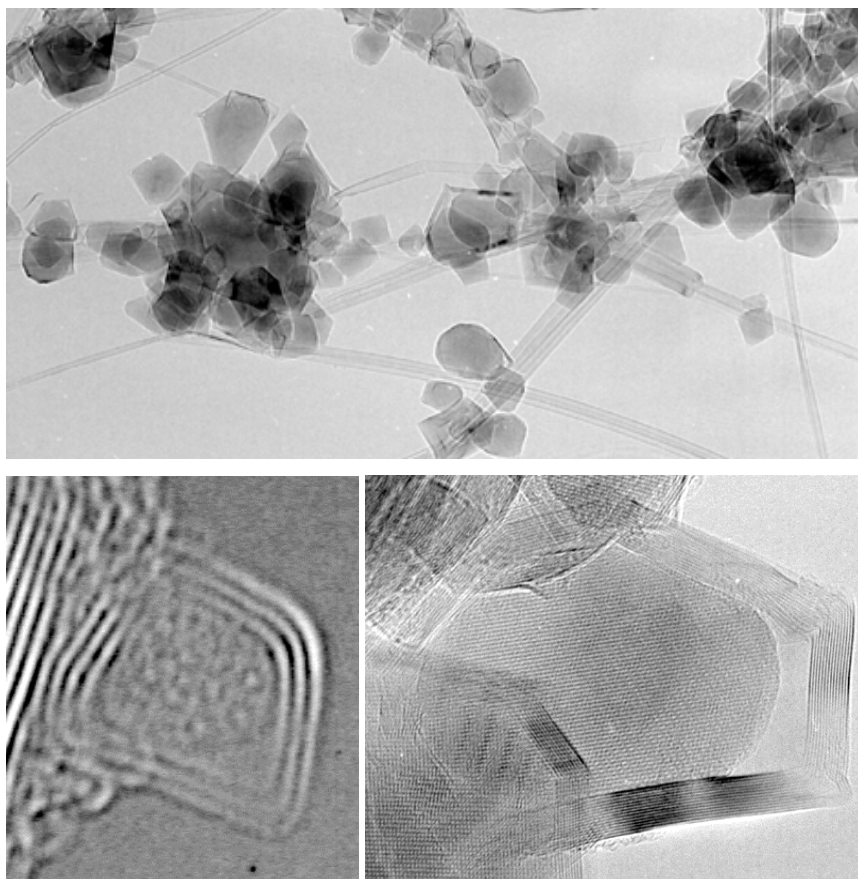


Fig. VII.19 At 50 mb, various structures collected from zone II (at surface of zone II) (TEM) The product contains a majority of BN/B particles with a thin BN shell, although large shells are not completely absent (down, right image).

At 500 mb, this type of agglutination is such that it often only leaves the very extremity of the fibre free. BN/B particles merge on fibre body during heating. Their matter seems to extend along fibres, and eventually form irregular h-BN covers. It is not clear why fibres are more saturated by onions with large BN shells.

At 50mb, a vertical crown is almost absent, although zone II exists. It is possible that the product fell from target while heating because of a low adherence on target. A low adherence may result from little merging of structures with each other. A fallen material was not collected in the chamber.

Under vacuum (10^{-5} mbar, under continuous pumping by an oil diffusion pump), heating produces a simple decomposition of BN. No crown or deposition ring is present around cavity. (Checked by SEM) The cavity is remarkably deep (~ 2.5 mm) because the dissociation temperature of BN decreases quickly with decreasing pressure. The cavity is not conical but almost cylindrical (radius on surface $380 \mu\text{m}$, radius down the cavity $225 \mu\text{m}$). This is due to the absence of liquid boron inside the cavity. (See Chap. V-II.5.3)

II.2. Influence of nitrogen pressure on global geography

Measurements for Fig.VII.20-21:

Pressure (mbar)	Vacuum	50	100 (Ref.)	300	500	Fitting function
Cavity Radius	380	295	300	285	282	$315 / P^{-0.016}$
Cavity depth	2408	927	824	626	626	$1720 / P^{-0.19}$
Total Radius	No	902	790	670	600	$1760 / P^{-0.17}$
Zone II thickness ($\mu\text{m} \pm 10\%$)	No	118	126	160	168	$1.11P + 115$

II.2.1 Zone II thickness and Cavity radius (Fig.VII.20-21)

Thickness of zone II is moderately affected by nitrogen pressure ($\sim 50 \mu\text{m}$ between 50 and 500 mbar on Fig.VII.21). This is consistent with a limited influence atmospheric pressure on target temperature. Most of the expansion is actually gained on the inner edge of the ring, because dissociation temperature of BN is rising with nitrogen pressure. The order of temperature change, as given by the phase diagram (Fig. I.4), for a pressure change from 50 to 500 mb is ~ 150 K. Considering the slope of temperature gradient at cavity edge, as estimated for standard condition ($3 \text{ K} \cdot \mu\text{m}^{-1}$), this correspond to $\sim 50 \mu\text{m}$ of inner edge shift. This fits well with the measurement.

Note: A shrink of same length should be observed for cavity edge, when measurement gives a shorter value ($\sim 20 \mu\text{m}$ between 50 and 500 mbar). However, this value is lost in uncertainties, and the 50 mb value is unreliable.

There may be also other influences of nitrogen pressure on zone II thickness. Pressure slightly influences global target temperature. Also, a shallower cavity may cause a stiffer temperature gradient on front surface. Else, there may be a pressure influence on boron solidification temperature.

It is actually remarkable that the evolution of zone II is opposed to all other dimensions near impact (Fig. VII.20-21), and, in particular, to the deposition of boron around the cavity. One could expect that a decrease of boron deposition zone would reduce the thickness of tube growth zone, but it is not the case.

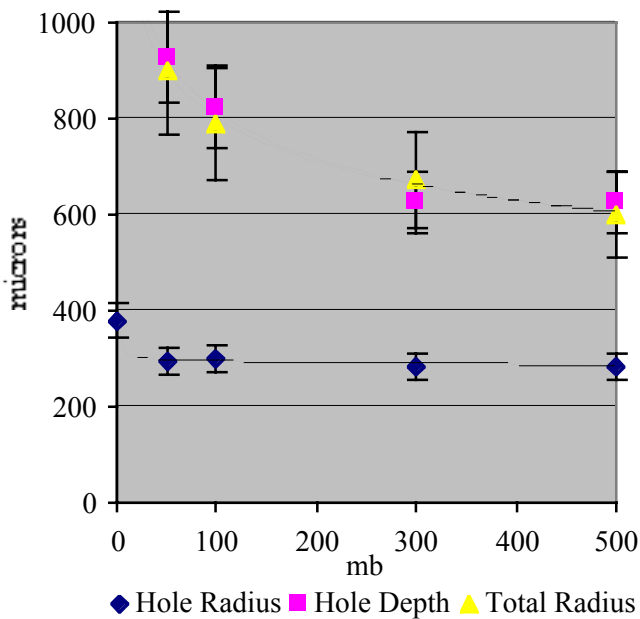


Fig. VII.20 Variation of cavity dimensions and deposition zone (zone III)

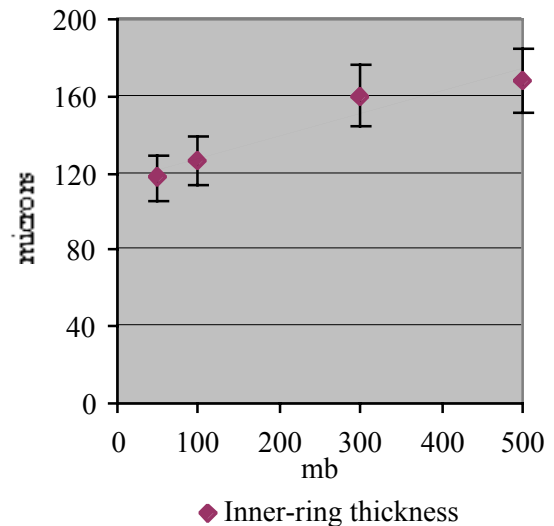


Fig. VII.21 Variation of zone II

II.2.2 Total diameter and cavity depth (Fig. VII.20)

The decreases with pressure, of cavity depth and total deposition radius, are remarkably linear. (Although the measurement uncertainty for total ring deposition is high.) A strict equality of the two quantities is a coincidence, determined by the choice of the standard experiment. Indeed, with different power, or different heating time, the two lengths are different. In the hypothesis of free evaporation, pressure may not affect the boron flux evaporating under the

beam. Hence, boron deposition length is primary dependent on diffusion coefficient in nitrogen gas. Diffusion length is roughly proportional to $D^{1/2}$. D is roughly proportional to mean free path in nitrogen, and to the inverse of the pressure. Hence deposition should ideally vary as $P^{-1/2}$. (See Chap. VI-I.4) This is similar to the observed function, considering the high degree of uncertainty.

Cavity depth, like cavity radius, is affected by the increase of dissociation temperature with pressure. For the case of vacuum (10^{-5} mb) experiment, the decrease of dissociation temperature with standard case is expected as high as 1000 K. (From phase diagram.) Considering the estimated temperature gradient for standard conditions, this correspond to ~ 1500 μm of additional depth. This fits well the experimental value ($2408-824=1584$ μm). However, from 50 to 500 mb, with the same estimation, depth should decrease by less than 50 μm . As the depth is actually decreased by ~ 300 μm , this is not the dominant influence.

Instead, during cavity drilling, a temporary equilibrium of cavity dimensions may be reached when the heat transmitted inside cavity by diffusion through the gas phase has reached a maximum. This maximum is obtained when cavity depth equals diffusion length of boron in nitrogen, hence deposition radius. This can explain the equality of the two quantities. (See also Chap V.II.5.3)

Note: This is only true as long as there is enough liquid boron inside cavity. After that, drilling should continue until temperature equilibrium is found, to a depth that little depends on pressure. If deposition radius is larger than final equilibrated depth, a temporary minimum should not be found before final stabilisation. This is possibly the case for vacuum (10^{-5} mb) and for He experiments.

II.2.3 Frontier between zone II and III

Experimentally, there is no observable boron melt between zone II and III, for 300 and 500 mb. Powders deposited on zone II are particles with larger BN shells, so that, liquid boron may not be easily released from their shell.

III. influence of laser power (from 40 to 80 W)

Measurements for Fig. VII.25-26:

Power (W)	40	50	60	70 (Ref.)	80	60 %
Cavity radius	No	190 - 280	282	300	322	37 %
Cavity Depth	No	< 214	531	824	1061	400 %
Total Radius	No	610 - 690	705	790	862	32 %
Zone II thickness ($\mu\text{m} \pm 10\%$)	No	0 - 60	60	126	200	560 %

Laser power has a clear influence on zone dimensions near impact. All dimensions increase almost linearly with laser power, which is mainly due to the increase of temperature in the target. On the other hand, laser power has no obviously observable influence on structures. Material from the crown, observed by TEM for any samples (except 40 W), featured the same structures of fibres and nano-particles, in the same proportions. (HR images used in chapter IV were shown with no distinction of laser power.)

Dissociation temperature was reached on target surface for laser power of 50 W and higher, but not for 40 W. (Fig. VII.22-24) SEM observations of the 40 W sample revealed the total absence of nano-structured matter, despite a heating close to dissociation temperature. (h-BN platelets were left unaffected by the beam.) By consequence, the growth of tubes and other nano-particles does not occur directly from h-BN platelet under nitrogen atmosphere, even at temperatures close to dissociation.

Note: The temperature decrease was obtained by lowering the pressure of the gas-mix in the laser. However, to get under 60W, it was necessary to also misalign the laser semi-reflecting mirror. As a result, at 50W, the beam was not Gaussian, and the impact was split in two zones of high temperature (separated by $\sim 250 \mu\text{m}$) In that case, zone II thickness is not uniform around cavity periphery. Also, the minimum value to reach dissociation is not that measured here ($\sim 40 - 50 \text{ W}$), but $\sim 30 \text{ W}$. (See Chap. II.)

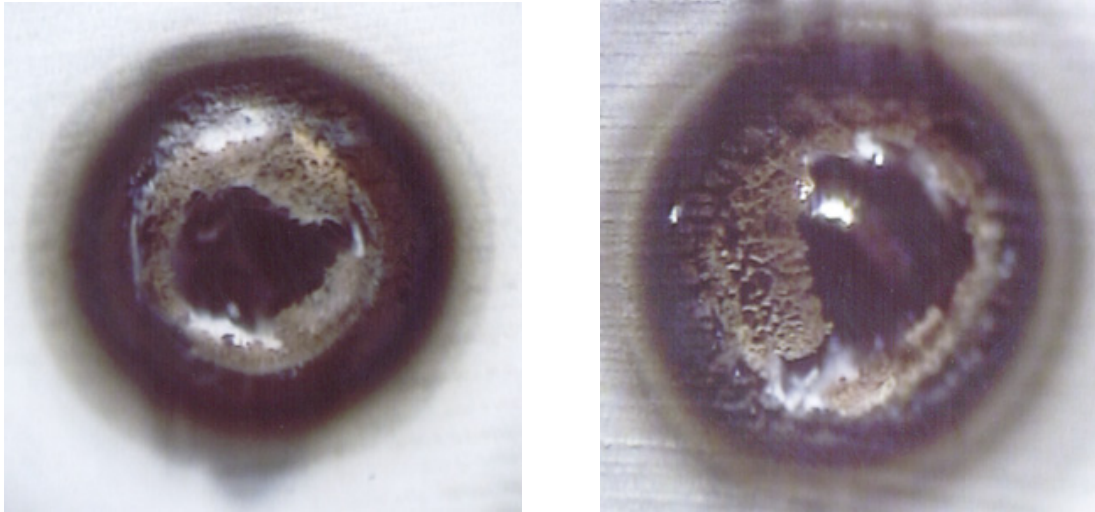


Fig. VII.22 Growth around impact for 60 (left) and 80 W (right) (binocular optical microscope)

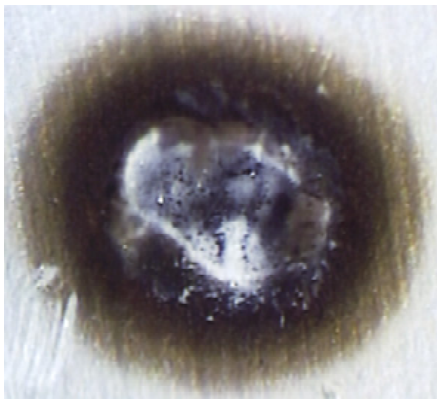


Fig. VII.23 For 50 W Impact is not circular because the beam is little Gaussian.



Fig. VII.24 For 40 W, dissociation temperature is not reached on the target. No nano-structure form.

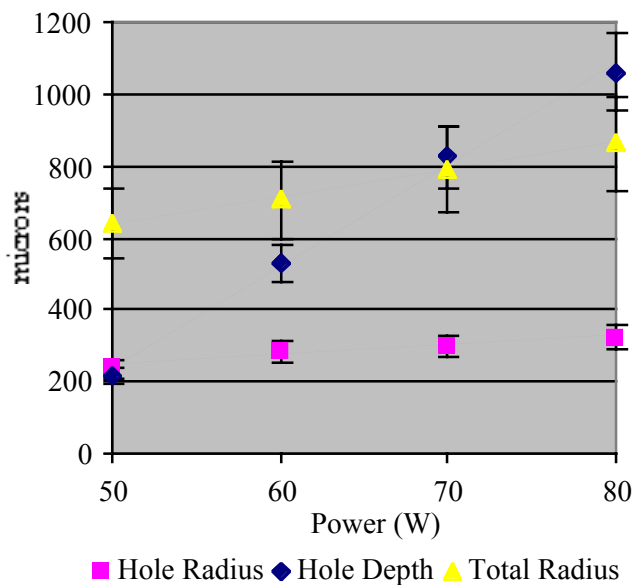


Fig. VII.25 Variation of cavity dimensions and deposition zone (zone III) with laser power

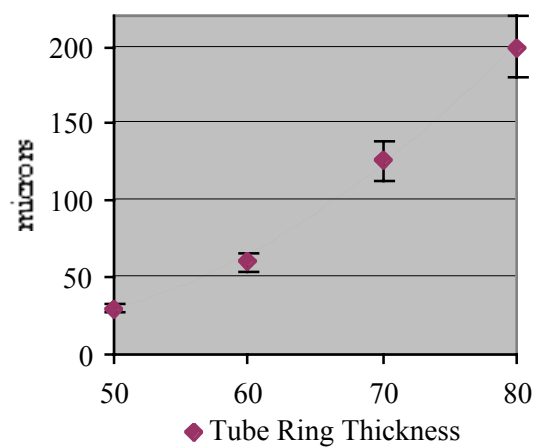


Fig. VII.26 Variation of zone II with laser power

III.1. Cavity radius and total deposition zone (Fig. VII.25)

Cavity radius and total deposition radius (zone III) both expands of about 35%, for 60 % of power increase. At constant pressure, the total deposition radius of boron is not affected by mean free path in nitrogen atmosphere. On the other hand, it depends on boron evaporation flux under the beam. Similarly, cavity radius depends on the radial heat flux in the target

Boron evaporation flux may be more or less proportional to laser power (hence it may increase by 60 %). Similarly, the radial heat flux in the target is more or less proportional to laser power. Boron spreading on target, and temperature on surface follow similar diffusion laws. Fluxes are given by $J \sim \text{Power}/r^2$ and, gradients by n_B (or T) $\sim \text{Power}/r$. For a given temperature (or concentration), cavity radius (or boron deposition length) should be roughly proportional to laser power. Measurement gives lower values (32 and 37 %) than 60%, but of a similar order.

III.2. Cavity depth and zone II thickness (Fig. VII.25-26)

Here cavity depth cannot vary with pressure (like in II.2.2.). A intermediate cavity stabilisation may be expected equal for each samples. However, cavity depth is also determined by laser power through the temperature of the target (as is cavity radius). (We suppose that there is no influence of the increasing boron evaporation with laser power.)

Cavity depth rises linearly with power, at a very high rate (400 %) which can not be accounted with the previous order of variation for cavity radius. Indeed, a deeper cavity does not cause a decrease of incident power/surface by $1/r^2$ down cavity. Hence there is no linearity of depth with P . Instead, a decrease of the incident energy per surface is caused by an angle of the irradiated surface and/or by diffusion of the heat flux in a larger solid angle. This should give a much slower variation with r .

Similarly, zone II thickness drastically increases with laser power (560 %). As long as boron is present under the beam, temperatures may be about constant in the cavity. (Because of heat transfers by diffusion in gas phase, inside cavity.) The increase of zone II thickness is mainly caused by a decrease of radial heat flux. Radial heat flux is decreased as the inverse of cavity surface, hence roughly as cavity depth.

IV. Heating in inert gas (He 100 mb)

For an experiment under He, the global geography of the target is different from that of a standard experiment in nitrogen, but the separation in three zones is identical. At high resolution, similar structures are found, although they are poor in nitrogen. Tubes are short and grow in low quantities.

Even under He, some nitrogen is present in the atmosphere. Indeed, the h-BN dissociated in the cavity is released in the atmosphere. From the size of the cavity, we expect a partial pressure $\sim 10^{-3}$ mbar:

$$P_{N_2} = \frac{N}{2} \cdot \frac{kT}{V} \quad (N = \text{number of dissociated BN pairs})$$

h-BN density, $\rho = 2.08 \text{ g/cm}^3$
 Cavity volume, $v \sim (0.05 \text{ cm})^3 = 1.25 \cdot 10^{-4} \text{ cm}^3$
 Chamber volume, $V = (0.5 \text{ m})^3 = 1.25 \cdot 10^{-1} \text{ m}^3$
 $T_{\text{amb}} = 293 \text{ K}$
 $k = 1.38 \cdot 10^{-23} \text{ J/K}^{-1}$
 Atomic weight, $Z_N = 14,01 \text{ Amu}$,
 $Z_B = 10,81 \text{ Amu}$
 With $\text{Amu} = 1.66 \cdot 10^{-24} \text{ g}$

$$\text{with, } N = \frac{\text{hollowed mass}}{\text{mass of one BN pair}} = \frac{\rho \cdot v}{(Z_N + Z_B) \cdot \text{Amu}} \sim 6.3 \cdot 10^{16}$$

This is very small compared to a helium pressure of 100 mb. The mean free path of a hypothetical B_2 molecule in such a residual atmosphere is ~ 30 cm. (See Chap. VI-I.1) Nitrogen can not influence particles diffusing in atmosphere. Therefore, only pure boron particles are spread on target around cavity. However, once collected by target surface, the deposit in contact with the atmosphere, sees a non-negligible flux of nitrogen.

IV.1. Geography on target for a heating in He

A zone equivalent to zone II is visible with a binocular microscope as a reddish zone. (Fig. VII.27) A macroscopic crown-like growth does not emerge vertically because tube growth is very limited. However, tubes grow on target surface. **Zone II thickness is equal to that of standard conditions.** (Fig. VII.28) Indeed, gas composition should not affect much target temperatures. (This is one of the strongest evidence that zone II is determined by a temperature range and not by a chemical condition.)

Cavity diameter and cavity depth, are also little different from a standard experiment. Target temperature is little affected by gas composition, and BN dissociation temperature in He may be close to that in nitrogen atmosphere, for same pressure. (Not obvious.)

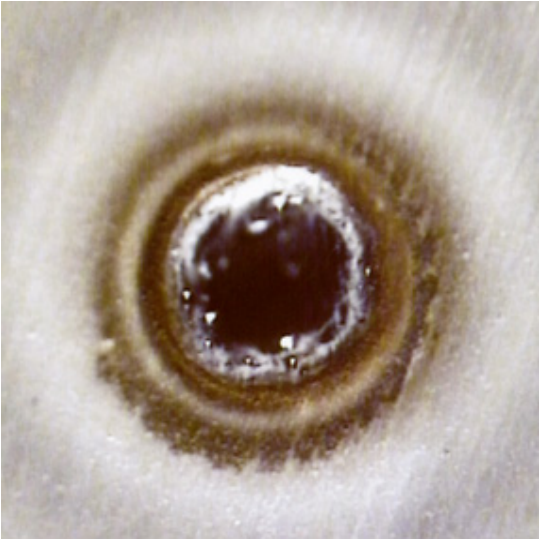
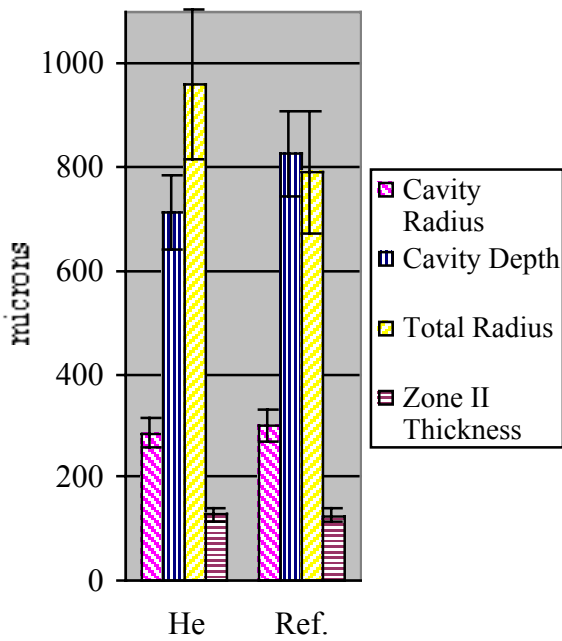


Fig. VII.27 Impact after heating in Helium. Boron deposit around the cavity is little recombined and shallow. Colours are more yellow-red than brown. (Boron nano-particles are not deposited as a $1/r$ concentration around cavity, although the reason is not clear.)



	He	Ref.
Cavity Radius	285	300
Cavity Depth	713	824
Total Radius	960	790
Zone II thickness ($\mu\text{m} \pm 10\%$)	127	126

Fig. VII.28 Comparison of dimension around impact for heating in helium and heating in standard conditions (in nitrogen)

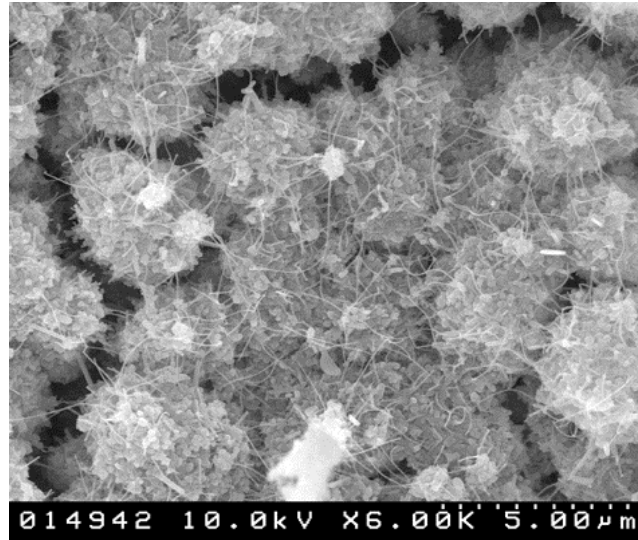


Fig. VII.29 Surface of zone II after heating in He (SEM) Target surface is covered by a shallow mat of fibres.

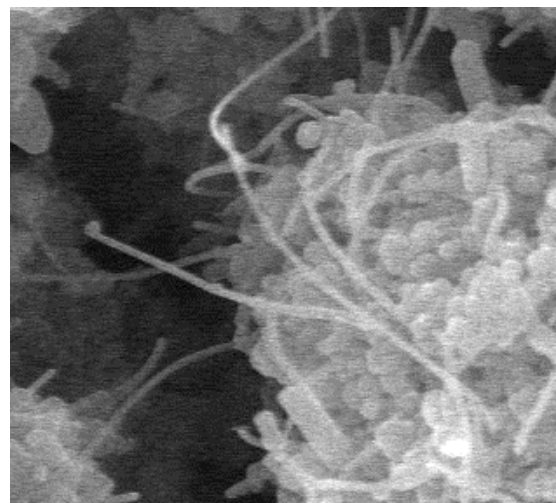


Fig. VII.30 A detail of upper image Many tubes have a spherical particle at free extremity.

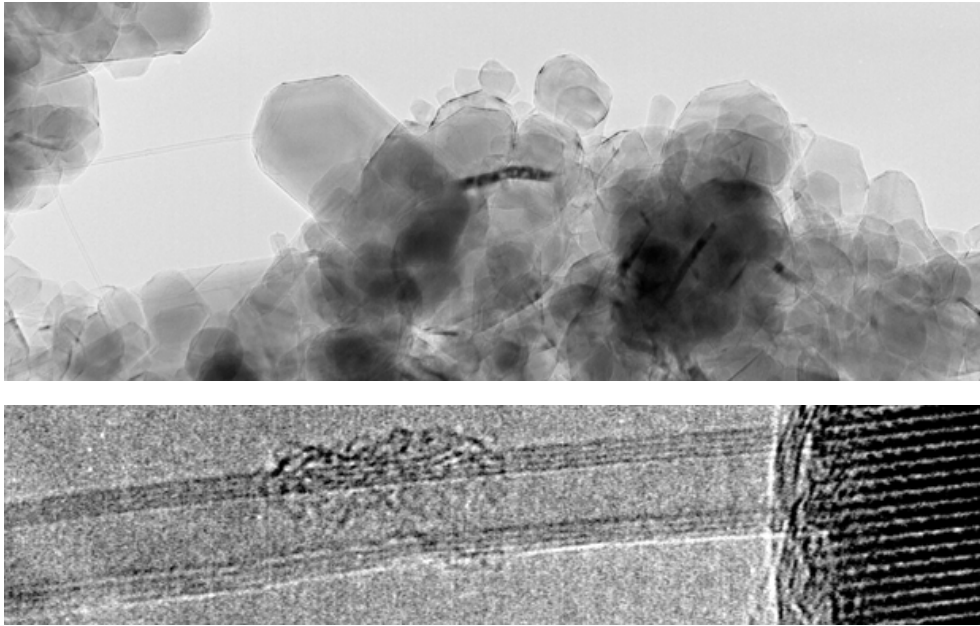


Fig. VII.31 Tubes and nano-particles after a heating in He (TEM) Morphologies are very similar to that of heating in nitrogen. Because powders were collected at target surface for TEM, only a few tubes could be observed.

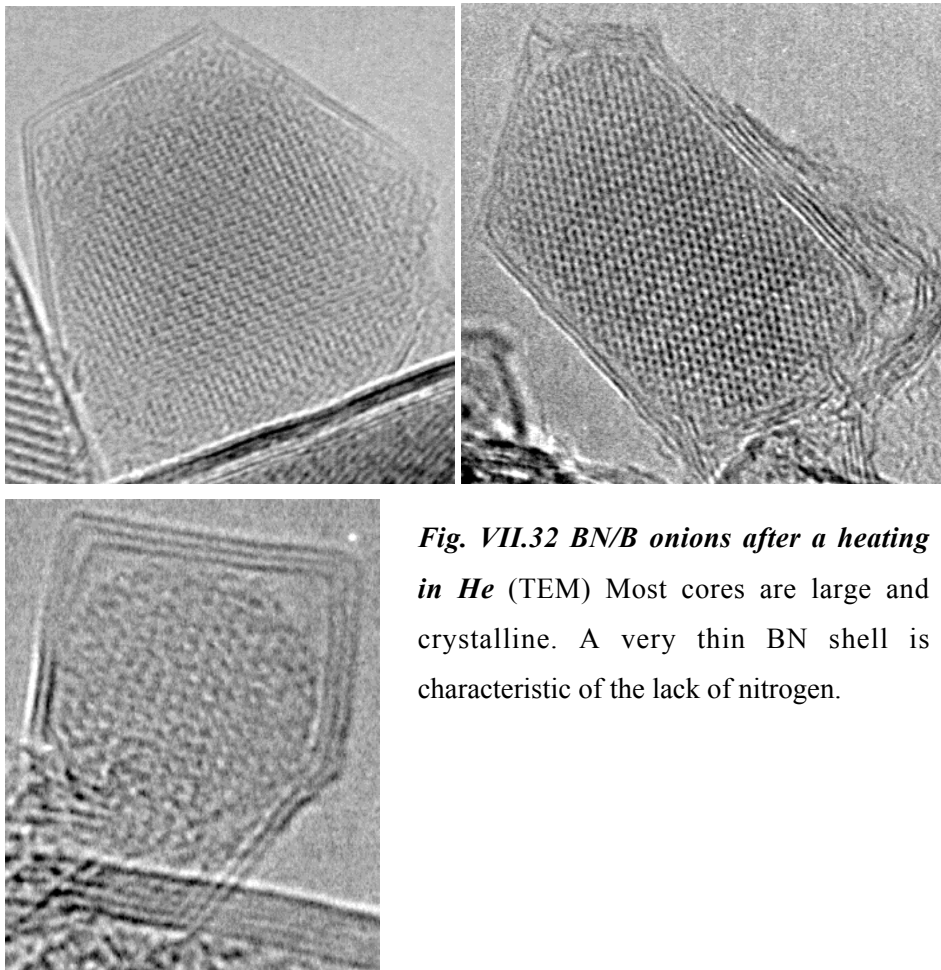


Fig. VII.32 BN/B onions after a heating in He (TEM) Most cores are large and crystalline. A very thin BN shell is characteristic of the lack of nitrogen.

The total deposition diameter (zone III) as observed by optical microscope is comparable to that of a nitrogen atmosphere. As boron distribution of particles over the surface is roughly proportional to the square root of the mean free path, boron particles should fly about $\sqrt{2}$ further in He than in N₂ at 100 mb. (See Chap. VI-I.1.) The total deposition diameter in He is actually equal to the total deposition diameter in 50 mb of nitrogen. Indeed, those two atmosphere have the same mean free path ($\sim 6 \mu\text{m}$) for boron molecules.

IV.2. High resolution observations

Tubes cover the surface of zone II as a shallow mat. They are shorter ($< 3 \mu\text{m}$) than for a heating in nitrogen. They often have a spherical particle at free extremity. On zone III, an agglutination of collected particles in micro-cluster, with size decreasing with distance from the cavity, is very similar to the standard case.

TEM observations were performed on powders roughly collected on the border of the cavity (so that it the origin of the observed structures is uncertain). Most of this material is composed of boron rich nano-particles, with a large crystalline boron core, covered with few layers of BN. (Fig. VII.31-32) Also, many BN shells are found empty, thin and very disordered. Possibility, the boron core has been ejected from their cavity, after shell rupture. (There is also minority of large BN shells with no boron core.) Some short tubes were present in this product, thin or not. An assembling in ropes could not be made clear, but the number of tubes observed was not enough for statistical validity.

V. Surface influence

The quantity of product finally produced and the shape of the crown growth is conditioned by the adherence of powders on target surface. Boron deposit, which is mainly spread on target during the first seconds ($\sim 15\text{s}$) of the heating should ideally adhere well. If this is not the case, tubes can little develop on deposit surface, after the spreading phase.

This is problematic because, during boron spreading, target temperatures are quickly rising, so that several phenomena may eject away boron deposit. Local thermal expansions in the target may cause h-BN platelet to effuse, especially in hottest zone. Effusion of gaseous impurities from inside target can have the same effect.

This effect is problematic if h-BN platelets in the target are not very dense. In that case, platelets near front surface will be easily ejected when temperature rises. This is the case when the front surface of the target has been polished with sandpaper before heating. On final surface little product is obtained. (Fig. VII.33) By contrast, in the reference experiment, the h-BN surface result from a SiC rotating saw which leaves a relatively smooth surface.

Also, this phenomenon is a possible explanation to the importance of doing a thermal shock before heating. (Target is heated with a defocused beam under vacuum for a ~ 5 seconds.) With a thermal shock, the final quantity of product is higher, the growth along the periphery of the cavity is more even, and its shape is reproducible from one experiment to another. This treatment probably prepares front surface to temperature rise. It may wash h-BN platelets poorly linked to front surface. It may also free the target from impurities near surface. Finally, it may make front surface more dense. Although physical origin is not clear, the value of ~ 5 s, which was found empirically, is to be compared with the time for global warming of the target (~ 15 s). (The out-gazing procedure, which is identical except for its duration (~ 5 min), does not produce the same effect.)



Fig. VII.33 *The final impact, when target front surface has been polished by rough sand paper*

Note: Practically, heating with a vertical beam, incident on up surface of the target could improve the adherence of structures on the target.

General conclusions of the study

1. A local heating, with a non-ablative laser beam, on a BN target, in low nitrogen pressure, produces a macroscopic growth of BN nano-tubes on target surface. Tubes grow on a ring around impact cavity, forming a crown perpendicular to target surface.

2. This is an efficient production method because:

- Tubes are extremely long (measured up to 120 microns) mostly thin (, although no single walled tube is observed,) and self-assembled in ropes. In the tubes, BN is stoichiometric, and well crystallised.
- Original BN/B nano-sized particles are also produced. They are faceted boron nitride onions, often containing a boron nano-crystal inside cavity.
- Procedure is simple and low cost. Quantity produced may be extended for commercial purposes, by scanning the laser beam (or the target), using a higher laser power, collecting material falling from the target,...

3. Boron recombines with nitrogen if and only if boron is liquid. (This is not specific to nano-sized particles.)

4. Tube growth is conditioned by the transformation of spherical boron-rich nano-particles under the simultaneous effect of temperature and recombination:

- Spherical boron rich nano-particles are spread around impact cavity, after evaporation and condensation of boron in the gas phase.
- Where boron is liquid, the particles recombine with nitrogen atmosphere, forming BN shells. During this process, some spherical nano-particles evolve toward tubular extrusions.

5. Axial extension is proposed to be driven by the temperature decrease, due to the formation of a temperature gradient along tube axis:

- The gradient is estimated in the order of 200 K for a few tens of microns.

- The growth speed of tubes is expected and measured quickly decreasing with tube length. A minimum value at start is 10 $\mu\text{m/s}$.

Some proposals for further Developments

Although the global influence of temperature in tube growth was described, a description of the local processes of growth, in tubes and in ropes is not completed yet. It is necessary to improve especially the understanding of:

- The dynamic of recombination, and its eventual influence on tube growth.
- The formation of ropes rather than individual tubes.
- The eventual feeding in boron by small molecules from the gas phase and its influence on tube growth.

More in-depth TEM studies and electron diffraction characterisation can bring a better understanding, but practical difficulties are encountered with electron charging effect and weak diffraction patterns. A further study of nitrogen pressure influence for short time of heating could help. It is also necessary to undertake a quantitative estimation of matter diffusion along a tube due to its temperature gradient.

Different variations of the experimental procedure can be undertaken:

- The same heating, but on a pure boron target (under nitrogen atmosphere). Similar results should be obtained, although experimental conditions have to be adapted. (See next page.)
- The same heating, but on a graphite target. This may or may not give the same result. A slightly higher laser power is necessary. (See next page.)
- Heating a deposit of boron rich particle between 2350 K and 2700 K, but without any boron vapours. If tubes grow from the deposit, then the flux of boron from atmosphere does not influence tube growth.
- Changing the uniformity of the heating (by changing the morphology of the target, for instance). This should influence temperature gradient along tubes, and hence possibly their growth.

Heating a pure boron target and a graphite target

(unfinished study)

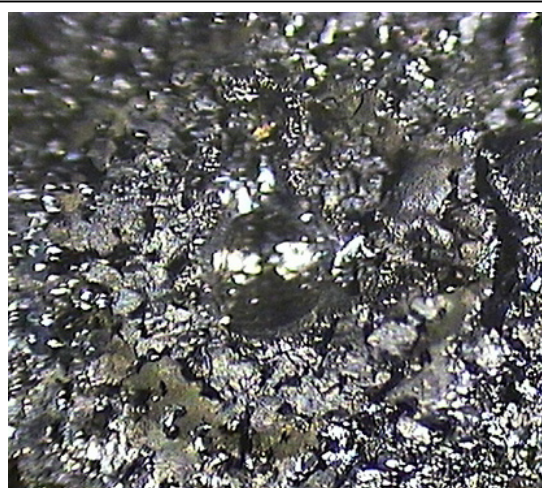
Experimental

Experiments with graphite and amorphous boron target were tried, using conditions as close to that of a standard experiment as possible. The boron target was a piece of solidified boron, with irregular shape (~ 8 mm large). The graphite target was prepared from a graphite rod, with the same procedure as used for a h-BN target. Both targets were out-gazed, and thermally shocked.

Boron

A boron target may give the same results than a h-BN target, according to the mechanisms described before. However, practically, the deposition of the boron rich particles on front surface may be problematic. The experimental procedure is still to be improved at present.

After heating in standard conditions, a cavity was left on target surface, at impact. The formation of a cavity could be due only to a local melting, without any evaporation of boron. However, there is a thin green-looking deposit



Impact on a pure boron target. A greenish ring is present around impact cavity.

around impact. It is mainly located at is some distance from the cavity, on a ring. This product is too thin to be collected for TEM. A SEM observation could not yet be undertaken because the size of the target prevents to use a TEM-type sample holder.

The most probable conclusion at present is that, boron is evaporated, condense and combine with N_2 atmosphere near irradiated zone. However, firstly, the supporting surface of zone II is expected to be liquid. Hence the deposit on its top may be unstable. Secondly, the adherence of the deposit on a solid boron surface may be poor.

Graphite

It is not obvious if a graphite target should produce a growth similar to what is obtained for h-BN, although it is possible. (See final discussion) The problem of supporting surface should not be more cumbersome for graphite than for h-BN. A tube growth as a limited ring should not be observed, because there is no constraint of recombination in the case of carbon.

Practically, for graphite, the sublimation temperature was not reached at impact on surface at 70 W. Irradiated zone was left unchanged. Indeed, a rough estimation in chapter II, showed that laser power should be higher than 70 W to reach sublimation in the case of graphite. (Chap II-IV)

No conclusion can yet be drawn for graphite, except for the fact that graphite do not form any nano-structured particle at these temperature, although the maximum temperature was close to sublimation temperature. This experiment should be undertaken again with a higher power laser.

Note: A similar study [6.3.6] has been undertaken, but in conditions such that the laser beam was ablative for the target. Tubes were collected away from target.

Are the present conclusion on mechanism extendable to carbon (and other diatomic material), and all synthesis method? (Free and opened discussion)

BN and carbon have different properties at high temperature and low pressure. As a diatomic material, BN dissociates, when carbon sublimates. Therefore, the hypothesis of a “shared” growth process is not obvious. However, the similarity of the many synthesis methods, favours the hypothesis of a similar growth process. For both materials, synthesis methods can be divided in two, slow CVD methods, at low temperatures (~ 1000 K), and violent methods, where temperature is up to an isotropic phase of the material. With CVD methods, long and thick tubes are formed, without any other morphology. On the opposite, with fast high temperature methods, like ablation or arc discharge methods, tubular and spherical morphologies are simultaneously synthesised. Tubes may be very thin, and tend to assemble in ropes, but they are usually shorter than for CVD methods. (The present method clearly belongs to fast-type methods.)

Condensation of spherical particles in gas phase

In fast methods, temperature rises up to the vapour phase, so that, nano-spherical particles are formed after vapour condensation in cool atmosphere, and onions are found “spread” in the reactor. In the case of CVD methods, temperatures do not allow such vapours, hence the formation of nano-sized spheres. However, the use of “template” surfaces, probably cause the accumulation of carbon atoms as nano-dots on surface. This is typically an accumulation on metallic nano-particles because of their reactivity with carbon. Alternatively, metallic particles flying in atmosphere may be accumulating carbon atoms, helped both by their reactivity and by their large cross-section.

For surface energy consideration carbon particles will develop graphite-type layers in the external shell. Such structuration is made easier by high temperatures, because temperature helps overtaking energy barriers. Similarly, a boron particle combining with nitrogen will develop h-BN layers as an external shell. The combination of B and N has no natural equivalent in carbon, however, we have seen that this combination may be independent of the formation of the structure itself. (In the present experiments, recombination conditions tube growth, but may not play any role in the kinetic of growth itself.)

Such nano-sized particles may be the origin of tube growth if they further evolve toward tubes. Indeed, it is remarkable that, in fast methods, tubes are always produced together with spherical morphologies. On the opposite, the production of spherical particles alone without tubes was reported ([4.7] for instance). Incidentally, for the arc discharge method, it has been observed that tubes rather grow on the cathode electrode. Indeed ionised anions mostly have a negative charge, so that they may stick on the cathode, where they can later develop a tube.

Can tube grow due to the non-uniformity of temperatures?

In the present work, we suggested that tube growth corresponds to the formation of a temperature gradient along tube axis. This concept may be extended to all methods, without distinction of material. However, it requires that one extremity of the tube is kept at a high temperature and, that the rest of the structure is able to release more heat than its gains. Estimations of Chap. VI-II.1 typically apply to a particle on a hot surface. For instance, it is clearly compatible with an arc discharge method, where electrodes are hot surfaces.

If an additional oven heating, and/or a flowing carrier gas are used, like in CVD or ablation methods, present estimations of the temperature gradient should be corrected. However, in the case of the ablation/oven methods many authors have suggested that tubes grow in plasma and not on target surfaces. In this hypothesis, a gradient may not occur along a growing tube. However, the presence of a metal catalyst at the extremity of a tube can induce a non-uniformity of temperatures along its axis, even if the tube has no physical contact with a hot surface. Also, it should be reminded that there has not yet been a clear experimental proof of a growth in plasma for the ablation method. (See [3.1.13] for a study of the laser plume.) It is still possible that tubes develop on target surfaces near impact, but are ejected from target under the ablation effect.

Finally, if a temperature gradient is the motor of the growth, the stiffer the gradient, the faster should be the growth. (See Chap. VI-II.2.2.2.) Tubes grown in flat gradients (At $T_S = 1000$ K, $\Delta T \sim 20$ K), will be slower to grow. This order of temperature is offered by CVD methods and by some cooler region in violent methods. On the opposite, a stiff gradient, as obtained in fast-type methods, may produce a fast growth. (The influence of temperature on tube thickness and on rope formation is not obvious.)

Stability of the heating

A stable temperature in zone of growth is necessary to grow a tube, at least during the typical time for tube growth. This is probably the reason for the unusual length of tubes produced here. It is actually remarkable to notice that laser ablation produces drastically enhanced results when two lasers are used simultaneously, making the irradiation close to that of a continuous laser. [6.3.1] (Actually, the use of pulse laser in nano-tube synthesis is rather historical. The first synthesis of C₆₀ was realised using a YAG laser, and most studies, have naturally followed this.) Similarly, for the arc discharge method, DC current yields better results than AC. [6.2.4]

In the case of a pulsed laser, if tubes grow near irradiated zone, stability is determined by the pulse period/inter-pulse period and by the time for temperature stabilisation in the target (~ 1 ms). 1 ms is a minimum time for stable temperatures near irradiated zone. Considering a tube growth speed ~ 10 μm/s, temperatures are stable at least for 10 nm of tube growth. This order of length may be compared to tube length obtain with a single-laser excimer ablation method for BN (< 100 nm). [4.3] In a case of an arc discharge with AC, electrode temperatures are only stable during 1/60 s (or 1/50 s). With a speed growth in the order of 10 μm/s, tubes should grow in stable condition for an order of ~ 160 nm.

Annex 1

Mathematica language codes for calculations used here

1. Temperature gradient near impact with conical and elliptic models (p.96)

```
(*reset of all variables and functions*)
ClearAll[pi,sig,power,k,tdiss,esurfB,esurfBN,esurf,tau,gam]
ClearAll[power1,power2,power3,power4,rdiss1,rdiss2,rdiss3,rdiss4,h1,h2,h3,h4,irt1,irt2,irt3,irt4]
ClearAll[rmax,zmax,rzone]
ClearAll[t,power,rdiss,h,r,t0,tinf,temp,fluxr,fluxrad,totrad]

(*absolute datas*)
pi=N[Pi];
sig=5.67*10^-8;      (*black body radiation constant*)
tdiss=2700;          (*dissociation temperature of h-BN*)
esurfB=0.23;         (*surface absorption of a B crystalline at ambient =0.23*)
esurfBN=0.85;        (*absorption of a BN surface*)
esurf=0.5;
gam=1.5;             (*correction of esurf from the shape of the hole*)
k=18;               (*thermal conductivity at high T*)

(*empirical datas*)
rmax=2*10^-3;        (*Target dimension*)
zmax=4*10^-3;
rzone=600*10^-6;     (*radius of the studied zone*)
power1=50;
power2=60;
power3=70;
power4=80;
rdiss1=235*10^-6;    (*r for dissociation/recombinaison limit*)
rdiss2=282*10^-6;
rdiss3=300*10^-6;
rdiss4=322*10^-6;
irt1=30*10^-6;       (*tube ring thickness, microns*)
irt2=60*10^-6;
irt3=126*10^-6;
irt4=200*10^-6;

Print["For Laser Power ",power1," ",power2," ",power3," ",power4," W"];

(*.....Spherical Model.....*)

t0[power_,rdiss_]:=gam*esurf*power/(2*pi*k*rdiss);

tinf[power_,rdiss_]:=tdiss-t0[power,rdiss];

temp[r_,power_,rdiss_]:=t0[power,rdiss]*rdiss/r+tinf[power,rdiss];

Plot[{temp[10^(-6)*r,power1,rdiss1],temp[10^(-6)*r,power2,rdiss2],
temp[10^(-6)*r,power3,rdiss3],temp[10^(-6)*r,power4,rdiss4]},
{r,rdiss1*10^6,rzone*10^6},Frame->True,GridLines->Automatic,
PlotRange->{tinf[power1,rdiss1],tdiss},FrameLabel->{"Spherical T (K) at r (microns)", ""}];

(*.....Elliptic model.....*)

ClearAll[gam,t0,tinf,temp]

h1=214*10^-6;
h2=531*10^-6;
h3=824*10^-6;
h4=1061*10^-6;

tau[rdiss_,h_]:=1-2*ArcTan[rdiss/h]*Sin[ArcTan[rdiss/h]]/pi;
gam[rdiss_,h_]:=1+esurfB*tau[rdiss,h]*(1-esurf)/(esurf*(1-(1-esurfB)*tau[rdiss,h])); (*correction of absorption for the shape of the hole*)

Print["gamma coef.",N[gam[rdiss1,h1]], " ",N[gam[rdiss2,h2]], " ",N[gam[rdiss3,h3]], " ",N[gam[rdiss4,h4]]];
```

```

t0[power_,rdiss_,h_]:=gam[rdiss,h]*esurf*power/(pi*k*(rdiss+(h^2)/rdiss));

tinf[power_,rdiss_,h_]:=tdiss-t0[power,rdiss,h];

temp[r_,power_,rdiss_,h_]:=t0[power,rdiss,h]*rdiss/r+tinf[power,rdiss,h];

a=Plot[{temp[10^(-6)*r,power1,rdiss1,h1],temp[10^(-6)*r,power2,rdiss2,h2],
temp[10^(-6)*r,power3,rdiss3,h3],temp[10^(-6)*r,power4,rdiss4,h4]},
{r,rdiss1*10^6,rzone*10^6},Frame->True,GridLines->Automatic,
PlotRange->{tinf[power1,rdiss1,h1],tdiss},FrameLabel->{"Elliptic T (K) at r (microns)",""},DisplayFunction->Identity];

irt={{(rdiss1+irt1)*10^6,temp[rdiss1+irt1,power1,rdiss1,h1]},
{(rdiss2+irt2)*10^6,temp[rdiss2+irt2,power2,rdiss2,h2]},
{(rdiss3+irt3)*10^6,temp[rdiss3+irt3,power3,rdiss3,h3]},
{(rdiss4+irt4)*10^6,temp[rdiss4+irt4,power4,rdiss4,h4]}};
b=ListPlot[irt,Prolog->PointSize[10],DisplayFunction->Identity];
Fit[irt,{1,x},x];
c=Plot[%,{x,rdiss1*10^6,rzone*10^6},DisplayFunction->Identity];

Show[{a,b,c},DisplayFunction->$DisplayFunction];

(*.....:Conical Model:.....*)

Clear[t0,a,b,c,irt]

t0[power_,rdiss_,h_]:=gam[rdiss,h]*esurf*power/(k*pi*h/Cos[ArcTan[rdiss/h]]);

Plot[temp[10^(-6)*r,power3,rdiss3,h3],
{r,rdiss3*10^6,rmax*10^6},Frame->True,GridLines->Automatic,
PlotRange->{tinf[power3,rdiss3,h3],tdiss},FrameLabel->{"ref. Conical, T (K) at r (microns)",""}];

a=Plot[{temp[10^(-6)*r,power1,rdiss1,h1],temp[10^(-6)*r,power2,rdiss2,h2],
temp[10^(-6)*r,power3,rdiss3,h3],temp[10^(-6)*r,power4,rdiss4,h4]},
{r,rdiss1*10^6,rzone*10^6},Frame->True,GridLines->Automatic,
PlotRange->{tinf[power3,rdiss3,h3],tdiss},FrameLabel->{"Conical T (K) at r (microns)",""},DisplayFunction->Identity];

irt={{(rdiss1+irt1)*10^6,temp[rdiss1+irt1,power1,rdiss1,h1]},
{(rdiss2+irt2)*10^6,temp[rdiss2+irt2,power2,rdiss2,h2]},
{(rdiss3+irt3)*10^6,temp[rdiss3+irt3,power3,rdiss3,h3]},
{(rdiss4+irt4)*10^6,temp[rdiss4+irt4,power4,rdiss4,h4]}};
b=ListPlot[irt,Prolog->PointSize[10],DisplayFunction->Identity];
Fit[irt,{1,x},x];
c=Plot[%,{x,rdiss1*10^6,rzone*10^6},DisplayFunction->Identity];

Show[{a,b,c},DisplayFunction->$DisplayFunction];

Print["Tinf : ",N[tinf[power1,rdiss1,h1]]," ",N[tinf[power2,rdiss2,h2]]," ",
N[tinf[power3,rdiss3,h3]]," ",N[tinf[power4,rdiss4,h4]]," °K"];

Print["Temperature at the target edge: ",
N[temp[rmax,power1,rdiss1,h1]]," ",N[temp[rmax,power2,rdiss2,h2]]," ",
N[temp[rmax,power3,rdiss3,h3]]," ",N[temp[rmax,power4,rdiss4,h4]]," K"];

(*Radiations*)

fluxrad[r_,power_,rdiss_,h_]:=esurfBN*sig*temp[r,power,rdiss,h]^4;

totrad[r_,power_,rdiss_,h_]:=2*pi*NIntegrate[t*fluxrad[t,power,rdiss,h],{t,rdiss,r}] +
pi*rdiss^2*fluxrad[rdiss,power,rdiss,h];

Plot[totrad[r*10^(-6),power3,rdiss3,h3],
{r,rdiss3*10^6,rmax*10^6},
Frame->True,GridLines->Automatic,PlotRange->{0,totrad[rmax,power3,rdiss3,h3]},
PlotLabel->"Radiative flux (W) from a disc r (microns)"];

Print["Total radiative power of the 5 back surfaces with this model: ",
N[fluxrad[rmax,power3,rdiss3,h3]*(5*zmax^2)]," W"];

(*Comparison conductive flux/radiated flux on front surface*)

flux[r_,power_,rdiss_,h_]:=k*rdiss*t0[power,rdiss,h]/(r^2);

Plot[{fluxrad[r*10^(-6),power3,rdiss3,h3],flux[r*10^(-6),power3,rdiss3,h3]},
{r,rdiss1*10^6,rmax*10^6},Frame->True,GridLines->Automatic,
PlotRange->{0,flux[rdiss3,power3,rdiss3,h3]/5},PlotLabel->"Radiative/Conductive flux at r (microns)"];

```

2. Dependance of maximum temperature with laser power (p.45)

(*This is a mathematica-calculation to estimate minimum power for reaching sublimation/dissociation for B BN and C. The limit conditions suppose that energy losses from front surface are negligible. This is only correct for a circle of radius R around the irradiated zone.*)

```
(*reset of all variables and functions*)
ClearAll[sig,p,w]
ClearAll[phi,k0,t0,k1,t1,tdiss,esurf,arete,alpha]
ClearAll[phiBN,k0BN,t0BN,k1BN,t1BN,tdissBN,esurfBN,areteBN,alphaBN,esurf2BN]
ClearAll[phiC,k0C,t0C,k1C,t1C,tsubC,esurfC,areteC,alphaC,esurf2C]
ClearAll[phiB,k0B,t0B,k1B,t1B,tevapB,esurfBmin,esurfBmax,areteB,alphaB,esurf2B]
ClearAll[x,xmax,p,k,tinf,t0simple,t0lax,f,ftemp,n]

(*absolute datas*)
pi=N[Pi];
sig=5.67*10^-8;      (*black body radiation constant*)
w=N[100*10^-6];     (*waist as defined in intensity*)
tamb=298;

k[t0_,k0_,t_,phi_]=k0*(t0/t)^(1+phi);

(*semi infinite target*)

t0simple1[esurf_,p_,arete_,k1_]:=tamb+(esurf*p/(2*pi*k1*w));

(*LAX*)

ftemp[x_,alpha_]=Exp[-0.25*x^2]*(w*alpha)/((w*alpha)+x);
xmax=5;
n[f_,alpha_]:=NIntegrate[f[x,alpha],{x,0,xmax}];
t0lax1[esurf_,p_,arete_,phi_,t0_,k0_,f_,alpha_]:=tamb*(1-n[f,alpha]*phi*esurf*p/(2*pi*k[t0,k0,tamb,phi]*w*tamb))^(-1/phi);

(*limited radiating target*)

tinf[esurf_,esurf2_,p_,arete_]:=0.75*(esurf*p/(esurf2*sig*6*arete^2))^0.25;
(*tinf could also be chosen such that temperature fits on target extremities*)

t0simple2[esurf_,esurf2_,p_,arete_,k1_]:=tinf[esurf,esurf2,p,arete]+(esurf*p/(2*pi*k1*w));

t0lax2[esurf_,esurf2_,p_,arete_,phi_,t0_,k0_,f_,alpha_]:=tinf[esurf,esurf2,p,arete]*
(1-n[f,alpha]*phi*esurf*p/(2*pi*k[t0,k0,tinf[esurf,esurf2,p,arete],phi]*w*tinf[esurf,esurf2,p,arete]))^(-1/phi);

(*APPLICATIONS*)

(*BN*)
tdissBN=2700;      (*dissociation temperature of h-BN*)
esurfBN=0.7;
esurf2BN=0.75;
alphaBN=1/(100*10^-6); (*absorption of the surface*)
areteBN=4.5*10^-3;  (*Target dimension*)

k0BN=50;  (*thermal conductivity, as a function of T*)
t0BN=295;
k1BN=18.29;
t1BN=2200;
phiBN=N[Log[k1BN/k0BN]/Log[t0BN/t1BN]-1];

(*
Plot[k[t0BN,k0BN,t,phiBN],{t,t0BN,tdissBN},Frame->True,PlotRange->{0,k0BN},
GridLines->Automatic,FrameLabel->{"k as function of T (K) for BN",""}];

Plot[ftemp[x,alphaBN],{x,0,xmax},PlotRange->{0,1}]; (*to check the validity of the integration over x*)
*)

Plot[{t0simple1[esurfBN,p,areteBN,k1BN],t0lax1[esurfBN,p,areteBN,phiBN,t0BN,k0BN,ftemp,alphaBN],tdissBN}
,{p,1,150},Frame->True,GridLines->Automatic,
PlotStyle->{{RGBColor[1,0,0],Dashing[{0.05,0.05]}},{RGBColor[0,1,0]},{RGBColor[0,0,1]}},
PlotRange->{0,3500},FrameLabel->{"Tmax on BN (K) for laser power (W)",""}]

Plot[{tinf[esurfBN,esurf2BN,p,areteBN],t0simple2[esurfBN,esurf2BN,p,areteBN,k1BN],
t0lax2[esurfBN,esurf2BN,p,areteBN,phiBN,t0BN,k0BN,ftemp,alphaBN],tdissBN}
,{p,1,150},Frame->True,GridLines->Automatic,
PlotStyle->{{RGBColor[0,0,0]},{RGBColor[1,0,0],Dashing[{0.05,0.05]}},{RGBColor[0,1,0]},{RGBColor[0,0,1]}},
PlotRange->{0,3500},FrameLabel->{"Tmax on BN (K) for laser power (W)",""}]
```

```
(*C*)
tsubC=3800;
esurfC=0.45;          (*absorption of the surface*)
esurf2C=0.85;
alphaC=1/(0.07*10^-6);
areteC=4.5*10^-3;    (*Target dimension*)

k0C=162.23;
t0C=300;
k1C=26.167;
t1C=3300;
phiC=N[Log[k1C/k0C]/Log[t0C/t1C]-1];

(*Plot[k[t0C,k0C,t,phiC],{t,t0C,tsubC},Frame->True,PlotRange->{0,k0C},
GridLines->Automatic,FrameLabel->{"k as function of T (K) for C", ""};*)

Plot[{t0simple1[esurfC,p,areteC,k1C],t0lax1[esurfC,p,areteC,phiC,t0C,k0C,ftemp,alphaC],tsubC}
,{p,1,150},Frame->True,GridLines->Automatic,
PlotStyle->{{RGBColor[1,0,0],Dashing[{0.05,0.05]}},{RGBColor[0,1,0]},{RGBColor[0,0,1]}},
PlotRange->{0,5000},FrameLabel->{"Tmax on C (K) for laser power (W)", ""}]

Plot[{tin[esurfC,esurf2C,p,areteC],t0simple2[esurfC,esurf2C,p,areteC,k1C],
t0lax2[esurfC,esurf2C,p,areteC,phiC,t0C,k0C,ftemp,alphaC],tsubC}
,{p,1,150},Frame->True,GridLines->Automatic,
PlotStyle->{{RGBColor[0,0,0]},{RGBColor[1,0,0],Dashing[{0.05,0.05]}},{RGBColor[0,1,0]},{RGBColor[0,0,1]}},
PlotRange->{0,5000},FrameLabel->{"Tmax on C (K) for laser power (W)", ""}]

(*B*)
tevapB=3500;
esurfBmin=0.25;      (*absorption of the surface*)
esurfBmax=0.75;
esurf2B=0.75;
alphaB=1/(10*10^-6);
areteB=8*10^-3;     (*Target dimension*)

k0B=190;
t0B=128;
k1B=9.85;
t1B=2338;
phiB=N[Log[k1B/k0B]/Log[t0B/t1B]-1];

Plot[{t0simple1[esurfBmin,p,areteB,k1B],t0lax1[esurfBmin,p,areteB,phiB,t0B,k0B,ftemp,alphaB],
t0simple1[esurfBmax,p,areteB,k1B],t0lax1[esurfBmax,p,areteB,phiB,t0B,k0B,ftemp,alphaB],tevapB}
,{p,1,150},Frame->True,GridLines->Automatic,
PlotStyle->{{RGBColor[1,0,0],Dashing[{0.05,0.05]}},{RGBColor[0,1,0]},{
RGBColor[1,0,0],Dashing[{0.05,0.05]}},{RGBColor[0,1,0]},{RGBColor[0,0,1]}},
PlotRange->{0,5000},FrameLabel->{"Tmax on B (K) for laser power (W)", ""}]

Plot[{tin[esurfBmin,esurf2B,p,areteB],t0simple2[esurfBmin,esurf2B,p,areteB,k1B],
t0lax2[esurfBmin,esurf2B,p,areteB,phiB,t0B,k0B,ftemp,alphaB],
tin[esurfBmax,esurf2B,p,areteB],t0simple2[esurfBmax,esurf2B,p,areteB,k1B],
t0lax2[esurfBmax,esurf2B,p,areteB,phiB,t0B,k0B,ftemp,alphaB],tevapB}
,{p,1,150},Frame->True,GridLines->Automatic,
PlotStyle->{{RGBColor[0,0,0]},{RGBColor[1,0,0],Dashing[{0.05,0.05]}},{RGBColor[0,1,0]},{
RGBColor[0,0,0]},{RGBColor[1,0,0],Dashing[{0.05,0.05]}},{RGBColor[0,1,0]},{RGBColor[0,0,1]}},
PlotRange->{0,5000},FrameLabel->{"Tmax on B (K) for laser power (W)", ""}]
```

3. First temperature rise (p.90)

```
Clear[p0,w,k,ro,c,esurf,a,temp,t1,t2,t]

p0=70;          (*laser power*)
w=113*10^-6;   (*beam waist*)
k=40;          (*mean thermal conductivity of h-BN*)
ro= 2.08*10^6; (*density of h-BN*)
c=1.5;         (*mean specific heat of h-BN*)
esurf=0.85     (*absorbance at surface for h-BN at 10.6 microns*)
a=k/(ro*c);    (*thermal diffusivity*)

t1=0;          (*time interval*)
t2=1*10^-2;

temp[t_]=4*esurf*p0*ArcTan[Sqrt[4*a*t]/w]/(k*Pi^(3/2)*w);
Plot[temp[t],{t,t1,t2},Frame->True,GridLines->Automatic,FrameLabel->{"s","K"}]
```

4. Laser Waist (p.36)

```
(*calcul algebrique pour le waist du laser apres passage de la lentille de l'enceinte*)

Clear[sig1,f1,f2,lamb,d,r,w01,zr1,zr2,w02,sig2,ds2,w2,x]

sig1=-0.5;      (*position object*)
f2=13*10^-2;   (*focale*)
f1=-f2;
lamb=10.6*10^-6; (*longueur d'onde*)

(* waist objet *)

d=2;          (*longueur laser*)
r=8;         (*courbure du miroir*)
Print["w01 = ",w01=((lamb/(2*Pi))^2*d*(r-d))^0.25]
Print["zr1 = ", zr1=N[2*Pi*w01^2/lamb]]

(*taille du waist image*)

Print["zr2 = ", zr2=-f1*f2/(zr1+sig1^2/zr1) ]
Print["w02 = ", w02=N[(lamb*zr2/(2*Pi))^0.5] ]

(*position*)

Print["sig2 = ", sig2=sig1*zr2/zr1 ]

(*incertitude sur la position de la cible*)

ds2=5*10^-3;
w2[x_]=w02*(1+(x/zr2)^2)^0.5;
Plot[w2[x*10^-6]*10^6, {x,-ds2*10^6,ds2*10^6},PlotRange->{0,2*w02*10^6},
Frame->True,GridLines->Automatic,FrameLabel->{"beam diameter around the waist plane",""}]

Output:
w01 = 0.00241745, zr1 = 3.4641, zr2 = 0.00477905, w02 = 0.0000897912, sig2 = -0.000689796
```

5. Gradient along a tube (p.113 and 116)

```
(*calcul for the temperature gradient induced by radiative effect along a tube*)

Clear[a,h1,h2,sig,k,r,kb,jn,tmin,tmin1,tmin2,tmin3,tmin4,t01,t02,t03,t04,ts,ts1,ts2,ts3,ts4,y,x]

h1=0; (*range of integration*)
h2=-115*10^-6; (*this value is changed in second part*)

sig=5.67*10^-8; (*stephan coef*)
k=18; (*thermal conductivity*)
r=1*10^-9; (*tube radius*)
kb=1.38*10^-23; (*boltzman coef*)
jn=1*10^26; (*nitrogen flux*)

a=2/(k*r);

(*With radiation only*)

tmin1=300;
tmin2=1300;
tmin3=2300;

tmin =tmin1;

t01=tmin+50;
t02=tmin+200;
t03=tmin+700;
t04=tmin+2000;

NDSolve[ {y"[x]-a*sig*(y[x])^4-tmin^4==0,y[h1]==t01,y'[h1]==-sig*(t01^4-tmin^4)/k}, {y, {x,h2,h1}},MaxSteps -> 2000];
NDSolve[ {y"[x]-a*sig*(y[x])^4-tmin^4==0,y[h1]==t02,y'[h1]==-sig*(t02^4-tmin^4)/k}, {y, {x,h2,h1}},MaxSteps -> 2000];
NDSolve[ {y"[x]-a*sig*(y[x])^4-tmin^4==0,y[h1]==t03,y'[h1]==-sig*(t03^4-tmin^4)/k}, {y, {x,h2,h1}},MaxSteps -> 2000];
NDSolve[ {y"[x]-a*sig*(y[x])^4-tmin^4==0,y[h1]==t04,y'[h1]==-sig*(t04^4-tmin^4)/k}, {y, {x,h2,h1}},MaxSteps -> 2000];

Plot[ {y[x*10^-6] /. %,y[x*10^-6] /. %,y[x*10^-6] /. %,y[x*10^-6] /. %%%, {x,h2*10^6,h1*10^6}
,Frame->True,PlotRange->{tmin,4000},GridLines->Automatic,FrameLabel->{"T as function of distance (microns)",""}]
```

(*With surface and gas*)

```
h2=-15*10-6;
ts1=1000; ts2=2300; ts3=2700; ts4=4000;
```

```
ts=ts1;
Clear[tmin]
Solve[(sig*(tmin4-0.25*ts4)-jn*(3/2)*kb*(ts-tmin))=0,tmin]
tmin=981.435;
```

```
t01=tmin+(ts-tmin)*0.01;
t02=tmin+(ts-tmin)*0.1;
t03=tmin+(ts-tmin)*0.5;
t04=tmin+(ts-tmin)*0.9;
```

```
NDSolve[{y'[x]-a*Abs[(sig*((y[x])4-0.25*ts4)-jn*(3/2)*kb*(ts-y[x]))]=0,y[h1]==t01,
y'[h1]==-(sig*(t014-0.25*ts4)-jn*(3/2)*kb*(ts-t01))/k},y,{x,h2,h1},MaxSteps->2000];
```

```
NDSolve[{y'[x]-a*Abs[(sig*((y[x])4-0.25*ts4)-jn*(3/2)*kb*(ts-y[x]))]=0,y[h1]==t02,
y'[h1]==-(sig*(t024-0.25*ts4)-jn*(3/2)*kb*(ts-t02))/k},y,{x,h2,h1},MaxSteps->2000];
```

```
NDSolve[{y'[x]-a*Abs[(sig*((y[x])4-0.25*ts4)-jn*(3/2)*kb*(ts-y[x]))]=0,y[h1]==t03,
y'[h1]==-(sig*(t034-0.25*ts4)-jn*(3/2)*kb*(ts-t03))/k},y,{x,h2,h1},MaxSteps->2000];
```

```
NDSolve[{y'[x]-a*Abs[(sig*((y[x])4-0.25*ts4)-jn*(3/2)*kb*(ts-y[x]))]=0,y[h1]==t04,
y'[h1]==-(sig*(t044-0.25*ts4)-jn*(3/2)*kb*(ts-t04))/k},y,{x,h2,h1},MaxSteps->2000];
```

```
Plot[{y[x*10-6]} /. %,y[x*10-6]} /. %%,y[x*10-6]} /. %%%,y[x*10-6]} /. %%%%,{x,h2*106,h1*106}
,Frame->True,PlotRange->{tmin,ts},
GridLines->Automatic,FrameLabel->{"T as function of distance (microns)",""}]
```

Annex 2

Some Physical Datas

h-BN rod composition

Industrial process as received from the maker:

“Borax is reacted with nitrogen in the form of ammonia. Tricalcium phosphate is used in the process and it is done at high temperatures. The tricalcium phosphate is then removed through another process resulting in pure h-BN. The rod is made by hot pressing.”

Boron nitride, 99.5% (metals basis)					
Stock Number:40463					
Analysis					
Chemical Composition					
B ₂ O ₃			5.9%		
Oxygen			5.7%		
Boron			41.82%		
Nitrogen			51.21%		
Elemental Analysis (Emission Spectroscopy, ppm)					
Aluminum	9	Gold	<1	Beryllium	<1
Calcium	394	Chromium	4	Copper	<1
Iron	<1	Magnesium	18	Manganese	1
Molybdenum	<1	Sodium	11	Nickel	<1
Lead	<1	Silicon	3535	Tin	<1
Titanium	<1	Vanadium	<1	Tungsten	<1
Zinc	2	Zirconium	<1		
Density:	2.08 g/cc				
Certified by:					
<i>Maria D'Amico</i>					
Quality Control					
 A Johnson Matthey Company					

JSPDS cards

34-421

		d Å	Int	hkl	d Å	Int	hkl
BN		3.3281	100	002			
Boron Nitride		2.1693	15	100			
		2.0619	6	101			
		1.8176	9	102			
		1.6636	6	004			
Rad. CuKα ₁ λ 1.540598 Filter Mono. d-sp Diff.		1.5509	<1	103			
Cut off 22.1 Int. Diffractometer I/I ₀		1.3198	2	104			
Ref. Nat. Bur. Stand. (U.S.) Monogr., 20 22 (1983)		1.2521	5	110			
Sys. Hexagonal S.G. P6 ₃ /mmc (194)		1.1720	5	112			
a 2.5041(7) b c 6.6562(4) A C 2.6578		1.1346	<1	105			
α β γ Z 2		1.1095	<1	006			
Ref. Ibid.		1.0843	<1	200			
D _x 2.280 D _m mp		1.0311	1	202			
		1.0005	3	114			
Color Colorless		0.9877	<1	106			
The sample was obtained from the Carborundum Company, Niagara Falls, New York, USA. CAS#: 10294-33-4. σ ₍₁₀₀₎ = ± 1. A high pressure wurtzite type form was described by Soma et al. (1974) and another high pressure zinc blende type structure was described by Coleburn and Forbes (1968). The structure was done by Pease (1952). F ₂₀ = 71.5(0.011,25). Silicon used as internal standard. PSC: hP4. To replace 9-12.		0.9086	<1	204			
		0.8319	<1	008			
		0.8304	1	116			
		0.8197	<1	210			
		0.7960	<1	212			

© JCPDS 1984

517

11-618

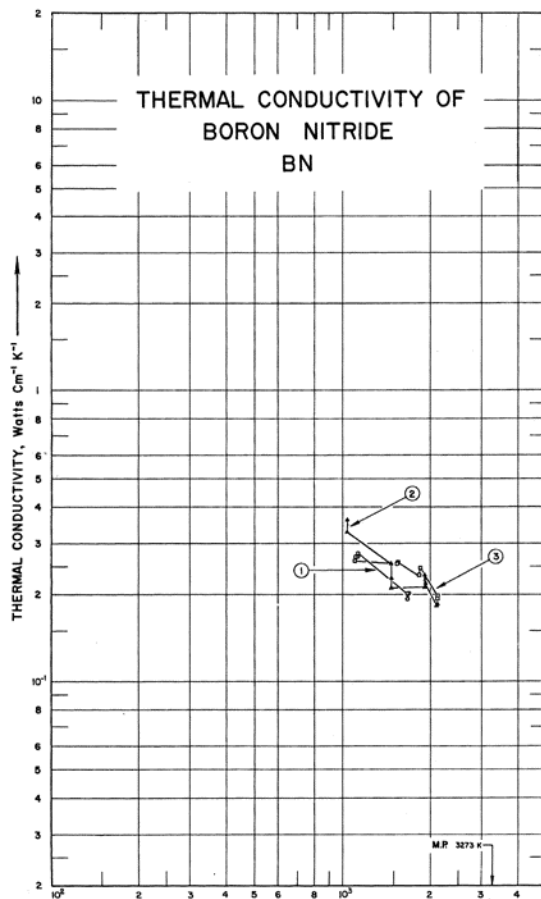
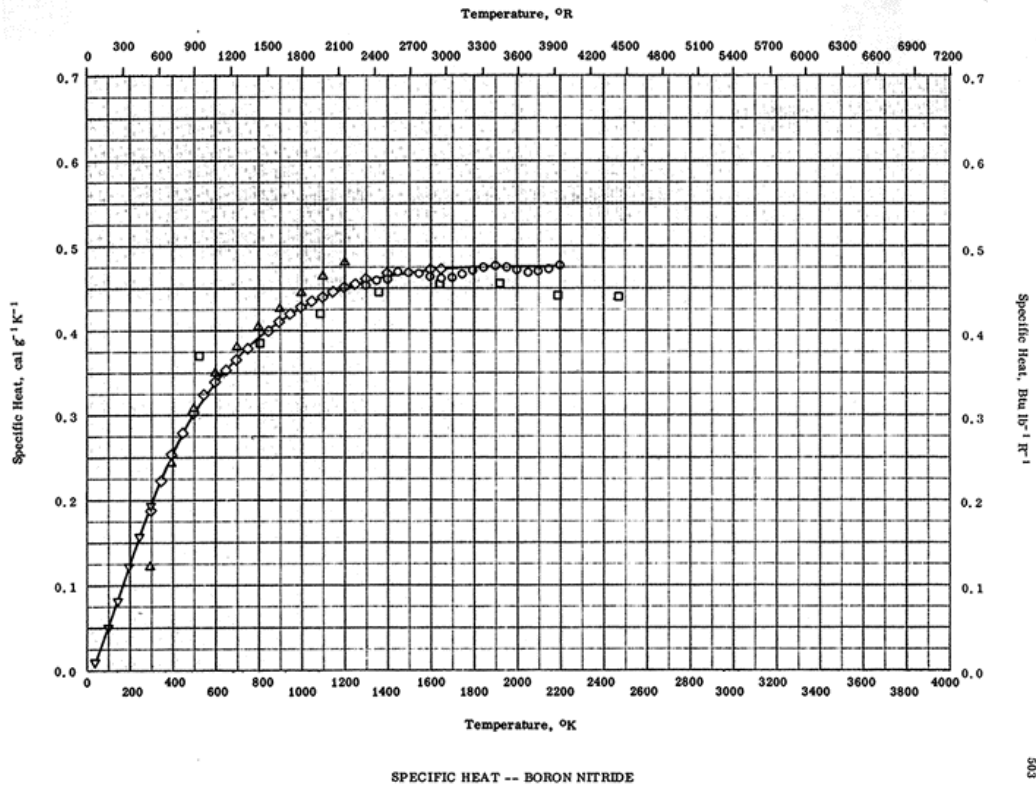
d	5.06	4.66	7.95	7.95	B (RHOMB.)			
I/I ₁	100	50	45	45	BORON			
Rad. CuKα A 1.5418 Filter Ni Dia.		d Å		I/I ₁	hkl	d Å	I/I ₁	hkl
Cut off I/I ₁ DIFFRACTOMETER		7.95	45	003	2.61	8	131	
Ref. AMENDOLA, A., POLYTECHNIC INST. OF BROOKLYN, N. Y. (1959)		7.39	25	012	2.59	6	223	
		5.48	20	110	2.57	6	312	
		5.06	100	104	2.52	6	208	
Sys. RHOMBOEDRAL * S.G. R3 m (166)		4.66	50	021	2.47	18	217, 306	
a _h 10.12 b _h c _h A C		4.51	20	113	2.41	14	134	
α 65°28' β γ Z D _x		4.41	16	202	2.39	8	119	
Ref. SANDS AND HOARD, J. AM. CHEM. SOC. 79 5582 (1957)		4.26	16	015	2.36	8	401	
		3.98	16	006	2.32	6	042	
ε α n ω β mp ε γ Color Sign		3.71	25	024	2.29	6	126, 315	
2V D		3.55	25	211	2.25	2	226	
Ref.		3.43	25	122	2.02	8	235	
* INDEXED ON BASIS OF HEXAGONAL PSEUDO CELL: a ₀ =10.95, c ₀ =23.84.		3.35	20	206				
		3.07	2	214				
		2.94	10	303				
		2.86	10	125				
		2.76	8	027				
		2.74	6	220				
		2.65	6	009				
SEE ALSO PATTERN FOR TETRAGONAL FORM.								

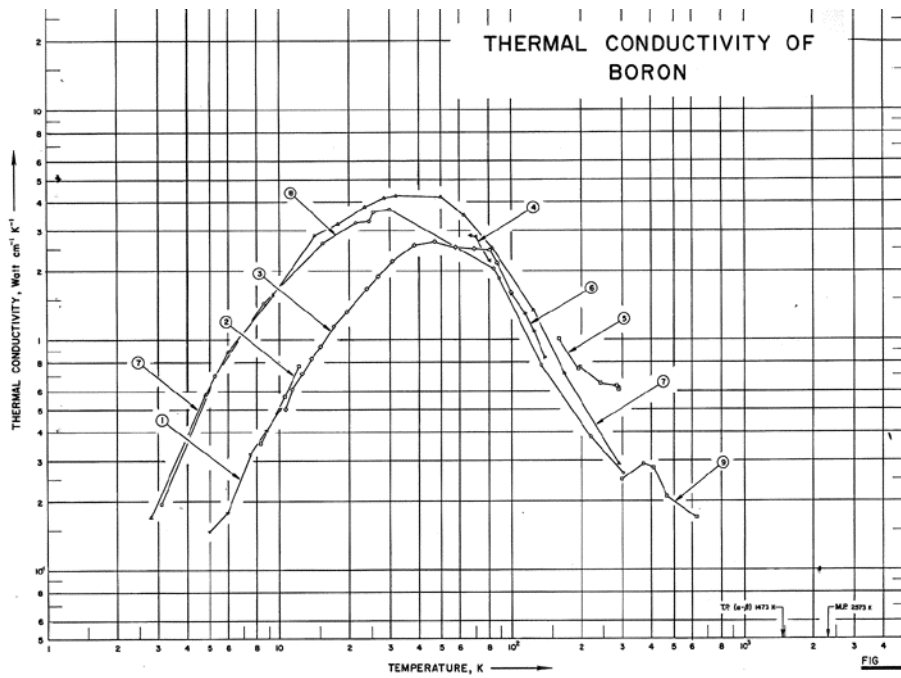
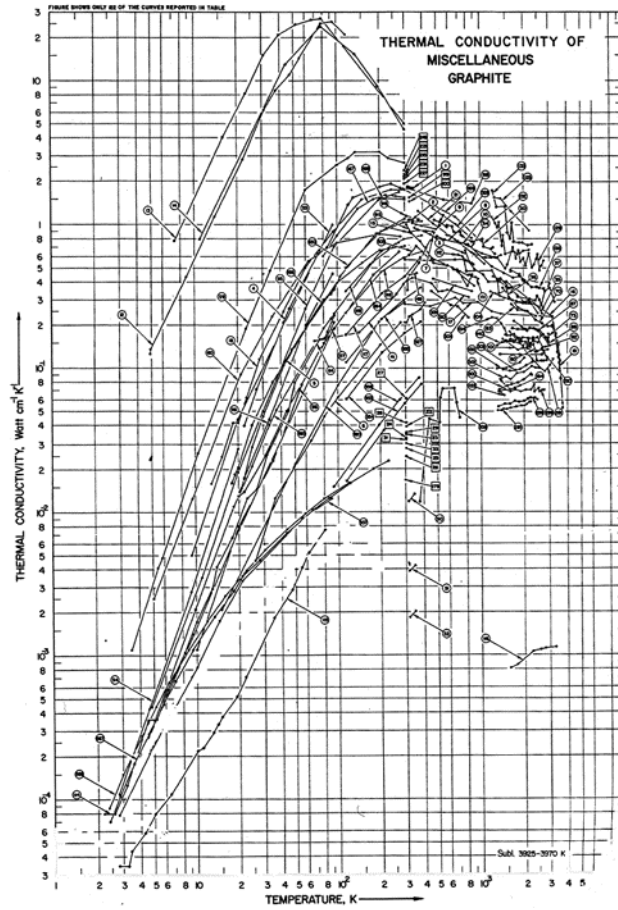
41-1487 JCPDS-ICDD Copyright (c) 1993 PDF-2 Sets 1-43 database Rad. = 1.54056 quality: 1

C	2-theta	Int.	hkl
Carbon	26.381	100	0 0 2
	42.221	2	1 0 0
	44.291	6	1 0 1
Graphite-2H	50.452	1	1 0 2
	54.542	4	0 0 4
Rad: CuKα ₁ Lambda: 1.54051 Filter: Ni d-sp: Diff.	59.692	1	1 0 3
Cut off: 22.1 Int: Diffractometer I/I ₀ : 7.78	77.243	3	1 1 0
Ref: Sanc, I., Polytechna, Foreign Trade Corporation, Panska, Czechoslovakia. ICDD Grant-in-Aid. (1990)	83.183	3	1 1 2
	86.823	1	0 0 5
Sys: Hexagonal S.G.: P6 ₃ /mmc (194)	93.594	1	2 0 1
a: 2.4704(15) b: c: 5.7244(38) A: C: 2.7220			
Ref: Ibid.			
Dx: 2.24 Dm: 2.16 SS/FOM: F(100)=0.942(13)			
Ref:			
Color: Black			
Pattern taken at 25(1) C. Specimen from METALCO, CZECHOSLOVAKIA. CSD no.: 7782-42-5. sigma(obs)= +/- 0.05. C type. Also called: clitorite. Also called: plumbago. Si used as external standard. PSC: hP4. To replace 1-040. 1-646, 2-456, 3-401, 23-64, 23-294 and 34-567 and validated by calculated pattern 23-294. Structure reference: Aust. J. Chem., 42 479 (1989). hvt: 12.01. Volume(ICDD): 35.54.			

Strong lines: 3.39/1 2.04/1 1.68/1 1.23/1 1.16/1 2.14/1 1.81/1 1.55/1

From [1.1.9]





Bibliography (~ 210 references)

Here is panel of articles describing different subjects of interested related to nanostructures of layered materials. Such articles are numerous, so that the present list is all but exhaustive. Furthermore, the evolution of this field is still very fast at present. It is difficult to keep informed day to day. Many recent articles may be unfairly omitted. Reference are classified by categories. A few references appear under two different caterogies. Some works that appeared to be “important” sources during this work are indicated in bold. (This is of course very subjective.)

[1] Datas

[1.1] Physical datas :

1. E. Rapoport, Ann. Chim. (Paris), 10 (7) 607-638 (1985)
2. Bundy, Hall, Strong and Wentorf (1955)
3. **JANAF thermochemical tables 3^{tr} edition (1985)**
4. **J. Margrave, The characterisation of high temperature vapors, p. 502, John Wiley & sons, Inc., New York, London, Sydney**
5. **E. A. Smith, Graphite and BN ("white graphite"): aspects of structure, powder size, powder shape, and purity, Powder Metallurgy 14, 27, 110 (1971)**
6. A. Lipp, K. A. Schwetz & K. Hunold, h-BN: fabrication, properties and applications, J. Eur. Ceram. Soc. 5, 3 (1989)
7. Graphite, Thermophysical Properties of High-Temperature Materials, Vol. 1, 118-121 / 124-131.
8. Properties of boron nitride, Thermophysical Properties of High-Temperature Materials, Vol. 5, 499-516
9. **Y.S. Touloukian, et al., Thermophysical properties of matter Vol. 2, IFI/Plenum, NewYork-washington (1970)**
10. **Y.S. Touloukian, D.P. Dewitt, Thermophysical properties of matter Vol. 8-Thermal radiative properties Y.S. IFI/Plenum, NewYork-washington (1972)**
11. Handbook of thin film process Technology, A1.5:2, IOP Publishing Ltd (1995)
12. JCPDS card
13. P. Pascal, Nouveau traité de chimie minérale VI, Masson, Paris
14. W. Spitzer and W. Kaiser, Optical properties of crystalline boron, Phys. Rev. Let. 1, 7, 230 (1958) (Errata, 15 nov)
15. E. Taft, H. Philipp, Optical properties of graphite, Phys. Rev. 138,1A, A197 (1964)
16. S. Ergun, Optical studies of carbon, Chemistry and physics of carbon Vol.3, Marcel derker, Inc., New York (1968)
17. K. Oda et al., Oxidation kinetics of h-BN powder, J. of mat. Science, 28, 6562 (1993)
18. **Etude bibliographique des effets d'un flux laser sur une cible, 2^{ieme} partie, Chauffage, fusion et vaporisation, p. 15, Rapport technique ONERA 5/7184 SY (1980)**
19. Effects of high-power laser irradiation p. 82, J. F. Ready, Academic press New York
20. Handbook of heat and thermo dynamics 5-14

[1.2] Mathematical references

1. **M. Lax, Temperature rise induced by a laser beam, J. of appl. Phys., 48, 9 3919 (1977), and M. Lax, Temperature rise by a laser beam II. The nonlinear case, Appl. Phys. Let., 33(8), 786 (1978)**
2. H. Ma, S. H. Lin, R. W. Carpenter, P. Rice, O. F. Sandey, Ad. in. calculation of band structure, x-ray emission, quantum yield and EELS of h-BN, J. Appl. Phys. 73, 11, 7422 (1993)
3. Tarrío, S. E. Schnatterly, Interband transitions, plasmons, and dispersion in h-BN, Phys. Rev B 40, 1, 7852 (1989)
4. J. C. Slater, G. F. Koster, simplified LCAO method for the periodic potential problem, Phys. Rev. 94, 6, 1498 (1954)
5. P. R. Wallace, The band theory of graphite, Phys. Rev. 71, 9, 622 (1947)
6. J. Furthmuller et al., Ab initio calculation of the structural and electronic properties of carbon and boron nitride

using ultrasoft pseudopotentials, *Phys rev B*, 50, 21, 15606 (1994)

[2] Potential for Applications

1. L. Rapoport, Y. Bilik, Y. Feldman, M. Homyonfer, S.R. Cohen, R. Tenne, Hollow nanoparticles of WS₂ as potential solid-state lubricants, *Nature* 387, 791 (1997) (exist supplementary material on line)
2. L. Rapoport & al., Inorganic fullerene-like material as additives to lubricants: structure-function relationship, *Wear* 225-229, 975 (1999)
3. S. J. Tans et al., Individual single-wall carbon nanotubes as quantum wires, *Nature* 386, 474 (1997)
4. S. J. Tans, A. R. M. Verschueren, C. Dekker, Room temperature transistor based on a single carbon NT, *Nature* 393, 49 (1998)
5. J. Kong, H. T. Soh, A. M. Cassell, C. F. Quate, H. Dai, Synthesis of individual single-walled carbon nanotubes on patterned silicon wafers, *Nature* 395, 878 (1998)
6. Y. Zhang, T. Ichihashi, E. Landree, F. Nihey, S. Iijima, Heterostructures of single-walled carbon nanotubes and carbide nanorods, *Science* 285, 1719 (1999)
7. H. Dai, J. H. Hafner, A. G. Rinzler, D. T. Colbert, R. E. Smalley, NT as nanoprobe in scanning probe microscopy, *Nature* 384, 147, (1996)
8. S. S. Wong, E. Joselevich, A. T. Wooley, C. L. Cheung, C. M. Lieber, Covalently functionalized NT as nanometre-sized probes in chemistry and biology, *Nature* 394, 52 (1998)
9. M. Watanabe, M. Tachikawa, T. Osaka, On the possibility of H intercalation of graphite-like carbon materials(...), *Electrochimica Acta* 42, 17, 2707 (1997)
10. A.C. Dillon, K.M. Jones, T. A. Bekkedahi, C.H. Kiang, D.S. Bethune, M.J. Heben, Storage of hydrogen in single-walled carbon nanotubes, *Nature* 386, 377 (1997) and Dillon et al. carbon NT materials for hydrogen storage, Proceedings of the 2000 DOE/NREL hydrogen program review NREL/CP-570-28890 (free download at present)
11. G. Che, B. B. Lakshmi, E. R. Fisher, C. R. Martin, Carbon nanotubule membranes for electrochemical energy storage and production, *Nature* 393, 346 (1998)
12. S. Fan et al., Self-oriented regular arrays of carbon nanotubes and their field emission properties, *Science* 283, 512 (1999)
21. B. Rinzler et al., unraveling nanotubes: field emission from an atomic wire, *Science*, 269, 1550 (1995)
13. W. Choi et al., Fully sealed, high-brightness carbon-NT field emission display, *Appl. Phys. Let.*, 75, 20, 3129 (1999)
14. S. Fan et al., Self oriented regular arrays of C NT and their field emission properties, *Science* 283, 512 (1999)
15. P. Král and D. tomanek, Laser-driven atomic pump, *82*, 26, 5373 (1999)

[3] Growth mechanisms

[3.1] Physical considerations :

1. **A. Oberlin, M. Endo, Filamentous growth of carbon through benzene decomposition, *J. of cryst. Growth* 32, 335 (1976)**
2. O. L. Louchev, Surface diffusion growth and stability mechanism of BN NT produced by laser beam heating under superhigh pressures, *Appl. Phys. Let.* 71, 24, 3522 (1997), O. A. Louchev, Y. Sato, NT self-organization: Formation by step-flow growth, *Appl. Phys. Let.* 74, 2, 194 (1999) and O. Loutchev et al., multi wall carbon NT: self-organisation and inhibition of step-flow growth kinetics, *J. of Appl. Phys.*, 15 march 2000
3. O. A. Louchev, Y. Sato, Coupling of kinetic and transport phenomena in self-organization of C-B-N nanotube growth into sandwich structures, *Appl. Phys. Let.* 77, 10, 1446 (2000)
4. K. Suenaga, F. Willaime. A. Loiseau, C. Colliex, Organisation of carbon and BN layers in mixed nanoparticles and NT synthesized by arc discharge, *Appl. Phys. A* 68, 301 (1999)
5. M. Endo, H. W. Kroto, Formation of carbon nanofibers, *J. Phys. Chem.* 96, 6941 (1992)
6. S. Iijima, T. Ichihashi, Y. Ando, Pentagons, heptagons and negative curvature in graphite microtubule growth, *Nature* 356, 776 (1992)
7. S. Iijima, P. M. Ajayan, T. Ichihashi, Growth model for carbon nanotubes, *Phys. Rev. Let.* 69, 21, 3100 (1992)
8. S. B. Sinnott et al., Model of carbon NT growth through chemical vapor deposition, *Chem. Phys. Let.* 315, 25 (1999)
9. E. G. Gamaly, T. W. Ebbesen, Mechanism of carbon NT formation in the arc discharge, *Phys. Rev. B* 52, 3, 2083 (1995)
10. J. H. J. Scott, S. A. Majetich, Morphology, structure, and growth of nanoparticles produced in a carbon arc, *Phys. Rev. B* 52, 17, 12564 (1995)
11. T. Guo et al., Self-Assembly of tubular fullerenes, *J. Phys. Chem.* 99, 10694 (1995)
12. A. Dillon et al., Controlling SWNT diameters with variation in laser pulse power, *Chem. Phys. Let.* 316, 13 (2000)

13. A. Poretzky, et al., Dynamics of single-wall carbon NT synthesis by laser vaporization, *Appl. Phys. A*, 70, 153 (2000)
14. S. Arepalli, P. Nikolaev, W. Holmes, C. Scott, Diagnostics of laser-produced plume under carbon NT growth conditions, *Appl. Phys. A* 70, 125
15. E. Munoz, et al., Single-walled carbon NT produced by cw CO₂-laser ablation: study of parameters important for their formation, *Appl. Phys. A*, 70, 145 (2000)
16. E. Gamly et al., Single walled carbon NT formation with a continuous CO₂-laser: experiments and theory, *Appl. Phys. A* 70, 161 (2000)
17. Rode et al., Formation of cluster-assembled carbon nano-foam by high-repetition-rate laser ablation, *Appl. Phys. A* 70, 135 (2000)
18. L. Chadderton and Y. Chen, NT growth by surface diffusion
19. F. Willaime, A. Loiseau, N. Demoncey, K. Suenaga, C. Colliex, and H. Pascard, Multicomponent and multiphase nanotubes: BN, BN-C and filled tubes, EUREM 2000

[3.2] Structural calculations (first principle)

1. maiti, C. J. Brabec, C. Roland, J. Bernholc, Theory of carbon nanotube growth, *Phys. Rev. B* 52, 20, 14850 (1995)
2. maiti, C. J. Brabec, J. Bernholc, Kinetics of metal-catalyzed growth of single walled carbon NT, *Phys. Rev. B*, 55, 10, R6097 (1997)
3. J. Bernholc et al., Theory of growth and mechanical properties of NT, *Appl. Phys. A* 66, 1 (1998)
4. M. B. Nardelli, J. Brabec, A. Maiti, C. Roland, J. Bernholc, Lip-lip interactions and the growth of multiwalled carbon NT, *Phys. Rev. Lett.* 80, 2, 313 (1998)
5. Y. H. Lee, S. G. Kim, D. Tomanek, Catalytic growth of single wall carbon NT: an ab initio study, *Phys. Rev. Lett.* 78, 12, 2393 (1997)
6. Y.-K. Kwon et al., Morphology and stability of growing multiwall carbon NT, *Phys. Rev. Lett.* 79, 11, 2065 (1997)
7. D. T. Colbert, R. E. Smalley, Electric effects in NT growth, *Carbon* 33, 7, 921 (1995)
8. C.-H. Kiang, W. A. Goddard III, Polyyne ring nucleus growth model for single-layer carbon NT, *Phys. Rev. Lett.* 76, 14, 2515 (1996)
9. J.-Ch. Charlier, X. Blase, A. De Vita, R. Car, Microscopic growth mechanisms for carbon and BN NT, *Appl. Phys. A* 68, 267 (1999)
10. Y. Xia et al., continuous growth of higher fullerenes through adducting small carbon clusters and annealing, *Phys. Rev. B* 57, 23, 14950 (1998)

[4] BN nanostructures

[4.1] synthesis of BN nanotubes by laser heating

T. Laude et al., Long ropes of BN NT grown by a continuous laser heating, *Appl. Phys. Lett.* 76, 22, 3239 (2000)

[4.2] synthesis of BN nanotubes by arc discharge methods

1. N. G. Chopra et al., Boron nitride nanotubes, *Science* 269, 966 (1995)
2. A. Loiseau, F. Willaime, N. Demoncey, G. Hug, H. Pascard, BN NT with reduced numbers of layers synthesized by arc-discharge, *Phys. Rev. Lett.* 76, 4737 (1996).
3. A. Loiseau et al., BN NT, *Carbon* 36, 5-6, 743 (1998)
4. Y. Saito, M. Maida, T. Matsumoto, Structures of BN NT with single-layer and multi-layers produced by arc discharge, *Jpn J. Appl. Phys.* 38, 159 (1999)
5. Y. Saito, M. Maida, Square, pentagon, and heptagon rings at BN NT tips, *J. of Phys. Chem A* 103, 10, 1291 (1999)
6. **J. Cumings, A. Zettl, Mass production of boron nitride double-wall nanotubes and nanococoons, *Chem. Phys. Lett.* 316, 211 (2000)**

[4.3] synthesis of BN nanotubes by laser ablation method

1. D. P. Yu et al., Synthesis of boron nitride nanotubes by means of excimer laser ablation at high temperature, *Appl. Phys. Lett.* 72, 16, 1966 (1998)
2. W. Zhou, Z. Zhang, Z. G. Bai, D. P. Yu, Catalyst effects on formation of BN nano-tubules synthesized by laser ablation, *Sol. St. Com.* 109, 555 (1999)

[4.4] synthesis of BN nanotubes by oven heating

1. P. Gleize, M. C. Schouler, P. Gabelle, M. Caillet, Growth of tubular BN filaments, *J. of Mat. Science* 29, 1575 (1994)
2. M. Terauchi, M. Tanaka, H. Matsuda, M. Takeda & K. Kimura, Helical nanotubes of hexagonal boron nitride, *J. of Elec. Micros.* 46, 1, 75 (1997)

3. Y. Chen, J. F. Gerald, J. S. Williams, S. Bulcock, synthesis of BN NT at low temperatures using reactive ball milling, *Chem. Phys. Lett.* 299, 260 (1999) and Y. Chen et al., A solid state process for formation of BN NT, *Appl. Phys. Lett.* 74, 20, 2960 (1999)

[4.5] Synthesis of some BN nanotubes by H. P. compression of c-BN micro-crystals in a diamond anvil cell induced by laser heating

D. Golberg et al, Nanotubes in boron nitride laser heated at high pressure, *Appl. Phys. Lett.* 69, 14, 2045 (1996)

[4.6] synthesis of BN nanotubes by "substitution" of C to BN in oxydizing atmosphere

1. W. Han, Y. Bando, K. Kurashima, T. Sato, Synthesis of boron nitride nanotubes from carbon nanotubes by a substitution reaction, *Appl. Phys. Lett.* 73, 21, 3085 (1998) and D. Goldberg et al., MoO₃-promoted synthesis of BN MWNT from C NT templates, *Chem. Phys. Lett.* 323, 185 (2000)
2. (See also H. Dai, E. W. Wong, Y. Z. Lu, S. Fan, C. M. Lieber, Synthesis and characterization of carbide nanorods, *Nature* 375, 769 (1995))

[4.7] synthesis of BN onions by laser pyrolyse in the gas phase

1. L. Boulanger, B. Andriot, M. Cauchetier, F. Willaime, Concentric shelled and plate-like graphitic BN nanoparticles produced by CO₂ laser pyrolysis, *Chem. Phys. Lett.* 234, 227 (1995)
2. M. I. Baraton et al., Nanometric BN powders: laser synthesis, characterization and FT-IR surface study, *J. of the Eur. Ceramic society* 371 (1994)

[4.8] synthesis of some BN nanotubes in plasma jet method

Y. Shimizu, Y. Moriyoshi, H. Tanaka, BN NT, webs, and coexisting amorphous phase formed by the plasma jet method, *Appl. Phys. Lett.* 75, 7, 929 (1998)

[4.9] EELS studies

1. C. Souche, B. Jouffrey, G. Hug, M. Nelhiebel, Orientation sensitive EELS analysis of BN nanometric hollow spheres, *Micron* 29, 6, 419 (1998)
2. P. Gleize, S. Herreyre, P. Gadelle, M. Mermoux, Characterization of tubular boron nitride filaments, *Mat. Sci. Lett.* 13, 1413 (1994)
3. M. Terauchi, M. Tanaka, T. Matsumoto, Y. Saito, EELS study of the electronic structure of BN NT

[4.10] Mechanical properties

N. G. Chopra & A. Zettl, Measurement of the elastic modulus of a multi-wall BN nanotube, *Sol. Sta. Com.* 105, 5, 297 (1998)

[4.11] Irradiation experiments

O. Stéphan, Y. Bando, A. Loiseau, F. Willaime, N. Shramchenko, T. Tamiya, T. Sato, Formation of small single-layer and nested BN cages under electron irradiation of nanotubes and bulk material, *Appl. Phys. A* 67, 107 (1998)

[4.12] Structural calculations

1. P. W. Fowler, K. M. Rogers, G. Seifert, M. Terrones, H. Terrones, Pentagonal rings and nitrogen excess in fullerene-based BN cages and nanotube caps, *Chem. Phys. Lett.* 299, 359 (1999)
2. A. Rubio, J. L. Corkill, M. Cohen, Theory of graphitic BN NT, *Phys. Rev. B* 49, 7, 5081 (1994)

[5] Other B/C/N nanotubes

1. O. Stéphan, P. M. Ajayan, C. Colliex, P. Redlich, J. M. Lambert, P. Bernier, P. Lefin, Doping graphitic and carbon nanotube structures with boron and nitrogen, *Science* 266, 1683 (1994)
2. Z. Weng-Sieh et al., Synthesis of B_xC_yN_z nanotubules, *Phys. Rev. B* 51, 16, 11229 (1995)
3. K. Suenaga, C. Colliex, N. Demoncy, A. Loiseau, H. Pascard, F. Willaime, Synthesis of nanoparticles and nanotubes with well-separated layers of BN and carbon, *Science* 278, 653 (1997)
4. Golberg, Y. Bando, W. Han, K. Kurashima, T. Sato, Single-walled B-doped carbon, B/N-doped carbon and BN nanotubes synthesized from SW carbon NT through a substitution reaction, *Chem. Phys. Lett.* 308, 337 (1999)
5. W. Han, Y. Bando, K. Kurashima, T. Sato, Boron-doped carbon NT prepared through a substitution reaction, *Chem. Phys. Lett.* 299, 368 (1999)
6. Y. Miyamoto, A. Rubio, M. L. Cohen, S. G. Louie, Chiral tubules of hexagonal BC₂N, *Phys. Rev. B* 50, 7, 4976 (1994)
7. Y. Miyamoto, A. Rubio, S. G. Louie, M. L. Cohen, Electronic properties of tubule forms of h-BC₃, *Phys. Rev. B* 50, 24, 18360 (1994)
8. D. Golberg, Y. Bando, K. Kurashima, T. Sasaki, Boron doped carbon fullerenes and nanotubules formed through electron irradiation-induced solid-state phase transformation, *Appl. Phys. Lett.* 72, 17, 2108 (1998)
9. C. Satishkumar et al., Boron-carbon NT from the pyrolysis of C₂H₂-B₂H₆ mixtures, *Chem. Phys. Lett.* 300, 473 (1999)
10. A. Gindulyte, W. N. Lipscomb, L. Massa, Proposed boron NT, *Inorg. Chem.* 37, 6544 (1998)

11. A. Gindulyte, N. Krishnamachari, W. N. Lipscomb, L. Massa, Quantum chemical calculation of proposed multicage boron fullerenes, *Inorg. Chem.* 37, 6546 (1998)

[6] Carbon nanostructures

[6.1] Generalities on carbon nanostructures :

1. T. Ebbesen, Carbon NT, *Physics Today*, June 1996, p.26
2. P. Bernier, Le carbone dans tous ses états, *La Recherche* 233, 22, 794 (1991)
3. P. Bernier, A. Loiseau, W. Maser, H. Pascard, F. Willaime, Du carbone pour emballer la matière, *La Recherche* 293, 24-26 (1996)
4. Journet, P. Bernier, Production of carbon nanotubes, *Appl. Phys. A* 67, 1-9 (1998)
5. *New Materials for the Twenty-First Century*, Peter J F Harris ISBN: 0521554462., Cambridge University Press

[6.2] synthesis of carbon nanostructures by arc discharge method

1. **C. Journet et al., Large scale production of single-walled carbon nanotubes by the electric-arc technique, *Nature* 388, 756 (1997)**
2. S. Iijima, Helical microtubules of graphitic carbon, *Nature* 354, 56 (1991)
3. S. Seraphin, D. Zhou, Single-walled nanotubes produced at high yield by mixed catalysts, *Appl. Phys. Lett.* 64, 16, 2087 (1994)
4. T. W. Ebbesen, P. M. Ajayan, Large-scale synthesis of carbon nanotubes, *Nature* 358, 220 (1992)
5. Y. Ando, S. Iijima, Preparation of carbon nanotubes by arc-discharge evaporation, *Jpn. J. Appl. Phys.* 32 (Part 2, No. 1A/B), L107-L109 (1993)
6. S. Iijima, T. Ichihashi, Single-shell carbon nanotubes of 1-nm diameter, *Nature* 363, 603 (1993)
7. S. Subramoney, R. S. Ruoff, D. C. Lorents, R. Malhotra, Radial single-layer nanotubes, *Nature* 366, 637 (1993)
8. **T. W. Ebbesen, H. Hiura, J. Fujita, Y. Ochiai, S. Matsui, K. Tanigaki, Patterns in the bulk growth of carbon nanotubes, *Chem. Phys. Lett.* 209 (1,2), 83 (1993)**
9. H. Zeng, L. Zhu, G. Hao, R. Sheng, Synthesis of various forms of carbon NT by AC arc discharge, *Carbon* 36, 3, 259 (1998)
10. S. Bethune, C. H. Kiang, M. S. de Vries, G. Gorman, R. Savoy, J. Vazquez, R. Beyers, Cobalt-catalysed growth of carbon nanotubes with single-atomic-layer walls, *Nature* 363, 605 (1993)

[6.3] synthesis of carbon nanostructures by laser ablation method

1. T. Guo, P. Nikolaev, A. Thess, D. T. Colbert, R. E. Smalley, Catalytic growth of SWNT by laser vaporization, *Chem. Phys. Lett.* 243, 49 (1995)
2. T. Guo et al., Self-Assembly of tubular fullerenes, *J. Phys. Chem.* 99, 10694 (1995)
3. **A. Thess et al., Crystalline ropes of metallic carbon nanotubes, *Science* 273, 483 (1996)**
4. Y. Zhang, H. Gu, S. Iijima, Single-walled carbon NT synthesized by laser ablation in a nitrogen atmosphere, *Appl. Phys. Lett.* 73, 26, 3827 (1998)
5. A. Dillon et al., Controlling SWNT diameters with variation in laser pulse power, *Chem. Phys. Lett.* 316, 13 (2000)
6. E. Munoz et al., Single-walled carbon NT produced by cw CO₂-laser ablation: study of parameters important for their formation, *Appl. Phys. A*, 70, 145 (2000)

[6.4] synthesis of carbon nanostructures by CVD methods

1. **A. Oberlin, M. Endo, Filamentous growth of carbon through benzene decomposition, *J. of Cryst. Growth* 32, 335 (1976)**
2. J. S. Speck, M. Endo, M. S. Dresselhaus, Structure and intercalation of thin benzene derived carbon fibers, *J. of Cryst. Growth* 94, 834 (1989)
3. R. Martin, Nanomaterials: A membrane-based synthetic approach, *Science* 266, 1961 (1994)
4. M. Endo et al., The production and structure of pyrolytic carbon nanotubes, *J. Phys. Chem. Solids* 54, 12, 1841 (1993)
5. M. Endo et al., Pyrolytic carbon NT from vapor-grown carbon fibers, *Carbon* 33, 7, 873 (1995)
6. M. J. Yacaman, M. M. Yoshida, L. Rendon, Catalytic growth of carbon microtubules with fullerene structure, *Appl. Phys. Lett.* 62, 6, 657 (1993)
7. M. Terrones et al., Controlled production of aligned nanotube bundles, *Nature* 388, 52 (1997)
8. **Z. W. Pan et al., Very long carbon nanotube, *nature*, vol. 394, 13 aug. 1998**
9. Z. F. Ren et al., Synthesis of large array of well aligned carbon nanotubes on glass, *Science* 282, 1105 (1998)
10. W. Z. Li et al., Large scale synthesis of aligned carbon nanotubes, *Science* 274, 1701 (1996)
11. S. Fan et al., Self-oriented regular arrays of carbon nanotubes and their field emission properties, *Science* 283, 512

(1999)

[6.5] synthesis of carbon nanostructures by other methods

1. J. B. Howard, K. D. Chowdhury, J. B. VanderSande, Carbon shells in flames, *Nature* 370, 603 (1994)
2. K. D. Chowdhury, J. B. Howard, J. B. VanderSande, Fullerene nanostructures in flames, *J. of Mat. Res.* 11, 2, 341 (1996)

[6.6] Synthesis of unusual morphologies

1. A. Krishnan et al., Graphitic cones and the nucleation of curved carbon surfaces, *Nature* 388, 451 (1997)
2. R. L. Jacobsen, M. Monthieux, Carbon beads with protruding cones, *Nature* 385, 211 (1997)
3. J. Liu et al., Fullerene 'crop circles', *Nature* 385, 780 (1997)
4. Y. Saito, T. Matsumoto, Carbon nano-cages created as cubes, *Nature* 392, 237 (1998)
5. P. Ajayan, Growth carbon micro-trees, *nature* 404, 243 (2000)

[6.7] Post-synthesis treatment of carbon nanotubes :

1. T. W. Ebbesen, P. M. Ajayan, H. Hiura, K. Tanigaki, Purification of nanotubes, *Nature* 367, 519 (1994)
2. K. Tohji et al., Purifying SWNT, *Nature* 383, 679 (1996)
3. S. C. Tsang, P. J. F. Harris, M. L. H. Green, Thinning and opening of carbon nanotubes by oxydation using carbon dioxide, *Nature* 362, 520 (1993)
4. P. M. Ajayan & S. Ijima, Capillary-induced filling of carbon nanotubes, *Nature* 361, 333 (1993)
5. S. C. Tsang, Y. K. Chen, P. J. F. Harris, M. L. H. Green, A simple chemical method of opening and filling carbon nanotubes, *Nature* 372, 159 (1994)
6. C. Guerret-Piécourt, Y. Le Bouar, A. Loiseau, H. Pascard, Relation between metal electronic structure and morphology of metal compounds inside carbon nanotubes, *Nature* 372, 761 (1994)
7. P. M. Ajayan, O. Stéphan, C. Colliex, D. Trauth, Aligned carbon nanotubes arrays formed by cutting a polymer resin-nanotube composite, *Science* 265, 1212 (1994)
8. Y. Ando, M. Ohkohchi, M. Wang, Regrowth of carbon NT and nanoparticles, *J. of Cryst. Growth* 166, 888 (1996)

[6.8] Structural considerations

1. G. P. Dimitrakopoulos, V. P. Dravid, T. Karakostas, R. C. Pond, The defect character of carbon NT and nanoparticles, *Act. Cryst.* A53, 341 (1997)
2. P. M. Ajayan, T. Ichihashi, S. Ijima, Distribution of pentagons and shapes in carbon NT and nano-particles, *Chem. Phys. Let.* 202, 5, 384 (1993)
3. Y. Kwon, D. Tomanek, Orientational melting in carbon nanotubes ropes, (1999)
4. **X. F. Zhang et al., Carbon-tubes; their formation process and observation by electron microscopy, *J. of Cryst. Growth* 130, 368 (1993)**

[6.9] Electron irradiation experiments :

1. F. Banhart, P. M. Ajayan, Carbon onions as nanoscopic pressure cells for diamond formation, *Nature* 382, 433 (1996).
2. P. Burden, J. L. Hutchison, Real-time observation of fullerene generation in a modified electron microscope, *J. Cryst. Growth* 158, 185 (1996)
3. P. M. Ajayan, V. Ravikumar, J. C. Charlier, Surface reconstructions and dimensional changes in single walled carbon NT, *Phys Rev. Let.* 81, 7, 1437 (1998)
4. F. Banhart, Laplacian growth of amorphous carbon filaments in a non-diffusion-limited experiment, *Phys. Rev. E* 52, 5, 5156 (1995)
5. D. Ugarte, Curling and closure of graphitic networks under electron beam irradiation, *Nature* 359, 707 (1992)

[6.10] conductivity in nanotubes :

1. J. W. Mintmire, D. I. Dunlap, C. T. White, Are fullerenes metallic ?, *Phys. Rev. Let.* 68, 5, 631 (1992).
2. T. W. Ebbesen, H. J. Lezec, H. Hiura, J. W. Bennett, H. F. Ghaemi, T. Thio, Electrical conductivity of individual carbon nanotubes, *Nature* 382, 54 (1996)
3. N. Hamada, S.-I. Sawada, New one-dimensional conductors: Graphitic Microtubules, *Phys. Rev. Let.* 68, 10, 1579 (1992)
4. **R. Saito, M. Fujita, G. Dresselhaus, M. S. Dresselhaus, Electronic structure of graphene tubules based on C60, *Phys. Rev. B* 46, 3, 1804 (1992)**
5. M. Bockrath et al., Luttinger-liquid behaviour in carbon NT, *Nature* 397, 598 (1999)
6. P. Delaney, H. J. Choi, J. Ihm, S. G. Louie, M. L. Cohen, Broken symmetry and pseudogaps in ropes of carbon NT, *Nature* 39, 466 (1998)

7. R. S. Lee, H. J. Kim, J. E. Fischer, A. Thess, R. E. Smalley, Conductivity enhancement in single-walled carbon NT bundles doped with K and Br, *Nature*, 388, 255 (1997)
8. W. G. Wildoer, L. C. Venema, A. G. Rinzler, R. E. Smalley, C. Dekker, Electronic structure of atomically resolved carbon NT, *Nature* 391, 59 (1998)
9. T. White, T. N. Todorov, Carbon NT as long ballistic conductors, *Nature* 393, 240 (1998)

[6.11] Phonons in nanotubes

J. Yu, R. K. Kalia, P. Vashishta, Phonons in graphitic tubules: a tight binding molecular dynamics study, *Chem. Phys.* 103, 15, 6697 (1995)

[6.12] Mechanical properties of nanotubes :

1. G. Overney & al., Structural rigidity and low frequency vibrational modes of long carbon tubules, *Z. Phys.* D27, 93 (1993).
2. B. I. Yakobson, C. J. Brabec, J. Bernholc, Nanomechanics of carbon tubes : instabilities beyond linear response, *Phys. Rev. Let.* 76, 14 (1996)
3. M. M. J. Treacy, T. W. Ebbesen & J. M. Gibson, Exceptionally high Young's modulus observed for individual carbon NT, *Nature* 381, 678 (1996)

[6.13] Magnetic Properties

1. R. Saito, G. Dresselhaus, M. S. Dresselhaus, Magnetic energy bands of carbon nanotubes, *Phys. Rev. B*, 50, 19, 14698 (1994)
2. A. Bachtold et al., Aharonov-Bohm oscillations in carbon NT, *Nature* 397, 673 (1999)

[6.14] STM studies:

K. Sattler, Scanning tunneling microscopy of carbon nanotubes and nanocones, *Carbon* 33, 7, 915 (1995)

[6.15] AFM studies:

1. M. R. Falvo et al., Nanometer-scale rolling and sliding of carbon NT, *Nature* 397, 236 (1999)
2. M. R. Falvo et al., Bending and buckling of carbon NT under large strain, *Nature* 389, 582 (1997)

[6.16] Diffraction Studies:

1. J. S. Speck, M. Endo, M. S. Dresselhaus, Structure and intercalation of thin benzene derived carbon fibers, *J. of Cryst. Growth* 94, 834 (1989)
2. S. Iijima, Helical microtubules of graphitic carbon, *Nature* 354, 56 (1991)
3. **X. F. Zhang et al., Carbon-tubes; their formation process and observation by electron microscopy, *J. of Cryst. Growth* 130, 368 (1993)**
4. X. B. Zhang, X. F. Zhang, S. Amelinckx, G. van Tendeloo, J. Van Landuyt, The reciprocal space of carbon tubes: a detailed interpretation of the electron diffraction effects, *Ultramicroscopy* 54, 237 (1994)
5. S. Iijima, T. Ichihashi, Single-shell carbon nanotubes of 1-nm diameter, *Nature* 363, 603 (1993)

[6.17] EELS Studies:

K. Yase et al., Angular-resolved EELS of a carbon nanotube, *Thin Solid Films*, 222 (1996)

[6.18] TEM modelisations:

X.-D. Fan, L. A. Bursill, Principles for structure analysis of carbon NT by HRTEM, *Phil. Mag. A* 72, 1, 139 (1995)

[7] Other materials

[7.1] MX₂

1. R. Tenne, L. Margulis, M. Genut, G. Hodes, Polyhedral and cylindrical structures of tungsten disulphide, *Nature* 360, 444 (1992)
2. L. Margulis, G. Salitra, R. Tenne, M. Talianker, Nested fullerene-like structures, *Nature* 365, 113 (1993)

[7.2] MCl₂

Y. R. Hacohen, E. Grunbaum, R. Tenne, J. Sloan, J. L. Hutchison, Cage structures and nanotubes of NiCl₂, *Nature* 395, 336 (1998)

[7.3] Silicon

1. S. Osawa, M. Harada, E. Osawa, (SiC)₆₀ an idealized superatom?, *Fullerene Sci. & Technol.* 3, 2, 225 (1995)
2. R. Kamalakaran, A. K. Singh, O. N. Srivastava, Formation and characterization of silicon nanoparticles-threads, tubules and possibly silicon fullerene-like structures, *J. Phys.: Condens. Matter* 7, L529 (1995)
3. S. Nagase, K. Kobayashi, Si₆₀ and Si₆₀X (X=Ne, F- and Na+), *Chem. Phys. Let.* 187, 3, 291 (1991)
4. D. L. Williamson et al., On the nanostructure of pure amorphous silicon, *Appl. Phys. Let.* 67, 2, 226 (1995)
5. T. Makimura, Y. Kunii, K. Murakami, Light emission from nanometer-sized silicon particles fabricated by the laser

ablation method, *Jpn. J. Appl. Phys.* 35 (Part 1, No. 9A), 4780 (1996)

6. K.-M. Ho et al., Structures of medium-sized silicon clusters, *Nature* 392, 582 (1998)

[7.4] Carbides (MC)

H. Dai, E. W. Wong, Y. Z. Lu, S. Fan, C. M. Lieber, Synthesis and characterization of carbide nanorods, *Nature* 375, 769 (1995)

[7.5] Nitrogen

A. A. Bliznyuk, M. Shen, H. F. Schaefer III, the dodecahedral N₂₀ molecule. Some theoretical predictions, *Chem. Phys. Lett.* 198, (3,4), 249 (1992)

[8]C60

[8.1] Generalities on C60

1. H. W. Kroto, J. R. Heath, S. C. O'Brien, R. F. Curl, R. E. Smalley, **C60 : Buckminsterfullerene, Nature 318, 162 (1985)**
2. A. Léger, L. d'Hendecourt, L. Verstraete, W. Schmidt, Buckminsterfullerene, part B: polyhedral carbon ions as good candidates to a solution of the longest unsolved spectroscopic problem in astronomy, *Quasicrystals, Networks and Molecules of Fivefolds Symmetry*, Ed. Hargittai I., p.247 (1990)
3. R. F. Curl, R. E. Smalley, Fullerenes, *Scientific American*, oct. 1991 p.32
4. J. E. Fisher, P. Bernier, Les cristaux de fullerènes, *La Recherche* 250, 24, 46 (1993)
5. H. W. Kroto, A. W. Allaf, S. P. Balm, C60 : Buckminsterfullerene, *Chem. Rev.* 91, 6, 1213 (1991)

[8.2] synthesis of C60

1. W. Krätschmer, L. D. Lamb, K. Fostiropoulos, D. R. Huffman, **Solid C60 : a new form of carbon, Nature 347, 354 (1990)**
2. R. E. Haufler et al., Efficient production of C60 (Buckminsterfullerene), C60H36, and the solvated buckide ion, *J. Phys. Chem.* 94, 24, 8634 (1990)
3. J. B. Howard, J. T. McKinnon, Y. Makarovskiy, A. L. Lafleur, M. E. Johnson, Fullerenes C60 and C70 in flames, *Nature* 352, 139 (1991)
4. W. R. Datars, S. Galts, T. Olech, P. K. Ummat, An efficient fulleride production system, *Can. J. Phys.* 73, 38 (1995)
5. L. D. Lamb, D. R. Huffman, Fullerene production, *J. Phys. Chem.* 54, 12, 1635 (1993)
6. I. Voicu, X. Armand, M. Cauchetier, N. Herlin, S. Bourcier, Laser synthesis of fullerenes from benzene-oxygen mixtures, *Chem. Phys. Lett.* 256, 3, 261 (1996)
7. T. Ishigaki et al., Characterization of fullerenes and carbon nanoparticles generated with a laser-furnace technique, *Appl. Phys. A* 70, 121 (2000)

[8.3] fullerite :

1. M. Ferretti, A. Parisini, M. Manfredini, P. Milani, Laser-induced graphitization of fullerite, *Chem. Phys. Lett.* 259, 432 (1996).
2. I. Rusakova, A. Hamed, P. H. Hor, TEM study of C70 polycrystalline films, *J. Mater. Res.* 9, 11, 2814 (1994)
3. K. Tanigaki, S. Kuroshima, T. W. Ebbesen, Crystal growth and structure of fullerene thin films, *Thin Sol. Films* 257, 154 (1995)

Résumé : Le faisceau d'un laser CO₂, continu et de basse puissance (40-80 W), focalisé sur une cible de nitrure de bore (BN) hexagonal (poudres pressées à chaud), n'induit pas d'ablation, mais un gradient de température stable, radial le long de la surface avant. Un tel chauffage, sous basse pression d'azote, produit une croissance macroscopique de nano-tubes de BN. Les tubes croissent sur un anneau autour de l'impact, formant une couronne de tubes enchevêtrés perpendiculaire à la surface de la cible.

Cette méthode est efficace pour synthétiser des nano-tubes de BN ainsi que des nano-particules sphériques de BN, souvent riches en bore. Les tubes sont extrêmement longs (mesurés jusqu'à 120 microns), fins (typiquement 2 à 4 couches) et souvent assemblés en cordes. Dans les tubes, le BN est stœchiométrique, et bien cristallisé. Les particules sphériques sont des oignons facettés de nitrure de bore, contenant souvent un nano-cristal de bore à l'intérieur de leur cavité. La méthode de synthèse est simple et peu coûteuse. La quantité produite peut être augmentée, en balayant le rayon laser (ou la cible), en utilisant une puissance laser plus élevée, ou en collectant le matériel détaché de la cible.

La croissance se produit à température élevée, mais pas directement depuis les plaquettes de h-BN. Après dissociation puis évaporation, le bore condense dans l'atmosphère d'azote, en formant les particules sphériques riches en bore, qui se déposent autour de l'impact. Le bore se recombine ensuite avec l'azote gazeux si et seulement si le bore est liquide; d'où une croissance sur un anneau de température déterminée. En formant des coquilles de BN, certaines particules sphériques évoluent vers des extrusions tubulaires. L'évolution d'une particule sphérique vers un tube peut être entraînée par la chute de sa température. Un gradient de température se forme le long du tube, essentiellement à cause du rayonnement thermique. Le gradient décroît exponentiellement avec la longueur du tube, de l'ordre de 200 K, sur une distance de quelques dizaines de microns. La vitesse de croissance diminue aussi rapidement avec la longueur de tube. Elle est de l'ordre de 10 µm/s en début de croissance.

Mots clés : nanotube, nitrure de bore, carbone, ablation laser, fullerène, oignon, nanostructure

Abstract: The beam of a CO₂ laser, both continuous and low power (40-80 W), focused on a hexagonal boron nitride (h-BN) target (hot pressed powders), induces no ablation, but a stable temperature gradient, radial along target surface. Such a heating, in low nitrogen pressure, produces a macroscopic growth of BN nano-tubes. Tubes grow on a ring around impact, forming a crown of entangled tubes, perpendicular to target surface.

This method is efficient to synthesise BN nano-tubes and other nano-spherical BN particles, often rich in boron. Tubes are extremely long (measured up to 120 microns), mostly thin (typically 2 to 4 layers) and self-assembled in ropes. In a tube, BN is stoichiometric and well crystallised. Spherical particles are faceted BN onions, often containing a boron nano-crystal inside their cavity. The synthesis method is simple and low cost. Quantity produced may be extended for commercial purposes, by scanning the laser beam (or the target), by using a higher laser power, or by collecting the material dropped from the target,...

Growth occurs at high temperature but not directly from h-BN platelets. After dissociation and evaporation, boron condenses in nitrogen atmosphere, forming spherical particles, rich in boron, which spread around impact. Then, boron recombines with gaseous nitrogen if and only if boron is liquid, and hence, growth occurs on a ring of specific temperatures. While forming BN shells, some spherical particles evolve toward tubular extrusions. The evolution of a spherical particle toward a tube can be driven by its temperature decrease. A temperature gradient forms along the tube, essentially because of thermal radiation. The gradient is exponentially decreasing with tube length, by an order of 200 K over a few tens of microns. Growth speed also decreases quickly with tube length. It is of an order of 10 µm/s in the beginning of the growth.

Keywords: nanotube, boron nitride, carbon, laser ablation, fullerene, onion, nanostructure